

**X-RAY OBSERVATIONS OF
SS 433 AND THE QSO MR 2251 – 178**

Hongchao Pan BSc, MSc

Thesis submitted for the degree of
Doctor of Philosophy
at the University of Leicester

October 1989

X-ray Astronomy Group
Department of Physics
University of Leicester

UMI Number: U022247

All rights reserved

INFORMATION TO ALL USERS

The quality of this reproduction is dependent upon the quality of the copy submitted.

In the unlikely event that the author did not send a complete manuscript and there are missing pages, these will be noted. Also, if material had to be removed, a note will indicate the deletion.



UMI U022247

Published by ProQuest LLC 2015. Copyright in the Dissertation held by the Author.
Microform Edition © ProQuest LLC.

All rights reserved. This work is protected against
unauthorized copying under Title 17, United States Code.



ProQuest LLC
789 East Eisenhower Parkway
P.O. Box 1346
Ann Arbor, MI 48106-1346



8558740097

x281593647

ABSTRACT

This thesis reports the results of the X-ray observations of the galactic binary source SS 433 and the QSO MR 2251 – 178 made with the *EXOSAT* and *GINGA* X-ray satellites.

The *EXOSAT* and *GINGA* study of SS 433 shows that both the X-ray intensity and spectrum of the binary vary over the periods of the 163 day jet precession and the 13 day binary motion. The X-ray luminosity of SS 433 is high at the phase corresponding to the maximum separation of the Doppler-shifted optical lines, and low when the jets become edge-on. An intensity decrease of up to 50% can be seen in each energy channel while the source changes from high to low luminosity. Over the 13 day binary cycle, the X-ray source is eclipsed by the companion star at the phase of the primary optical minimum. Five such events were observed by the *EXOSAT* and *GINGA* satellites at different phases of jet precession. The X-ray spectrum of SS 433 consists of a thermal continuum and a Doppler energy shifted broad emission line. It is proved, in this thesis, that the X-ray emission of SS 433 originates in the jets and is thermal in nature. The X-ray sources of SS 433 are stable and its properties are strongly modulated by the relativistic motion of the X-ray emitting material in the jets, the jet precession and the binary motion. With the constraints from the X-ray observations, a general picture of the X-ray jets of SS 433 is established in this thesis. The X-ray jets are a continuous super-sonic plasma flow and are generated inside the funnels of a thick accretion disc located around a black hole.

Variable X-ray absorption and soft X-ray excess are found in the X-ray spectrum of MR 2251 – 178 with the *EXOSAT* observations. While there is an overall correlation between the ME(2-10 keV) and LE(0.1-2 keV) fluxes the pattern of variability can not be described by simple intensity, absorption or slope variations. It is shown, in this thesis, that it is possible to explain all the observed features by adopting the 'warm' absorber model in which the absorbing material is partially ionized by the flux of extreme ultra-violet and X-ray photons from the central continuum source. The preferred location of the absorbing material is close to the central continuum source. The recent evidence for 'cool' material in the centre of Seyfert galaxies is thus extended to include an object of significantly higher luminosity.

Declaration

I hereby declare that no part of this thesis has been previously submitted to this or any other university as part of the requirements for a higher degree. The work described here was conducted by the undersigned except for the contributions from colleagues and other workers as indicated in the text.

Hongchao Pan
潘洪潮

Hongchao Pan

潘洪潮

October 1989

Publications

Some of the work reported in this thesis has been or will be published elsewhere, as follows,

1. "Soft X-ray Excess and Variable X-ray Absorption in the QSO MR 2251 – 178", H.C. Pan, G.C. Stewart and K.A. Pounds, *Big Bang, Active Galactic Nuclei and Supernovae*, P347, Ed. S. Hayakawa and K. Sato, Universal Academy Press, Tokyo, 1989.
2. "Photo-ionization and Variability of X-ray Absorption in the QSO MR 2251 – 178", H.C. Pan, G.C. Stewart and K.A. Pounds, *Physics of Neutron Stars and Black Holes*, P375, Ed. Y. Tanaka, Universal Academy Press, Tokyo, 1988.
3. "GINGA Observations of the X-ray Eclipse of SS 433", N. Kawai, M. Matsuoka, H.C. Pan and G.C. Stewart, *Physics of Neutron Stars and Black Holes*, P231, Ed. Y. Tanaka, Universal Academy Press, Tokyo, 1988.
4. "GINGA Observations of the X-ray Eclipse of SS 433", N. Kawai, M. Matsuoka, H.C. Pan and G.C. Stewart, *Publ. Astron. Soc. Japan*, **41**, 491, 1989.
5. "The Variable X-ray Absorption and Soft X-ray Excess of the QSO MR 2251 – 178", H.C. Pan, G.C. Stewart and K.A. Pounds, *Mon. Not. R. astr. Soc.*, 470(in press), 1989.
6. "X-ray Observations of SS 433 and its Jets", G.C. Stewart, H.C. Pan, and N. Kawai, 23 ESLAB proceedings (in press), 1989.

獻給我的母親父親及妻子

To My Mother, Father, Wife and All My Family

Contents

1	Active Galactic Nuclei, Astrophysical Jets and SS 433	1
1.1	Introduction	1
1.2	Active Galactic Nuclei	2
1.3	Astrophysical Jets	4
1.4	SS 433 — Observations vs Models	8
1.4.1	X-ray Observations	8
1.4.2	Observations in Other Energy Bands	12
1.4.3	The ‘Standard’ Kinematic Model	14
1.5	Theories of Jet Acceleration and Collimation	15
1.6	Thesis Outline	18
2	X-ray Astronomy with the EXOSAT and GINGA Satellites	20
2.1	Introduction	20
2.2	EXOSAT Observatory	21
2.2.1	The Satellite	21
2.2.2	EXOSAT Experiments	23

2.3	GINGA X-ray Satellite	26
2.3.1	The Satellite	26
2.3.2	GINGA Experiments	28
2.4	The EXOSAT and GINGA Background	30
2.4.1	The Origin of the X-ray Detector Background	30
2.4.2	EXOSAT Background	31
2.4.3	GINGA Background	32
2.5	X-ray Data Analysis	35
2.5.1	Data Analysis in X-ray Astronomy — General Description	35
2.5.2	Leicester Data Analysis System	36
2.5.3	EXOSAT Raw Data Reduction	37
2.5.4	GINGA Raw Data Reduction	38
3	EXOSAT Observations of SS 433	39
3.1	Introduction	39
3.2	Observations and Data Analysis	40
3.3	Results	45
3.3.1	Modulation at the 163 Day Jet Precession Period	47
3.3.2	Modulation at the 13 Day Binary Period	57
3.3.3	A Possible Soft X-ray Excess in the Spectrum of SS 433	66

3.4	Discussion	69
3.4.1	Origin of the Energy-shifted X-ray Line	69
3.4.2	Origin of the Continuum Emission and Its Nature	70
3.4.3	Visibility of Lines — Where Is the Red Component?	71
3.4.4	Implications of the Variable Line Width	71
3.5	Summary	73
4	GINGA Observations of SS 433	75
4.1	Introduction	75
4.2	GINGA Observations and Data Analysis	76
4.3	Observation Results	84
4.3.1	X-ray Light Curves	84
4.3.2	Energy Spectrum	90
4.3.3	Spectral Evolution	97
4.4	Discussion	104
4.4.1	Is There An X-ray Eclipse - and What Is Eclipsed?	104
4.4.2	Implication of the Intensity Drop at Post-eclipse Phase in 1987 May — Oscillation of the Accretion Disc?	106
4.4.3	Implications of Variable Line Width — Again	108
4.5	Summary	110

5	The Geometric Parameters of SS 433	
	— constraints from the EXOSAT & GINGA observations	112
5.1	Introduction	112
5.2	Assumptions, Definitions and Constraints	113
5.3	Mathematical Description of System Geometry	116
5.3.1	Coordinates of SS 433 in the Sky System	116
5.3.2	Eclipse Conditions	119
5.3.3	Doppler Effect in the Jets of SS 433	122
5.4	Constraints on the Parameters of the SS 433 Geometry	124
5.5	Discussion	132
5.6	Geometrical Models of SS 433	135
5.7	Summary	138
6	Physical Properties of the X-ray Jets in SS 433	140
6.1	Introduction	140
6.2	Theory and Technique Details	141
6.2.1	Theory	141
6.2.2	Technique Details	144
6.3	Results	145
6.3.1	Parameter Distribution along the X-ray Jets of SS 433	145
6.3.2	Comparisons with the Observations	151

6.4	Discussion	158
6.4.1	Geometrical Models of SS 433 — Further Discussion	158
6.4.2	Physical Properties of the SS 433 Jets	159
6.4.3	Jet Acceleration Mechanisms	162
6.5	Summary	164
7	The Variable X-ray Absorption and Soft X-ray Excess of the QSO MR 2251 – 178	166
7.1	Introduction	166
7.2	EXOSAT Observations	168
7.3	Results	170
7.3.1	Intensity Variability	172
7.3.2	X-ray Spectrum	173
7.3.3	Variability of X-ray Absorption	173
7.4	Models	179
7.4.1	Two Emission Component Model	179
7.4.2	Leaky Cold Absorber	179
7.4.3	Warm Absorber	179
7.5	Discussion	185
7.6	Conclusions	187

8	Conclusions	188
8.1	Introduction	188
8.2	Summary of the Work Reported in This Thesis	189
8.2.1	SS 433	189
8.2.2	QSO MR 2251 – 178	192
8.3	Future Prospects	192
8.3.1	Future Observations of SS 433 & MR 2251 – 178	192
8.3.2	Future Theoretical Modelling of SS 433	194
8.4	SS 433, Astrophysical Jets and AGN	195
	Appendices	197
A	Transformation of Coordinate Systems Used for Analysis of SS 433	197
B	Calculation of the Roche Lobe of a Binary System	202
C	Hydrodynamic Equations	206
D	Configurations of Three Suggested Geometrical Models of SS 433	209
	References	222
	Acknowledgements	231

Chapter 1

Active Galactic Nuclei, Astrophysical Jets and SS 433

1.1 Introduction

It has been known for some years that a few percent of galaxies contain hyperactive central regions (Begelman, Blandford & Rees 1984). The power output from this active region can exceed the luminosity of a thousand normal galaxies (i.e. $\sim 10^{46}$ erg s⁻¹) and equal the mass-energy equivalent of several solar masses per year. However, the seat of this activity is, compared with the size of a galaxy (tens of kiloparsecs), extraordinarily compact as indicated by rapid variability of the radiation flux on time scales as short as minutes. The term Active Galactic Nuclei (AGN) is a common name used for signifying any extragalactic object with such substantial emission in excess of normal stellar processes such as starlight, HII regions, supernovae etc. AGN include quasi-stellar objects (QSOs), quasi-stellar radio sources (Quasars), Seyfert galaxies, radio galaxies, Low Ionization Nuclear Emission Regions (LINERs), BL Lac objects and some narrow emission line galaxies (e.g. Lawrence 1987; Netzer 1987).

Powerful extragalactic radio sources comprise two extended regions containing magnetic fields and synchrotron-emitting relativistic electrons, each linked by a jet to a central compact radio source located in the nucleus of the associated galaxy (e.g. Begelman, Blandford & Rees 1984). These jets are collimated streams of plasma that emerge from the nucleus in opposite

directions and are responsible for transporting mass, momentum and energy from the nucleus of active galaxy into the extended radio sources. The properties of Active Galactic Nuclei are sufficiently similar, although there are differences, as shown by the very different radio features, that there is little doubt that they can be accounted for by a similar or closely related physical model. Therefore, a better observational and theoretical understanding of the nature and origin of these jets may eventually provide insights into the nature of all active nuclei, not just those associated with strong radio sources.

Astrophysical jets, which are often defined as sources showing an elongated morphology (Bridle & Perley 1984), have recently been observed in a wide range of celestial objects from powerful extragalactic sources to the galactic objects. Among these jet sources, the ‘unique’ galactic object SS 433, due to its close distance and its observable features over the whole electromagnetic waveband, has been attracting the close attention of many astronomers for the past ten years. The discovery of mildly relativistic jets in SS 433 led to the conjecture that SS 433 may be a scaled-down version of some of the extragalactic radio sources. Probing the nature and origin of the jets in SS 433 may lead directly, therefore, to an understanding of some of the astrophysical jets which power extragalactic radio sources.

The basic properties of AGN, astrophysical jets and SS 433 are reviewed in the following sections as the background for the discussions in this thesis. The model theories used to interpret SS 433 phenomenon and jet formation are also summarized below. The final section of this chapter gives an overview of the thesis.

1.2 Active Galactic Nuclei

Active Galactic Nuclei are among the most luminous and compact objects in the universe and observed throughout the whole electromagnetic spectrum from 100 MHz radio waves to 100 MeV γ -rays (Begelman, Blandford & Rees 1984). Although the observational properties of AGN are extremely diverse, there is, as argued by Lawrence (1987), only one kind of Active Galactic Nucleus and the varieties arise from three degree of freedom: dust opacity, viewing angle of a relativistic jet and duty cycle of activity. Fig. 1.1 gives a sketch of a typical AGN structure.

It is widely accepted that the central engine of AGN consists of a super massive accretor,

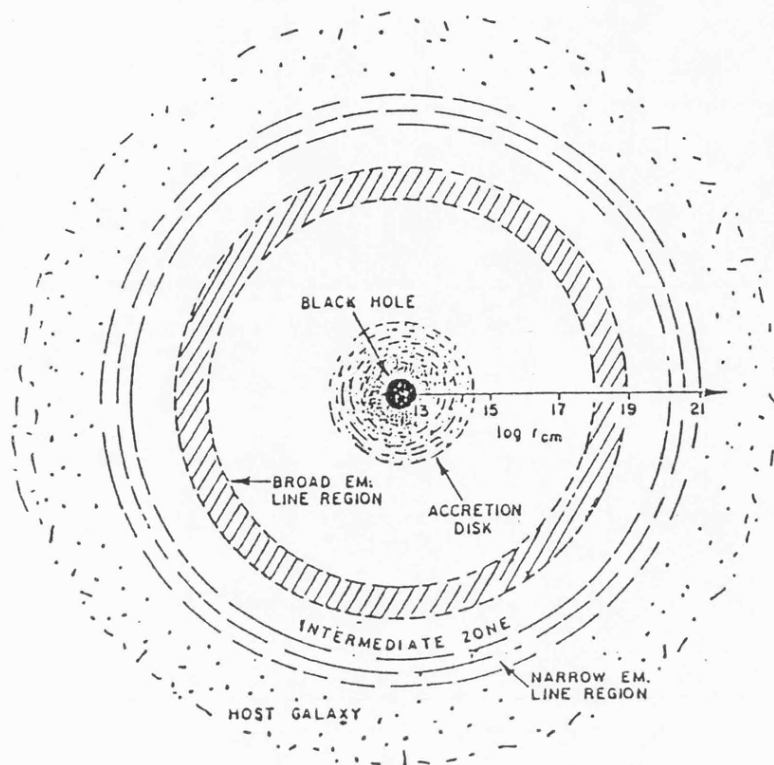


Figure 1.1: The structure of a typical AGN, taken from Krolik (1988)

probably an accreting black hole and an accretion disc surrounding it where the kinetic energy and angular momentum of accreting material is dissipated into radiation or outward moving matter winds and beams. The overall dimensions (see Netzer 1987), as deduced from light variability arguments, are of the order of $10^{16}L_{46}$ cm where L_{46} is the optical-UV luminosity in the unit of 10^{46} erg s^{-1} .

Outside the central engine is the line emitting region of AGN, which can be divided into the Broad Line Region (BLR) with dimension of $\sim 10^{18.5}L_{46}$ cm, and the Narrow Line Region (NLR) with dimension $\sim 10^{21}L_{46}$ cm. The BLR is a region composed of small photo-ionized clouds, or filaments, with typical density of $\sim 10^{10}$ cm^{-3} , column density of 10^{22-23} atoms cm^{-2} and covering factor of ~ 0.15 (Smith *et al.* 1981). These clouds, moving with relative velocities of 3000-10000 $km s^{-1}$, give rise to the broad line profiles. The NLR consists of lower density ($\sim 10^{4-6}$ cm^{-3}) photo-ionized gas which occupies a relatively large volume of space. Because the density is low (especially in the outer regions), strong narrow forbidden lines (e.g. [OIII]) can be seen. The full widths at half maxima (FWHM) of the Doppler broadened lines lie in the range 150 \sim 1400 $km s^{-1}$ (Gaskell 1987). It is not clear whether there is a smooth transition zone, of intermediate densities and velocities,

between these two regions. The powerful ultraviolet continuum suggests photo-ionization as the dominant heating and excitation process in the BLR and NLR.

The continuum radiation of AGN evenly spreads over up to ten decades in frequency from the radio into the γ -ray range. The X-ray spectral index, α , seems to be 'universal' in the sense that α , for most observed AGN cluster tightly around a value of 0.7 (Rothschild *et al.* 1983; Turner & Pounds 1989).

The physical processes responsible for the continuum emission from AGN are not clearly known and three basic processes, bremsstrahlung, synchrotron radiation, and Compton scattering, are normally involved .

1.3 Astrophysical Jets

The jet family comprises various members with diverse properties. The observations of astrophysical jets have been reviewed by several workers (see Mihalas & Winkler 1986; Kundt 1987) and the various examples are illustrated below.

Extragalactic Jets

The jets in the extragalactic radio sources are the most intensively studied jet class. An

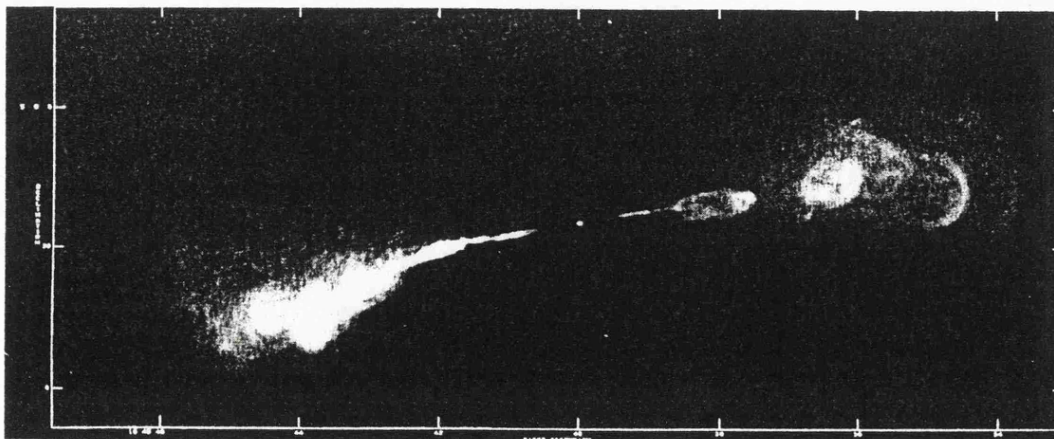


Figure 1.2: 6 cm VLA imaging of Hercules A with a 0.5 arcsec beam, taken from Dreher & Feigelson (1984)

example of these jets is shown in Fig. 1.2.

(a) powerful radio galaxies

The jets from powerful radio galaxies are typically 100-300 kpc in linear extent and tend to be edge brightened. The hot spots at the ends of jets indicate that these jets are highly supersonic. The ratios of the large jet and counterjet flux and the persistence of one-sidedness on the VLBI scale, suggests that the jets are at least mildly relativistic.

(b) weak radio galaxies

The jets associated with weak radio galaxies generally appear, by contrast, more complex and are edge darkened. The jets are believed to be sub- or trans-sonic flows because most of the radio power in a weak source originates fairly close to the associated galactic nuclei and because the more distant regions exhibit irregular morphology.

(c) quasars

The jets associated with quasars show some unique morphological characteristics. They are nearly all one-sided and far more radio luminous than the jets associated with comparably strong radio galaxies.

(d) Seyfert galaxies

Jets are also found in the nuclei of many Seyfert radio sources. These jets are very faint and twisted with length of ≤ 1 kpc.

Stellar Jets

(a) young stellar objects

The jets often appear in very young stars, the Pre-T-Tauri or Herbig-Haro-exciting stars. These jets are supersonic with velocity of $50 \sim 400 \text{ km s}^{-1}$. The jets have lengths of $\sim 0.01 - 0.2 \text{ pc}$ and opening angles of $3^\circ - 10^\circ$.

(b) Sco X-1

Sco X-1, which resembles an extragalactic triple radio source, consists of a central component coincident with the position of the X-ray and optical source, and two

separate jet-like lobes at distances of ~ 1 pc on opposite sides of the central source.

(c) Cyg X-3

Recent VLBI observations show evidence for jets in this intense, highly variable source. Two oppositely directed lobes are found to expand asymmetrically at a speed of $\sim 0.35c$.

(d) SS 433

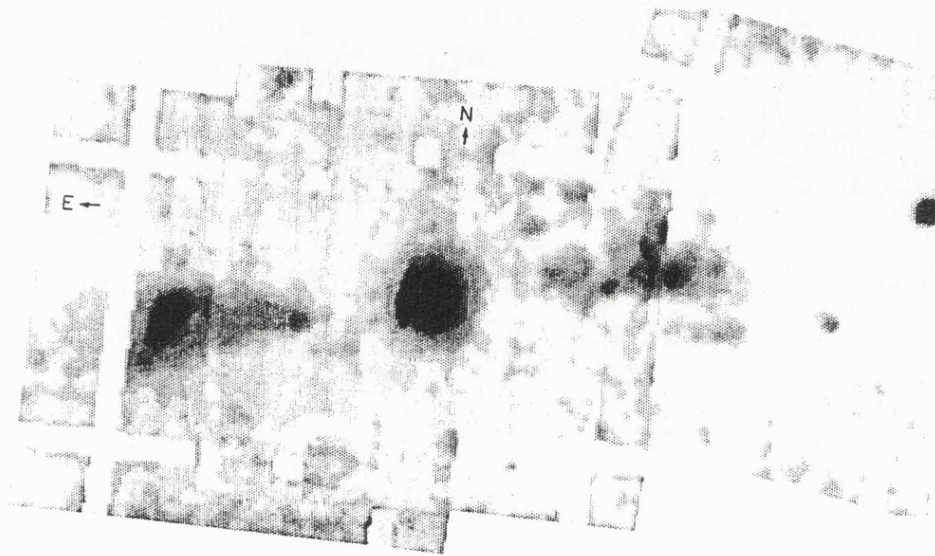


Figure 1.3: Jets in SS 433, IPC X-ray imaging taken from Watson *et al.* (1983)

The X-ray image of the region around SS 433 is shown in Fig. 1.3. The bright central region includes the X-ray emission from the jet at radii close to the compact object. Also, clearly visible, are the regions where the outer portions of the jet interact with the surrounding medium.

(e) CH Cyg/R Aquarii

The symbiotic stars CH Cyg and R Aquarii exhibit linear radio features that have been interpreted as jets. In the case of CH Cyg, the outflow velocity is in excess of 3000 km s^{-1} and the presence of a white dwarf accreting at or near the Eddington limit has been inferred. The jet feature in R Aquarii has also been seen in the optical and near ultraviolet.

Galactic Centre

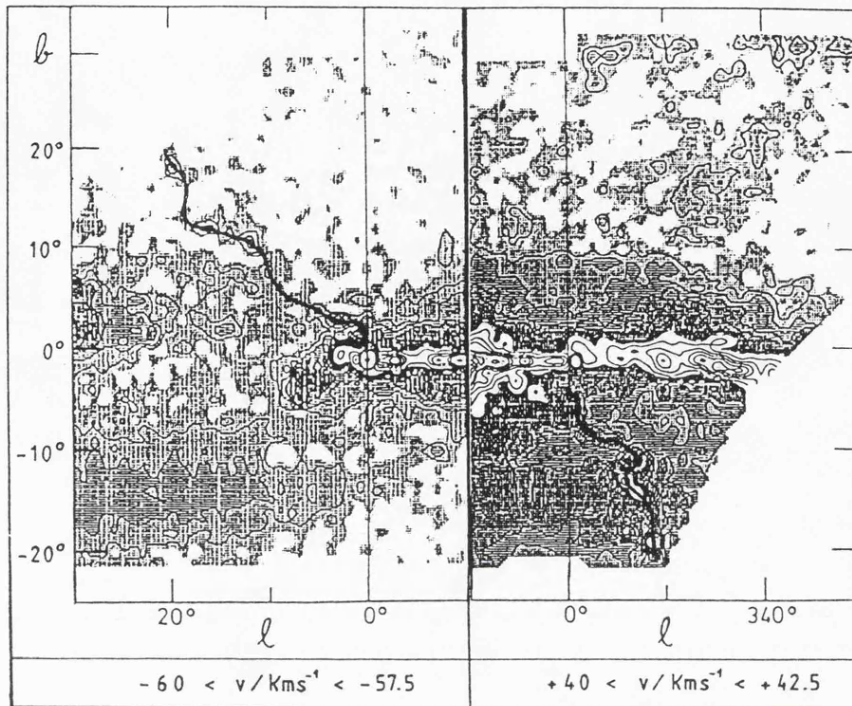


Figure 1.4: 21 cm radio map of our Galactic Center, taken from Kundt (1987)

An unusually intense radio source, which is almost coincident with an infrared source and the dynamical center of a conspicuous distribution of gas clouds is contained in our galactic center. The elongated radio feature perpendicular to the galactic plane has been interpreted as a pair of jets. Fig. 1.4 gives the map of the twin-jet in our galactic center.

Supernova Remnants

The morphological similarity between bipolar jet flows and certain peculiarities of supernova shells is attributed to the existence of jets in the supernova remnants. As an example, a deep [OIII] photograph of the Crab Nebula is shown in Fig. 1.5 where a feature protruding from the northern rim of the Crab Nebula can be seen. It is suggested that the jet in the supernova remnants originates from the central pulsar.

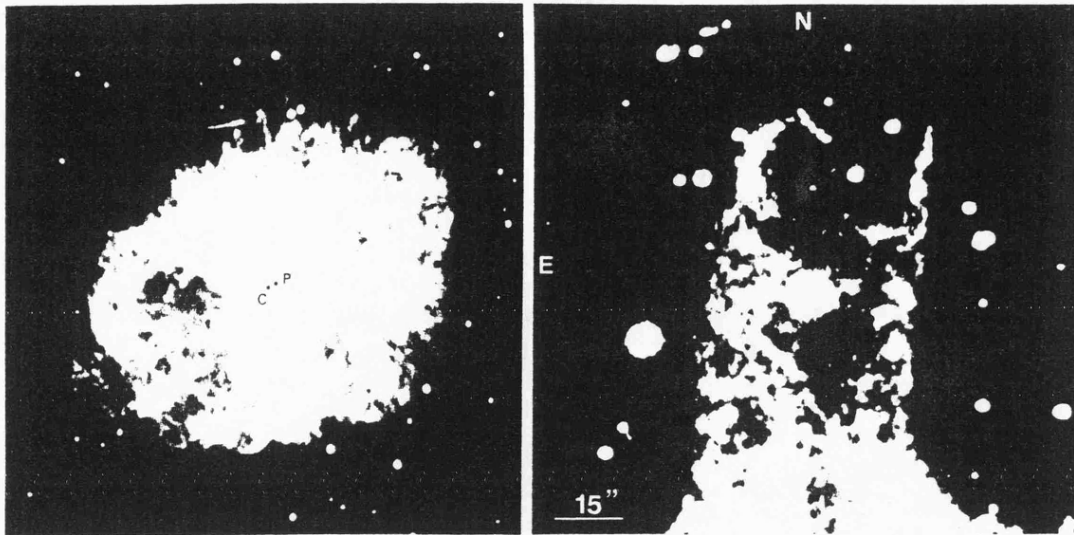


Figure 1.5: Deep optical emission line imaging of Crab Nebula, left: Crab Nebula with jet feature, right: detail structure of the jet, taken from Fesen & Gull (1986)

1.4 SS 433 — Observations vs Models

SS 433, the 13 day galactic binary source centrally located in the elliptical supernova remnant W50 whose radio and X-ray overlay map is shown in Fig. 1.6, has been intensively monitored in a wide energy band from radio to γ -ray since the discovery of the extraordinary, time-variable Doppler-shifted Balmer and HeI emission lines in 1978. It has now been established beyond reasonable doubt that SS 433 is a luminous binary system exhibiting collimated jets of gas whose axis precesses with a period of ~ 163 days. The previous observations of this ‘unique’ object have been comprehensively summarized by Margon (1984) and the following discussions only give its basic properties.

1.4.1 X-ray Observations

Over the past twenty years since the launch of *UHURU* in 1970, numerous X-ray observations of SS 433, which cover every phase of the jet precession and binary motion of the source, have been carried out with the X-ray satellites *UHURU* (1970 December-1973 March) (Forman *et al.* 1978), *ARIEL-5* (1974 November-1980 January) (Seward *et al.* 1976; Ricketts *et al.* 1981), *HEAO A-2* (1977 October-1978 October) (Marshall *et al.* 1979), *EINSTEIN* (1979 April-1980 October) (Seward *et al.* 1980; Seaquist *et al.* 1982; Watson *et al.* 1983; Grindlay *et al.* 1984), *ARIEL-6* (1979 August, 1980 July, August) (Ricketts *et al.* 1981), *TENMA* (1983 September)

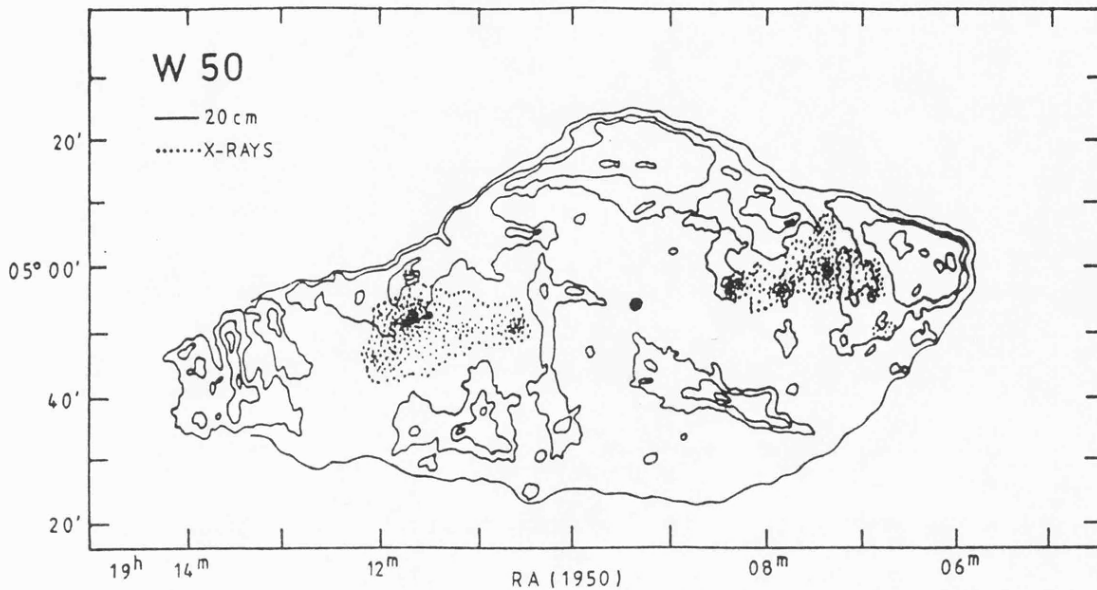


Figure 1.6: Radio and X-ray map of W50 with SS 433 located at the center, taken from Kundt (1987)

(Matsuoka, Takano & Makishima 1986), *EXOSAT* (1983 October-1985 October) (Watson *et al.* 1986; Stewart *et al.* 1987 and this thesis) and *GINGA* (1987 May-1989 May, this thesis). The first reported observations of the X-ray source A1909+04 of SS 433 in this rather crowded region of the X-ray sky were made during 1974 November-1975 July by Seward *et al.* (1976) with the *ARIEL-5* sky survey detectors. In these observations, the source A1909+04 was reasonably well located and its errorbox overlapping part of the supernova remnant W50 indicated the association of the X-ray source with W50. Noticing the point source feature and the intensity variability of A1909+04, Seward *et al.* suggested the source as a candidate for the remnant of the Supernova progenitor. Combining the X-ray observations spanning over the period of 1970 December-1973 March, Forman *et al.* included 4U1908+05 (SS 433) in the 4U catalog in which the position and intensity of the source is given. A typical observed 2-10 keV flux for the source is about $1 \times 10^{-10} \text{ erg cm}^{-2} \text{ s}^{-1}$, which implies an X-ray luminosity of a few times $10^{35} \text{ erg s}^{-1}$, much smaller than the inferred optical luminosity and the kinetic energy of the material in the jets. Although *UHURU* and early *ARIEL-5* observations yielded some significant results, they did not suggest anything unusual about the object as compared with the several dozen brighter X-ray sources in the plane of the Galaxy. *EINSTEIN* and *EXOSAT* first revealed the exciting features of SS 433 at X-ray energies.

The spatial structure of the large-scale X-ray jets of SS 433 was directly observed by the imaging detectors on the *EINSTEIN* Observatory. The first X-ray imaging presented by

Seward *et al.* (1980) showed that 90% of the soft (1-3 keV) X-ray flux is coincident with the optical object while the remaining 10% is contained in two diffuse X-ray emission lobes, symmetrically extending at least 30 arc min from SS 433, and exactly aligned along the long axis of W50. Thus from these imaging observations, the association of SS 433 and W50 is irrevocably confirmed, the evidence for the existence of the ejected jets is further strengthened, the ambiguity in the kinematic beam model between the inclination of the precession axis and the opening half angle of the cone is removed, and a minimum age of several thousand years is established for the ejection phenomenon. Analysis of further imaging data by Watson *et al.* (1983) shows that the spectrum of the X-ray lobes differs markedly from the central source, and the emission from the X-ray lobes must reflect the interaction of the ejected jets with the ambient medium surrounding the star and within W50. The observed X-ray imaging of SS 433 with *EINSTEIN* also offers an explanation of why W50 is so much larger than any other remnants with similar age.

The X-ray intensity variability of SS 433, as first seen during the *ARIEL-5* observations (Seward *et al.* 1976) and confirmed later by Marshall *et al.* (1979) with the *HEAO A-2* experiment, is highly significant with a factor of $2 \sim 3$ on the typical time scale from days to months. Although flare like events occasionally correlated with radio flares were reported by Seaquist *et al.* (1982) from the *EINSTEIN* Observatory observations, no short-term (minutes to seconds) variability has yet been found, in contrast to many, but not all, compact galactic X-ray sources. Either the nature of the compact object in SS 433 is different from the bright X-ray variables, or, perhaps more likely, our view in X-rays does not extend completely into the central, compact volume. The *HEAO A-2* and *EINSTEIN* data are of insufficient quantity to search for X-ray variability analogs to the 163 day period; a tentative discussion of this effect in the very extended *ARIEL-5* observations over 1974-1980 period is given by Ricketts *et al.* (1981), in which the folded light curve showed modulation of the X-ray flux in the 163 day jet precession period. No evidence for periodicity at 13 day was found by *ARIEL-5* due to the varying lengths of the observation periods in each data point. A search for variability synchronized with the 13 day orbital period has been reported by Grindlay *et al.* (1984), with inconclusive results: variability at this frequency is not statistically significant, but the data when phased with the optically measured binary period do agree in phase with broad band photometry. Given the number of different phases of interest in the SS 433 orbital period, the importance of this agreement is unclear. The modulation of the X-ray intensity with the binary phase was finally confirmed by *EXOSAT* observations (Stewart *et al.* 1987; and this

thesis) made over one binary cycle with sampling interval of ~ 1 -3 days. A simultaneous X-ray and optical primary eclipse was found and the analysis of the partial X-ray eclipse set some constraints on the parameters of the system such as mass ratio of the two bodies and the length of the X-ray jets, though fairly large uncertainties were left because of the incomplete coverage of the eclipse period.

The existence of an emission line feature in the X-ray spectrum of SS 433 was first reported by Marshall *et al.* (1979) from the *HEAO A-2* experiment over the 2-30 keV energy range. Due to the lack spatial resolution, the data of *HEAO A-2* must apply to the sum of compact and the diffuse components of the source. The X-ray spectrum could be fitted with either a power law or with a thermal bremsstrahlung, but both models require a very prominent (580 eV equivalent width) emission line at 6.8 keV. The observed equivalent width suggests a thermal plasma of temperature ~ 14 keV, with large uncertainty. A spectrum from *ARIEL-6* (Ricketts *et al.* 1981) shows a similar emission feature. Both *HEAO A-2* and *ARIEL-6* spectra were obtained at the epoch when the accretion disc was edge-on in which the Doppler-shift effect of the iron line is not obvious, so the modulation of the iron line in the X-ray spectrum of SS 433 by the jet precession period was not found by *HEAO A-2* and *ARIEL-6*. The iron line feature was missed from the spectrum obtained from the *EINSTEIN* observations (Grindlay *et al.* 1984). However, as the iron line of SS 433 was still observed by *ARIEL-6* in 1980 between two *EINSTEIN* observations, this could be due to the poor energy resolution of the MPC at 6 keV because over the whole period of *EINSTEIN* Observatory, no iron line was observed for any object (Band 1988). Using *EXOSAT* observations, Watson *et al.* (1986) showed that the centre energy of the emission line in the X-ray spectrum is modulated with the 163-day precession period with the same Doppler shift as the optical emission lines. The centre energy of the emission line is consistent with that of helium-like iron. Only the blue-shifted line was visible in the spectra. These results were interpreted as showing that the X-ray emission was from a thermal plasma in the relativistic jet near the compact object, and that emission from the jet at the far side from the observer was hidden by the accretion disc so that only the blue-shifted portion of the jet was visible. A thermal bremsstrahlung with inclusion of a black body component gives the acceptable model fit for the *EXOSAT* spectrum.

1.4.2 Observations in Other Energy Bands

1) Radio Observations

Observations of SS 433 have been made at radio wavelengths with a large variety of techniques, including single-dish studies at many frequencies, the Very Large Array (VLA) and the Very-Long-Baseline Interferometry (VLBI).

The intensity of the central source of SS 433 is very highly and erratically variable, at least by a factor of four, at virtually all the radio wavelengths, on timescales as rapid as one day, and occasionally hours (Margon, 1984 and references therein). The flux density in the observed regimes is around 10^{22} erg s⁻¹ Hz⁻¹, so that the total flux in the radio is of order 10^{32} erg s⁻¹ (Shaham 1981). No variations analogous to the 163 and 13 day optical cycles of SS 433 have been found although extensive observations have been analyzed (Johnston *et al.* 1981, 1984). The coupling between radio and optical variability is weak or perhaps nonexistent (Margon 1984). The evidence for correlated radio and X-ray variability was seen in one of the two simultaneous X-ray and radio observations (Seaquist *et al.* 1982).

The strong variability makes it hard to determine a radio spectrum of SS 433, however, a spectral index $\alpha \simeq 0.1$ for the range 0.408-5 GHz is found (Ryle *et al.* 1978) and in the range of 2.7-10.5 GHz, a negative α value ~ -0.6 is obtained (Seaquist 1981), common for non-thermal sources.

Radio observations have confirmed the existence of corkscrew-shaped trails, which are the instantaneous locus of gas clouds that, individually, move in straight lines away from the central source. The VLA measurements (Gilmore & Seaquist 1980; Gilmore *et al.* 1981; Hjellming & Johnston 1981ab) demonstrate that changes in the arc second radio structure of SS 433 on time scales of tens of days can be correlated with expected space motions of the precessing jets with a precession cone half angle $\sim 20^\circ$, and inclination $\sim 80^\circ$. This provides strong support for the ‘standard kinematic model’ (explained below). The VLA data, combined with the kinematic model parameters, also allow the determination of the position angle of the jet axis on the sky (i.e. P.A. $\simeq 100^\circ$) and give a good estimate of the distance to SS 433 (5.5 ± 0.5 kpc) (Hjellming & Johnston 1985).

2) Infrared Observations

SS 433, as a weak but detectable infrared source (Band 1986) is variable on various time scales of hours or less (Clark & Milone 1981; Kodaira & Lenzen 1983; Kodaira, Nakada & Backman 1985) and days (Wynn-Williams & Becklin 1979; Clark & Milone 1981). Both flux and colour of the source vary substantially from night to night with the possible periodicities similar to the 163 and 13 day optical cycles of SS 433. From the comparison of the infrared light curves with the optical ones of Leibowitz *et al.* (1984), it is concluded, within the context of an accretion disc model, that the majority of the infrared flux in the SS 433 system comes from the disc, and that the hot spot responsible for the ‘hump’ in the visual and infrared light curves has colour similar to the average of the disc (Kodaira, Nakada & Backman 1985).

Continuum colors are around $J(1.25 \mu) = 9.8$; $H(1.64 \mu) = 9.1$; $K(2.2 \mu) = 8.5$; $L(3.5 \mu) = 7.7$; and $L'(3.8 \mu) = 7.6$ (Shaham 1981). The infrared spectrum when corrected for the interstellar reddening fits reasonably well to a hot blackbody with free-free emission from ionized gas (McAlary & McLaren 1980). The total flux is of order $\leq 10^{35} \text{ erg s}^{-1}$. Line emission has been found and the lines have complex structures (Shaham 1981).

3) Optical Observations

SS 433 is relatively bright in the optical region of the spectrum and the optical observations of SS 433 constitute the richest set of data.

The observed optical emission lines include the Balmer and HeI lines in the ‘Moving’ system, as well as H_α , H_β , and H_γ , HeI5875, 6678, 7065, HeII4686 and CIII/NIII 4640/50 in the ‘rest’ system (Margon 1984).

The enormous frequency shifts of the Balmer and HeI lines arise from the radial projections of motions in the inner beam region, which is restricted to about $10^{14} - 10^{15} \text{ cm}$ by the brightness of the lines as well as the simultaneity of their intensity variations. The ‘moving’ optical lines have fluxes of $\geq 10^{34} \text{ erg s}^{-1}$ and also a variable structure. Evidence for an accretion disc is present in the short-term variations of the velocities, which are interpreted as arising from ‘nodding’ motions of the disc (Katz *et al.* 1982), and in the variations in the line intensities (Anderson, Margon, & Grandi 1983).

The ‘stationary’ lines have a complex and variable structure (e.g. Margon *et al.* 1979; Murdin,

Clark & Martin 1980; Dopita & Cherepashchuk 1981; Crampton & Hutchings 1981; Kopylov, Kumaigorodskaya & Somova 1985; Falomo *et al.* 1987), and show several components which evolve in time with possible periodicities of 13 and 163 day in their centers.

Other emission lines are occasionally found in the optical spectra. Absorption lines of FeII are reported to appear occasionally, and exhibit the 13 and 163 day periodicities (Shaham 1981; Margon 1984).

The continuum colors of SS 433 average around $V=14.2$, $B=16.3$, $U=16.9$, and $M_v \leq -3.5$ and the visible flux is $\leq 10^{37}$ erg s^{-1} (Shaham 1981; Margon 1984). The flux is variable with time scales of hours and days. This variability has 13 and 163 day periods. Very rapid optical variability (0.1 ms - 1 s) has not been found (Margon 1984).

4) Ultraviolet Observations

Although the interstellar extinction makes it very hard to detect SS 433 in the ultraviolet, the ultraviolet observations of SS 433 reported by Benvenuti (1979) set an upper limit of 10^{33} erg s^{-1} on the observed reddened $\lambda\lambda 1200 - 3300$ flux. The corresponding de-reddened value is, probably, $\geq 10^{41}$ erg s^{-1} .

5) Gamma-ray Observations

Gamma-ray observations of SS 433 reported by Lamb *et al.* (1983) suggest the existence of one or possibly two intense Gamma-ray emission lines near 1 MeV, from which a Gamma-ray luminosity $\sim 2 \times 10^{37}$ erg s^{-1} is inferred assuming isotropic radiation. The observed wavelengths of the Gamma-ray features have been attributed to a nuclear transition of ^{24}Mg at the Doppler shift of the jets appropriate for the epoch of the Gamma-ray observations, although there are several difficulties with this interpretations.

1.4.3 The ‘Standard’ Kinematic Model

The observational data can be almost universally interpreted in terms of a ‘standard’ kinematical model which was first suggested by Milgrom (1979) and developed by Abell and Margon (1979) with the determination of the parameter values.

In this kinematic model, the gas material is expelled at a remarkably stable speed of $0.26c$ from a central source into two jets that are collimated and oppositely aligned to within a few degrees. The jet directions trace out the surface of a cone of half-angle 20° and the central axis of this cone is inclined at 79° to the line of sight. The axis of these jets rotates with a period of ~ 163 days, which is generally interpreted as resulting from precession of the accretion disc.

There is a significant amount of scatter about this mean precessional motion naively describable as velocity deviations of several thousand km s^{-1} ; this scatter has been resolved into periodic and random components, each of which contains interesting information (see Margon 1984). The kinematic model also leaves unspecified almost all of the interesting aspects of the system such as the nature of the compact object and the companion star, the mechanisms of jet acceleration, collimation and precession.

Usually the jets are assumed to be accelerated within the central region of an accretion disc, a natural locus of high luminosity and energy density. They are also assumed to be directed along its instantaneous axis, so that their changing directions reflect the changing orientation of the disc. Models (Katz 1980; van den Heuvel, Ostriker & Petterson 1980) in which the entire accretion disc precesses because of the presence of a binary companion are attractive, in part because they predict and naturally explain its presence. This companion also supplies the disc with matter. More complex models have been suggested (Sarazin, Begelman & Hatchett 1980).

1.5 Theories of Jet Acceleration and Collimation

Observations have revealed the ‘unique’ features of the collimated material jets in various celestial objects. However, the interpretation of the initial acceleration and collimation of these astrophysical jets remains a major unsolved problem in astrophysics. In principle, jets will be created wherever two basic elements, collimator and propulsor, exist. The collimator can be a nozzle in a spinning cloud, as first proposed by Blandford and Rees (1974) for jet collimation and acceleration (see below), or a funnel in a thick accretion disc, which was originally suggested by Lynden-Bell (1978) and has been investigated further by several workers. The jets formed in the collimator near the compact object can be accelerated,

basically, by thermal gas pressure, magnetic stress, and radiation pressure and accordingly the jet model are summarized below.

Thermal Pressure Driven Jets

1) Nozzles

In this twin-exhaust model, the relativistic plasma generated in the centre of a spinning cloud of denser gas is collimated into the two oppositely-directed jets due to the hydrodynamic pressure of the thermal gas in the cloud. The jet flows become trans-sonic when the external gas pressure falls to roughly half of the stagnation pressure of the jet flows. The shapes of the jets adjust so that they act like de Laval nozzles.

This mechanism, however, does not seem adequate to explain the formation of jets in SS 433 because SS 433 is a galactic object and probably has no dense ellipsoidal gaseous envelope as required by the model. The model is not suitable for extragalactic jets either since the VLBI observations indicate that the jets are collimated on scales ≤ 1 pc and the necessary gas pressure for the model would lead to an X-ray luminosity in excess of the observed value.

2) Thermally Driven Winds

The gas in the outer parts of an orbiting accretion disc is heated by the X-rays radiated by AGN. Its sound speed will exceed the escape velocity when the gas is heated to the Compton temperature (Blandford, 1986). Most of the incident radiation will then be converted into the kinetic energy of a quasispherically escaping wind. If some supplementary collimating process is present, slow speed jets would be created.

Hydromagnetic Jets

Jets may be produced electromagnetically in the accretion disc. The potential difference across a disc threaded by open magnetic field lines is, if certain conditions are satisfied, sufficient to accelerate particles to relativistic velocities (Begelman, Blandford & Rees 1984).

In the mechanism of hydromagnetic jets, the 'hoop' stresses associated with toroidal magnetic field, which are wrapped around the jet and exist both in the jet itself and in the surrounding gas, pinch the outflowing gas and create jets.

Radiation Driven Jets

1) Line Locking

Jet acceleration by radiation pressure with ‘line locking’ fixing the terminal velocity, a process previously suggested for quasar absorption lines (Strittmatter & Williams 1976 and references therein), was first considered in the context of SS 433 by Milgrom (1979) and studied in some detail by Shapiro *et al.* (Shapiro, Milgrom & Rees 1986 and references therein) and Pekarevich *et al.* (1984).

Consider an element of gas in a radiation field of a continuum source. Suppose that the dominant momentum transfer is through Lyman-line absorption by some hydrogenic ion in the gas and that the underlying continuum radiation flux is sharply reduced at frequencies above the Lyman edge of that ion. The gas which starts at rest can then be accelerated outward by radiation pressure up to a terminal velocity $\beta_t = 0.28$ when the Doppler-shifted value of the Lyman-edge wavelength becomes to equal to the local, comoving Lyman α wavelength.

The line-locking mechanism can explain the value, constancy, and uniformity of the observed jet velocity in SS 433. However, in order for line locking by the hydrogen atoms in the jet of SS 433 to occur, three conditions have to be satisfied: (1) the radiative acceleration of the flow must begin at a minimum distance of 2×10^{13} cm so that the continuum luminosity is sufficient to accelerate the jet; (2) the gas must be highly clumped to have an efficient acceleration; (3) the underlying radiation must be highly collimated along the jet axes if highly super-Eddington luminosities are to be avoided. These conditions, in turn, make it difficult for the line locking to work.

2) Radiation Acceleration in a Funnel

The configuration of a thick accretion disc with two narrow funnels along its rotation axis is obtained when large accretion rates, leading to dense, radiation supported bright discs, are present (Calvani & Nobili 1983). Plasma will then be collimated into two narrow funnels formed along the rotation axis of a thick accretion disc orbiting a supermassive black hole, and accelerated to form the relativistic jet by radiation pressure (assuming Thompson scattering).

The main problem with this mechanism is that when the radiation drag is considered, only

mildly relativistic velocities can be obtained ($\gamma \sim 1.5$) unless more exotic systems are considered (such as that for an electron-positron beam) (Piran 1982; Abramowicz & Sharp 1983).

1.6 Thesis Outline

This thesis contains results of the X-ray observations of galactic binary source SS 433 and the QSO MR 2251 – 178. The observations were made with the X-ray instruments aboard the European X-ray Observatory satellite (*EXOSAT*) and Japanese X-ray satellite *GINGA*.

SS 433 was intensively monitored both by *EXOSAT* (over the period of 1983 October-1985 October) and *GINGA* (in 1987, 1988 and 1989 May). The purposes of these observations were to study the nature of the SS 433 X-ray spectrum; to investigate the variations of the X-ray spectrum and intensity of SS 433 over the periods of jet precession and binary motion; and to precisely determine the X-ray eclipse profile so that strong constraints can be put on the binary system.

The X-ray results of MR 2251 – 178 are from the 15 separate *EXOSAT* observations. The variable X-ray absorption and soft X-ray excess in the X-ray spectrum of MR 2251 – 178 are of particular interest in these *EXOSAT* observations. By studying the spectrum of the QSO, a better understanding of the physical conditions of the central region of MR 2251 – 178 can be achieved.

A brief introduction to the experiments on board the *EXOSAT* and *GINGA* satellites is given in Chapter 2 and the methods used for the reduction of the *EXOSAT* and *GINGA* data are summarized in the same chapter. The results of a full data analysis of the *EXOSAT* observations of SS 433 are presented in Chapter 3, in which the modulations of jet precession and binary motion on the X-ray properties of SS 433 are greatly revealed. In Chapter 4, three observations made with the *GINGA* satellite around the primary optical minimum are reported. From these observations, the X-ray eclipse profile is determined with the best accuracy ever. Based on the results of the X-ray observations presented in this thesis, constraints on the system geometry of SS 433 are derived in Chapter 5 and at the same time mathematics which can be adopted to generally describe the motion of the binary is established. With the X-ray spectra obtained over the X-ray eclipse by the *GINGA* observations, a model independent jet temperature profile is derived in Chapter 6. The physical conditions of the X-ray jets

of SS 433 and the constraints on the jet formation mechanisms from the X-ray observations are also discussed in this Chapter. In Chapter 7, the results of *EXOSAT* observations of the QSO MR 2251 – 178 are presented and the relationships between photo-ionization effect, soft X-ray excess, and variation of the X-ray absorption is discussed. Finally, in Chapter 8, a summary of the work reported in the thesis on SS 433 and MR 2251 – 178 is given and future prospects for the study of these two objects are discussed.

Chapter 2

X-ray Astronomy with the EXOSAT and GINGA Satellites

2.1 Introduction

Since the discovery of the first non-solar X-ray source, Sco X-1, by Giacconi *et al.* in June 1962 (Giacconi 1980), X-ray astronomy has become an indispensable tool in the study of the universe and profoundly changed our view of astrophysical phenomena. The launch of a series of X-ray satellites from *UHURU* to *EINSTEIN* in the 1970's has rapidly accelerated the development of X-ray astronomy and brought it to maturity.

Launched on May 26 1983 from the Vandenberg Air Force Base in California with a Thor-Delta rocket, *EXOSAT*, the European X-ray observatory satellite, has undoubtedly become another cornerstone in the development of X-ray astronomy. Although the satellite was built by the European Space Agency (ESA) it has benefited the astronomical community worldwide. During its operational life time, from its launch in 1983 May to the premature end of its mission in 1986 April due to the failure of the attitude control system, *EXOSAT* made 1780 pointed observations of a wide variety of objects, and was the main source of X-ray data for the whole astronomical community during that period.

The purpose of the *EXOSAT* mission was the detailed study of cosmic X-ray sources in the energy range of 0.05-50 keV, which involved the precise location of X-ray sources and the

study of their spectroscopic and temporal characteristics. These scientific objectives were satisfied by the four instruments aboard the observatory, which consisted of two identical low energy (0.05-2 keV) imaging telescopes (LE1, LE2), a medium energy (ME) large area proportional counter array ranging from 1 to 50 keV and a gas scintillation proportional counter spectrometer (GSPC) covering the energy range 2-30 keV.

GINGA, the third Japanese X-ray astronomy satellite, following *HAKUCHO* and *TENMA*, was launched with a Mu-3S-II-3 rocket on February 5 1987, shortly after the end of the *EXOSAT* mission, from the Kagoshima Space Centre in Japan. The satellite comprises three instruments: the large area proportional counter (LAC), which is the main experiment on the satellite, the all sky monitor (ASM), and the gamma-ray burst detector (GBD). The main objective of the *GINGA* mission is the study of time variability and spectrum of galactic and extragalactic X-ray sources in the energy range of 1.5-37 keV using the LAC.

In the following sections, the experiments aboard the *EXOSAT* (section 2.2) and *GINGA* (section 2.3) satellites are briefly reviewed. The background experienced by the satellites is described in section 2.4 and X-ray data reduction method is introduced in section 2.5. All information on the *EXOSAT* satellite in this chapter is derived from descriptions given by Taylor *et al.* (1981), de Korte *et al.* (1981), Turner *et al.* (1981), Peacock *et al.* (1981) and White & Peacock (1988) and that on *GINGA* is taken from Makino (1987) and Turner *et al.* (1989).

2.2 EXOSAT Observatory

2.2.1 The Satellite

An exploded view of the *EXOSAT* satellite is shown in Fig. 2.1. *EXOSAT* was designed as a three-axis stabilized space platform with an inherent orbit correction capability. The four X-ray instruments were mounted on this platform and were all co-aligned with the optical axis, defined by two star trackers each mounted on an LE telescope.

A highly eccentric ($e \sim 0.93$, apogee 191,000 km, perigee 350 km, inclination 72.5°) and long-period (90.6 hours) orbit was selected for the satellite to maximize the number of possible

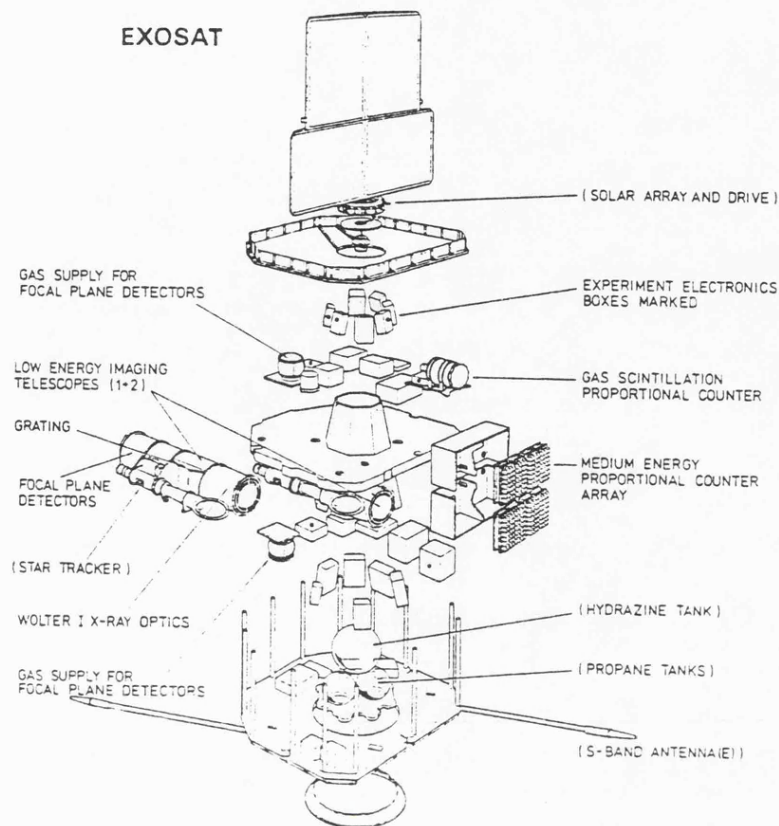


Figure 2.1: An exploded view of the *EXOSAT* Observatory, taken from Taylor *et al.* (1981)

lunar occultations and to allow long uninterrupted observations. With this unique orbit, the observatory could operate in two principle modes: (1) pointing mode, in which the observatory could point continuously up to 76 hours at any target subject only to celestial constraints imposed by the sun, the moon and the earth; (2) occultation mode which was to be used primarily by the medium energy experiment to locate X-ray sources to a limiting accuracy of a few arc seconds, although this second capability was never used.

The attitude and orbit control system (AOCS) of the satellite used a propane cold-gas thruster system for both slew manoeuvres and fine pointing, and three gyros, together with one of two star trackers and a sun sensor for attitude control. Four manoeuvre rates were available. The attitude could be maintained to within ~ 1 arc second.

Due to the highly eccentric orbit, *EXOSAT* was visible from the Villafranca ground station in Spain for practically the entire operation time and there was no need to use any on-board data storage. The *EXOSAT* data were processed and compressed by the on-board computer (OBC) and transmitted to the station at a telemetry rate of 8 kb/s. The OBC also controlled the operation of the AOCS.

2.2.2 EXOSAT Experiments

1.) EXOSAT Low Energy Imaging Telescope Experiments (LE)

The *EXOSAT* low energy (LE) experiments comprised two practically identical telescopes covering the energy range of 0.05-2 keV. As displayed in Fig. 2.2a, each of the telescopes consisted of double nested Wolter I optics with a geometric area of $\sim 90 \text{ cm}^2$ and a focal plane assembly containing a channel multiplier array (CMA) and a position sensitive proportional counter detector (PSD), either of which could be placed at the X-ray focus.

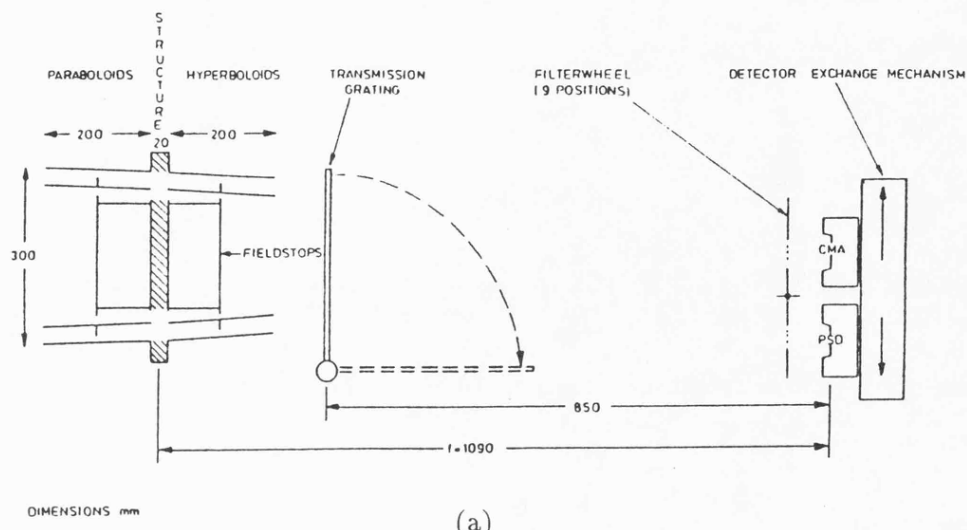
The LE experiment could be operated in the imaging mode with either the PSD or the CMA in the focal plane. By inserting filters (up to four) with various transmission bands into the focused X-ray beam in front of the CMA, broad-band spectrophotometry could be performed. The most commonly used filters during the mission were 3000Å Lexan (3Lx), AL/P and boron. By placing a transmission grating in the X-ray beam behind the mirror, high resolution spectroscopy could be achieved.

The CMA consisted of a multi-channel chevron with no inherent spectroscopic capability. The choice of filter dictated the energy response with the overall energy window covered by the filter combinations ranging from 0.05 to 2.0 keV. Its field of view was 2.2° and the spatial resolution varied from ~ 10 arc seconds FWHM on-axis to ~ 300 arc seconds at the edge of the field of view. There were two CMAs aboard the satellite. One CMA (in telescope 2) failed on 1983 October 28, while the other CMA (in telescope 1) functioned perfectly until the end of the satellite operations.

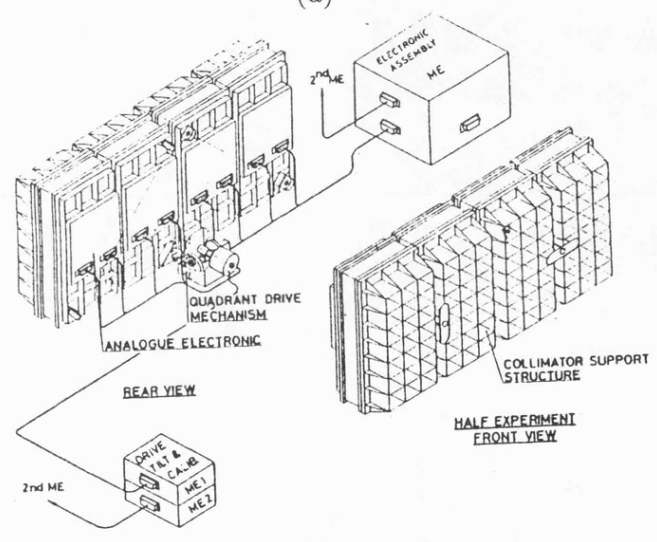
The PSD was a parallel plate proportional detector with a $1.7 \mu\text{m}$ polypropylene entrance window and filled with P20-gas (80% Argon-20% methane) at 1.1 bar. The detector was sensitive in the energy range 0.1-2 keV and had intrinsic energy resolution. The field of view of the PSD was 1.5° and its spatial resolution depended on the X-ray energy and the location of the focused X-ray on the detector. Unfortunately both PDS's failed early in the performance verification phase because of a form of internal breakdown.

2.) EXOSAT Medium Energy Experiment (ME)

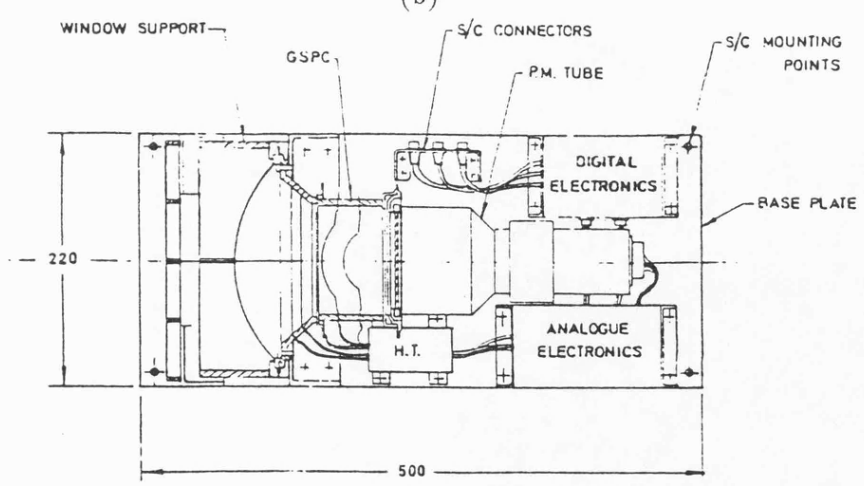
The medium energy experiment aboard the *EXOSAT* satellite was a large area multi-wire



(a)



(b)



(c)

Figure 2.2: a) A schematic of a single telescope system, from de Korte *et al.* (1981); b) A schematic of one half of the array of the ME experiment, taken from 'EXOSAT Observers Guide II'; c) The EXOSAT GSPC experiment, from 'EXOSAT Observers Guide II'.

proportional counter array consisting of eight detectors with a total effective area of ~ 1600 cm². A schematic of one half of the detector array is given in Fig. 2.2b.

Each detector comprised two gas cells made from a single block of machined beryllium to minimize payload mass. The front cell was filled with a gas mixture of Argon and Carbon Dioxide, and had a ~ 37 or 62 μm beryllium window. It was sensitive to X-ray radiation in the energy range 1-20 keV. The rear was a Xenon cell with a 1.5 mm beryllium window, covering the energy range of 5-50 keV. Both cells were at a pressure of two atmospheres.

The collimators, which were formed from lead glass microchannel plates, defined the square field of view of the ME detectors to be $0.75^\circ \times 0.75^\circ$ (FWHM) and also supported the thin beryllium windows for the Argon cell.

The eight detectors were grouped in pairs to form quadrants and the four quadrants were each mounted on hinges and driven by two separate mechanisms so that they could be co-aligned to observe an X-ray source or offset to simultaneously monitor the background.

Anticoincidence and pulse rise time discrimination techniques were combined to reduce the particle background and achieve the required background rejection efficiency for the *EXOSAT* ME experiment. The measured efficiency for background rejection was 99% in Argon cell and 98% in Xenon cell.

The output from each gas cell was pulse height analysed into 128 channels. The broad energy range (1-50 keV) and good energy resolution ($\Delta E/E \sim 20\%$ at 6 keV) of the ME experiment were sufficient to detect iron lines in many X-ray sources. The large effective area and narrow field of view of the detector array, backed up by the unique conditions provided by the satellite orbit, made it suitable for the detailed study of the time variable features of X-ray sources.

3.) EXOSAT Gas Scintillation Proportional Counter (GSPC)

The gas scintillation proportional counter (GSPC) on *EXOSAT* was a single spherical electric field detector which, as shown in Fig. 2.2c, consisted of a gas cell filled with a one atmosphere mixture of 95% Xenon and 5% Helium, and a 4 mm thick UV transmissive exit window. The gas cell had a thin machineable ceramic body and a spherical section free-standing beryllium X-ray entrance window with a 20 cm diameter and 175 μm thickness.

Although the GSPC was sensitive in the 2-80 keV band, the energy ranges of 2-32 keV (gain 1.0) and 2-16 keV (gain 2) were most commonly used during the mission. These energy ranges were divided into a maximum of 256 PHA (pulse height analysis) channels. As a medium energy broad band spectrometer, the GSPC had a factor of two improved energy resolution ($\Delta E/E \sim 10\%$ FWHM at 6 keV) compared to the *EXOSAT* ME experiment. However, its effective area was an order of magnitude lower (only 165 cm²) than that of the ME proportional counter array so that the GSPC was used in conjunction with the ME experiment to perform detailed measurements of the spectra of strong sources.

The burst length discrimination technique, which rejected events with exceptionally long and short durations, was used for particle background rejection in GSPC. The achieved background rejection efficiency below 10 keV was 97% and from 10 to 20 keV was 96%. This lower background rejection efficiency severely limited the sensitivity of the spectrometer.

The 45' (FWHM) field of view of the GSPC was defined by a mechanical collimator similar to the individual detector collimator used on the *EXOSAT* ME experiment. With such narrow field of view, the diffuse X-ray background in GSPC was negligible.

Unlike the ME experiment, the GSPC could only operate co-aligned with the optical axes of all other experiments and could not monitor the background simultaneously. A number of different modes were available for the GSPC through changing the dynamic range of the detector.

2.3 GINGA X-ray Satellite

2.3.1 The Satellite

The satellite configuration is displayed in Fig. 2.3. There are three instruments, the Large Area Counters, the Gamma-ray Burst Detector and the All Sky Monitor, mounted on the satellite. The total weight of the satellite is about 420 kg.

GINGA is three-axis stabilized with a momentum wheel to control the movement of the spacecraft in the X-Y plane, which is defined as parallel to the plane of the solar paddles, and three magneto-torquers to manoeuvre and stabilize the Z-axis, which is perpendicular to the

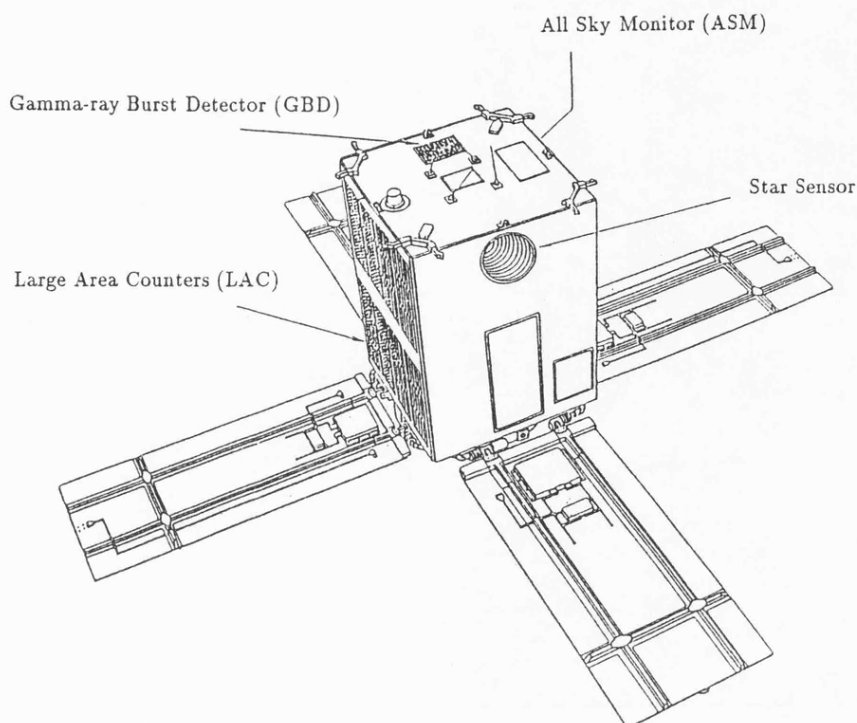


Figure 2.3: *GINGA* satellite, taken from Turner *et al.* (1989)

X-Y plane. The satellite attitude is measured and controlled with four gyros and two CCD star trackers in a closed loop system. The pointing accuracy is better than six arcminutes, while the attitude reconstruction has an accuracy of approximately one arcminute.

GINGA is a low inclination, low altitude orbit satellite. The perigee and apogee of the satellite are about 550 km and the orbital inclination is 31° . The satellite has a period of 95 minutes and is in contact with the ground station on five of the fifteen orbits in an observing day. Such orbital parameters imply that there is up to a 30 minute earth occultation for each orbit.

The data are stored during the orbit in an on-board bubble-memory data recorder with a capacity of 41.9 Mbits, and transmitted to the ground station on the five contact orbits at two frequencies, UHF and S-band, with a choice of three different bit rates.

The satellite Z-axis should be held at angles greater than 135 degrees away from the sun in order to satisfy the power constraints and the angle between the sun and LAC has to be greater than 90° so that the occasional solar contamination of the observations can be avoided. These constraint limit the region of sky observable with the LAC, However, the entire sky is accessible in a six months period.

2.3.2 GINGA Experiments

1.) GINGA large area counter (LAC)

The large area proportional counter, the main instrument of *GINGA*, consists of eight identical sealed collimated proportional counters, covering the energy range 1.5-37 keV. The effective area of each counter is 565 cm² so that the total effective area of LAC is $\sim 4500\text{cm}^2$.

Each counter has a 62 μ beryllium entrance window and a 3.9 cm active depth, and is filled with a 1.86 atmosphere gas mixture of 75% Argon, 20% Xenon and 5% Carbon Dioxide at 273 K. It is five-side guarded in order to minimize background counts. An exploded view of one of these counters is shown in Fig. 2.4.

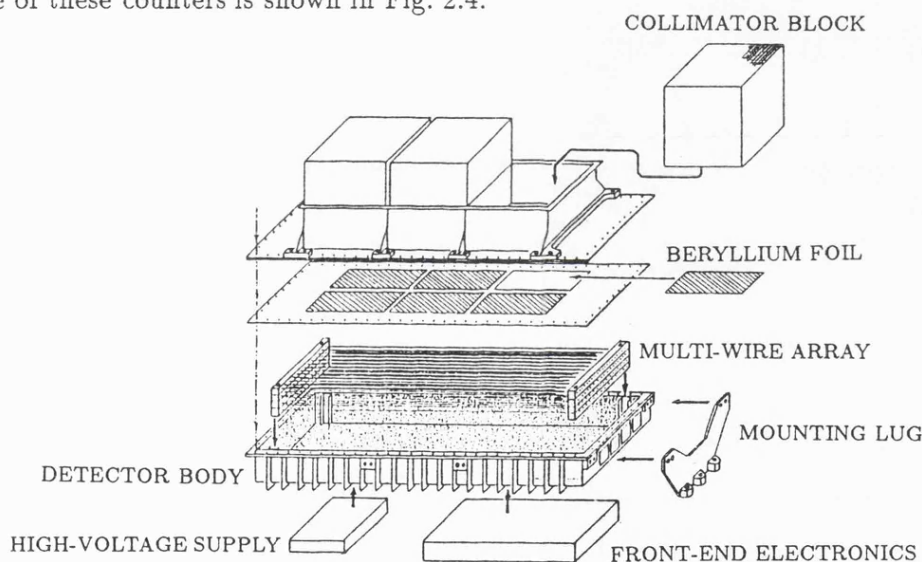


Figure 2.4: An exploded view of one of LAC counters, taken from Turner *et al.* (1989)

The field of view of LAC is elliptical ($1^\circ \times 1.8^\circ$ FWHM), with the longer side parallel to the Z-axis, and is defined by honeycomb hexagonal collimators made of thin stainless steel sheet. This field of view gives a 3σ confusion limit of ~ 0.2 mCrab.

Two main modes, MPC and PC, are available for the digital data processing. In the MPC mode, the qualified X-ray events are pulse-height analysed into 48 channels over the energy range 0-37 keV. The first 32 energy channels cover from 0 to 18.5 keV with 0.58 keV per channel, and the remaining 16 channels correspond 18.5-37.0 keV (1.16 keV per channel). The energy resolution of the LAC at 6 keV is 18% (FWHM) and scales as $E^{-0.5}$ over the full energy range. The time resolution is mode-dependent. The highest one is 0.98 ms at the expense of spectral information in PC mode.

2.) GINGA all sky monitor

The all sky monitor (ASM) aboard *GINGA* consists of two proportional counters, each having three independent counting cells and fields of view criss-cross to each other. The total effective area of the ASM is about 400 cm² and the effective energy range covers approximately 1.5-30 keV.

The counters are filled with 1 atmosphere Xenon and have 50 μ beryllium windows. The field of view of each cell, defined by a stacked-mesh collimator, is 1° \times 45° FWHM, and is tilted with respect to the spacecraft Z-axis. Different slant angles for the individual cells will resolve source confusion.

The ASM experiment can continuously monitor many sources in a wide area of the sky and record significant intensity variations as well as transient phenomena. A scan of the sky is performed by slowly rotating the spacecraft around the Z-axis at a fixed slew rate of 20 min/revolution or 0.3°/sec.

3.) GINGA gamma-ray burst detector (GBD)

The GINGA gamma-ray burst detector (GBD) comprises a proportional counter (PC) and a NaI(Tl) scintillation counter (SC), which can detect gamma-ray bursts with a high time resolution and measure the burst spectra over a wide energy band ranging from 1.5 to 400 keV.

The proportional counter is filled with one atmosphere Xenon gas and has a 64 μ beryllium window. The counter has a 100 cm² effective area and is sensitive over the energy range of about 1.5-30 keV, which is divided into 16 PHA channels on a pseudo-logarithmic scale. No collimator is used.

The NaI(Tl) scintillator is 1 cm thick, and has a 0.25 mm aluminum entrance window. Its effective area is 60 cm². The counter covers the hard X-ray energy range from about 10 to 400 keV with 32 PHA channels. Again, there is no collimator installed.

A separate solid state detector with 1 cm² area is used to monitor the radiation environment. Whenever an excessive flux is recorded, a warning signal is produced and distributed to the LAC, ASM and GBD.

2.4 The EXOSAT and GINGA Background

2.4.1 The Origin of the X-ray Detector Background

In X-ray astronomy, the background in the X-ray detector is an important factor. The detector background rate is largely determined by high energy radiation. This can arise from various components including penetrating cosmic rays and their secondaries produced in nearby matter, diffuse cosmic X-rays, and the trapped electrons and protons in the earth's magnetic field (Van Allen belts or earth's radiation belts). In addition, radioactivity induced in the detectors or spacecraft materials by the cosmic rays and the trapped protons in the geomagnetic field can also contribute to the detector background. For detectors operating in the soft X-ray band below 1 keV, even UV skyglow can produce undesirable effects (Peterson 1975).

The relativistic galactic cosmic rays are isotropically distributed in near earth space with intensity on the order of $1\text{-}3 \text{ nuclei cm}^{-2} \text{ s}^{-1}$ (Peterson 1975). They can contribute to the detector background by directly ionizing the material in the sensitive volume of the detector or via nuclear and electromagnetic interactions producing secondaries in the atmosphere, the spacecraft, or the material immediately local to the sensitive volume. For example, the gamma rays produced by cosmic rays can enter the detector within the aperture (appear as an incident flux), or after being scattered by the shield or collimator.

The trapped radiation from Van Allen belts is another important contributor to the detector background, particularly for instruments on spacecraft with low inclination and low altitude orbit such as *GINGA*. The highest intensities of the trapped radiation occur in the region known as the South Atlantic Anomaly (SAA), where energetic charged particles, intensive secondary gamma rays and neutrons produce sufficient background to cause very high counting rates in anticoincidence shields and detectors. It is necessary to turn off the detector high voltage supplies when the spacecraft passes through the SAA to prevent premature failure of proportional counters or gain changes in the photomultipliers of scintillation counters. Thus the SAA typically causes a loss of observing time of $\sim 20 - 25\%$ (Peterson 1975).

While the electron component only influences the background during exposure to high electron fluxes, the effects of the protons can persist by inducing radioactivity in the satellite

material. These could arise either from activation by captured neutrons generated in reactions occurring in mass outside the detector or from spallation radioactivity due to breakup of target nuclei (Peterson 1975).

The cosmic diffuse X-rays form a background against which observations are made. Although there are no certain models for the origin of these cosmic diffuse X-ray radiation, it is suggested that for the cosmic diffuse X-ray radiation below 100 keV they may originate in rapidly evolving AGN and for those higher than 10 MeV may be due to early explosive galaxies (e.g. Ikeuchi 1988).

2.4.2 EXOSAT Background

Since *EXOSAT* was launched in a highly eccentric orbit and its instruments were operated above 50,000 km, outside the earth's radiation belts, the background contribution of the trapped electrons and protons was negligible. In general, at least two components, i.e. the particle induced background and the diffuse X-ray background, must be considered in the *EXOSAT* experiments.

Although the particle induced background rate was rather high in the LE experiment with the PSD in the focal plane, it was reduced to less than $0.12 \text{ cts cm}^{-2} \text{ s}^{-1}$ using the rise time discrimination technique in the PSD with efficiency of 60%. The total background counts in the PSD was expected to be about $0.4 \text{ cts cm}^{-2} \text{ s}^{-1}$ in 0.1-2.0 keV band. The background in the configuration with the CMA in the focal plane was dominated by two rather different components, the CMA dark current and the UV sky background. The filters helped to reduce the contamination of UV photons. The particle background rate of the CMA depended on the level of solar activity. The minimum value was $8 \times 10^{-6} \text{ cts s}^{-1} \text{ pixel}^{-2}$ (1pixel = 4×4 arc seconds) in the central region and this level was achieved for about 10% of the observations. For the remaining 90%, the particle background count rate was within a factor of two of the quiescent value on the average. The sensitivity of the CMA was limited by the background.

The dominant background in the *EXOSAT*ME experiment was not the cosmic diffuse X-rays, because the ME field of view was rather small, but the particle events from the solar wind and radioactive lines caused by the decay of residual plutonium in the beryllium windows and detector bodies. The typical background count rate in the Argon chamber was 4.3 cts s^{-1}

per detector in the 1-10 keV band and in the Xenon chamber was 40.6 cts s^{-1} per detector in the 10-30 keV band after the particle background rejection techniques were applied. The ME background was generally very stable, although there were occasional background flares due to enhancements in the solar particle flux. These flare events were easily removed from the analysis and did not result in a substantial loss of data. Clearly the sensitivity to the observations of weak sources was limited by the level and variability of the in-orbit ME background.

Burst length discrimination was used for the GSPC particle background rejection. The residual of the rejected particle background in the GSPC was 45.4 cts s^{-1} in the 2-32 keV energy band. The GSPC background varied on time scales of several days and years. The spectral shape of the background was found to be constant for the short time scale variations and slightly variable on longer time scales. Again, due to the small field of view of the GSPC, the diffuse X-ray background was negligible. The background rejection efficiency of the GSPC was not as high as that in ME instrument, thus it severely limited the sensitivity of the experiment.

2.4.3 GINGA Background

GINGA is a low earth orbit satellite and operates at an altitude of 5,000 km high. Therefore, all the background components described in section 2.4.1 have to be taken into account during its operations.

The origin and behaviour of the *GINGA* LAC background has been studied in detail by Hayashida *et al.* (1989). In general, the LAC background comprises the cosmic diffuse X-ray background and the internal background induced by charged particles and gamma rays in the satellite orbit. The diffuse X-rays enter the counter within the field of view of the collimator, or leak through the detector walls. The charged particles and gamma rays arise from the cosmic rays and the trapped particles in the earth radiation belts, and their induced radiations form the *GINGA* in-orbit background. Occasional contaminations from the sun and the bright limb of the earth can occur for some orientations of the spacecraft during the observations.

The internal background caused by charged particles and gamma rays was minimized by

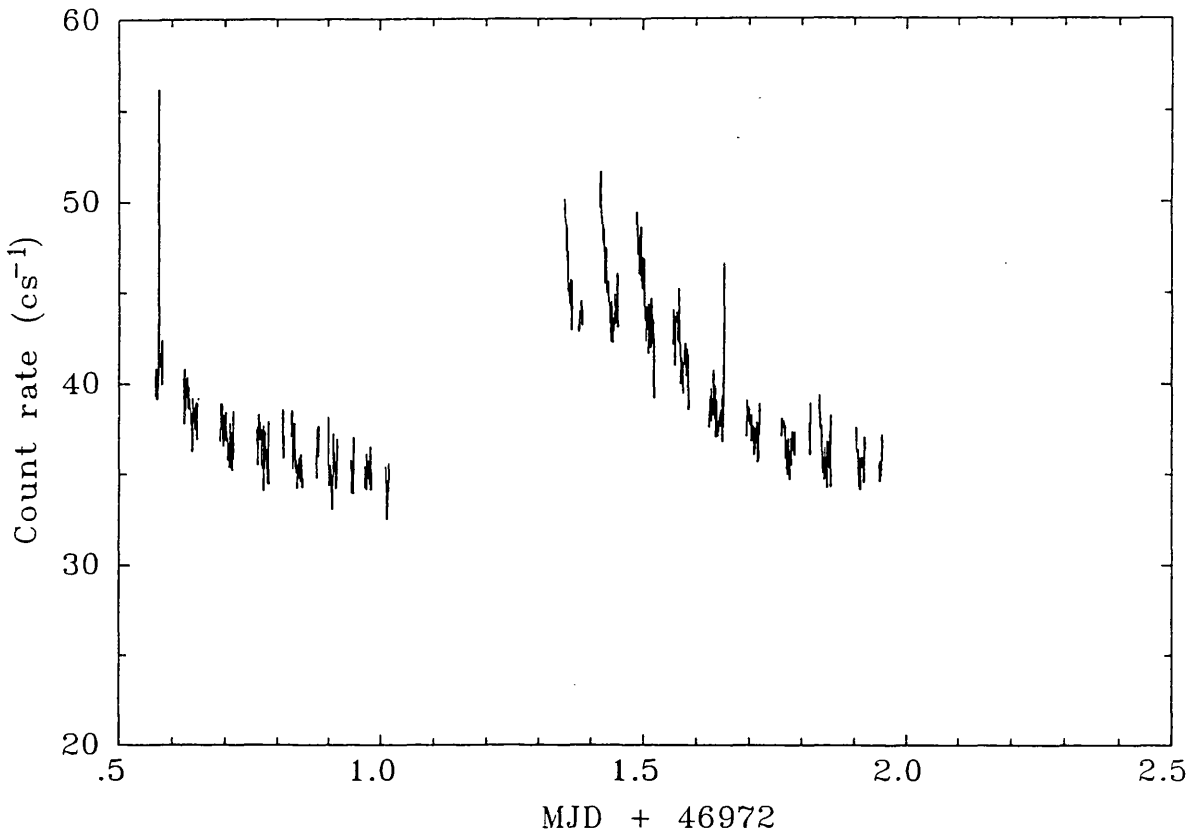


Figure 2.5: Time variation of the *GINGA* internal background

using a highly efficient wall-less guard counter system, and the contribution of the diffuse X-rays from outside the collimator field of view is reduced by shielding the LAC with 0.2 mm thick tin shields. Keeping the field of view of LAC away from the sun (relative angle greater than 90°) during the operations reduces the solar contamination.

The internal LAC background varies with time, as shown in Fig. 2.5, and satellite positions in a complex way. The background rate peaks every 24 hours, corresponding to the satellite passing through the SAA, and then decays on a short (~ 1 hour) and a long (~ 10 hour) time scale as the satellite emerges from the SAA, due to the radioactivity induced in the satellite material by the protons in the SAA. The spectrum of the internal background is complex and includes various fluorescent lines. The diffuse X-ray background of LAC is constant with time but varies over the sky plane. The diffuse background rate measured over the full LAC energy range is ~ 18 cts s^{-1} , while the total background rate varies from about 70 cts s^{-1} to 150 cts s^{-1} . Fig. 2.6 shows the spectrum of the LAC background.

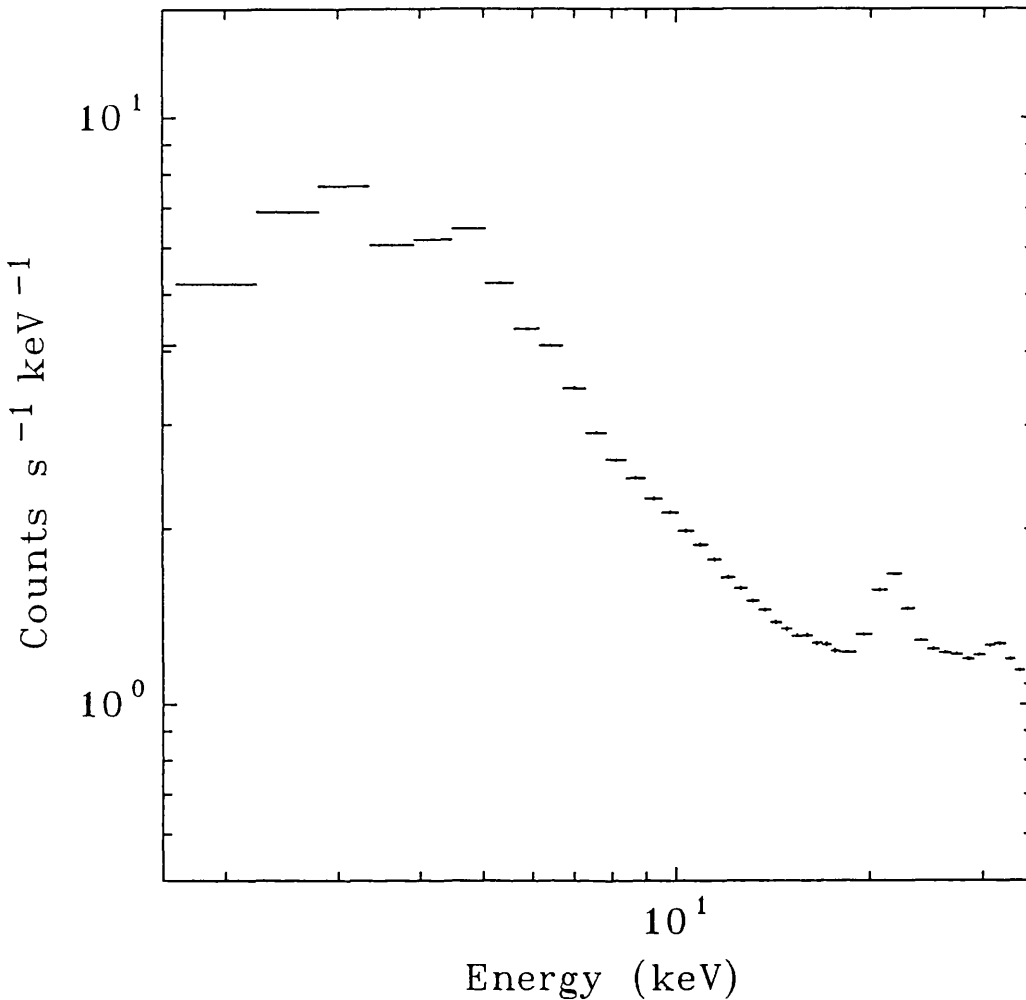


Figure 2.6: The spectrum of the *GINGA* LAC background

Unlike the *EXOSAT*ME experiment, the *GINGA* LAC has no direct means of simultaneously monitoring the internal background and the background is estimated from indirect measurements by using a number of housekeeping and other count rates, from both the LAC and the accompanying instruments on *GINGA*. The two methods generally used for estimating of the background radiation are specified in Hayashida *et al.* (1989).

The major limitation of the LAC sensitivity is not from source counting statistics, but from the systematic error in background subtraction. However, this uncertainty is not simply due to the accuracy with which the internal background can be estimated, but, in most cases, dominated by the uncorrected intrinsic fluctuations of the diffuse X-ray background over the sky plane. The 3σ sensitivity of the LAC in the 2-10 keV band is 2.6 cts s^{-1} , which equals a flux of about $6 \times 10^{-12} \text{ ergs cm}^{-2} \text{ s}^{-1}$ for a Crab-like spectrum.

2.5 X-ray Data Analysis

2.5.1 Data Analysis in X-ray Astronomy — General Description

X-ray astronomy studies astrophysical phenomena in the energy band from a hundred eV to a hundred keV, where the particle nature of electromagnetic radiation dominates completely. X-ray data are collected on a photon-by-photon basis by detectors, and observable properties of sources such as intensity, location, angular extent, or spectral shape are therefore statistical quantities to be estimated from the observational data to within a statistically determined error.

There are three different counting rates to be considered during the observations: 1) the photon flux from the X-ray source being observed; 2) the photon flux from the diffuse X-ray background; 3) the flux of the in-orbit background generated by charged particles and gamma rays. The origin and behaviour of the detector background have been described in the above section. In general, measurement of the X-ray source must be made by subtracting the backgrounds.

The detected X-ray photons can convey much information about sources such as their spatial structure, temporal variability, and spectral characteristics etc. This information may be extracted through the various techniques of data analysis, including imaging processing, time series analysis, and spectral model fitting etc.

X-RAY IMAGING PROCESSING The recorded position and energy of each detected X-ray photon, combined with the satellite housekeeping information, are sorted into a raster X-ray image on the ground. After the reconstruction of the X-ray image, various procedures may be carried out. The location of the X-ray source may be determined within an error box. The intensity of the source is then calculated by subtracting background estimated in a source-free region of the image from the flux extracted within the source error box. The X-ray spectrum of the source may be obtained by constructing X-ray images over different energy band. A time series of the source may also be estimated from a series of image. The intensity contour can be produced by mapping the whole image.

X-RAY TIMING ANALYSIS The X-ray photons are counted in time sequence and the X-ray light curve of the source may be obtained by subtracting a suitable background rate.

The periodic oscillations of the source can be searched for by constructing a power density spectrum of the light curve.

X-RAY SPECTRAL FITTING The X-ray spectrum of the source can be determined from simultaneous flux observations at a number of energies. The assumed spectral model, with the considerations of the detector performance, background and dead time losses etc, may be tested using Pearson's χ^2 statistic (e.g. Lampton, Margon & Bowyer 1976) and accepted or rejected on the basis of χ^2 probabilities. Once the accepted model has been found, the confidence region for the values of the model's adjustable parameters could be derived using the $\chi_{min}^2 + 1 < \chi^2$ error estimation method (Lampton, Margon & Bowyer 1976).

2.5.2 Leicester Data Analysis System

The analysis of the *EXOSAT* and *GINGA* data is conducted within the Leicester Data Analysis System (LDAS), which consists of more than 50 different application programmes written almost entirely in FORTRAN. These programmes may be used to transform the X-ray satellite raw data from the tape into the standard format data files on the computer disc, and conduct various processes such as imaging processing, timing analysis, and spectral modelling etc, on the X-ray data.

All the programmes within LDAS input and output programme parameters by means of the QX parameter system, which is based on set of simple FORTRAN subroutines. The QX parameter system operates just like FORTRAN READs and WRITEs but with much greater flexibility. All the data files produced and processed by the LDAS programmes make use of the Starlink Hierarchical Data System (HDS). In HDS, the data are stored and accessed by name rather than by their position in the file. Thus the HDS provides a very flexible method of accessing data stored on file.

These flexibilities are achieved using the QCL command language as a separate environment from which all the LDAS programmes can be run. Various processes such as manipulation of QX parameters, access and manipulation of variables in HDS data files, graphical output, running user programs, executing DCL commands, and executing QCL procedures etc can be conducted within QCL.

GRP, as an integral part of QCL, provides all graphics in the LDAS. In addition using GRP commands interactively, a number of standard GRP procedures are also available to do common plotting operations.

2.5.3 EXOSAT Raw Data Reduction

The *EXOSAT* data are available in the form of *EXOSAT* Final Observation Tapes (FOTs). A particular FOT contains data from only one of the *EXOSAT* instruments. The basic unit of data is the 'observation', within which the spacecraft status is supposed to be constant so that all the data can be described by a single set of mode and configuration parameters. Different observations may use different OBC modes or have different hardware settings. A new observation is also started whenever its duration would exceed 14,400 seconds or when there would be more than 32767 records in any of the raw data files. When a new observation is started for one of these reasons, or when the spacecraft mode changes in some way which is irrelevant, it may be necessary to join two or more raw data files together. Various raw data types are used and each type is put on to a separate raw data file with the data type code (defined by ESOC) as the file extension. Most raw data are stored on unformatted direct-access files with a record structure defined by ESOC.

A set of six programmes within the LDAS may be used to extract data from FOTs and produce standard format data files on disc. The *EXOSAT* raw data for a given instrument are extracted from one or more FOTs and copied to a set of disc files. The most useful data in the disc based housekeeping files are then extracted and put in a single file describing the whole observing period. Before sorting the data, it is necessary to produce a log showing which raw data files are fully compatible with each other so that they may be joined together during the sorting process. Finally, one or more (if the observations are compatible) data files are sorted and converted into HDS output files. This output file has header parameters attached giving information about the time, attitude, mode, configuration etc. The sorted file is self-describing and self-sufficient.

2.5.4 GINGA Raw Data Reduction

The basic unit of *GINGA* data, as delivered to the UK, is called the First Reduction File (FRF). FRFs use the EBCDIC codes and IBM format, and are delivered on tapes. These data are converted to a VAX format and stored in the Leicester *GINGA* data base on the University VAX Cluster, so that users can easily access them.

Each FRF contains Operational Status (OS) data which define the instrument gain, anti-coincidence matrix, discriminator settings, HV settings, and housekeeping (HK) data, as well as the detector counting rates. The FRF is not equivalent to the *EXOSAT* observation as described above, but rather arbitrarily sub-divided.

The FRFs which contain on-source and off-source observations can be restored to the disc from the Leicester tape archive, and then be sorted into data cubes of source and background (off-source) observations. Poor quality data such as those contaminated by the background flare must be removed from these sorted data cube files before background estimate and subtraction can be done. Due to the lack of simultaneous background in the LAC when source observations are made, an off-source observation of the blank sky is used for estimating the background during the on-source observations. After this pseudo-background has been subtracted from the source observations and the data in the background subtracted source files have been corrected for the attitude variations of the detectors, various analysis such as time series and spectral fitting can be done using the standard programmes in the LDAS.

The *GINGA* specific software, formed as an interface between the Japanese data tapes and the existing LDAS software, provides a basis tool to do the above jobs.

Chapter 3

EXOSAT Observations of SS 433

3.1 Introduction

X-rays from SS 433 were first detected with the first X-ray satellite *UHURU* (see review on the observations of SS 433 in Chapter 1). However, its unique properties in the X-ray range were first disclosed with observations by the *EXOSAT* satellite in 1983-1985. A strong iron emission line which displays large energy shifts varying as a function of the 163-day precession phase was observed with *EXOSAT* (Watson *et al.* 1986). These energy shifts are consistent with the Doppler shifts predicted in the kinematic model for the relativistic jets in SS 433. This implies that the X-ray emitting material is physically associated with the jets. An X-ray eclipse, simultaneous with the optical eclipse, which corresponds to the primary optical minimum at the jet precession phase 0.6, was also observed with *EXOSAT* (Stewart *et al.* 1987) and the duration of the eclipse was used to put a constraint on the system geometry.

The analysis of the X-ray observations of SS 433 reported by Watson *et al.* (1986) and Stewart *et al.* (1987) concentrated on the Doppler-shifted iron emission line in the spectrum and the X-ray intensity variation of SS 433 over the 13 day binary period. However, a complete analysis of the X-ray data was not attempted.

In this chapter, results of a detailed analysis of the *EXOSAT* Low Energy (LE) and Medium Energy (ME) observations of SS 433 are presented with an emphasis on the modulations of the X-ray features of SS 433 caused by the two periods (jet precession and binary motion).

A partial X-ray eclipse, which has not been reported before, is found in both the LE and ME data from the observation made in May 17-18 1985, at a jet precession phase of 0.06 when the lower jet approaches the observers. This partial X-ray eclipse, adds further evidence to support the ‘standard kinematical model’. The most striking result of this full analysis of *EXOSAT* data of SS 433 is the discovery of the modulation of X-ray line width by the jet precession, which gives us important information on the physical condition of the jets of SS 433. The properties of the X-ray spectra of SS 433 over 163-day precession and 13-day binary phases are also given and their implications on the characteristics of the X-ray radiation region are discussed in this chapter. Most of these properties are reported for the first time.

3.2 Observations and Data Analysis

The X-ray observations of SS 433 presented here comprise a total of 15 separate pointings carried out with the Low Energy imaging telescope and the Medium Energy detectors aboard the *EXOSAT* Observatory in the period 1983 October-1985 October. Simultaneous observations with the *EXOSAT* Gas Scintillation Proportional Counter (GSPC) were also made. Because SS 433 is near the threshold for obtaining a good spectrum in the GSPC, the poor quality GSPC data do not satisfy the requirements of the current work which aims at detailed spectral analysis and, therefore, have not been considered here. Seven of the *EXOSAT* observations were made with coordinated optical photometry in 1984 September-October and covered one complete binary cycle. The observation times range from 3 to 13 hours and the individual exposure times are from about 4300 s to 47000 s. Details of the observations are given in Table 3.1 and the location of each pointing in the binary and jet precession phase-space is plotted in Fig. 3.1. The definitions of jet precession and orbital phases are given in chapter 5.

The first X-ray imaging of SS 433 (Seward *et al.* 1980) showed that 90% of the low-energy (1-3 keV) X-ray flux is from the central object and 10% of this flux is from two diffuse X-ray emission lobes. The *EXOSAT* LE observations, however, only point to the central source of SS 433 and the diffuse X-ray emission lobes are not included in the sensitive portion of the field of view of LE telescopes. As an example, the contour map of this soft X-ray emission given by Watson *et al.* (1983) is re-plotted in Fig. 3.2 with a dotted square box indicating

Table 3.1: EXOSAT Observing log for SS 433 (1983-1985)

No.	Start (UT)	End (UT)	MJD at Mid- Observation	Total Exposure (sec)		$\phi_{13.08}$		$\psi_{162.5}$		
				ME	LE(3Lx)	LE(AL/P)	From	To	From	To
1	13/10/83 22:23	14/10/83 11:25	45621.2043	37630	41690	41475	0.478	0.519	0.483	0.487
2	15/10/83 03:15	15/10/83 14:05	45622.3612	16149	37975		0.570	0.604	0.491	0.493
3	16/10/83 02:33	16/10/83 14:34	45623.3565	21863	5782	19543	0.644	0.682	0.497	0.500
4	17/04/84 16:49	18/04/84 05:33	45807.9661	45830	18508	11847	0.756	0.796	0.633	0.636
5	21/09/84 15:15	21/09/84 18:38	45964.7059	11920	8024		0.753	0.764	0.598	0.599
6	24/09/84 10:26	24/09/84 14:48	45967.5256	13790	7597		0.967	0.981	0.616	0.617
7	25/09/84 09:13	25/09/84 15:31	45968.5153	22210	18577		0.039	0.059	0.621	0.623
8	27/09/84 02:10	27/09/84 06:16	45970.1757	12670	12077		0.170	0.183	0.632	0.633
9	29/09/84 11:58	29/09/84 16:13	45972.5870	19100	9772		0.354	0.367	0.647	0.648
10	01/10/84 20:27	01/10/84 23:22	45974.9129	4330	9440		0.534	0.543	0.661	0.662
11	04/10/84 21:18	05/10/84 00:09	45977.9470	7220	8726		0.766	0.775	0.680	0.681
12	17/05/85 20:18	18/05/85 07:50	46203.0861	40890	16069	21400	0.963	1.000	0.064	0.067
13	27/05/85 20:38	28/05/85 07:17	46213.0817	36270	33730		0.729	0.763	0.126	0.129
14	20/07/85 19:20	21/07/85 06:17	46267.0337	33950			0.853	0.888	0.458	0.461
15	05/10/85 05:18	05/10/85 20:40	46343.5410	47030	40339		0.694	0.743	0.928	0.932

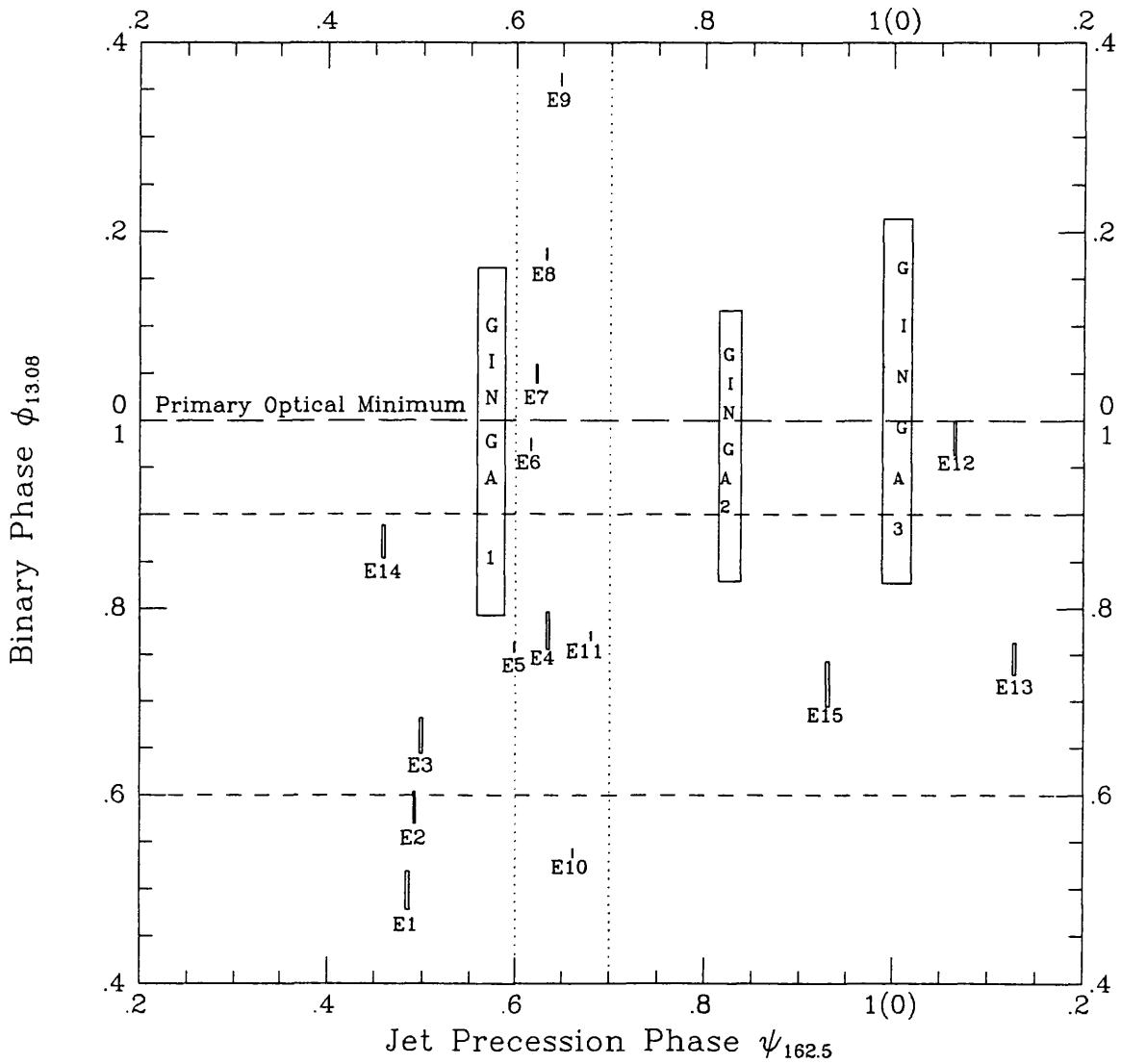


Figure 3.1: Distributions of *EXOSAT* pointings and *GINGA* observations (Chapter 4) in the binary and jet precession phase-space, where ‘E’ represents *EXOSAT* observation and digital follows indicates the log number in table 3.1. Precession phase 0.5 corresponds to maximum separation of the moving lines.

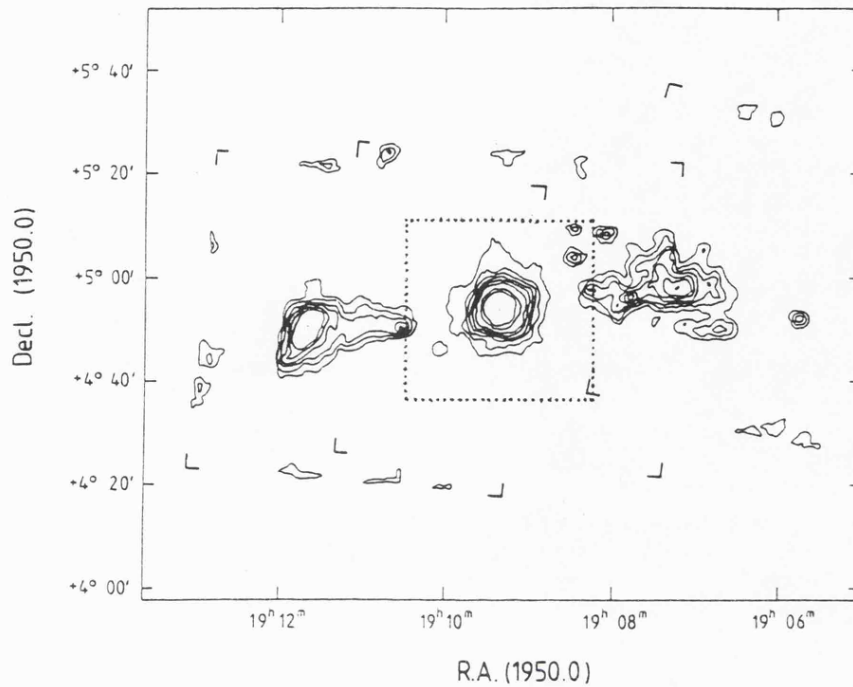


Figure 3.2: The soft X-ray contour of SS 433 stellar and diffuse sources, taken from Watson *et al.* (1983). The dotted square box here represents the field of view of the *EXOSAT* LE telescopes.

the field of view of the *EXOSAT* Low Energy telescopes.

A typical *EXOSAT* image of SS 433 is shown in Fig. 3.3 in which the black diffuse point at the imaging centre is the X-ray central source of SS 433 and the solid-line diamond box indicates the hotspot of the LE telescope.

Count rates for the LE observations are extracted from a 100×100 (arcsec)² cell centered on the source (small square box in Fig. 3.3) and the background count rates from adjacent source-free regions (with an area nine times that of the source box) subtracted so that the LE count rates could well represent the X-ray emission from the central X-ray source. Count rate corrections for mirror vignetting, dead time and scattering due to the instrumental response are also applied.

The ME count rates refer to the full on-source half-array after subtraction of background count rates obtained from stable offset half-array data with the appropriate 'difference spectrum' correction (Parmar & Izzo 1986).

The X-ray background for each energy channel of the ME detectors is carefully checked and

SS433.IMAG%DATA_ARRAY

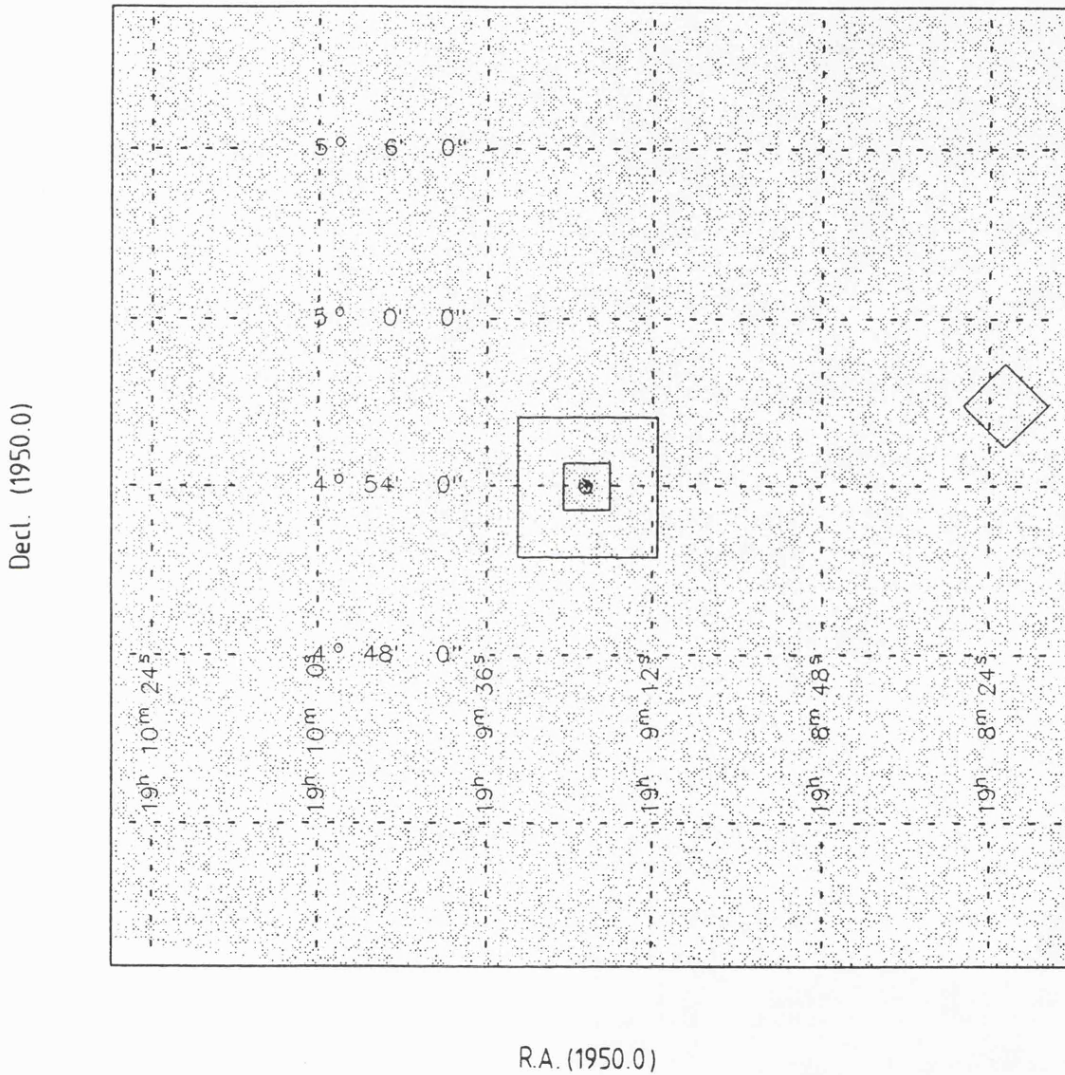


Figure 3.3: The X-ray image of SS 433 from *EXOSAT* observations, where the black diffuse point at the image centre is the X-ray central source of SS 433. The X-ray background rate is estimated within the big square box but outside the small one, and subtracted from the count rate estimated inside the small error box.

the observations presented here only include those made during periods of stable background.

ME spectra from the argon chambers of the ME detectors are obtained after correcting for background and dead time. Spectral fits are performed on the ME spectra and on the combined LE and ME measurements for each observation by comparing spectral data with the convolution of the instrument response function and input spectra.

Various spectral models are chosen to fit the SS 433 spectrum which, consists of a continuum and (a) broad emission line feature(s). Six continuum models were applied in the spectral fitting. These models are classified as single component continuum including black body, thin-thermal bremsstrahlung and non-thermal power law, and two component continua such as Comptonized bremsstrahlung, a thin-thermal bremsstrahlung with inclusion of a black body component, and a power law plus exponential cut-off function. The line feature is approximated by a Gaussian profile specified with three parameters, energy, flux and width.

The Comptonized bremsstrahlung model makes use of the prescription given by Lamb and Sanford (1979) which can be used whenever condition $\tau \leq (\frac{m_e c^2}{2T_e})^{1/2}$ is approximately satisfied, where τ is the optical depth, T_e , the electron temperature, m_e is the electron mass and c speed of light. The power-law with exponential cut-off was used to describe the spectra obtained by *TENMA* (Matsuoka, Takano & Makishima 1986), which is expressed as $E^{-\alpha}$ for $E \leq E_c$ and $E^{-\alpha} \exp[-(E - E_c)/E_f]$ for $E > E_c$, where E_c is the cut-off energy and E_f the folding energy.

3.3 Results

Over the period of *EXOSAT* observations, the X-ray source of SS 433 was quite stable and there were no significant variations on time scales shorter than ~ 5 min. No X-ray flare events similar to those seen by the *EINSTEIN* satellite have been detected despite the longer overall time of *EXOSAT* observation. This may be partly due to the different sampling technique used.

The X-ray flux of SS 433 over 2-10 keV band recorded by *EXOSAT* ranges between 1.3×10^{-10} erg cm⁻² s⁻¹, typically 50% higher than those observed by the *EINSTEIN* MPC. With a distance of 5 kpc, this gives a 2-10 keV luminosity of $\sim 10^{36}$ erg s⁻¹. In the *EXOSAT* Low

Table 3.2: SS 433 count rates of each EXOSAT pointing

No	$\phi_{13.08}$	$\psi_{162.5}$	Low Energy		Medium Energy	
			3LX ($\times 10^{-2}$ ct s $^{-1}$)	AL/P	(1-5 keV) (ct s $^{-1}$ detector $^{-1}$)	(5-10 keV)
1	0.499	0.485	1.63 ± 0.17	1.52 ± 0.27	2.80 ± 0.01	2.20 ± 0.01
2	0.587	0.492	1.59 ± 0.08		2.65 ± 0.01	1.96 ± 0.01
3	0.662	0.499	1.56 ± 0.26	1.51 ± 0.14	2.65 ± 0.01	1.89 ± 0.02
4	0.776	0.635	—	—	—	—
5	0.759	0.598	1.03 ± 0.21		2.69 ± 0.02	2.07 ± 0.02
6	0.974	0.616	0.65 ± 0.24		1.57 ± 0.02	0.89 ± 0.02
7	0.049	0.622	0.75 ± 0.12		1.61 ± 0.02	0.93 ± 0.02
8	0.177	0.632	0.93 ± 0.17		2.40 ± 0.02	1.60 ± 0.02
9	0.361	0.647	1.26 ± 0.21		2.03 ± 0.02	1.44 ± 0.02
10	0.539	0.661	0.99 ± 0.17		1.99 ± 0.02	1.54 ± 0.02
11	0.771	0.680	1.23 ± 0.18		2.24 ± 0.02	1.51 ± 0.02
12	0.982	0.066	0.84 ± 0.13	0.53 ± 0.11	1.41 ± 0.01	0.72 ± 0.01
13	0.746	0.127	0.68 ± 0.09		1.41 ± 0.01	0.92 ± 0.01
14	0.871	0.459			2.85 ± 0.01	1.87 ± 0.01
15	0.719	0.930	0.86 ± 0.10		1.67 ± 0.02	1.04 ± 0.02

Energy telescopes, SS 433 is detected as an unresolved point source at count rates of 0.005 to 0.02 counts s $^{-1}$. Table 3.2 lists X-ray counting rates of LE, 1-5 keV and 5-10 keV energy bands for each pointing except the one made in April 17-18, 1984, which was contaminated by the background radiation.

The shape and behaviour of the X-ray spectrum of SS 433 obtained with the *EXOSAT* also differs from that of the *EINSTEIN* reported by Grindlay *et al.* (1984). In both the GSPC (Watson *et al.* 1986; Stewart & Watson 1986) and the ME data there is a clear evidence for the existence of an energy-shifted emission line at all times. There is also some variation of the continuum spectrum between different observations.

Spectral fits were performed with various models described in the section above. Parameters from fitting the ME spectrum alone are completely consistent with those from fitting

combined ME and LE spectrum. The model with a single black body component as continuum never fits any of the spectra, while the other five models can give reasonably good fits to the observed data. In most circumstances, two-component continuum model could fit the spectra better than that the single component model does, but none of them gives statistically acceptable fits. All these models produce similar spectral shapes to the observed counting rate spectrum. However, due to the limited bandpass of the *EXOSAT* instruments, the model which is the most suitable to SS 433 could not be distinguished simply from the obtained χ^2 statistics. Also, the *EXOSAT* data could not accurately limit the temperature of bremsstrahlung models with temperatures above 30 keV due to the limited bandpass.

3.3.1 Modulation at the 163 Day Jet Precession Period

1. X-ray intensity variation over 163 day period

X-ray count rates over LE, 1-5 keV and 5-10 keV energy bands extracted from observations made in the binary phase 0.60-0.90 are shown folded on the jet precession period in Fig. 3.4 (see table 3.2 for detail).

Modulation of the X-ray intensity by the jet precession is significant in each energy band. The maximum X-ray intensity is reached at around phase 0.5 when the approaching jet is crossing the line of sight and the Doppler red-, blue-shifted optical lines are at their maximum separation in energy. The lower state of the intensity occurs at about phase 0.13 when two jets of SS 433 are edge-on and the separation of the energy-shifted lines is small.

The X-ray intensity range from higher to lower fluxes is $\sim 50\%$ in the energy bands of LE, 1-5 keV and 5-10 keV and the consistency of the fractional intensity decrease in each energy band implies that the X-ray spectrum below 10 keV does not vary considerably over the jet precession period and the X-ray intensity is scaled up and down almost by the same factor in each energy band from phase to phase.

The relativistic beaming factors predicted from the standard kinematic model (see formula in Chapter 5) have similar patterns as the folded 163 day X-ray light curves do, and may explain the major part of the observed intensity variations. The variations of the beaming factor of the top jet emission, when normalized to the fluxes over phases 0.45-0.7, are displayed

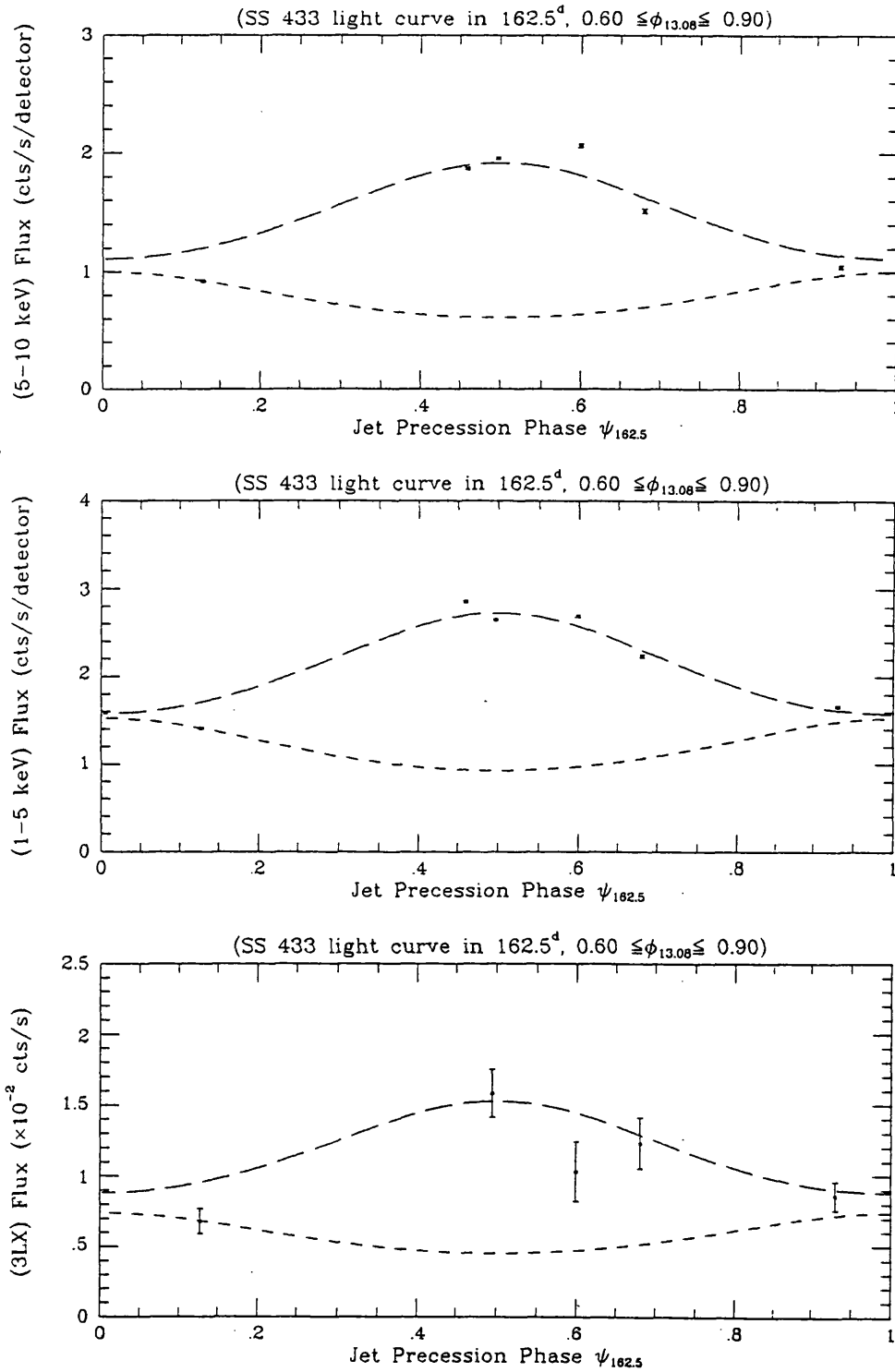


Figure 3.4: The folded 163 day X-ray light curve of SS 433, where the long-dash line represents the predicted beaming factor from the top jet and the short-dash line is that from the lower jet, both are normalized to corresponding fluxes.

using the long-dash curves in Fig. 3.4 and the pattern of the lower jet beaming factor, when normalized to the data outside phase 0.45-0.7, are plotted using the short-dash lines. If, most of the red jet is obscured by the accretion disc at most precession phases (see discussion below), the beaming factor can fit the folded 163 day light curves fairly well, which implies that the long term changes of the X-ray intensity is strongly modulated by the precession of the relativistic jets. In addition, when occultation of the lower portion of the jets due to precession of the disc is taken into account, the entire range of fluxes can be accounted for. This shows remarkable long term stability of the X-ray emission suggesting either a very constant accretion rate, or some control mechanism for the jets. The observed *GINGA* fluxes (see next chapter) are also consistent with the *EXOSAT* values.

2. X-ray spectral variation over 163 day period

Six spectra are used to trace the modulation of jet precession on the X-ray spectrum of SS 433. Fig. 3.5 shows all six SS 433 spectra and table 3.3 gives details of spectral parameters.

1) X-ray continuum

There is no obvious 163 day modulation on the X-ray continuum parameters of SS 433, although the bremsstrahlung temperature tends to increase at the source high intensity state when a thin-thermal bremsstrahlung is used as the continuum. The spectral parameters of the continuum obtained from the model fitting stay fairly constant within the statistical error and systematic uncertainty over the jet precession cycle.

A ~ 25 keV bremsstrahlung or a power law with a ~ 1.5 photon index is needed to get a good fit to all the six spectra when a single component continuum with low-energy absorption is assumed for the SS 433 spectrum. In both cases, the equivalent neutral hydrogen column density is consistent with $\sim 8 \times 10^{21} \text{ cm}^{-2}$. Because the spectrum is only available up to 15 keV in the *EXOSAT* ME Argon detectors, the difference between thermal bremsstrahlung and non-thermal power law can not be told by the data available.

Adding Compton scattering component to the bremsstrahlung continuum does not significantly improve χ^2 . The derived bremsstrahlung temperature T_e is ~ 6 keV and optical depth $\tau \sim 12$ for all six spectra. These parameters obviously disobey the condition $\tau \leq (\frac{m_e c^2}{2T_e})^{1/2}$ within which the approximate formula of Comptonized bremsstrahlung can be used. However,

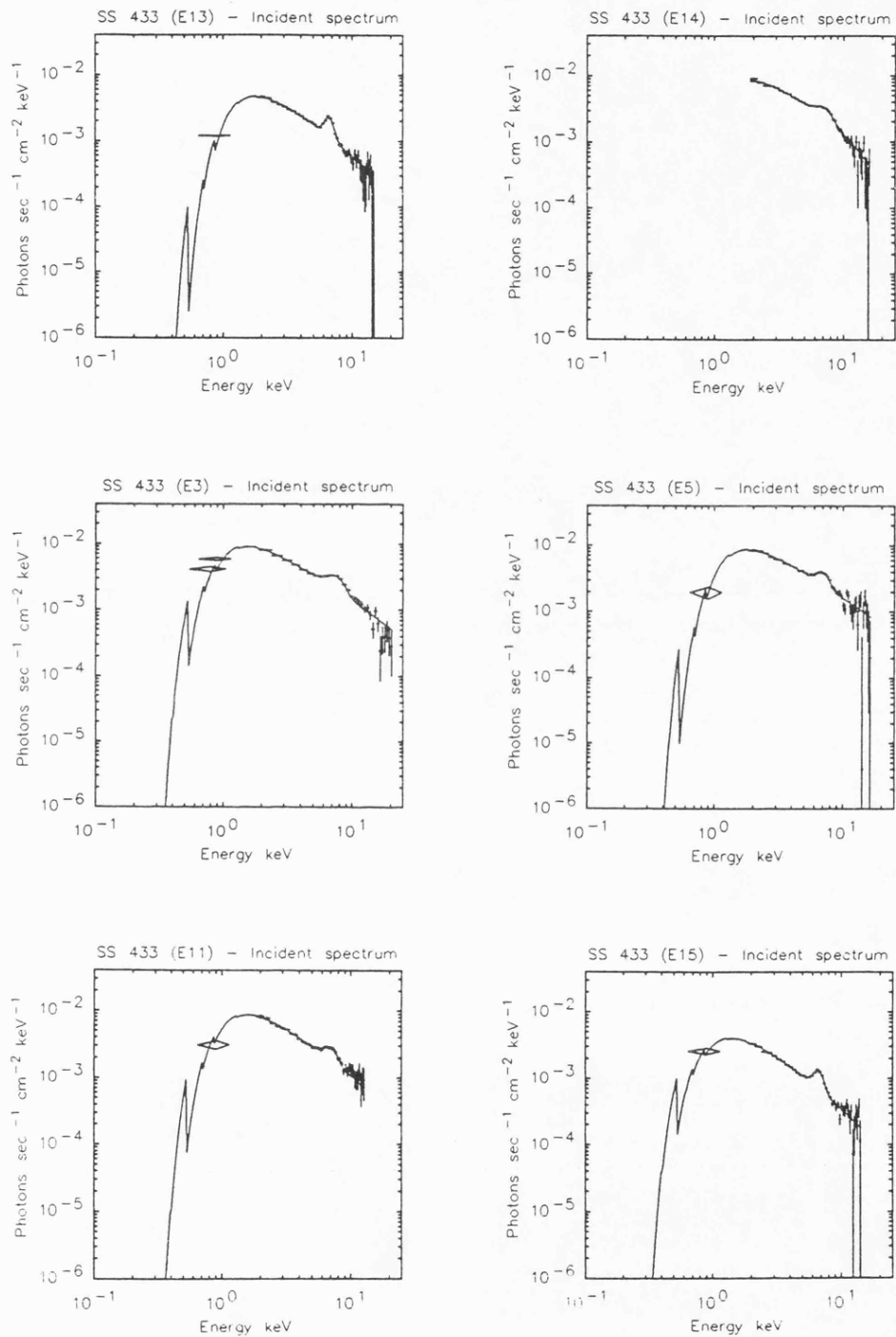


Figure 3.5: The X-ray spectra of SS 433 over 163 day cycle, where the jet precession phase for each spectrum is E13-0.127, E14-0.459, E3-0.496, E5-0.599, E11-0.680, E15-0.930.

Table 3.3: Evolution of SS 433 spectra over jet precession period

Model 1: (a bremsstrahlung + a broad line)Xlow energy absorption									
continuum parameters			emission line parameters						
Log $\psi_{162.5}$	T_{brem}	column N_{H}	energy	flux ($\times 10^{-2}$)	width	reduced			
No	(keV)	($\times 10^{+21} \text{ cm}^{-2}$)	(keV)	(photon $\text{cm}^{-2} \text{ s}^{-1}$)	(keV)	$\chi^2(\text{d.o.f})$			
13	0.127	$22.84^{+4.80}_{-3.80}$	$6.68^{+0.30}_{-0.29}$	$0.15^{+0.02}_{-0.02}$	$0.53^{+0.12}_{-0.12}$	1.9(39)			
14	0.459	$28.89^{+5.37}_{-3.86}$	$7.24^{+1.27}_{-0.99}$	$0.34^{+0.06}_{-0.05}$	$1.11^{+0.14}_{-0.13}$	3.4(44)			
3	0.496	$111.00^{+49.00}_{-32.74}$	$7.60^{+0.29}_{-0.06}$	$0.38^{+0.03}_{-0.02}$	$1.15^{+0.06}_{-0.06}$	4.2(28)			
5	0.599	$142.50^{+920.50}_{-72.96}$	$7.07^{+0.14}_{-0.07}$	$0.29^{+0.05}_{-0.04}$	$0.80^{+0.21}_{-0.08}$	2.0(44)			
11	0.680	$38.80^{+28.97}_{-11.13}$	$7.11^{+0.16}_{-0.18}$	$0.21^{+0.04}_{-0.05}$	$0.80^{+0.13}_{-0.19}$	1.5(34)			
15	0.930	$22.34^{+4.46}_{-3.55}$	$6.69^{+0.06}_{-0.06}$	$0.09^{+0.01}_{-0.01}$	$0.59^{+0.09}_{-0.09}$	1.4(38)			

Model 2: (a power law + a broad line)Xlow energy absorption									
continuum parameters			emission line parameters						
Log $\psi_{162.5}$	Photon Index	column N_{H}	energy	flux ($\times 10^{-2}$)	width	reduced			
No		($\times 10^{+21} \text{ cm}^{-2}$)	(keV)	(photon $\text{cm}^{-2} \text{ s}^{-1}$)	(keV)	$\chi^2(\text{d.o.f})$			
13	0.127	$10.73^{+0.49}_{-0.43}$	$6.64^{+0.06}_{-0.06}$	$0.15^{+0.02}_{-0.02}$	$0.52^{+0.12}_{-0.13}$	2.1(39)			
14	0.459	$13.00^{+1.09}_{-1.04}$	$7.23^{+0.09}_{-0.09}$	$0.40^{+0.07}_{-0.06}$	$1.22^{+0.16}_{-0.14}$	4.1(44)			
3	0.496	$6.20^{+0.61}_{-0.45}$	$7.59^{+0.07}_{-0.06}$	$0.40^{+0.05}_{-0.03}$	$1.19^{+0.11}_{-0.07}$	3.8(28)			
5	0.599	$7.92^{+1.73}_{-0.97}$	$7.03^{+0.12}_{-0.08}$	$0.27^{+0.03}_{-0.02}$	$0.78^{+0.30}_{-0.07}$	2.0(44)			
11	0.680	$7.14^{+1.41}_{-1.19}$	$7.05^{+0.17}_{-0.15}$	$0.21^{+0.04}_{-0.05}$	$0.79^{+0.16}_{-0.19}$	1.2(34)			
15	0.930	$7.13^{+1.75}_{-1.11}$	$6.66^{+0.06}_{-0.05}$	$0.09^{+0.01}_{-0.01}$	$0.58^{+0.10}_{-0.09}$	1.7(38)			

Table 3.3: Evolution of SS 433 spectra over jet precession period (continue)

Model 3: (a Comptonized bremsstrahlung + a broad line)Xlow energy absorption									
continuum parameters					emission line parameters				
Log $\psi_{162.5}$	T_{brem} (keV)	Optical depth	column N_{H} ($\times 10^{21} \text{ cm}^{-2}$)	energy (keV)	flux ($\times 10^{-2}$) (photon $\text{cm}^{-2} \text{ s}^{-1}$)	width (keV)	reduced χ^2 (d.o.f)		
13	0.127	$4.32^{+1.55}_{-0.72}$	$11.84^{+2.04}_{-0.87}$	$9.62^{+0.28}_{-0.28}$	$6.67^{+0.06}_{-0.06}$	$0.14^{+0.02}_{-0.02}$	$0.47^{+0.12}_{-0.14}$	1.9(38)	
14	0.459	$4.67^{+0.15}_{-0.12}$	$11.97^{+1.82}_{-3.49}$	$9.61^{+0.69}_{-0.73}$	$7.22^{+0.11}_{-0.11}$	$0.29^{+0.05}_{-0.05}$	$1.03^{+0.14}_{-0.14}$	3.2(44)	
3	0.496	$6.38^{+1.02}_{-0.92}$	$11.99^{+1.30}_{-0.93}$	$5.74^{+0.33}_{-0.35}$	$7.52^{+0.07}_{-0.08}$	$0.34^{+0.03}_{-0.04}$	$1.07^{+0.08}_{-0.09}$	3.4(27)	
5	0.599	$5.67^{+0.49}_{-0.87}$	$14.75^{+1.89}_{-2.50}$	$7.59^{+1.35}_{-1.19}$	$7.06^{+0.12}_{-0.11}$	$0.25^{+0.04}_{-0.04}$	$0.75^{+0.11}_{-0.15}$	1.9(43)	
11	0.680	$9.24^{+11.34}_{-3.89}$	$8.19^{+3.03}_{-3.94}$	$6.07^{+1.00}_{-0.82}$	$7.05^{+0.19}_{-0.19}$	$0.19^{+0.05}_{-0.05}$	$0.73^{+0.16}_{-0.24}$	1.4(33)	
15	0.930	$4.69^{+22.66}_{-0.90}$	$11.00^{+0.32}_{-11.00}$	$4.92^{+0.73}_{-0.69}$	$6.69^{+0.06}_{-0.06}$	$0.09^{+0.01}_{-0.01}$	$0.56^{+0.10}_{-0.10}$	1.4(37)	

Model 4: (a bremsstrahlung + a black-body + a broad line)Xlow energy absorption									
continuum parameters					emission line parameters				
Log $\psi_{162.5}$	T_{brem} (keV)	T_{bbod} (keV)	column N_{H} ($\times 10^{21} \text{ cm}^{-2}$)	energy (keV)	flux ($\times 10^{-2}$) (photon $\text{cm}^{-2} \text{ s}^{-1}$)	width (keV)	reduced χ^2 (d.o.f)		
13	0.127	$12.42^{+0.53}_{-0.47}$	$2.62^{+0.18}_{-0.22}$	$9.54^{+0.21}_{+0.20}$	$6.67^{+0.07}_{-0.06}$	$0.14^{+0.02}_{-0.02}$	$0.43^{+0.13}_{-0.15}$	1.8(39)	
14	0.459	$13.29^{+0.63}_{-0.53}$	$3.24^{+0.20}_{-0.23}$	$10.67^{+0.91}_{-0.85}$	$7.23^{+0.11}_{-0.12}$	$0.32^{+0.05}_{-0.04}$	$1.08^{+0.13}_{-0.13}$	3.4(44)	
3	0.496	$11.75^{+0.23}_{-0.23}$	$4.05^{+0.10}_{-0.10}$	$6.24^{+0.30}_{-0.31}$	$7.45^{+0.08}_{-0.08}$	$0.30^{+0.03}_{-0.03}$	$1.02^{+0.08}_{-0.09}$	2.6(28)	
5	0.599	$13.22^{+0.69}_{-0.65}$	$3.55^{+0.16}_{-0.14}$	$8.73^{+0.85}_{-0.86}$	$7.05^{+0.10}_{-0.12}$	$0.25^{+0.03}_{-0.04}$	$0.78^{+0.12}_{-0.16}$	1.9(44)	
11	0.680	$9.43^{+0.50}_{-0.26}$	$5.64^{+0.55}_{-0.66}$	$7.41^{+0.93}_{-0.83}$	$6.91^{+0.20}_{-0.15}$	$0.18^{+0.03}_{-0.04}$	$0.68^{+0.17}_{-0.18}$	1.1(34)	
15	0.930	$12.03^{+0.47}_{-0.42}$	$3.11^{+0.25}_{-0.30}$	$5.36^{+0.65}_{-0.61}$	$6.69^{+0.06}_{-0.06}$	$0.09^{+0.01}_{-0.01}$	$0.57^{+0.09}_{-0.10}$	1.4(38)	

Table 3.3: Evolution of SS 433 spectra over jet precession period (continue)

Model 5: (a power law with exponential cut-off + a broad line) \times low energy absorption											
Log No	$\psi_{162.5}$	Photon Index	continuum parameters			emission line parameters					
			cut-off Energy (keV)	folding energy (keV)	column N_H ($\times 10^{21} \text{ cm}^{-2}$)	energy (keV)	flux ($\times 10^{-2}$) (photon $\text{cm}^{-2} \text{ s}^{-1}$)	width (keV)	reduced χ^2 (d.o.f)		
13	0.127	$1.42^{+0.06}_{-0.05}$	$5.35^{+2.39}_{-0.84}$	$22.63^{+16.13}_{-14.24}$	$9.98^{+0.53}_{-0.47}$	$6.70^{+0.07}_{-0.06}$	$0.15^{+0.02}_{-0.03}$	$0.47^{+0.13}_{-0.19}$	1.8(37)		
14	0.459	$1.40^{+0.29}_{-1.40}$	$7.82^{+3.45}_{-4.22}$	$12.63^{+21.64}_{-5.53}$	$13.94^{+4.45}_{-4.50}$	$7.15^{+0.24}_{-0.15}$	$0.25^{+0.14}_{-0.10}$	$1.00^{+0.19}_{-0.24}$	1.0(37)		
3	0.496	$1.26^{+0.04}_{-0.04}$	$13.62^{+2.18}_{-1.93}$	$8.79^{+13.30}_{-4.97}$	$5.74^{+0.55}_{-0.49}$	$7.55^{+0.07}_{-0.07}$	$0.36^{+0.04}_{-0.04}$	$1.11^{+0.09}_{-0.09}$	3.5(26)		
5	0.599	$1.17^{+0.07}_{-0.08}$	$6.73^{+5.32}_{-5.83}$	$38.62^{+130.09}_{-27.72}$	$7.20^{+1.50}_{-1.40}$	$7.10^{+0.13}_{-0.10}$	$0.27^{+0.05}_{-0.06}$	$0.80^{+0.13}_{-0.18}$	2.0(42)		
11	0.680	$1.42^{+0.07}_{-0.07}$	$26.70^{+\infty}_{-2.89}$	—	$7.13^{+1.33}_{-1.16}$	$7.07^{+0.15}_{-0.16}$	$0.21^{+0.03}_{-0.04}$	$0.79^{+0.13}_{-0.16}$	1.2(42)		
15	0.930	$1.40^{+0.10}_{-0.12}$	$3.88^{+1.86}_{-0.83}$	$26.53^{+22.69}_{-8.18}$	$4.93^{+1.43}_{-1.10}$	$6.70^{+0.07}_{-0.06}$	$0.09^{+0.01}_{-0.01}$	$0.61^{+0.10}_{-0.10}$	1.4(36)		

according to Lamb and Sanford (1979), this kind of result could be regarded as empirical and the model may continue to be physically justifiable. The use of a power law with exponential high energy cut-off can give reasonably good fits to all six spectra with χ^2 similar to other spectral model's. The parameters produced by the model are almost consistent with the results reported by Matsuoka *et al.* (1986) with *TENMA* GSPC spectrum, which has a ~ 1.4 power law index, ~ 7 keV cut-off energy and ~ 12 keV folding energy. This consistency indicates that the *TENMA* results can be used here as a constraint to the SS 433 spectrum at the jet precession phase which is not covered by *EXOSAT*. The combination of a ~ 12 keV bremsstrahlung and a ~ 4 keV black body continuum can be also used to give good fits to the six spectra. A similar column density is required in these two component models, being $\sim 8 \times 10^{21} \text{ cm}^{-2}$.

2) X-ray emission line

In contrast to the continuum, the modulation of the emission line of the spectrum is significant. All the line parameters, i.e., line energy, line flux and width, vary from phase to phase. This conclusion is independent of the continuum model assumed.

a) line energy

As reported by Watson *et al.* (1986), only one emission line is seen in the X-ray spectrum when ME data are taken from above 2 keV. Its energy varies from 6.68 ± 0.06 to 7.60 ± 0.06 keV with jet precession phase. As suggested by Watson *et al.* (1986), the behaviour of this X-ray emission line can be immediately interpreted as arising from the changing Doppler shifts of a line with a rest-frame energy near 7 keV.

The line energy as a function of jet precession phase is displayed in Fig. 3.6 where the results from the *GINGA* (Chapter 4 in this thesis) and *TENMA* (Matsuoka, Takano & Makishima 1986) observations are also included and indicated with 'G' & 'T'. It is clearly demonstrated that the line energy follows the Doppler shift expected in the kinematical model of the jets, i.e., it follows the same Doppler curves as that seen in the optical 'moving lines'. The long-dash curve in Fig. 3.6 represents the predicted energy for the line from top jet and the short-dash for the line from lower jet.

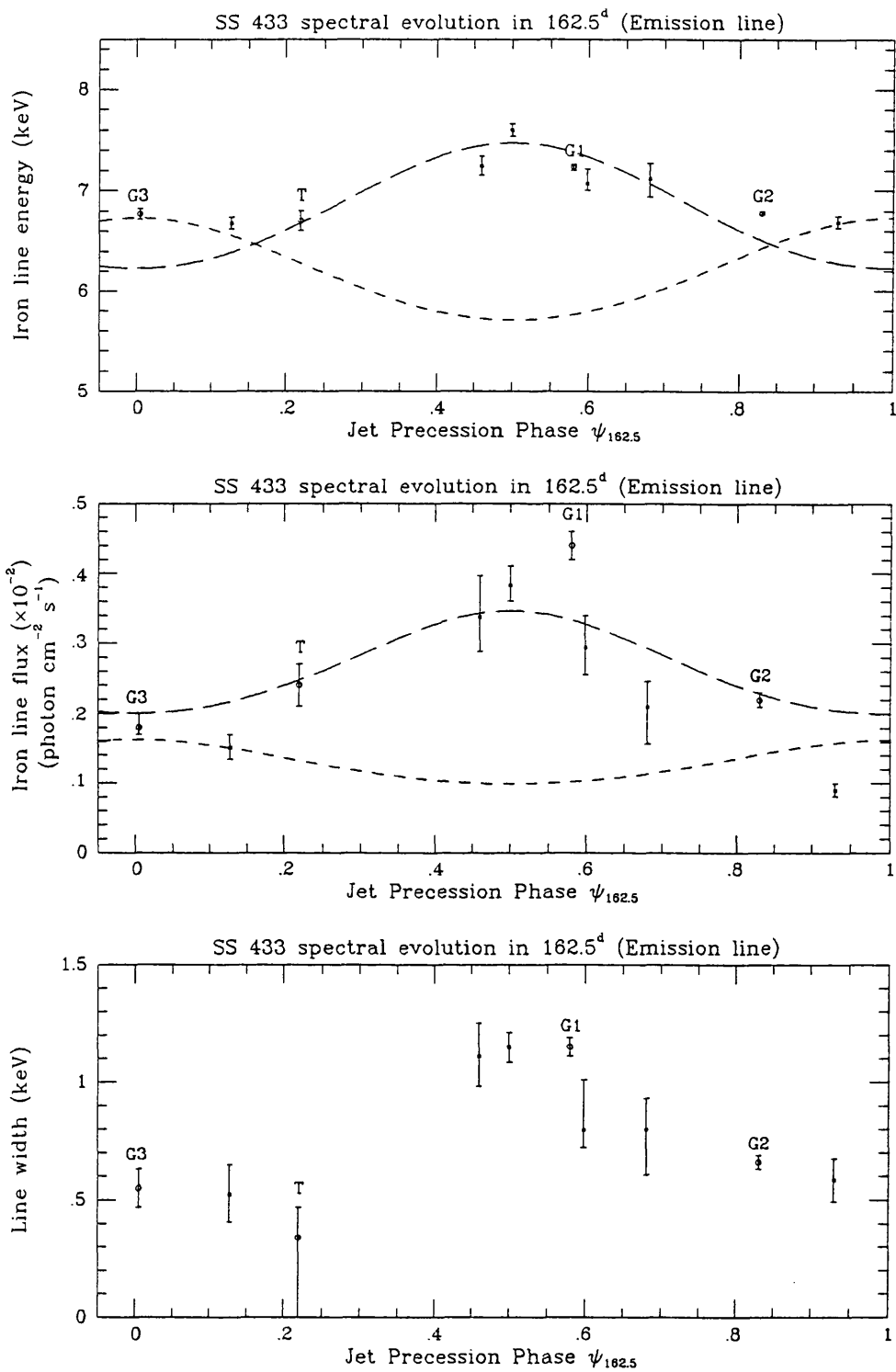


Figure 3.6: X-ray line parameter evolution over 163 day period. Top: the X-ray line energy, Mid: the line flux, Bottom: the line width (1σ of Gaussian profile). The long-dash curves represent the predicted values of the parameters from the top jet while the short-dash lines are those for the lower jet. 'T' and 'G' indicate the results taken from *TENMA* and *GINGA* observations.

b) line flux

Modulation of jet precession on the line intensity is obvious and shown in Fig. 3.6 where the *GINGA* and *TENMA* results are plotted. This property is reported for the first time. The line flux varies in the range from $(0.09 \pm 0.01) \times 10^{-2}$ photons sec cm^{-2} to $(0.38 \pm 0.03) \times 10^{-2}$ photons sec cm^{-2} . Although the amplitude of the line flux variation is larger than the continuum, it basically follows the variation of the continuum intensity as displayed in Fig. 3.4, implying the X-ray line and continuum emissions are from the same regions.

The relativistic motion of the X-ray line emitting material and the jet axis precession also play great roles in changing the iron line flux. If, assuming that the dominant line emission is from the top jet when the top jet is approaching the observer and from the lower jet while the lower jet approaches, and normalizing the beaming factors to the *EXOSAT* data points, a reasonably good fit to the data (including those from *GINGA* and *TENMA*) is derived. In addition, the occultation of the X-ray emitting regions by the accretion disc is also important to modulate the X-ray line flux.

c) line width

The emission line width, which is 1σ of fitted Gaussian profile, is found to vary over the jet precession cycle. The line becomes broad (1.15 ± 0.06 keV) when the jet approaches the observer and narrow (0.53 ± 0.12 keV) when the jet is edge-on. The points labeled with 'T' and 'G' in Fig. 3.6 represent the results from *TENMA* and *GINGA*.

This is the first discovery of this striking feature of the emission line in the spectrum of SS 433. There are a number of alternative explanations for the modulation by the jet precession phase of the line width. The first one is line broadening by Compton scattering. The radiated X-ray photons travel outward from the source via different optical depth and experience different scattering (more, when the optical depth is large and less, when the depth is small). Therefore, each time the jets of SS 433 are observed at different jet precession phase, different photons which have traveled through different optical depths are seen. For the very hot plasma in the jets (see Chapter 6), an optical depth of ~ 1 is required to give the observed width. Another possibility is that the observed line feature actually consists of several line components such as Doppler red- and blue-shifted hydrogen-like and helium-like iron lines due to the temperature distribution along the jets and the energy resolution of the detector is not good enough to

separate them. Different observations will detect the X-ray emission from the jet material with different temperatures, thus resultant lines with variable line width. Line broadening caused by opening angle of jet is also another possibility. Further discussions of these models are presented in section 3.4.4 and section 4.4.3 of Chapter 4.

3.3.2 Modulation at the 13 Day Binary Period

1. X-ray intensity variation over 13 day binary period

1) X-ray eclipse at precession phase 0.6

The results of the simultaneous optical and X-ray observations of SS 433 over one binary cycle have been reported by Stewart *et al.* (1987). In their report, the variation of the X-ray intensity has been described in detail. With improved background subtraction in this full analysis of *EXOSAT* observations, the X-ray light curve over LE, 1-5 keV and 5-10 keV bands are plotted in Fig. 3.7.

The X-ray light curves presented here are similar to those reported by Stewart *et al.* (1987) except that the X-ray counts are binned in slightly different energy ranges, and perhaps that the spectrum softening is found to be obvious during the X-ray eclipse. While the shape of the light curve is broadly constant with energy, the fractional intensity decrease is larger at hard X-ray energies than that in soft X-rays.

As described by Stewart *et al.* (1987), the X-ray intensity reduced at around MJD45968, coincident with the primary optical minimum. This intensity reduction is interpreted by Stewart *et al.* (1987) as the occultation by the companion star of the X-ray emitting region — the jets. The intensity recovered after the primary minimum phase to a level lower than that before the start of the eclipse. There are no certain interpretations to the intensity difference between pre- and post-eclipse phase. It may be due to the effect of jet precession or changing of the accretion rate. Detailed discussion is presented in the next chapter.

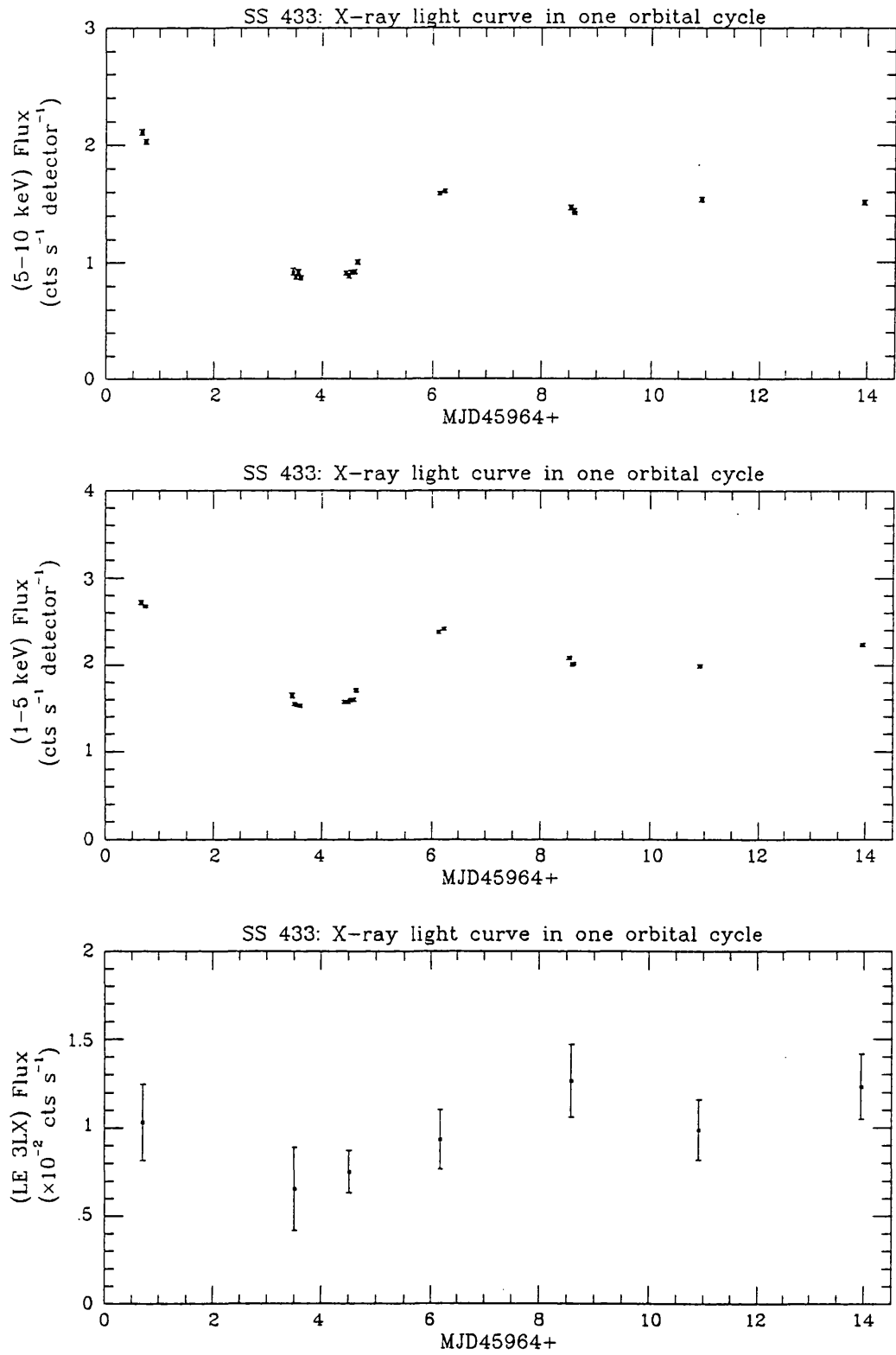


Figure 3.7: X-ray light curve of SS 433 over one binary cycle.

Table 3.4: Observing log for the X-ray eclipse of SS 433 in 1985 May (times in UT)

No.	Start	End	Binary Phase	Exposure (secs)	
				ME (Argon)	LE
1	17th 20:18:17	17th 21:42:17	0.965	5040	3797 (3LX)
2	17th 21:42:17	17th 23:05:37	0.970	5000	4770 (3LX)
3	17th 23:05:37	18th 00:28:57	0.974	5000	4769 (3LX)
4	18th 00:28:57	18th 01:58:47	0.979	5390	2733 (3LX)
5	18th 02:08:47	18th 03:32:07	0.984	5000	7314 (AL/P)
6	18th 03:32:07	18th 04:55:27	0.988	5000	4677 (AL/P)
7	18th 04:55:27	18th 06:18:47	0.993	5000	4618 (AL/P)
8	18th 06:18:47	18th 07:49:47	0.997	5460	4791 (AL/P)

2) X-ray eclipse at precession phase 0.06

Fig. 3.1 clearly shows that point E12 is another *EXOSAT* observation which was made corresponding to the primary optical minimum. The data of this observation was therefore carefully analyzed and the indication of an X-ray eclipse at the jet precession phase 0.06 is indeed found.

The observation was made from 20^h : 18^m of May 17 to 7^h : 50^m of May 18 1985, which corresponds to the binary phase of 0.96-1.00, well inside the duration of the primary optical minimum. The detail observing log of the eclipse is given in table 3.4 and the light curves of various energy ranges are shown in Fig. 3.8. The decrease of the X-ray intensity is significant, however, because the observation was made at the low state of the source and inside the eclipse, the decreasing fraction was not as high as that of the eclipse at jet precession phase 0.6. There is also indication that the spectrum became softer when the intensity decreased.

This eclipse is for the first time found to occur at the period when the lower jet approaches to the observer and its discovery adds further evidence to support the 'standard kinematical model'.

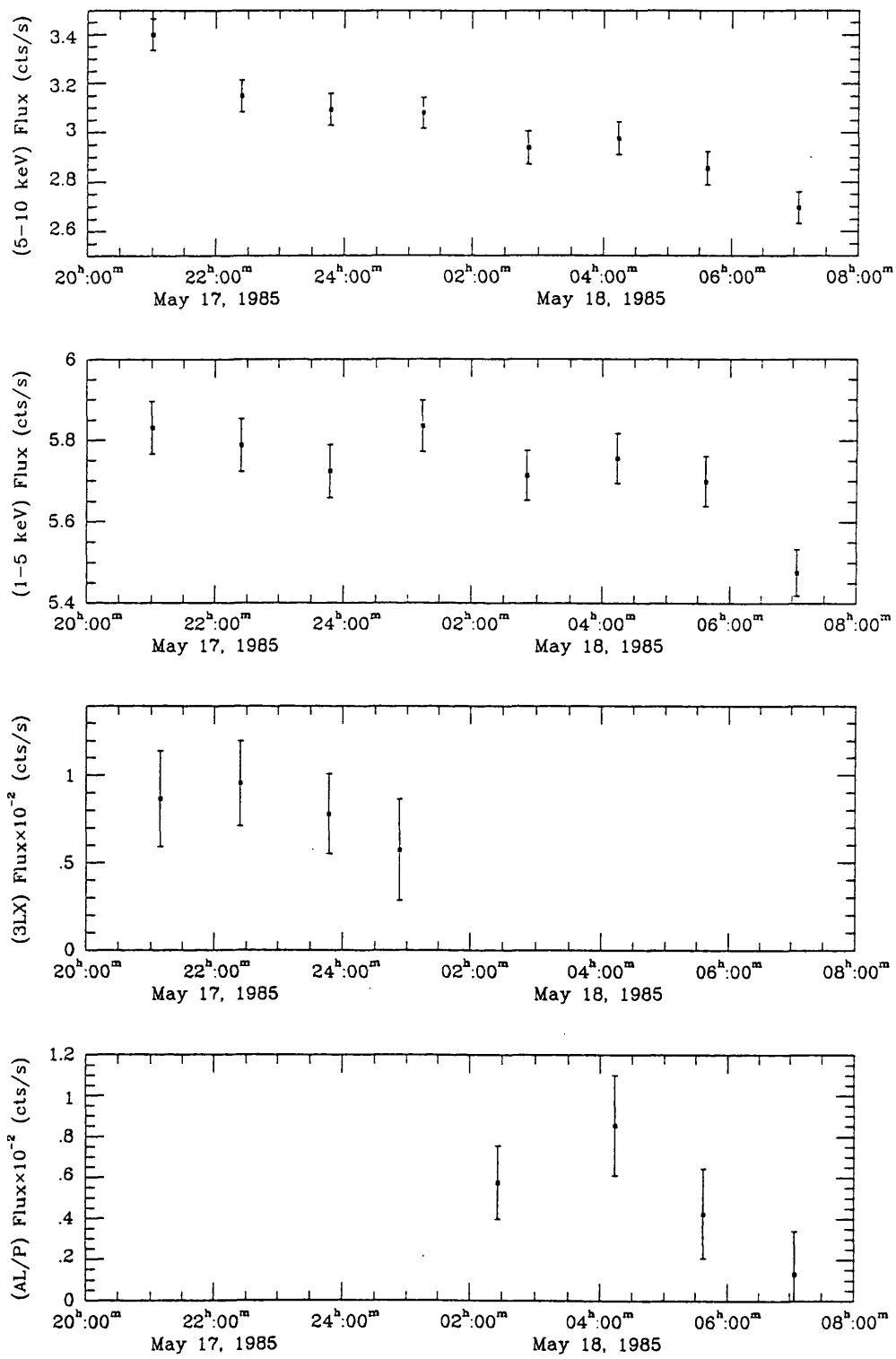


Figure 3.8: X-ray eclipse light curve at precession phase 0.06

2. X-ray spectral variation over 13 day binary period

There are significant binary modulations on both continuum and emission line of all the seven spectra of SS 433 obtained in a 13 day cycle. The spectra over the binary period are shown in Fig. 3.9 and the detail results of the spectral model fits are listed in table 3.5. The LE measurements are consistent with those of ME.

1) X-ray continuum

The X-ray continuum of SS 433 varies over the binary phase.

When a thin thermal bremsstrahlung is used to fit the X-ray continuum, the variation of the bremsstrahlung temperature is correlated with the X-ray intensity, although the temperature is not very well determined due to the shortage of the spectral range covered by ME detectors. The temperature is higher whenever the luminosity is at high state.

However, there is no modulation on the bremsstrahlung temperature when the Comptonized bremsstrahlung continuum is assumed, the temperature is consistent with ~ 6 keV. The optical depth is correlated with the X-ray intensity, decreasing with the drop of the flux of SS 433. Again, this model disobeys the requirements for its application and should be regarded as empirical.

The bremsstrahlung temperature in the model of the combined thermal bremsstrahlung and black body varies from 13.2 ± 0.7 keV at the phase of the maximum X-ray intensity to 7.5 ± 0.3 keV when the source reaches its lowest state. The black body temperature does not vary significantly and is consistent with ~ 4 keV.

When a non-thermal power law continuum is applied to the X-ray spectrum of SS 433, there is a strong modulation on the photon index, which varies from 1.2 ± 0.1 where the X-ray intensity is high to 1.9 ± 0.3 when the intensity decreases to its minimum. Coupling power law with an exponential high energy cut-off function does not improve χ^2 . The derived photon indices have similar values and behaviour as the single power law model. Accordingly, the derived parameters for this model are not listed in table 3.5.

The equivalent neutral hydrogen column density, which is responsible for the absorption of soft X-rays, is not modulated by the binary motion, and is consistent with $\sim 8 \times 10^{21}$ cm⁻²

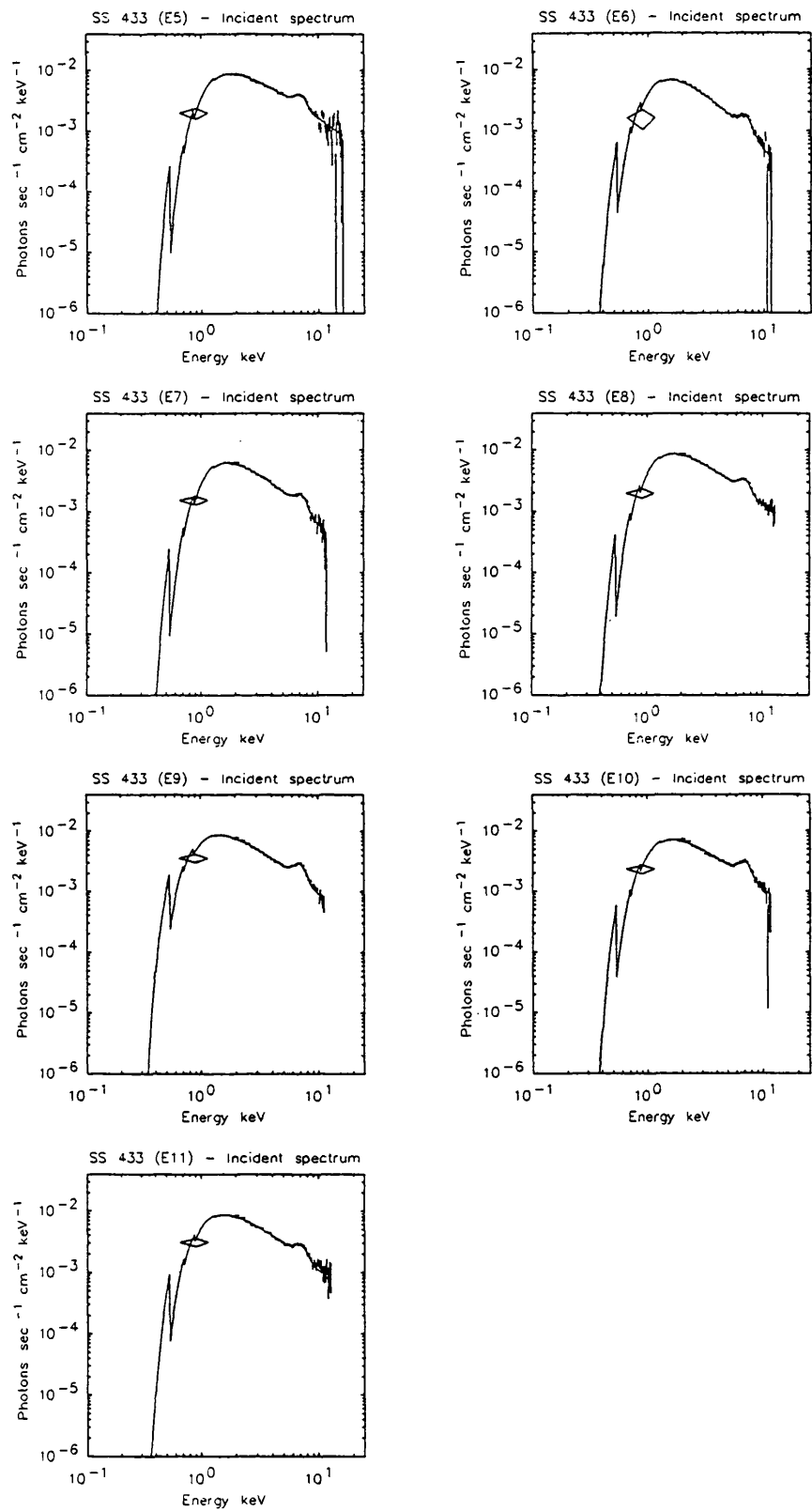


Figure 3.9: The X-ray spectra over 13 day cycle, where the binary phase for each spectrum is E5-0.759, E6-0.974, E7-0.049, E8-0.177, E9-0.361, E10-0.539, E11-0.771.

Table 3.5: Evolution of SS 433 spectra over one binary cycle

Model 1: (a bremsstrahlung + a broad line)×low energy absorption									
Log $\phi_{13.08}$	continuum parameters			emission line parameters					
	T_{brem} (keV)	column N_{H} ($\times 10^{21} \text{ cm}^{-2}$)	energy (keV)	flux ($\times 10^{-2}$) (photon $\text{cm}^{-2} \text{ s}^{-1}$)	width (keV)	reduced χ^2 (d.o.f)	No	Log $\phi_{13.08}$	reduced χ^2 (d.o.f)
5	142.50 $^{+920.50}_{-72.96}$	8.21 $^{+0.81}_{-0.99}$	7.07 $^{+0.14}_{-0.07}$	0.29 $^{+0.05}_{-0.04}$	0.80 $^{+0.21}_{-0.08}$	2.0(44)			
6	12.29 $^{+2.52}_{-2.13}$	6.78 $^{+1.39}_{-1.21}$	7.07 $^{+0.35}_{-0.10}$	0.15 $^{+0.03}_{-0.02}$	0.78 $^{+0.70}_{-0.09}$	1.4(31)	6	0.974	1.4(31)
7	16.20 $^{+4.31}_{-5.36}$	8.16 $^{+1.25}_{-1.04}$	7.19 $^{+0.15}_{-0.08}$	0.16 $^{+0.03}_{-0.03}$	0.81 $^{+0.12}_{-0.12}$	1.4(31)	7	1.049	1.4(31)
8	51.43 $^{+30.89}_{-14.11}$	7.53 $^{+0.95}_{-0.86}$	7.11 $^{+0.11}_{-0.10}$	0.23 $^{+0.04}_{-0.03}$	0.77 $^{+0.09}_{-0.16}$	1.3(34)	8	1.176	1.3(34)
9	31.06 $^{+1.15}_{-0.71}$	4.93 $^{+0.55}_{-0.52}$	7.01 $^{+0.07}_{-0.06}$	0.27 $^{+0.02}_{-0.02}$	0.79 $^{+0.03}_{-0.03}$	1.6(30)	9	1.360	1.6(30)
10	77.79 $^{+5.37}_{-5.08}$	6.16 $^{+0.88}_{-0.79}$	7.10 $^{+0.09}_{-0.12}$	0.28 $^{+0.03}_{-0.03}$	0.80 $^{+0.08}_{-0.07}$	2.0(32)	10	0.539	2.0(32)
11	38.80 $^{+28.97}_{-11.13}$	5.93 $^{+0.94}_{-0.86}$	7.11 $^{+0.16}_{-0.18}$	0.21 $^{+0.04}_{-0.05}$	0.80 $^{+0.13}_{-0.19}$	1.5(34)	11	0.771	1.5(34)

Model 2: (a power law + a broad line)×low energy absorption									
Log $\phi_{13.08}$	continuum parameters			emission line parameters					
	Photon Index	column N_{H} ($\times 10^{21} \text{ cm}^{-2}$)	energy (keV)	flux ($\times 10^{-2}$) (photon $\text{cm}^{-2} \text{ s}^{-1}$)	width (keV)	reduced χ^2 (d.o.f)	No	Log $\phi_{13.08}$	reduced χ^2 (d.o.f)
5	1.22 $^{+0.06}_{-0.04}$	7.92 $^{+1.73}_{-0.97}$	7.03 $^{+0.12}_{-0.08}$	0.27 $^{+0.03}_{-0.02}$	0.78 $^{+0.30}_{-0.07}$	2.0(44)			
6	1.85 $^{+0.22}_{-0.18}$	11.67 $^{+3.68}_{-2.86}$	7.07 $^{+0.19}_{-0.16}$	0.18 $^{+0.08}_{-0.04}$	0.97 $^{+0.31}_{-0.30}$	1.2(31)	6	0.974	1.2(31)
7	1.62 $^{+0.23}_{-0.11}$	10.21 $^{+2.23}_{-1.26}$	7.11 $^{+0.21}_{-0.12}$	0.14 $^{+0.05}_{-0.03}$	0.80 $^{+0.24}_{-0.16}$	1.3(31)	7	1.049	1.3(31)
8	1.39 $^{+0.06}_{-0.06}$	8.94 $^{+1.41}_{-1.29}$	7.08 $^{+0.09}_{-0.11}$	0.24 $^{+0.03}_{-0.04}$	0.79 $^{+0.11}_{-0.17}$	1.2(34)	8	1.176	1.2(34)
9	1.47 $^{+0.01}_{-0.01}$	6.29 $^{+0.56}_{-0.61}$	7.00 $^{+0.10}_{-0.09}$	0.28 $^{+0.03}_{-0.02}$	0.87 $^{+0.14}_{-0.10}$	1.4(30)	9	1.360	1.4(30)
10	1.32 $^{+0.01}_{-0.02}$	6.76 $^{+0.83}_{-0.77}$	7.03 $^{+0.76}_{-0.73}$	0.28 $^{+0.03}_{-0.02}$	0.79 $^{+0.05}_{-0.04}$	1.9(32)	10	0.539	1.9(32)
11	1.43 $^{+0.07}_{-0.08}$	7.14 $^{+1.41}_{-1.19}$	7.05 $^{+0.17}_{-0.15}$	0.21 $^{+0.04}_{-0.05}$	0.79 $^{+0.16}_{-0.19}$	1.2(34)	11	0.771	1.2(34)

Table 3.5: Evolution of SS 433 spectra over one binary cycle (continue)

Model 3: (a Comptonized bremsstrahlung + a broad line)×low energy absorption											
		continuum parameters				emission line parameters					
Log $\phi_{13.08}$	T_{brem}	Optical	column N_{H}	energy	flux ($\times 10^{-2}$)	width	reduced				
No	(keV)	depth	($\times 10^{+21} \text{ cm}^{-2}$)	(keV)	(photon $\text{cm}^{-2} \text{ s}^{-1}$)	(keV)	$\chi^2(\text{d.o.f})$				
5	0.758	5.67 $^{+0.49}_{-0.87}$	14.75 $^{+1.89}_{-2.50}$	7.59 $^{+1.35}_{-1.19}$	0.25 $^{+0.04}_{-0.04}$	0.75 $^{+0.11}_{-0.15}$	1.9(43)				
6	0.974	6.07 $^{+7.90}_{-2.09}$	6.59 $^{+4.38}_{-4.77}$	6.99 $^{+1.36}_{-1.24}$	0.15 $^{+0.16}_{-0.02}$	0.79 $^{+0.62}_{-0.10}$	1.4(30)				
7	1.049	5.07 $^{+10.91}_{-1.68}$	9.17 $^{+3.91}_{-2.93}$	8.34 $^{+1.22}_{-1.07}$	0.16 $^{+0.03}_{-0.03}$	0.81 $^{+0.14}_{-0.14}$	1.4(30)				
8	1.176	7.26 $^{+32.41}_{-2.22}$	9.73 $^{+0.42}_{-7.60}$	8.04 $^{+0.95}_{-0.87}$	0.22 $^{+0.04}_{-0.04}$	0.74 $^{+0.10}_{-0.17}$	1.3(33)				
9	1.360	7.21 $^{+8.79}_{-2.70}$	8.74 $^{+3.13}_{-4.71}$	5.19 $^{+0.80}_{-0.71}$	0.26 $^{+0.04}_{-0.03}$	0.78 $^{+0.06}_{-0.05}$	1.6(28)				
10	0.539	5.03 $^{+3.46}_{-0.51}$	12.75 $^{+2.89}_{-3.48}$	6.47 $^{+1.08}_{-1.14}$	0.27 $^{+0.35}_{-0.04}$	0.80 $^{+0.08}_{-0.08}$	2.0(30)				
11	0.771	9.24 $^{+11.34}_{-3.89}$	8.19 $^{+3.03}_{-3.94}$	6.07 $^{+1.00}_{-0.82}$	0.19 $^{+0.05}_{-0.05}$	0.73 $^{+0.16}_{-0.24}$	1.4((33)				

Model 4: (a bremsstrahlung + a black-body + a broad line)×low energy absorption											
		continuum parameters				emission line parameters					
Log $\phi_{13.08}$	T_{brem}	T_{bbod}	column N_{H}	energy	flux ($\times 10^{-2}$)	width	reduced				
No	(keV)	(keV)	($\times 10^{+21} \text{ cm}^{-2}$)	(keV)	(photon $\text{cm}^{-2} \text{ s}^{-1}$)	(keV)	$\chi^2(\text{d.o.f})$				
5	0.758	13.22 $^{+0.69}_{-0.65}$	3.55 $^{+0.16}_{-0.14}$	8.73 $^{+0.85}_{-0.86}$	0.25 $^{+0.03}_{-0.04}$	0.78 $^{+0.12}_{-0.16}$	1.9(44)				
6	0.974	7.49 $^{+0.30}_{-0.26}$	4.74 $^{+0.72}_{-1.44}$	8.25 $^{+0.92}_{-0.89}$	0.15 $^{+0.06}_{-0.03}$	0.79 $^{+0.31}_{-0.13}$	1.3(31)				
7	1.049	10.31 $^{+0.48}_{-0.42}$	3.79 $^{+0.62}_{-0.80}$	8.81 $^{+0.88}_{-0.83}$	0.15 $^{+0.03}_{-0.03}$	0.80 $^{+0.14}_{-0.14}$	1.3(31)				
8	1.176	11.67 $^{+0.46}_{-0.33}$	4.50 $^{+0.31}_{-0.34}$	9.36 $^{+0.76}_{-0.79}$	0.23 $^{+0.03}_{-0.04}$	0.77 $^{+0.11}_{-0.17}$	1.2(34)				
9	1.360	10.19 $^{+0.32}_{-0.50}$	3.84 $^{+0.72}_{-0.50}$	6.11 $^{+0.69}_{-0.66}$	0.29 $^{+0.06}_{-0.04}$	0.89 $^{+0.16}_{-0.14}$	1.4(29)				
10	0.539	10.37 $^{+0.71}_{-0.64}$	3.24 $^{+0.20}_{-0.21}$	6.68 $^{+0.99}_{-0.88}$	0.26 $^{+0.05}_{-0.05}$	0.80 $^{+0.10}_{-0.09}$	1.8(31)				
11	0.771	9.43 $^{+0.50}_{-0.26}$	5.64 $^{+0.55}_{-0.66}$	7.41 $^{+0.93}_{-0.83}$	0.18 $^{+0.03}_{-0.04}$	0.68 $^{+0.17}_{-0.18}$	1.1(34)				

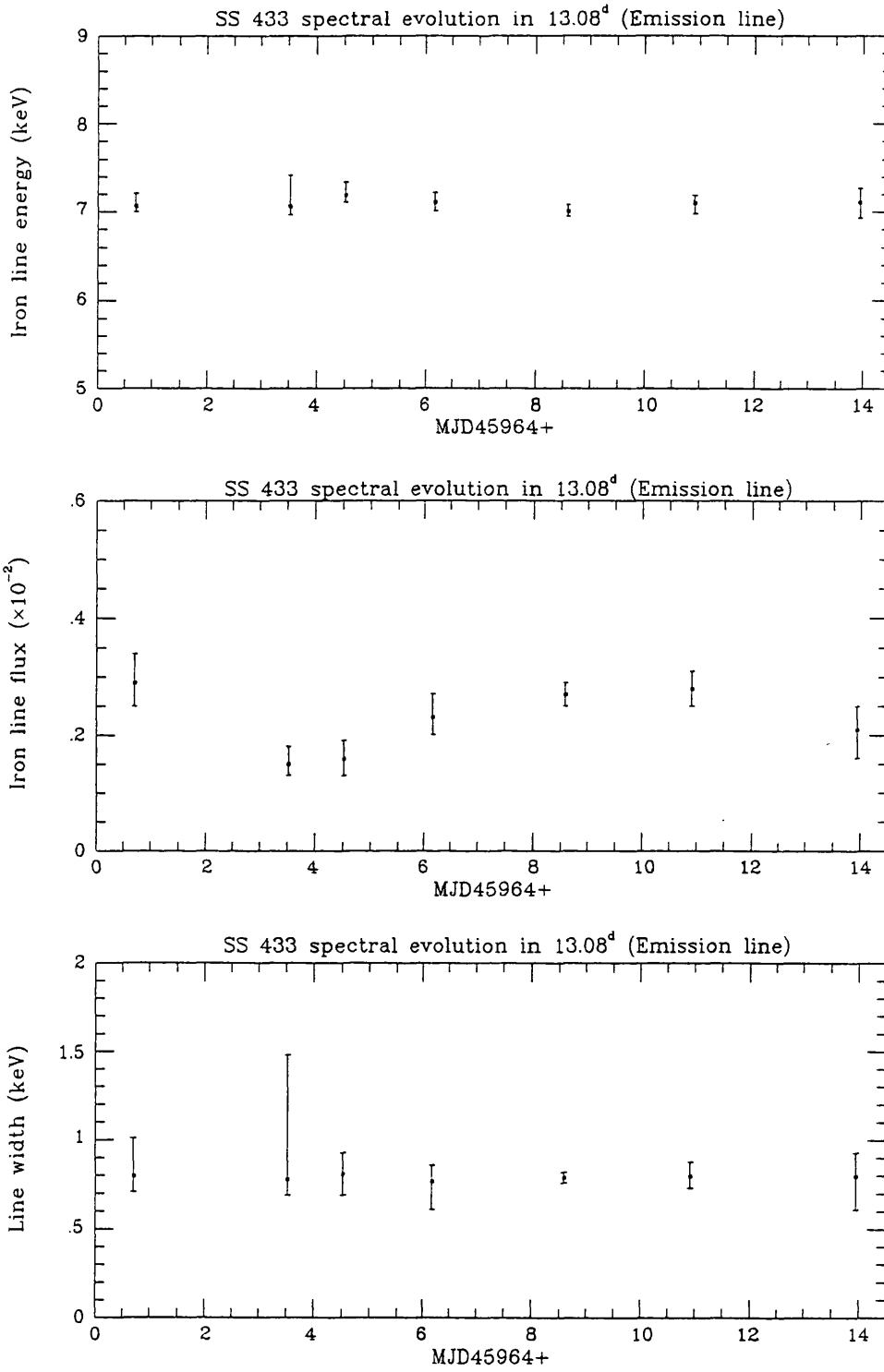


Figure 3.10: X-ray line parameter evolution over 13 day period. Top: the X-ray line energy, Mid: the line flux, Bottom: the line width (1σ of Gaussian profile).

for any assumed continuum.

2) X-ray emission line

The parameters of the X-ray emission line are roughly independent of the assumed continuum model.

As shown in Fig 3.10, the binary motion only influences the line flux, which decreases from $(0.29 \pm 0.05) \times 10^{-2}$ photons sec cm^{-2} to $(0.15 \pm 0.03) \times 10^{-2}$ photons sec cm^{-2} at around the optical primary minimum. The correlated variation of the X-ray line flux and the continuum intensity indicates that equivalent width of the line keeps constant over the binary phase and implies that the X-ray continuum and emission line are indeed associated with each other and from the same X-ray radiation region — the jets.

The X-ray emission line energy keeps constant over the binary phase, which is 7.1 ± 0.2 keV, completely consistent with the Doppler-shifted energy of 6.7 keV iron line predicted from motion of the jet material outward for the corresponding precession phase.

There is no binary modulation on the X-ray line width. The line width stays fairly constantly at ~ 0.8 keV.

3.3.3 A Possible Soft X-ray Excess in the Spectrum of SS 433

The derived neutral hydrogen column density from fitting the *EXOSAT* spectrum above 2 keV is consistent with $\sim 8 \times 10^{21}$ cm^{-2} , lower than 1.5×10^{22} cm^{-2} expected from optical extinction for the same object (Murdin, Clark & Martin 1980; Wagner 1983). This may indicate the influence of the soft X-ray emission on the determination of real properties of the SS 433 spectrum.

To investigate the effect of this soft X-ray radiation, the soft X-ray spectrum was then carefully checked. A strange line-like bump over 1-2 keV energy range is found in every X-ray spectrum of SS 433 when ME spectrum is extracted from above 1 keV. Although it is difficult to derive any reliable information on this strange feature because it is near the edge of the energy range of ME instrument, the consistency of count rate at the red of this line-like bump with LE flux indicates that this soft bump could be real.

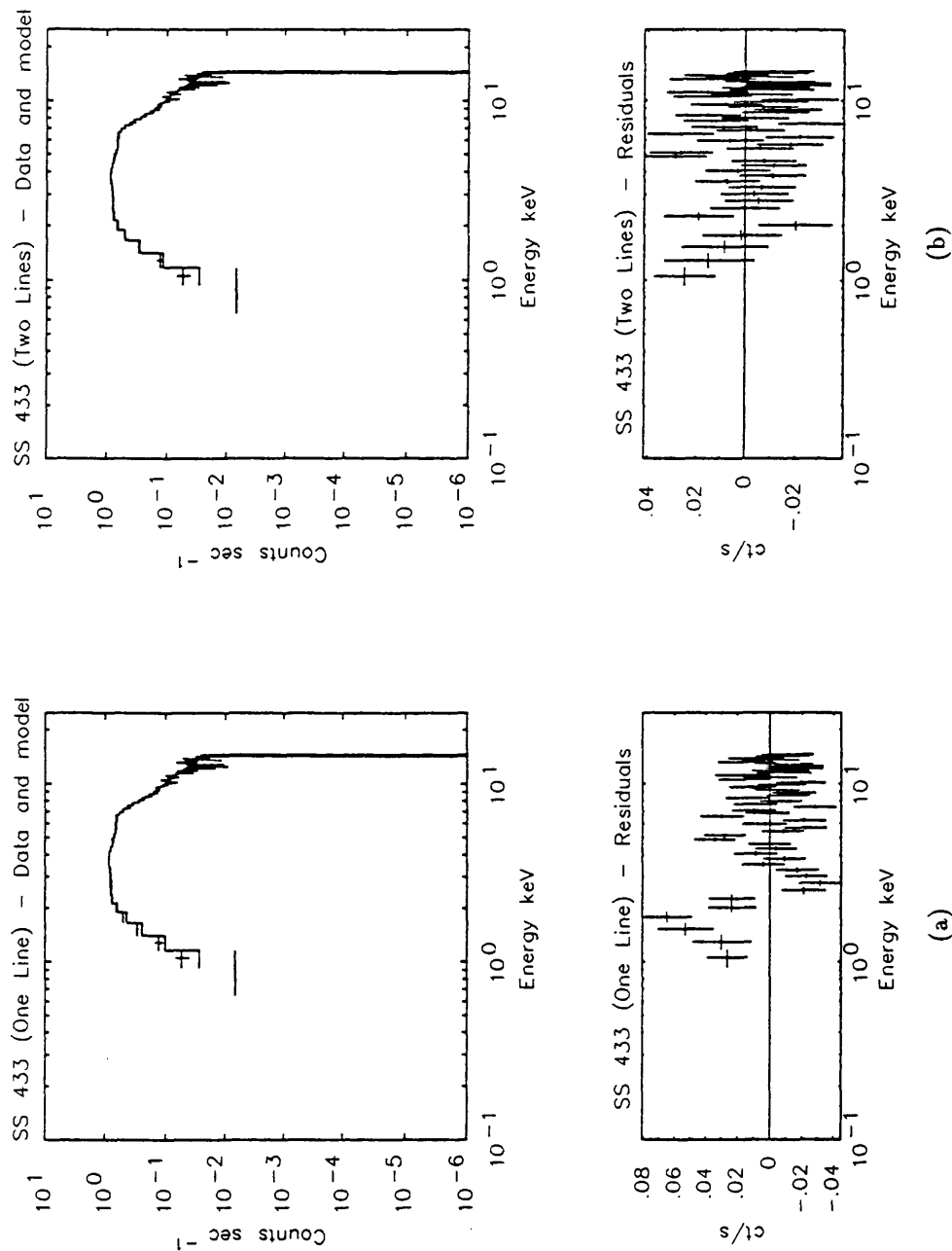


Figure 3.11: Soft X-ray excess in SS 433 spectrum. (a) fitting the spectrum without introducing a line in 1-2 keV clearly indicates a soft excess; (b) fitting line-like bump with another broad emission line.

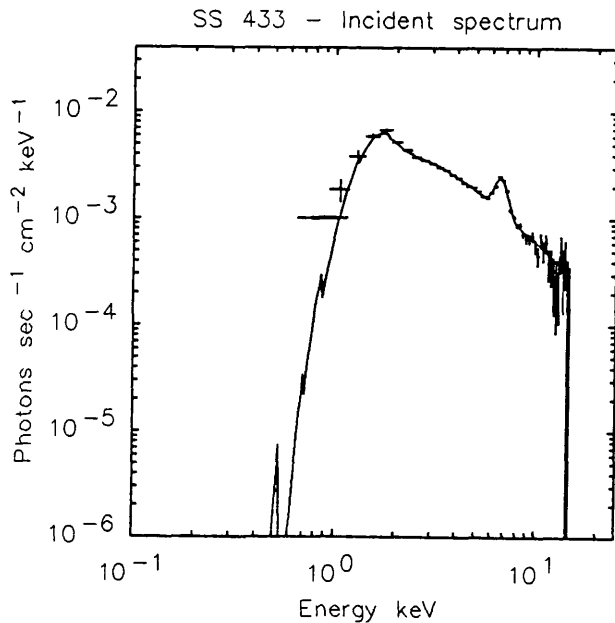


Figure 3.12: SS 433 spectrum which includes two emission lines located at 1.6 keV and 6.7 keV respectively.

The excess emission between 1-2 keV is clearly seen in Fig. 3.11(a) from the residuals of fitted X-ray spectrum by the model including a bremsstrahlung continuum and a broad emission line centered at 6.7 keV. These residuals can be well fitted by another broad emission line as shown in Fig. 3.11(b). Fig. 3.12 gives the incident spectrum which comprises two emission lines, one corresponding to the Doppler energy shifted iron line and another positioned in the 1-2 keV band.

The parameters of this soft broad line are dependent on the continuum assumed and vary from observation to observation. No periodic variation is found. The inclusion of this soft X-ray excess does not greatly affect the determinations of the parameters of X-ray continuum and 6.7 keV line feature, except that the derived column density becomes higher and is then consistent with the value obtained from the optical observations.

GINGA observations presented in next chapter also show the same feature. However, due to the poor sensitivities of both *EXOSAT* and *GINGA* experiments to the X-ray emissions in 1-2 keV band, it is not possible to make any conclusion from current work.

Explanations of this soft X-ray feature are not yet known. If it is real, it could be due to 1.9-2.0 keV SiXIV line emissions from the accretion disc or simply due to the contamination

of the soft X-ray radiations from the X-ray lobes. Further observations in the energy band below 3 keV are necessary to distinguish this features.

3.4 Discussion

3.4.1 Origin of the Energy-shifted X-ray Line

The *EXOSAT* observations of SS 433 presented here have revealed the presence of an emission line whose energy varies with time. As argued by Watson *et al.* (1986), the natural interpretation of these results is that the X-ray emission line in SS 433 must originate in the relativistic jets. A helium-like iron line with energy of 6.7 ± 0.1 keV in the jet coordinate (rest frame), shifts its energy due to the Doppler effect as the jet material moving outward at speed of $0.26c$. With the precessing of the jet axis, the Doppler shifts of this 6.7 keV line vary from phase to phase, as do other parameters of the emission line. A good fit between the expected and measured line energies is achieved when the parameters of the ‘standard kinematical model’ of Margon (1984) and a rest energy for the emission line of 6.7 ± 0.1 keV are adopted (see Fig. 3.6). The rest energy strongly suggests thermal emission with Fe_{xxv} dominating.

Another result which supports the jet origin of emission line is the observed modulation of the line flux by the jet precession and orbital motion. When the jet points towards the observers, the Doppler-boosting effect makes the source brightest and the observed line flux reaches its maximum. With the jet moves away the line of sight, the line flux decreases again. The similarity of the Doppler beaming factor ($\sim 1/(1+z)^3$) and the shape of the X-ray intensity over the 163 day jet precession phase strongly implies that the line emission is associated with the jet material moving at the relativistic speed. The variation of the line width, as argued below, may be also an evidence for this line origin.

The equivalent width of the Doppler energy-shifted lines is $\sim (1.2 - 1.5) \pm 0.5$ keV. It is about a factor of two larger than that of the lines produced in thermal plasma with solar abundance, and the temperatures derived from the spectral fitting.

3.4.2 Origin of the Continuum Emission and Its Nature

The results presented above also strongly suggest that most (> 50 percent) of the X-ray continuum flux must originate in the jets and be thermal bremsstrahlung. The shape of the X-ray spectrum of SS 433 and the variation of its X-ray intensity over the jet precession cycle indicate that the modulation of the jet precession on the X-ray continuum flux is mainly due to the beaming and geometrical effects. Here again, the effects of the relativistic motion of the jet material and the precession of the jet axis play great roles in changing the observed X-ray features of SS 433. With different view angle to the jet, the different luminosity is seen due to the different Doppler-boosting factor. The compatibility of the measured equivalent width of the line with (within a factor of ≤ 2) that expected for an X-ray plasma with a temperature of a few keV for material with cosmic abundances also requires that most of the X-ray continuum flux is from the jets and the X-ray spectrum of SS 433 is predominantly thermal. The constancy of the equivalent width of the X-ray emission line during the two X-ray eclipses further strengthens the association of the X-ray emission line and the continuum radiation.

No emission line was observed by *EINSTEIN* (e.g. Grindlay *et al.* 1984). The X-ray spectrum was described with power law. These results, with the observation of simultaneous radio and X-ray flares (Seaquist *et al.* 1982), were interpreted in terms of non-thermal X-ray production processes and led to the development of detailed non-thermal models for SS 433 (Grindlay *et al.* 1984; Band & Grindlay 1984, 1985). Although it is not possible to judge which is the best model to describe the nature of the SS 433 X-ray radiation simply from fitting the present *EXOSAT* spectrum which has a limited energy range, thermal X-ray radiation from the jets of SS 433 is strongly suggested. As each observation is much longer than the radiative cooling time, the observed X-ray spectrum will actually be the integration of the thermal bremsstrahlung radiation with various temperatures along the jets (see Chapter 6 for the detailed model). The earlier *EINSTEIN* results may also have been consistent with the X-ray emission from SS 433 being predominantly thermal as the *EINSTEIN* experiment was not sensitive to any line emission, and had an even more limited band-pass and resolution than *EXOSAT*.

3.4.3 Visibility of Lines — Where Is the Red Component?

A major difference between the optical moving lines and the X-ray result, however, is that in the X-ray data only one line is visible and another — the red component is missing from the spectrum at any time. As interpreted above, the strength of the emission lines is subject to a strong modulation with changing Doppler shift. However, the ‘missing’ line cannot be easily explained by this Doppler boosting of the radiation from the jets, at least for most of the observations, as the gain in strength of the observed line relative to the unobserved line is too small to cause the line to be undetectable.

The most natural explanation for the non-observation of one line is that the line of sight to that jet is such that the jet is obscured by material which also responds to the 163 day clock in the system. The most natural location for this material is in the accretion disc. For the relevant jet to be obscured at a particular phase, the relative sizes of the jet and the accretion disc are constrained.

Alternatively, it is still possible but unlikely, that some fraction of red component is indeed seen but submerged by the strong wing of the blue shifted line. Suppose that bremsstrahlung temperature decreases along the jet, various iron line species would be produced by the jet material because of the temperature distribution and these multiple line radiations under the operation of the relativistic effect, are strong enough to obscure the line emission from the receding jet and make the resultant line feature becomes intense and broad with energy centered at the blue-shifted side.

3.4.4 Implications of the Variable Line Width

The origin of the 163 day modulation of the line width observed with *EXOSAT* is a complex question to answer. With the shortage of the energy resolution of the present X-ray instrument, it is hard to make this answer unambiguous and alternative explanations will exist until further observations can be made.

The 163 day modulation of the X-ray line width is an important discovery from which the physical condition and the structure of the X-ray jets will finally be found. There are several mechanisms which will possibly produce broad line at the phase when one of the jets is

approaching to the observer and crossing the line of sight, and line with narrow profile while the jets become edge-on.

Compton scattering is a possible mechanism which will broaden the line, if the jet has sufficient optical depth. When the jet is approaching to the observer, the photons which have experienced more scattering are received and a broader line will appear in the X-ray spectrum. Photons which have been scattered less will be seen while the jets are seen edge-on. Detailed modelling of this mechanism will disclose the physical condition of the jets and impose a strict constraint on the jet acceleration theory.

It is also possible that the velocity dispersion of the jet material will broaden the emission line. If the structure of jet is not a cylinder shape but a cone with its vertex at the exit from the funnel, the material moving along the axis of the jet cone will produce lines with energy coincide with the value predicted from the kinematic model, while the material moving on the surface of the jet cone will give the lines distributed around the lines generated by the on-axis material. Thus the observed line becomes broad. With the jet precession, different view angles to the axis and the surface of jet cone are formed, these geometrical effects result in the 163 day modulation of the line width. However, to explain the large broadening, an opening angle of $\sim 50^\circ$ is required for the cone.

Another possible way to explain the modulation of line width by the jet precession is that the observed line feature is composed of various line species generated by the material with different ionization degree such as hydrogen-like and helium-like iron ions. Because there is a temperature distribution along the jet, hot at the jet bottom and relatively cold on the top, ions at different ionization stages will exist in the jet. When the jet points to the observer, the hotter and higher ionization regions as well those of colder and lower ionization are seen, the observed emission line, because it consists of various lines with different line energies, will be broader. When the jet becomes edge-on, the hotter base of the jet is obscured by the accretion disc, only those line radiations from cold region are observed and the line in the spectrum will become narrow.

The relativistic effect may also play certain roles in broaden the line. When the jet material is ejecting towards the observer, the two wings of the line have different Doppler shifts and line is broad; while the jet is edge-on, the relativistic motion of the emitting material almost has no influence to the emitted line.

Of the above mechanisms, Compton broadening is most likely to be the true cause, with the other effects contributing but not substantially.

3.5 Summary

The *EXOSAT* study of SS 433 has shown that jet precession strongly modulates the X-ray intensity over 163 day jet precession cycle. The source is at its high luminosity state when the angle between the line of sight and jet precession axis becomes minimum and the maximum separation of the Doppler red- and blue-shifted optical lines is seen; the low luminosity state occurs at the phase when jets are edge-on. A large (up to 50%) energy independent intensity decrease is seen while the source changes from its high state to low state.

Two X-ray eclipses, which occurred in the period of the optical primary minimum and corresponding to different jet precession phase have been observed with *EXOSAT*. The simultaneous optical monitor of SS 433 over one binary cycle at jet precession phase 0.6 when the source was still at its high luminosity state clearly indicated that the X-ray eclipse was completely coincident with the primary optical luminosity drop, which is interpreted as the occultation of the accretion disc by the companion star. The X-ray eclipse at precession phase 0.06 was found for the first time.

The modulations of the jet precession and orbital motion on the X-ray spectrum are also found with the *EXOSAT* observations. Although the X-ray continuum of SS 433 stays fairly constant over 163 day jet precession phase, the modulation on the X-ray emission line is extraordinary. All parameters which describe the line feature vary with the precession of jets. The Doppler energy shift profile of the iron line is completely consistent with that predicted from 'standard kinematic model'. The line flux changes following the variation of the X-ray continuum over 163 day cycle, implying that the line and continuum radiations are associated with each other. Detailed modelling on the variable line width will reveal the physical condition and structure of the jets. Over 13 day binary cycle, there is strong modulation on the X-ray continuum and line flux, however, the line energy and width keep fairly constant.

The most recent results of *EXOSAT* observations can be well interpreted within the framework of the 'standard kinematic model'. Most of the X-rays (both continuum and line) must

originate in the relativistic jets and be thermal in nature. The relativistic motion of the jet material, the precession of jet and the binary motion play great roles in changing the observed X-ray features. Thus, modelling of the X-ray data can provide significant information on these phenomena.

Chapter 4

GINGA Observations of SS 433

4.1 Introduction

Optical observations have established the binary nature of SS 433. The orbital period is determined from the 13.1 day modulations in either the optical light curve (Kemp *et al.* 1986) or the Doppler velocity of the ‘stationary lines’ (Crampton & Hutchings 1981). There exist two minima in the optical light curve of SS 433, phased on a 13.1 day binary period. The primary minimum is ascribed to a conjunction when the accretion disc is partially occulted by the normal companion star, while the secondary minimum is interpreted as the eclipse of the normal star by the accretion disc. This phasing is deduced based on the phase of the Doppler curve of the lines associated with the accretion disc (Crampton & Hutchings 1981).

In the X-ray energy range, there has been an attempt to detect the binary modulation of the X-ray intensity from the MPC data of the *EINSTEIN* observatory (Grindlay *et al.* 1984). Although these observations were suggestive of an X-ray intensity reduction at the phase of the optical primary minimum, they were taken from many orbital cycles with various intensity states, and it was difficult to derive any firm conclusion on the parameters of the system. The partial eclipse of the X-ray intensity was confirmed by *EXOSAT* observations made over one binary cycle with a sampling interval of ~ 1 -3 days (Stewart *et al.* 1987; and Chapter 3 in this thesis). The analysis of the X-ray eclipse set some constraints on the parameters of the system such as mass ratio of the two bodies and the length of the X-ray jets, though fairly large uncertainties were left because of incomplete coverage of the eclipse period (Stewart *et*

al. 1987).

This chapter describes three well-sampled observations of the X-ray eclipse of SS 433 from ingress to egress with the *GINGA* LAC. The observations were all centered at the phase of optical primary minimum, but were at different jet precession phases. The aims of these observations were to confirm the previous results reported with *EINSTEIN* and *EXOSAT*, to precisely determine the nature of the X-ray eclipse so that a more accurate estimate of the parameters of the SS 433 system could be made (see Chapter 5), and to map the temperature distribution along the jets so that a physical model of the X-ray emission in the jets could be created (see Chapter 6). In the following section, the *GINGA* observations and data reduction are introduced. The observation results are presented in section 4.3 and their implications are discussed in section 4.4. Section 4.5 gives a summary of the results of the *GINGA* observations.

4.2 *GINGA* Observations and Data Analysis

GINGA LAC observations of SS 433 were made on three occasions, in 1987 May 18.0-23.0, 1988 May 18.9-22.7 and 1989 May 7.1-12.1. The duration of each observation was chosen to cover an X-ray eclipse which lasting for more than 1.2 days (Stewart *et al.* 1987; Chapter 3 in this thesis) at the phase corresponding to the optical primary minimum. The primary optical minima were predicted to occur at 1987 May 20.9 ± 1.6 (UT), 1988 May 21.1 ± 1.7 and 1989 May 9.3 ± 1.8 from the ephemeris given by Kemp *et al.* (1986) (see Eq. (5.29)) or, 1987 May 20.88 ± 0.06 , 1988 May 21.18 ± 0.08 and 1989 May 9.39 ± 0.10 by the formula of Gladyshev, Goranskii and Cherepashchuk (1987) (see Eq. (5.30)). The precession phase for the 1987 May observation was 0.56-0.59, which is slightly later than phase 0.5, the epoch corresponding to the maximum separation of the two moving lines from the relativistic jets. For the observation made in 1988 May, the jet precession phase was from 0.82 to 0.84, at which the two moving lines have crossed over and are separating again. In the period of 1989 May 7.1-12.1, the precession phase was 0.99-1.02 during which the lower jet approaches the observer. The locations of the three X-ray eclipse observations with *GINGA* are also plotted in the binary and jet precession phase-space diagram, Fig. 3.1.

Most of the observations in 1987 May were made in MPC-2 mode, in which spectral informa-

Table 4.1: GINGA Observation Log (SS 433, 1987 May)

No.	Date (5/87)	Time		MJD At Mid-Obs. (MJD46933 +)	Binary Phase $\phi_{13.08}$	Exposure (sec)
		Start	End (UT)			
1	18	03:23	03:38	0.1464	0.792	900
2		05:53	06:12	0.2517	0.800	1100
3		06:40	06:55	0.2830	0.803	900
4		09:07	09:20	0.3843	0.810	800
5		10:43	10:52	0.4497	0.815	500
6		11:32	11:45	0.4850	0.818	800
7		12:20	12:28	0.5168	0.821	500
8		12:53	13:10	0.5428	0.823	1000
9		14:30	14:47	0.6100	0.828	1000
10		16:08	16:25	0.6782	0.833	1000
11		17:45	18:05	0.7465	0.838	1200
12		19:23	19:43	0.8148	0.843	1200
13		21:00	21:22	0.8825	0.849	1300
14		22:35	23:00	0.9497	0.854	1500
15	19	00:13	00:35	1.0168	0.859	1300
16		01:50	02:12	1.0839	0.864	1300
17		02:48	02:50	1.1175	0.867	100
18		03:28	03:48	1.1516	0.869	1200
19		06:00	06:17	1.2558	0.877	1000
20		06:45	07:02	1.2870	0.879	1000
21		09:13	09:25	1.3883	0.887	700
22		10:02	10:15	1.4225	0.890	800
23		11:20	11:52	1.4832	0.894	1900
24		12:27	12:32	1.5203	0.897	300
25		12:58	13:15	1.5463	0.899	1000
26		14:03	14:10	1.5880	0.902	400
27		14:33	14:52	1.6128	0.904	1100
28		16:12	16:32	1.6817	0.910	1200
29		17:52	18:10	1.7506	0.915	1100
30		19:28	19:50	1.8189	0.920	1300
31	21:05	21:28	1.8866	0.925	1400	
32	22:42	23:07	1.9543	0.930	1500	
33	20	00:17	00:42	2.0203	0.936	1400
34		01:57	02:03	2.0833	0.940	300
35		04:32	04:38	2.1910	0.949	400
36		06:08	06:22	2.2604	0.954	800
37		06:52	07:08	2.2917	0.956	1000
38		10:57	11:02	2.4578	0.969	300
39		11:27	11:57	2.4873	0.971	1800
40		12:33	12:38	2.5249	0.974	300
41		13:02	13:20	2.5492	0.976	1100

Table 4.1: GINGA Observation Log (SS 433, 1987 May) (continued)

No.	Date (5/87)	Time		MJD At Mid-Obs. (MJD46933 +)	Binary Phase $\phi_{13.08}$	Exposure (sec)
		Start	End			
		(UT)				
42	21	14:10	14:15	2.5920	0.979	300
43		14:40	14:58	2.6175	0.981	1100
44		16:18	16:38	2.6863	0.986	1200
45		17:57	18:17	2.7546	0.992	1200
46		19:33	19:55	2.8223	0.997	1300
47		21:08	21:33	2.8895	1.002	1500
48		22:47	23:12	2.9578	1.007	1500
49		00:23	00:47	3.0243	1.012	1200
50		02:03	02:25	3.0932	1.018	1100
51		04:38	04:48	3.1968	1.025	600
52		06:15	06:28	3.2650	1.031	800
53		06:57	07:08	3.2934	1.033	700
54		07:52	07:57	3.3293	1.036	300
55		08:35	08:52	3.3634	1.038	1000
56		09:55	10:00	3.4149	1.042	300
57		10:07	10:27	3.4282	1.043	1200
58		11:32	11:48	3.4861	1.048	1000
59		13:08	13:25	3.5532	1.053	1000
60		14:47	15:05	3.6221	1.058	1100
61		16:23	16:45	3.6904	1.063	1300
62		18:00	18:22	3.7575	1.068	1300
63	19:37	20:00	3.8252	1.074	1400	
64	21:13	21:40	3.8935	1.079	1600	
65	22:50	23:20	3.9618	1.084	1800	
66	22	00:30	00:53	4.0289	1.089	1300
67		02:13	02:32	4.0990	1.094	1000
68		03:08	03:10	4.1314	1.097	100
69		04:45	04:53	4.2008	1.102	500
70		05:23	05:45	4.2321	1.105	1300
71		06:22	06:27	4.2668	1.107	300
72		07:03	07:22	4.3003	1.110	1100
73		08:42	08:57	4.3675	1.115	900
74		11:38	11:55	4.4907	1.124	1000
75		13:15	13:32	4.5579	1.130	1000
76		14:52	15:10	4.6256	1.135	1100
77		16:32	16:50	4.6950	1.140	1100
78		18:07	18:28	4.7622	1.145	1300
79		19:42	20:07	4.8293	1.150	1500
80		21:18	21:47	4.8976	1.155	1700
81	22:57	23:27	4.9664	1.161	1700	

tion is taken at 48 PHA channels over the energy range 1-36 keV with a resolution of $\sim 19\%$ at 6 keV. The time resolution in this mode is 0.125 s for the satellite orbits with ground contact (four orbits per day), and 0.5 s for the remaining 11 orbits. The data were obtained in segments with a typical length of 20 minutes, separated either by earth occultation of the source or portions of orbits with high background due to charged particles at high geomagnetic latitude or South Atlantic Anomaly. For spectral analysis data were accumulated for each segment of which there were total of 81. A detailed observation log is given in table 4.1.

Some 1987 May observations were also made in PC mode to search for the fast time variability. For these observations, the time resolution is about 1 ms and four energy channels are used. Observations in PC mode were made for three orbits on May 18 and May 19 in 1987 before the eclipse ingress.

Observations in 1988 May and 1989 May were carried out with LAC in MPC1 mode, in which the data were collected over the energy range of 1-36 keV from 48 PHA channels with the time resolution of 500 ms, 4s and 16s corresponding to the contact and remote orbits respectively. Observational logs can be found in table 4.2 (for 1988 May observations) and table 4.3 (for 1989 May observations). A total of 70 spectra are obtained in 1988 observations and in 1989 May, 73 spectra are accumulated. The typical exposure time for each spectrum is longer than 1000 sec.

The background rates for each observation were estimated using the techniques described in Hayashida (1989). For the observations made in 1987 May and 1988 May, the background is generated from a source-free observation adjacent to SS 433 observations. In 1989 May, the background is estimated from many source-free observations. The background estimate was subtracted from the data. The influence of the sun has been considered and the contaminated data points have been deleted. The count rate corrections for dead time and detector attitude drift have also been made. Systematic errors due to the spacecraft attitude correction and to background subtraction are less than a few percent.

With the field of view of $1^\circ \times 2^\circ$ FWHM, the LAC does not have sufficient angular resolution to permit a separation between the compact and diffuse X-ray components of SS 433. The X-ray flux from the lobe of W50 was one third of that from the central point source during the *EINSTEIN* IPC observations, but the intensity of the point source was then exceptionally low (~ 1 IPC counts ~ 1 mCrab). The spectrum of the lobes is also significantly softer

Table 4.2: GINGA Observation Log (SS 433, 1988 May)

No.	Date (5/88)	Time		MJD At Mid-Obs. (MJD47299 +)	Binary Phase $\phi_{13.08}$	Exposure (sec)
		Start	End (UT)			
1	18	21:30	22:21	0.9135	0.830	3100
2		23:10	23:58	0.9818	0.836	2600
3	19	00:48	01:35	1.0495	0.841	2200
4		02:10	03:11	1.1114	0.846	3700
5		03:47	04:44	1.1774	0.851	3400
6		05:20	05:40	1.2295	0.855	1000
7		05:50	06:20	1.2538	0.856	1700
8		06:59	07:14	1.2960	0.860	900
9		07:34	07:57	1.3232	0.862	1400
10		08:34	08:50	1.3626	0.865	1000
11		09:16	09:36	1.3932	0.867	1200
12		10:15	10:31	1.4326	0.870	1000
13		10:58	11:08	1.4604	0.872	600
14		11:48	12:10	1.4991	0.875	1300
15		12:40	12:43	1.5286	0.877	200
16		15:00	15:25	1.6340	0.885	1000
17		16:37	17:04	1.7017	0.891	1400
18		17:27	17:35	1.7300	0.893	500
19		18:15	18:42	1.7700	0.896	1600
20		19:00	19:12	1.7960	0.898	700
21		19:52	20:49	1.8475	0.902	3200
22		21:34	22:24	1.9159	0.907	3000
23		23:09	23:59	1.9821	0.912	3000
24	20	01:01	01:36	2.0544	0.918	2100
25		02:12	03:12	2.1128	0.922	3600
26		03:49	04:49	2.1800	0.927	3400
27		05:24	05:37	2.2297	0.931	800
28		05:56	06:26	2.2575	0.933	1800
29		07:01	07:17	2.2980	0.936	1000
30		07:39	08:01	2.3264	0.938	1300
31		08:37	08:54	2.3652	0.941	1000
32		10:24	10:31	2.4358	0.947	400
33		10:57	11:07	2.4601	0.949	600
34		11:51	12:09	2.5000	0.952	1100
35		12:41	12:44	2.5295	0.954	200

Table 4.2: GINGA Observation Log (SS 433, 1988 May) (continued)

No.	Date (5/88)	Time		MJD At Mid-Obs. (MJD47299 +)	Binary Phase $\phi_{13.08}$	Exposure (sec)
		Start	End (UT)			
36		13:29	13:47	2.5683	0.957	1100
37		15:04	15:29	2.6366	0.962	1500
38		15:57	16:02	2.6667	0.964	300
39		16:41	17:07	2.7043	0.967	1600
40		18:19	18:46	2.7726	0.973	1500
41		19:01	19:11	2.7957	0.974	800
42		19:57	20:52	2.8507	0.979	3100
43		21:36	22:17	2.9144	0.983	2400
44		22:25	22:30	2.9358	0.985	300
45		23:23	00:05	2.9890	0.989	2500
46	21	00:57	01:43	3.0556	0.994	2800
47		02:22	03:18	3.1181	0.999	3400
48		03:58	04:55	3.1852	1.004	2900
49		05:33	05:45	3.2355	1.008	700
50		06:03	06:30	3.2616	1.010	1600
51		07:12	07:23	3.3038	1.013	700
52		07:47	08:07	3.3310	1.015	1200
53		08:45	09:00	3.3698	1.018	900
54		09:27	09:37	3.3970	1.020	600
55		10:22	10:38	3.4375	1.023	1000
56		11:07	11:10	3.4641	1.025	200
57		12:02	12:18	3.5069	1.029	1000
58		13:38	13:57	3.5747	1.034	1100
59		15:13	15:35	3.6418	1.039	1300
60		16:03	16:08	3.6707	1.041	300
61		16:50	17:15	3.7101	1.044	1500
62		17:38	17:47	3.7378	1.046	500
63		18:27	19:23	3.7882	1.050	3400
64		20:03	20:58	3.8547	1.055	3300
65		21:50	22:35	3.9253	1.061	2700
66		23:23	00:12	3.9913	1.066	2900
67	22	00:50	01:48	4.0550	1.071	3500
68		02:27	03:13	4.1181	1.075	2800
69		13:54	14:00	4.5812	1.111	400
70		15:15	15:30	4.6408	1.115	900

Table 4.3: GINGA Observation Log (SS 433, 1989 May)

No.	Date (5/89)	Time		MJD At Mid-Obs. (MJD47653 +)	Binary Phase $\phi_{13.08}$	Exposure (sec)
		Start	End (UT)			
1	07	01:13	01:40	0.0600	0.827	1664
2		02:42	03:16	0.1244	0.832	2048
3		04:22	04:50	0.1919	0.837	1664
4		12:03	12:46	0.5170	0.862	896
5		13:43	14:26	0.5867	0.868	1536
6		15:15	16:06	0.6533	0.873	2432
7		16:51	17:42	0.7200	0.878	2688
8		18:27	19:16	0.7859	0.883	2944
9		20:12	20:54	0.8563	0.888	2560
10		21:48	22:39	0.9259	0.894	3072
11		23:15	00:04	0.9857	0.898	2816
12	08	00:57	01:38	1.0539	0.903	2432
13		02:42	03:14	1.1235	0.909	1920
14		04:24	04:46	1.1909	0.914	1280
15		06:05	06:19	1.2583	0.919	896
16		07:41	07:49	1.3228	0.924	512
17		09:23	09:25	1.3917	0.929	128
18		10:27	10:31	1.4369	0.933	256
19		12:03	12:09	1.5043	0.938	384
20		12:33	12:43	1.5265	0.939	640
21		13:43	13:47	1.5731	0.943	256
22		14:05	14:26	1.5939	0.945	1280
23		15:15	16:06	1.6531	0.949	2944
24		16:51	17:40	1.7191	0.954	2816
25		18:27	19:14	1.7850	0.959	2688
26		20:11	20:52	1.8554	0.965	2432
27		21:39	22:37	1.9220	0.970	3328
28		23:13	00:02	1.9843	0.974	2944
29	09	00:55	01:34	2.0517	0.980	2304
30		02:40	03:10	2.1213	0.985	1792
31		04:20	04:41	2.1880	0.990	1280
32		07:41	07:45	2.3213	1.000	256
33		10:25	10:29	2.4354	1.009	256
34		12:01	12:07	2.5028	1.014	384
35		12:29	12:41	2.5243	1.016	768
36		15:32	16:04	2.6583	1.026	1920

Table 4.3: GINGA Observation Log (SS 433, 1989 May) (continued)

No.	Date (5/89)	Time		MJD At Mid-Obs. (MJD47653 +)	Binary Phase $\phi_{13.08}$	Exposure (sec)	
		Start	End (UT)				
37	10	16:49	17:38	2.7176	1.030	2688	
38		18:25	19:14	2.7843	1.036	2816	
39		20:03	20:52	2.8524	1.041	2944	
40		21:37	22:26	2.9176	1.046	2944	
41		23:13	00:02	2.9843	1.051	2944	
42		00:55	01:34	3.0517	1.056	2304	
43		02:38	03:07	3.1198	1.061	1792	
44		04:20	04:39	3.1872	1.066	1152	
45		05:58	06:11	3.2531	1.071	768	
46		07:38	07:45	3.3206	1.077	384	
47		08:47	08:49	3.3665	1.080	128	
48		09:17	09:21	3.3880	1.082	256	
49		10:23	10:27	3.4339	1.085	256	
50		10:50	10:59	3.4546	1.087	512	
51		11:59	12:05	3.5013	1.090	384	
52		12:24	12:39	3.5220	1.092	896	
53		13:35	14:22	3.5820	1.097	2048	
54		15:11	15:60	3.6494	1.102	2944	
55		16:47	17:34	3.7154	1.107	2816	
56		18:23	19:10	3.7820	1.112	2816	
57		19:59	20:48	3.8494	1.117	2944	
58		21:35	22:24	3.9161	1.122	2944	
59		23:13	23:58	3.9828	1.127	2560	
60		11	00:55	01:29	4.0502	1.132	2048
61			02:35	03:03	4.1176	1.138	1664
62			04:16	04:35	4.1843	1.143	1152
63			10:46	10:59	4.4531	1.163	768
64			12:20	12:39	4.5206	1.168	1152
65			13:45	14:22	4.5857	1.173	2176
66			15:09	15:55	4.6472	1.178	2688
67			16:45	17:31	4.7139	1.183	2816
68			18:35	19:10	4.7865	1.189	2048
69	19:57		20:50	4.8494	1.193	3200	
70	21:33	22:32	4.9183	1.199	2688		
71	23:09	23:51	4.9791	1.203	2560		
72	12	00:53	01:27	5.0487	1.209	2048	
73		02:46	02:59	5.1198	1.214	768	

than the the point source spectrum. Although it is difficult to compare the intensity during the *EINSTEIN* observations and the present ones because of the different energy range, the intensity of SS 433 during the present observations seems much larger (~ 9 -16 mCrab for 1987 May observation and ~ 8 -10 mCrab in 1988 May and 1989 May). The contribution of the lobes to the X-ray flux detected by the *GINGA* LAC is therefore unlikely to be significant, particularly as the collimator response at the lobes is $\leq 40\%$.

The galactic ridge emission (Warwick *et al.* 1985; Koyama *et al.* 1986) contaminated the SS 433 observations by *TENMA* (Matsuoka, Takano & Makishima 1986). For the *GINGA* LAC, however, the contribution from the ridge emission is small. The smaller field of the LAC does not extend to the galactic plane where the surface brightness is the highest when pointed at SS 433 ($b = 2.2^\circ$). The solid angle itself is smaller by a factor of ~ 3 -4 than that of *TENMA*. Examination of an empty sky field with the same absolute galactic latitude and near SS 433 suggests that the contribution from the ridge emission is less than 0.5 mCrab.

As in Chapter 3, the spectra of SS 433 from *GINGA* observations are fitted with several kinds of possible models. The models consist of either single-component or two-component continua together with a broad Gaussian emission line and with a low energy cut-off due to the neutral absorption (Morrison & McCammon, 1983). The range of continuum models includes thin thermal bremsstrahlung, Comptonized bremsstrahlung, combined bremsstrahlung and black body, power-law, and power-law with exponential high energy cut-off, as discussed in Chapter 3.

4.3 Observation Results

4.3.1 X-ray Light Curves

1) X-ray eclipse light curve at precession phase 0.58

The observed X-ray light curves in several energy bands are shown in Fig. 4.1. Each data point reflects the average intensity over a continuous data span, typically 20-30 minutes in duration, taken roughly once per satellite orbit at times of low charged particle background.

SS 433 X-ray Light Curves 18-23/5/1987

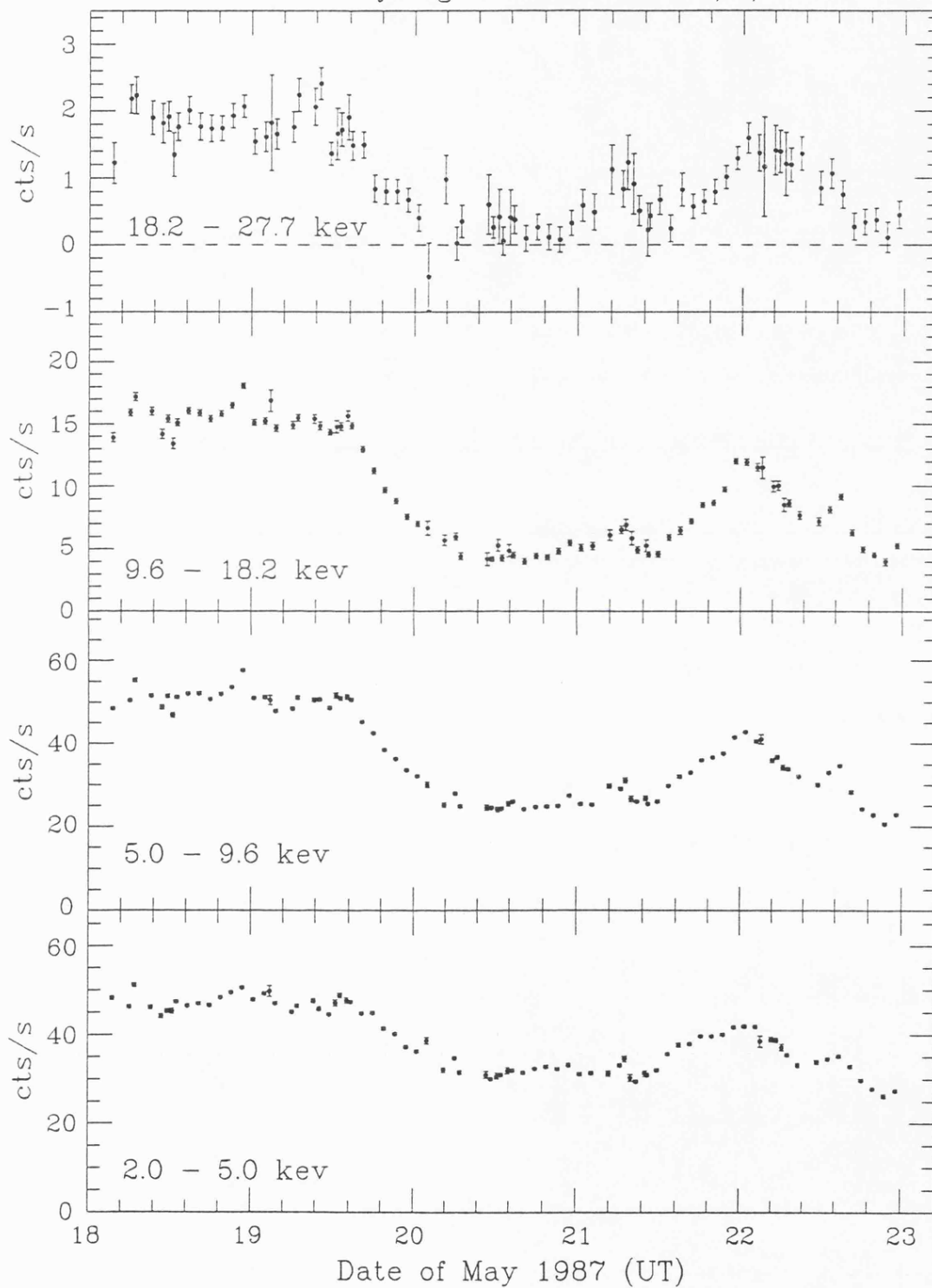


Figure 4.1: X-ray light curves of SS 433 (*GINGA* observations, 1987 May)

The X-ray intensity started to decrease on 1987 May 19.6, and a minimum was reached around May 20.2. The low state in intensity continued for ~ 1.5 days. The intensity started to rise again on May 21.5 and reached a maximum on May 22.0, at a level somewhat lower than that observed prior to the intensity reduction. The intensity fell again after this maximum until the observations were terminated at May 23.0.

Similar behaviour is apparent in all energy bands, but the fractional flux reduction is larger at higher energies (see Fig. 4.1). The eclipse fraction is more than 80% in the energy range 18-28 keV, $\sim 70\%$ in 9-18 keV, $\sim 50\%$ over 5-9 keV and about 30% for 2 to 5 keV. Due to the diffuse component within the field of view of LAC ($1^\circ \times 2^\circ$ FWHM), the eclipse fraction quoted above are lower limits, although the difference from the real value should be small as discussed in the previous section. Most of the flux change was accomplished within ~ 0.5 days for both ingress and egress, and at the bottom of the eclipse the X-ray flux was relatively constant within $\sim 10\%$ for ~ 1.5 days. These general features of the light curve impose significant constraints in modelling the eclipse (presented in Chapter 5).

A search for variability on various time scales was made. No periodic variability was seen in the PC data on the time scales from 4 ms to 500 sec. Aperiodic variability was seen on time scales longer than 100 s with an amplitude of $\sim 10\%$, as has been previously reported for the *EINSTEIN* data (Grindlay *et al.* 1984) and the *EXOSAT* data (Stewart *et al.* 1987).

2) X-ray eclipse light curve at precession phase 0.83

The spectra obtained by the LAC in 1988 May are much softer than those of 1987 May and there is no significant flux above 19 keV.

The light curve of SS 433 obtained in 1988 May are plotted in Fig. 4.2 for the X-rays over energy ranges of 2-5, 5-9.6 and 9.6-18.2 keV. Similar to the case in Fig. 4.1 above, each data point represents a time averaged intensity over various durations and is taken in the period of low in-orbit background.

It is clear that a large fractional decrease of the X-ray intensity above 5 keV occurred beginning at day 19.85. The minimum intensity state was reached at about day 20.23 and lasted for ~ 1.5 day until day 21.8 at which the intensity started to rise again. By the end of the observations, the intensity of the source in each energy band had reached the level when the

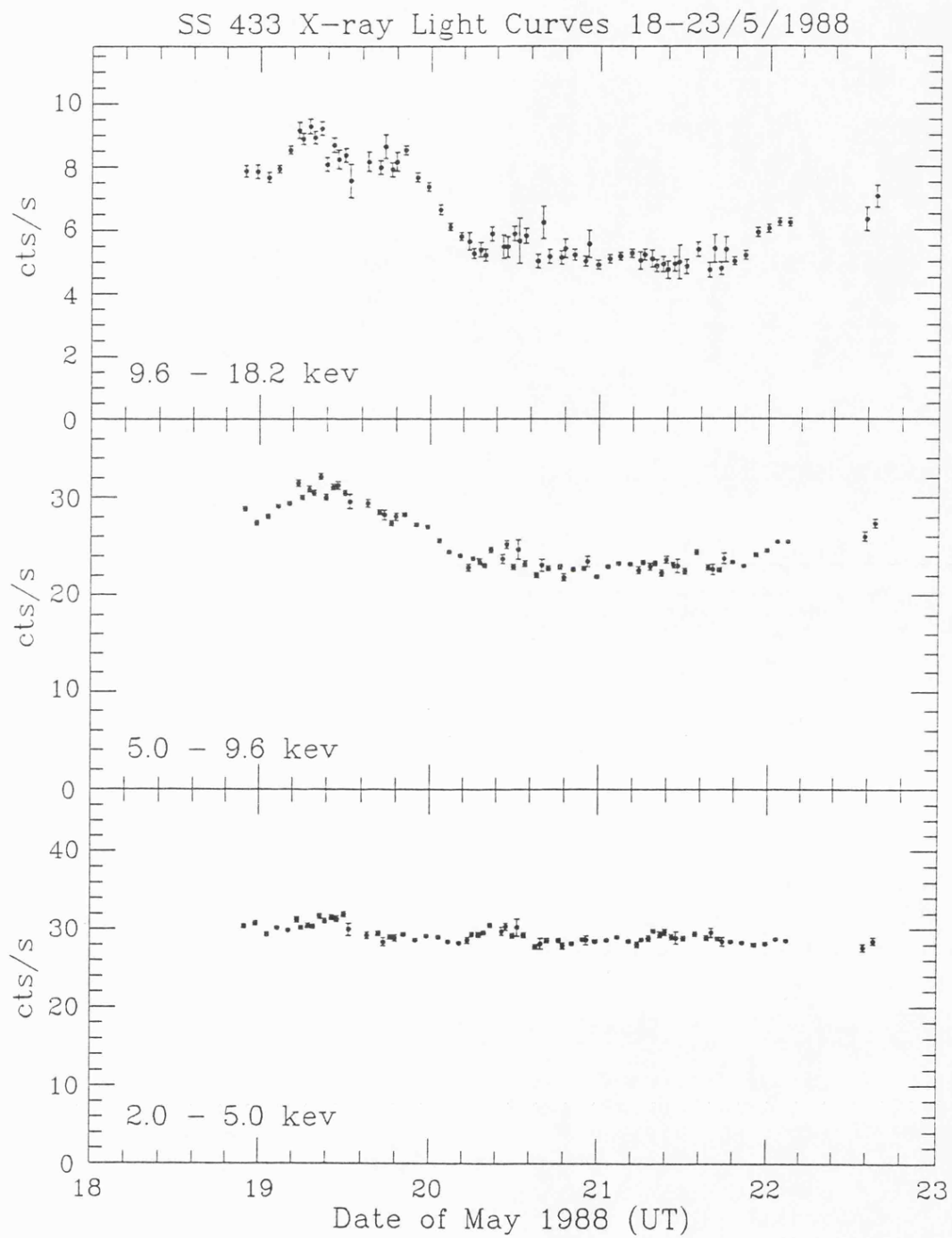


Figure 4.2: X-ray light curves of SS 433 (*GINGA* observations, 1988 May)

observations started. However, due to the switch-off of the LAC in day 22.2-22.5, it is not possible to determine when the source intensity recovered during this period. One surprising result is that there is little significant variation for the X-ray intensity over 2-5 keV band.

The duration of the minimum intensity state here is consistent with 1.5 day, the same as derived from the 1987 May observations. The eclipse at phase 0.83 is much shallower than that at 0.58, but the intensity reductions have similar behaviours, i.e., the fraction of the flux reduction is larger at higher energies than that at lower energies. The reduction fraction in energy range of 9.6-18.2 keV during the eclipse is about 40% and 20% for the 5-9.6 keV flux.

3) X-ray eclipse light curve at precession phase 1.0

The X-ray light curves of SS 433 obtained in 1989 May 7-12 are displayed for the energy bands 1-5 keV, 5-9 keV, 9-18 keV and 18-28 keV in Fig. 4.3. The precession phase of the *GINGA* observations is close to that of the *EXOSAT* observed eclipse in 1985 May (E12). The flux level of SS 433 at this phase is almost equal to that of 1987 inside eclipse flux.

Although SS 433 is at its low state when the observations were made, it is obvious from the light curve in Fig. 4.3 that the X-ray intensity in energy band 5-9 keV and 9-18 keV decrease at the beginning of the observations and reach its low state around the primary optical minimum May 9.3. The intensity increases again after May 9.3 until the end of the observations when the flux reaches a level higher than that at the start of the observations.

The reduction of the X-ray intensity from May 7 to May 9.3 in the 5-9 keV and 9-18 keV energy bands is $\sim 20\%$.

SS 433 X-ray Light Curves 7-12/5/1989

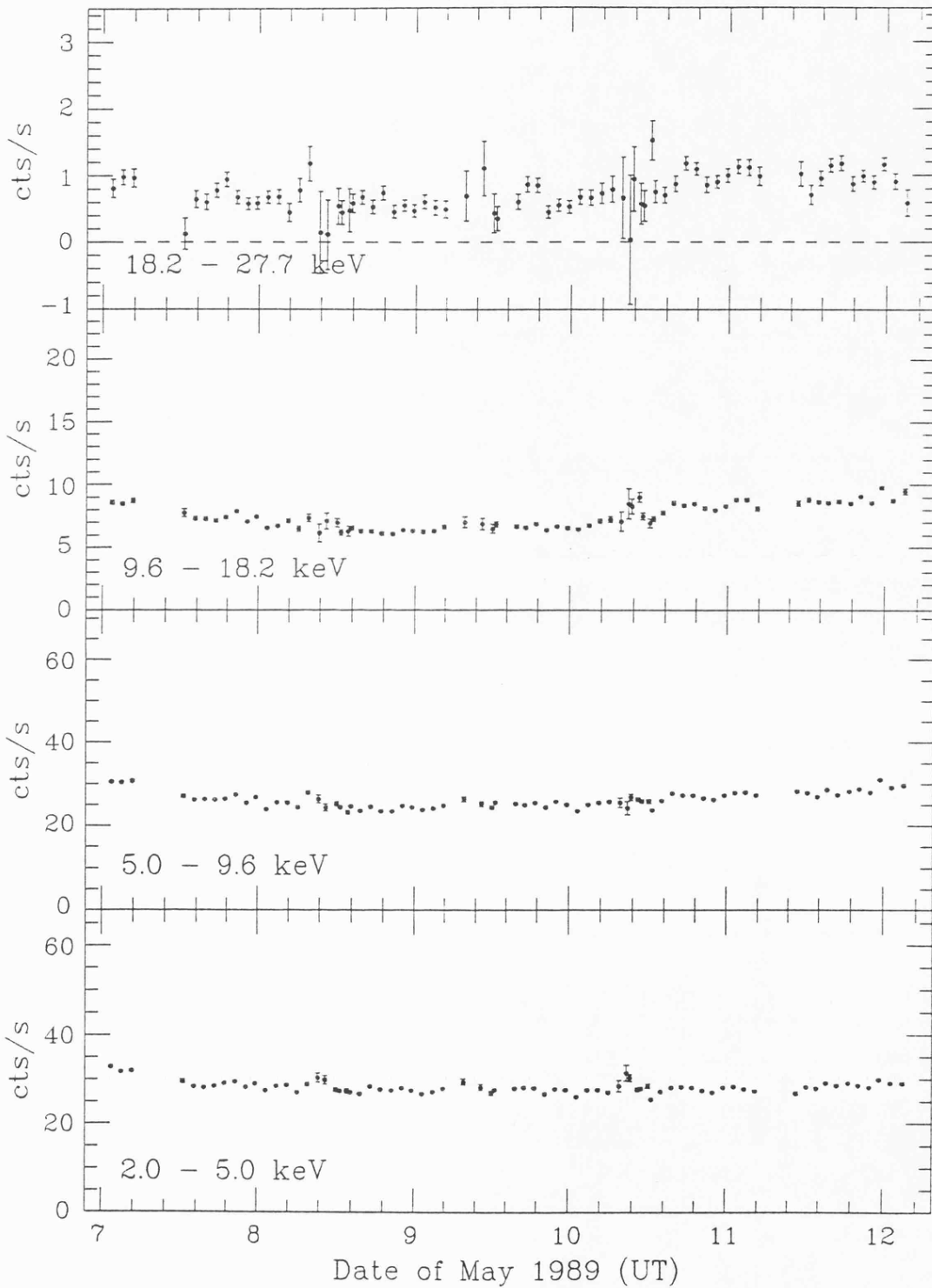


Figure 4.3: X-ray light curves of SS 433 (*GINGA* observations, 1989 May)

4.3.2 Energy Spectrum

Figure 4.4, 4.5 and 4.6 show the typical spectrum of SS 433 at the different binary and jet precession phases, each having a single intense, energy-shifted broad emission line. Spectrum (a) of each Figure is integrated at the high state in X-ray intensity, presumably well outside the eclipse phase (from May 18.60 to May 18.96 for 1987 observations at jet precession 0.58, from May 19.16 to May 19.53 for observations made in 1988 at jet precession 0.83, and 1989 May 7.05-7.20 at jet precession phase 1.0). Spectrum (b) of Figure 4.4-4.6 is integrated at the low-intensity phase, presumably well within the eclipse (May 20.54-May 20.90, 1987; May 21.04-May 21.40, 1988; and May 8.97-9.66, 1989). The effective exposure for both spectra in Fig. 4.4 is above 7000 seconds and about 14000 seconds for the spectra in Fig. 4.5. For Fig. 4.6, exposure time is ~ 5376 sec for spectrum (a) and ~ 11904 sec for spectrum (b).

In general, the *GINGA* SS 433 spectrum consists of a broad emission line and an underlying continuum. Although none of the assumed models gives fully acceptable fits to these integrated spectra, significantly better fits for the spectra are obtained with thin-thermal bremsstrahlung. The pure power-law model, which was applied to describe the *EINSTEIN* MPC data (Grindlay *et al.* 1984) gives significantly worse fit than any other model and is not favored by the high quality *GINGA* data with its wide energy band and, therefore, is not considered in this chapter. Fitting the spectra with two-component continuum models produces χ^2 not significantly better than the fit with a single thermal bremsstrahlung model. All these models give very similar continuum shapes and derived spectral parameters are consistent with the *EXOSAT* results presented in last chapter, but have a much greater precision.

Most of the residual to the fits of the spectra in Fig. 4.4 and 4.5 is located from 3 keV to 10 keV, with a similar waving form independent of the continuum model. This suggests the Gaussian representation of the broad emission line is too crude, as indeed would be expected for the line broadening mechanisms suggested in Chapter 3. A much improved fit was in fact found if the line was modelled by a profile composed of different power-laws for the blue and red wings, a close approximation to the effect of Comptonization in a hot plasma.

The X-ray spectrum of SS 433 is simply described in the following using the parameters of the model with a single-component thermal bremsstrahlung as continuum, a Gaussian profile as emission line plus neutral absorption. The choice of this simple continuum is justified because

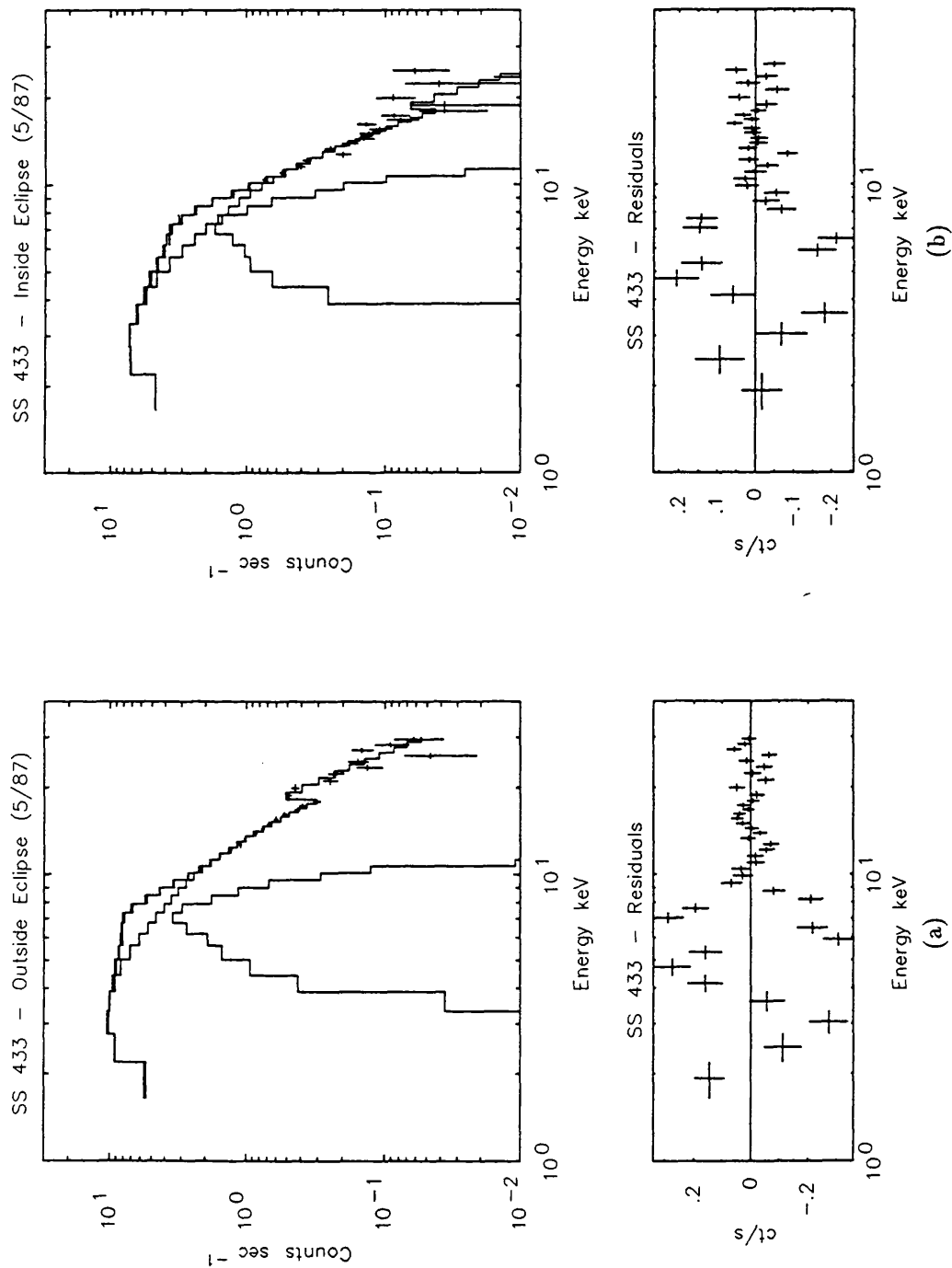


Figure 4.4: X-ray spectra of SS 433 from *GINGA* observations in 1987 May. (a) the spectrum integrated outside the eclipse between 1987 May 18.60-18.96; (b) the spectrum integrated inside the eclipse during 1987 May 20.54-20.90.

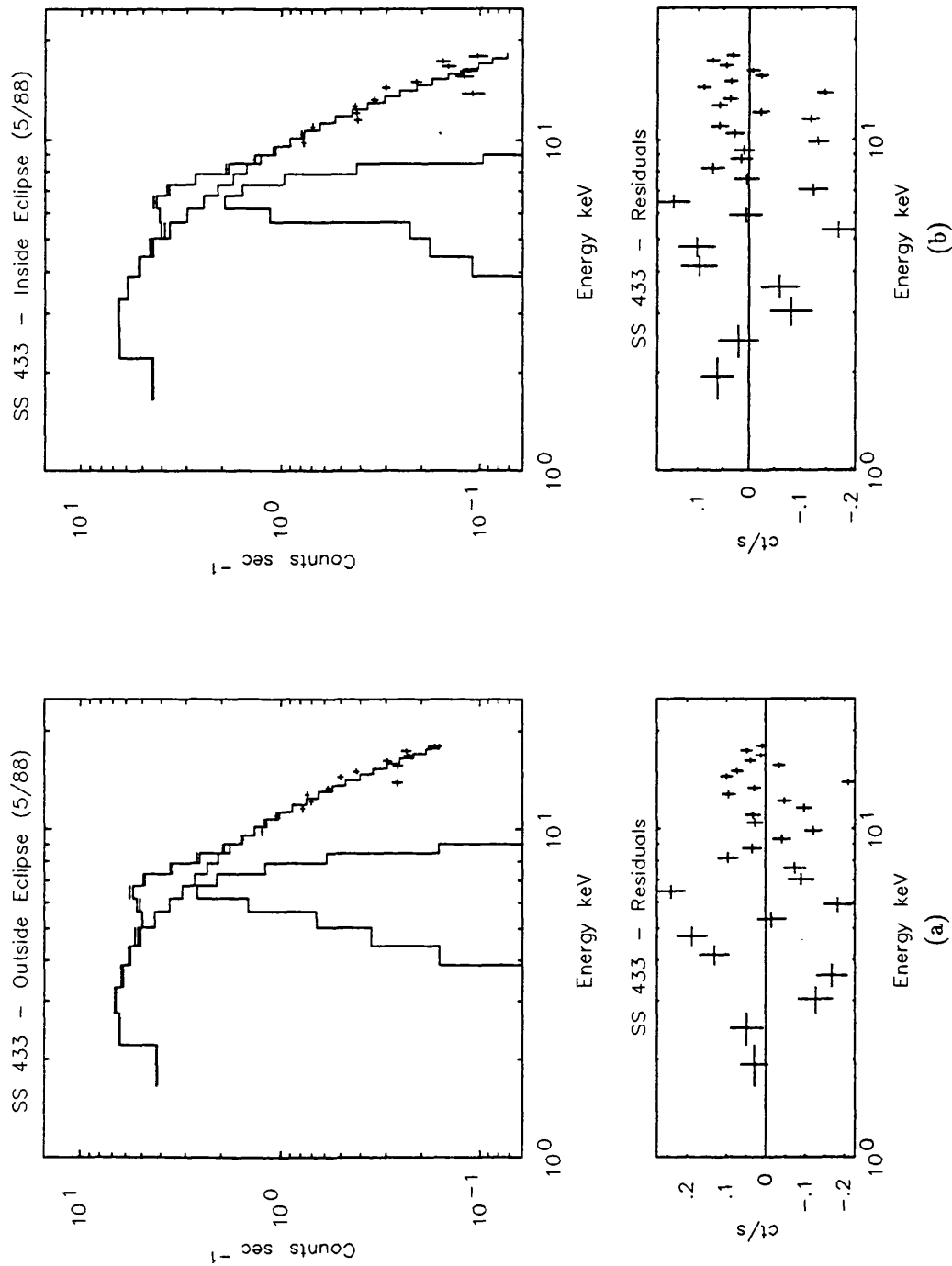


Figure 4.5: X-ray spectra of SS 433 from *GINGA* observations in 1988 May. (a) the spectrum integrated outside the eclipse between 1988 May 19.16-19.53 and (b) the spectrum integrated inside the eclipse during 1988 May 21.04-21.40.

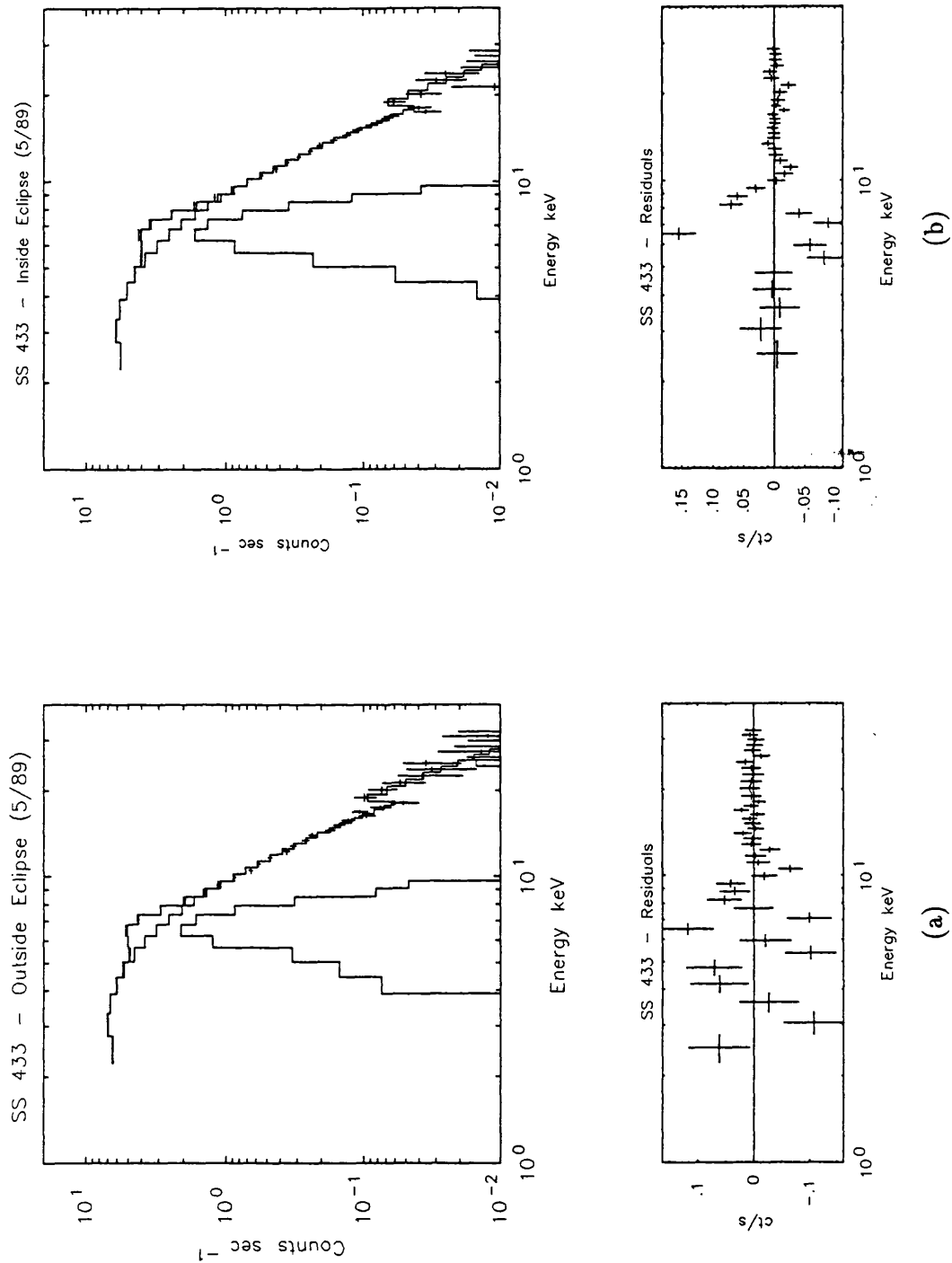


Figure 4.6: X-ray spectra of SS 433 from *GINGA* observations in 1989 May. (a) the spectrum integrated outside the eclipse between 1989 May 7.05-7.20 and (b) the spectrum integrated inside the eclipse during 1989 May 8.97-9.66

it gives better fits to most individual spectra (corresponding to those listed in table 4.1-4.3) than any other assumed model does, and also the determination of the bremsstrahlung temperature only depends on the shape of the continuum and does not interact with the other model parameters. For example, including a blackbody as a secondary component of the continuum gives better fits to some of the spectra, however, this secondary acts either to replace part of the first continuum component's fit or simply compensate some of the emission line's fit. So does the power-law with high energy cut-off model. It should be noted, however, that the temperature derived in the fitting procedure is only an indicative 'average' temperature.

If only the spectra outside the eclipses are considered, i.e., the influence of the binary motion can be ignored, a $25.54^{+1.03}_{-0.78}$ keV bremsstrahlung temperature is derived from 1987 May observations (see Fig. 4.4(a)), $20.50^{+0.54}_{-0.64}$ keV for 1988 May pointings (Fig. 4.5(a)) and $16.34^{+1.72}_{-1.35}$ keV for 1989 May observations (Fig. 4.6(a)), when a bremsstrahlung model is adopted. The difference in bremsstrahlung temperature among these three spectra indicates that the spectrum becomes softer while the jets are edge-on, which may suggest the occultation of the higher temperature regions of the jet by the accretion disc.

The softening of the spectra during the eclipse seen in the light curves is represented by the fall of temperature of thermal bremsstrahlung component. This is also true in the case of two-component continuum model with the inclusion of a blackbody component although the absolute temperatures derived are lower. For the spectrum in Figure 4.4, the thermal bremsstrahlung temperature decreases from $25.54^{+1.03}_{-0.78}$ keV out of eclipse (a) to $7.33^{+0.30}_{-0.28}$ keV during the eclipse (b). In Fig. 4.5, the temperature of spectrum (a) is $20.50^{+0.54}_{-0.64}$ keV and $10.38^{+0.17}_{-0.19}$ keV for spectrum (b). For the 1989 May observations, the temperature varies from $16.34^{+1.72}_{-1.35}$ keV in Fig. 4.6(a) to $13.96^{+0.86}_{-0.72}$ keV in Fig. 4.6(b).

Whatever the continuum model used, the column densities of the most spectra obtained with *GINGA* are $N_{\text{H}} \leq 8 \times 10^{21} \text{ cm}^{-2}$ (assuming relative X-ray absorption cross sections as in Morrison and McCammon 1983). These column densities are less than the value of $N_{\text{H}} \simeq 1.5 \times 10^{22} \text{ cm}^{-2}$ derived (using Gorenstein 1975) from the optical extinction $A_{\text{v}} = 7 \sim 8$ (Murdin, Clark & Martin 1980; Wagner 1983), suggesting that the soft X-ray excess seen in the *EXOSAT* observations also exists in the *GINGA* X-ray spectra of SS 433.

Noticing the constant soft X-ray intensity over the period of the *GINGA* eclipse observations

in 1988 May and 1989 May, one might conclude that the soft X-ray excess is contributed by the diffuse X-ray lobes of SS433. As the central source of SS 433 decreases in flux, the overall spectrum in the LAC should soften since the soft ‘background’ emission from the lobes will remain constant (for a fixed pointing direction). However, as discussed in the previous section, the soft X-ray from the two diffuse lobes is not strong enough to distort the X-ray spectrum observed with *GINGA*. Less modulation of these soft X-ray flux in the 1988 & 1989 observations may imply that in these two phases, the accretion disc has obscured the high temperature X-ray regions which used to be shadowed by the companion star in the jet precession phase of 1987 May, and the rest of the X-ray jet can be hardly covered by the companion star. In fact, this argument is supported by the fact that the flux level outside 1988 eclipse is almost equal to that inside 1987 eclipse. This result should put a strong constraint on the thickness of the accretion disc.

It is also possible, as discussed in last chapter, that the observed soft X-ray excess is due to the existence of another emission line over 1-2 keV. Including another broad line with its line energy fixed at 1.5 keV (because the reliable *GINGA* data must be taken from ≥ 2 keV) to fit the soft part of the spectrum gives relatively high column density, which is almost consistent with that from optical observations.

The value of the line energy determined does not depend on the choice of continuum model, being 7.23 ± 0.03 keV for the spectra in Fig. 4.4, 6.78 ± 0.02 keV for spectra in Fig. 4.5 and 6.77 ± 0.05 keV for spectra in Fig. 4.6. For the blue-shifted line at the precession phase 0.58, the blue shift factor is $(1+z) \sim 0.91$ and the energy at the rest frame for the observed 7.23 keV line is ~ 6.6 keV. if the systematic effects due to uncertainties in continuum and line profile are included, the line energy is completely consistent with the 6.7 ± 0.1 keV result by Watson *et al.* (1986) (and also last chapter). At the precession phase 0.83 & 1.0, either the blue shift or red shift factors is $(1 \pm z) \sim 1.0$, obviously, the derived energy 6.78 keV is consistent with the *EXOSAT* results (see Fig. 3.6 where the *GINGA* results are plotted).

The line width is roughly independent of the assumed continuum except that occasionally the derived line width from two-component continuum models is slightly smaller than that from single thermal bremsstrahlung model. The line width has Gaussian $\sigma \sim 1.2$ keV (i.e. FWHM ~ 2.8 keV) for the observations made in 1987 May, $\sigma \sim 0.66$ keV (FWHM ~ 1.55 keV) for 1988 May spectra and $\sigma \sim 0.55$ keV (FWHM ~ 1.30 keV) in 1989 May. The line width

derived from the *GINGA* observations has been plotted in Fig. 3.6 and is totally consistent with the *EXOSAT* results reported in last chapter, i.e., the line becomes broad when the jets point to the observer and narrow while the jets are edge-on.

Similarly the line intensity is also roughly independent of the choice of continuum. In fact, its determination depends on the value of the line width. When two-component continuum models are applied and the derived value for the line width becomes slightly smaller than that of the single continuum component model, the line flux will be smaller, and vice versa. For the spectrum integrated outside the eclipse in 1987 May (Fig. 4.4(a)) the line flux is $(0.44 \pm 0.02) \times 10^{-2}$ photons $\text{cm}^{-2} \text{s}^{-1}$ and for spectrum (b) in Fig. 4.4 $(0.24 \pm 0.02) \times 10^{-2}$ photons $\text{cm}^{-2} \text{s}^{-1}$. The line fluxes for the spectra in Fig. 4.5 are $(0.22 \pm 0.01) \times 10^{-2}$ and $(0.16 \pm 0.01) \times 10^{-2}$ photons $\text{cm}^{-2} \text{s}^{-1}$ respectively. For the observations in 1989 May, line flux of the spectrum in Fig. 4.6(a) is $(0.18 \pm 0.02) \times 10^{-2}$ photons $\text{cm}^{-2} \text{s}^{-1}$ and $(0.15 \pm 0.01) \times 10^{-2}$ photons $\text{cm}^{-2} \text{s}^{-1}$ for the spectrum in Fig. 4.6(b). As shown in Fig. 3.6, the line flux derived from the *GINGA* spectra is consistent with that in the *EXOSAT* spectra at the corresponding jet precession and orbital phases.

The broad emission feature was also fitted with two emission lines. Many combinations of free and fixed parameters for the energy and width of emission lines were tried. Using two narrow lines never gave a good fit to the data. If one line was allowed to be broad, setting the width and energy as free parameters, parameters of one of the lines converged to those of the single line solution while the intensity of the other line converged to zero. The only case for which a positive intensity was obtained for both lines was when the energy of the two lines were fixed at 5.8 keV and 7.4 keV, energies of red- and blue-shifted lines with a rest-frame energy of 6.7 keV at the jet precession phase 0.58 when the observations were made in 1987 May, and the width of the lines was allowed to be broad around 1 keV (Gaussian sigma). Here the sum of the intensity of the two lines (blue line: 0.36×10^{-2} photons $\text{cm}^{-2} \text{s}^{-1}$, red line: 0.09×10^{-2} photons $\text{cm}^{-2} \text{s}^{-1}$ for spectrum (a) in Fig. 4.4, and 0.20×10^{-2} photons $\text{cm}^{-2} \text{s}^{-1}$ and 0.05×10^{-2} photons $\text{cm}^{-2} \text{s}^{-1}$ for Fig. 4.4(b)) is essentially equal to the line intensity of the single-line model (0.44×10^{-2} photons $\text{cm}^{-2} \text{s}^{-1}$ for Fig. 4.4(a) and 0.24×10^{-2} photons $\text{cm}^{-2} \text{s}^{-1}$ for Fig. 4.4(b)), and the average energy of the photons in the lines remains the same as the line center of the single-line model. It is naturally expected if the line intensity is not coupled to the model of continuum. However, the evidence for the red line is not strong, since the resultant χ^2 of the two-line solution is not significantly

better than that of the single-line solution. Due to the systematic uncertainties in profile of broad lines and the shape of continuum, the better model on the basis of small change in χ^2 between the single-line and two-line solutions cannot be distinguished. It is nevertheless true that the intensity in blue-shifted line is much larger than that of the red-shifted line, and that the intensity of the blue-shifted line is different by a factor of ~ 2 between the two spectra in Figure 4.4. In the case of 1988 May observations which were made at the phase when the jets were edge-on, the Doppler blue- and red- shifted lines are not separated much in energy and have similar line energy, consistent with 6.7 keV. It is then impossible to distinguish them from the data even if the two lines were indeed simultaneously observed.

4.3.3 Spectral Evolution

The spectral evolution during the present *GINGA* observations are shown in terms of the spectral parameters obtained using the model with thermal bremsstrahlung continuum and a single Gaussian broad emission line. The reason for using this model is that it has the smallest number of parameters among the models giving reasonably small χ^2 , as discussed in the previous subsection. Although the resultant χ^2 for the fitting is too large for the integrated spectra shown in Figure 4.4-4.6, the spectra with shorter integration times corresponding to each point in Figure 4.7-4.9, which show the time variations of the spectral parameters over the periods of the *GINGA* observations, usually have a statistically acceptable χ^2 even with this simple model.

The evolution of the X-ray spectrum (both continuum and emission line) over the jet precession period is obvious. The derived temperatures from spectra Fig. 4.4(a), Fig. 4.5(a) and Fig. 4.6(a) are $25.54^{+1.03}_{-0.78}$ keV, $20.50^{+0.54}_{-0.64}$ keV and $16.34^{+1.72}_{-1.35}$ keV, and are consistent with the results reported in the last chapter for the *EXOSAT* observations. The temperature difference, however, does indicate the softening of the spectra while the jets precess from face-on to edge-on. The emission line features, as presented in last subsection, are obviously modulated by the jet 163 day precession. The energy-shifted lines locate at the positions on the spectra coincident with those predicted from the standard kinematical model. The results of the spectral fits in the *GINGA* observations are therefore compatible with those of the *EXOSAT* observations.

The model parameters as a function of time are plotted in Fig. 4.7(a)-(b) for the *GINGA*

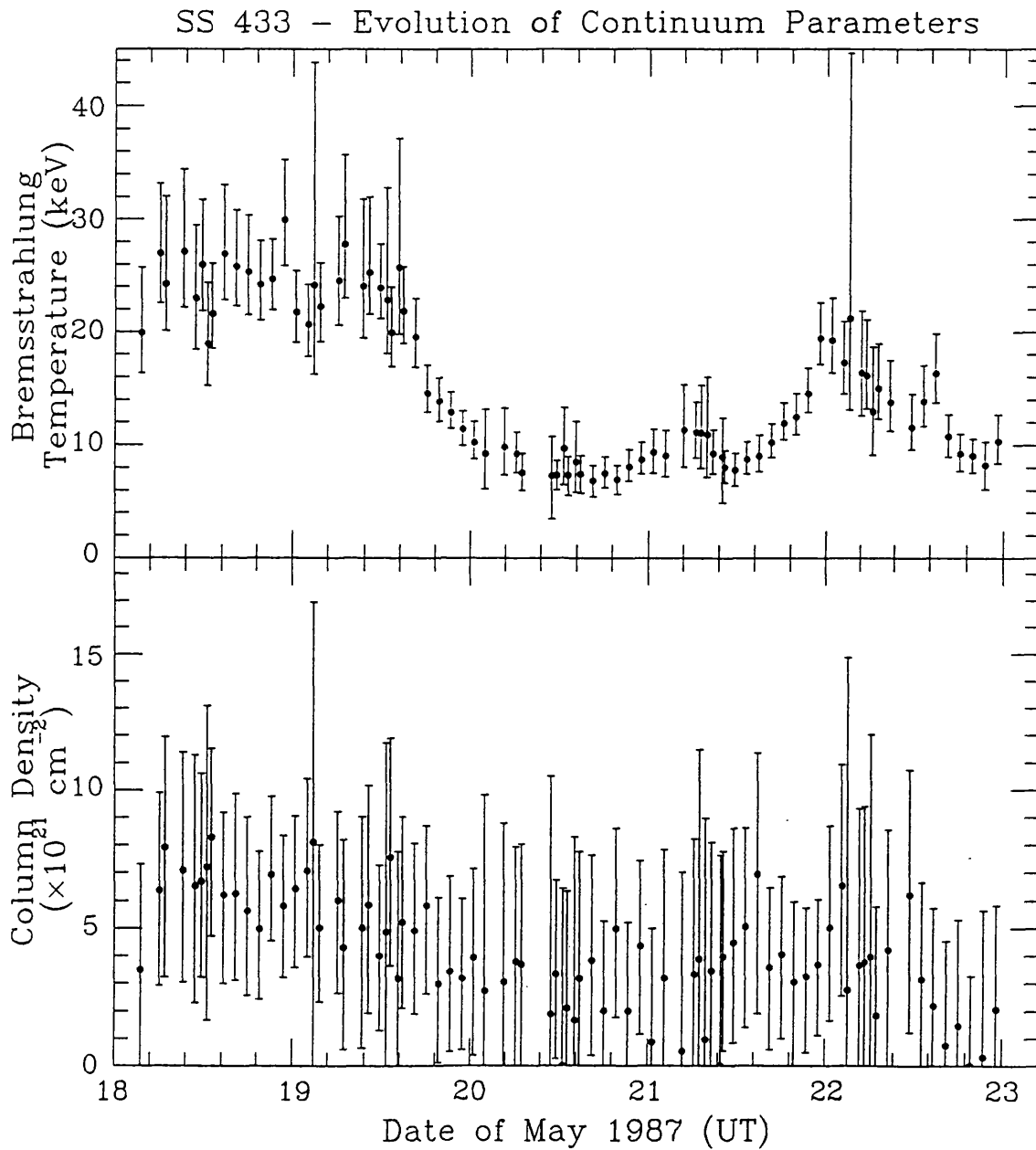


Figure 4.7: (a) SS 433 spectral evolution - continuum, described by the model of a single bremsstrahlung component with low energy absorption. The dropping of the bremsstrahlung temperature represents the softening of the X-ray spectrum during the eclipse. (*GINGA* observations, 1987 May)

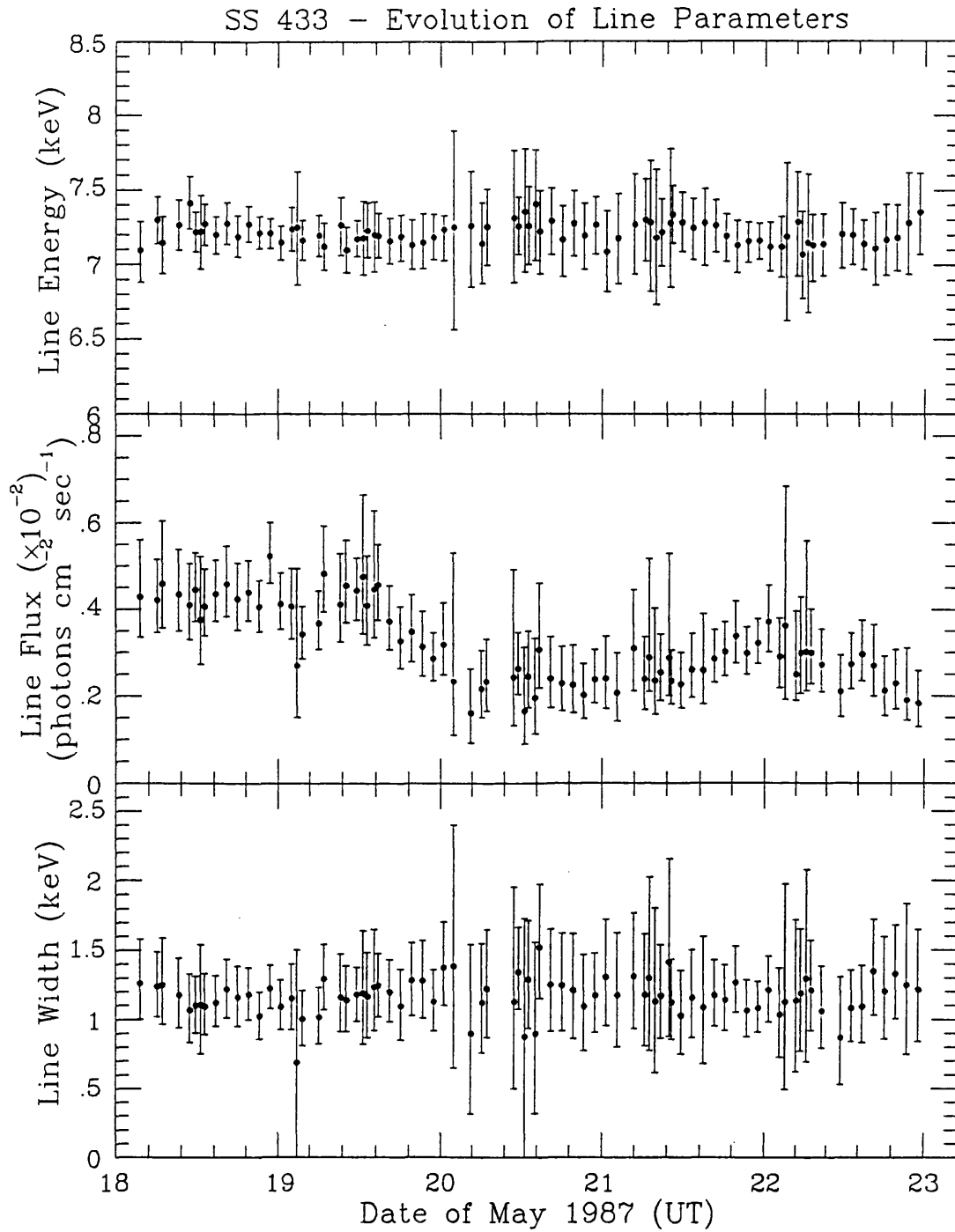


Figure 4.7: (b) SS 433 spectral evolution - emission line parameters, with single bremsstrahlung plus low energy absorption as continuum (*GINGA* observations, 1987 May)

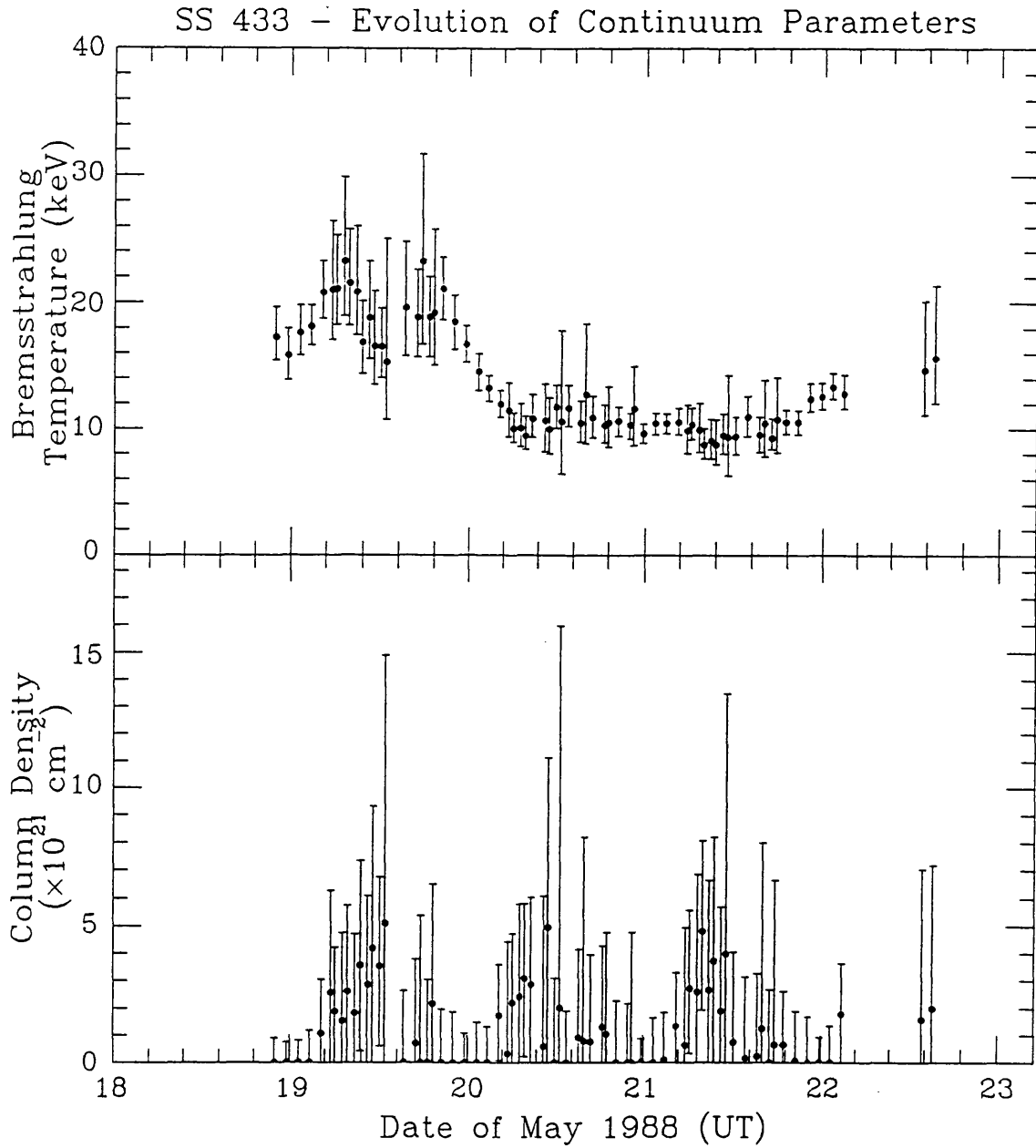


Figure 4.8: (a) SS 433 spectral evolution - continuum, described by the model of a single bremsstrahlung component with low energy absorption. The dropping of the bremsstrahlung temperature represents the softening of the X-ray spectrum during the eclipse. (*GINGA* observations, 1988 May)

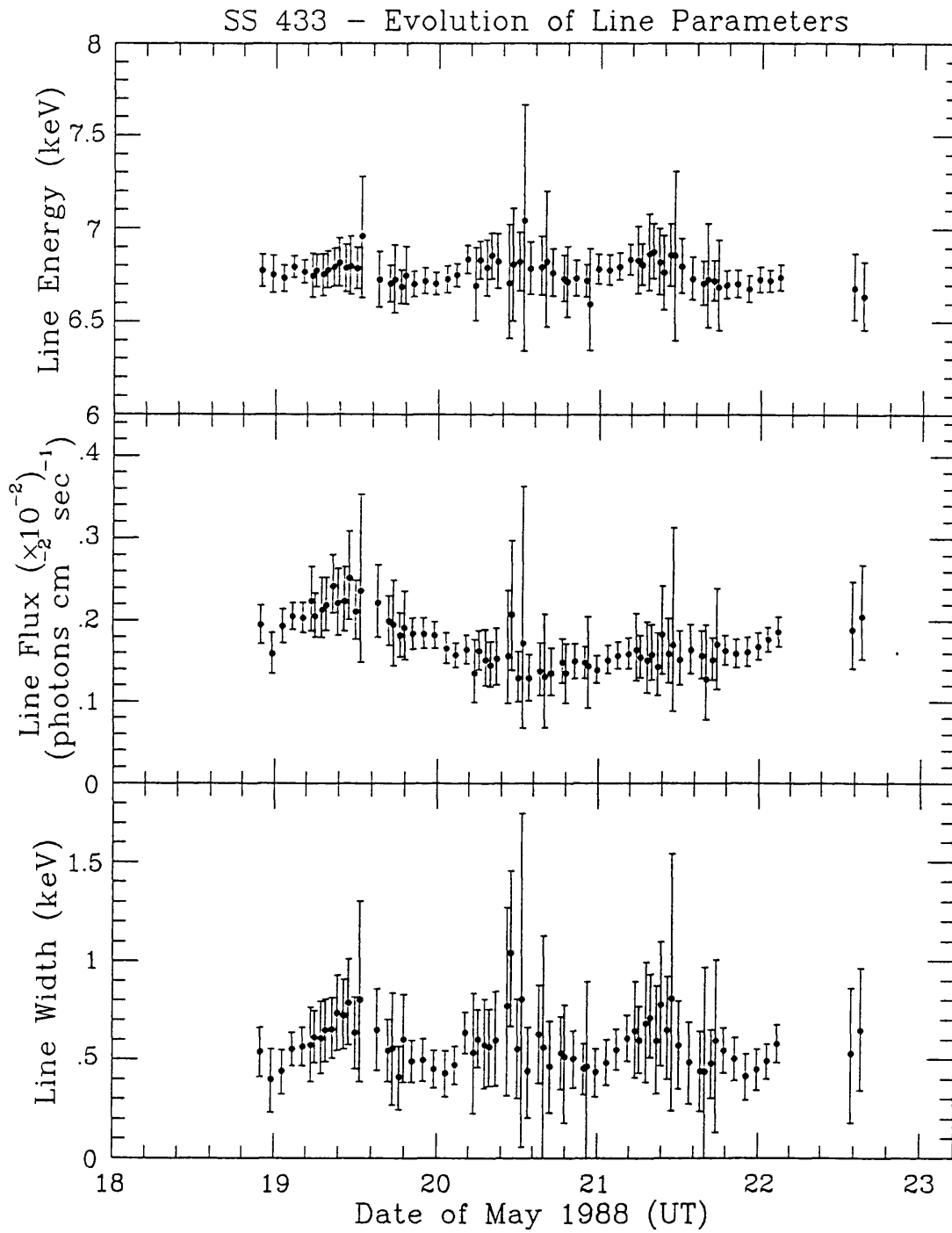


Figure 4.8: (b) SS 433 spectral evolution - emission line parameters, with single bremsstrahlung plus low energy absorption as continuum (*GINGA* observations, 1988 May)

SS 433 - Evolution of Continuum Parameters

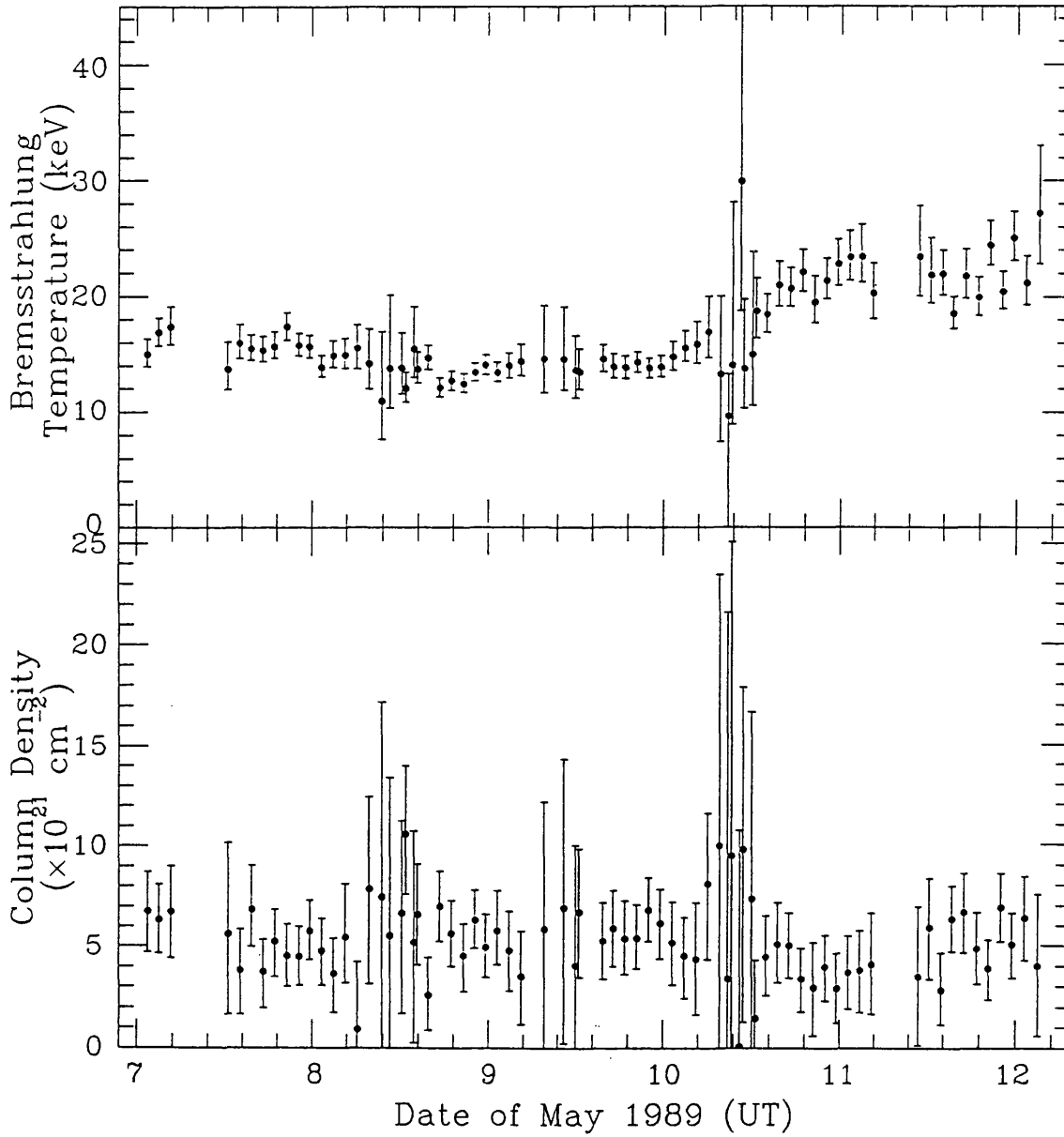


Figure 4.9: (a) SS 433 spectral evolution - continuum, described by the model of a single bremsstrahlung component with low energy absorption. The dropping of the bremsstrahlung temperature represents the softening of the X-ray spectrum during the eclipse. (*GINGA* observations, 1989 May)

SS 433 - Evolution of Line Parameters

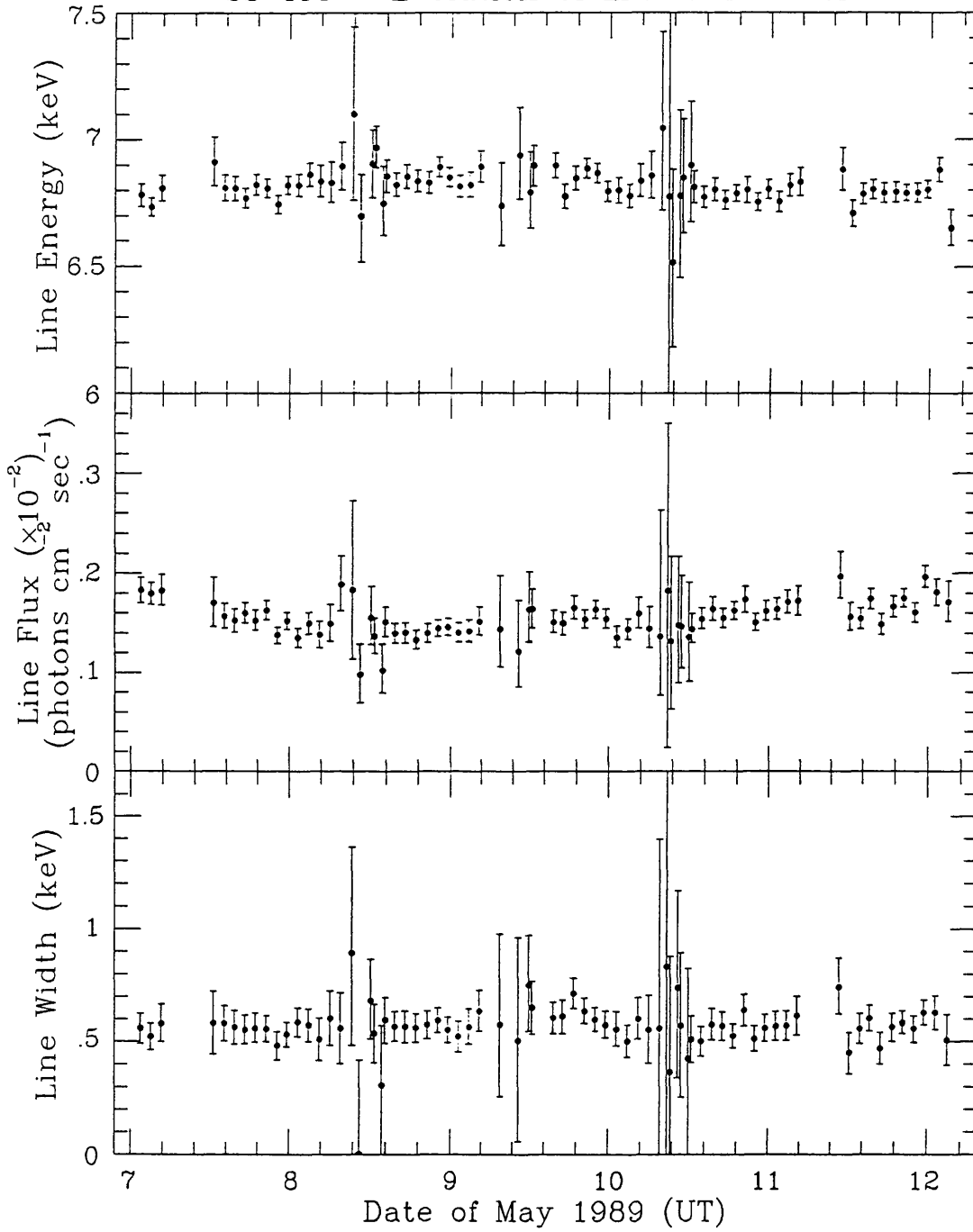


Figure 4.9: (b) SS 433 spectral evolution - emission line parameters, with single bremsstrahlung plus low energy absorption as continuum (*GINGA* observations, 1989 May)

observations in 1987 May, Fig. 4.8(a)-(b) for those in 1988 May and for 1989 May, Fig. 4.9(a)-(b). Among the parameters shown, the line intensity and the temperature of the continuum changed along with the continuum intensity, whereas the other parameters stayed relatively constant.

The change in the derived continuum temperature reflects the spectral softening seen during the eclipse. The absorption column does not change very much, as is expected from the shallow eclipse in lower energy band.

Of more interest is the behaviour of the emission line during the eclipse. In particular, the detailed time variation of the emission line intensity is measured for the first time. The line intensity varies through the eclipse following the continuum intensity at 5-10 keV on the whole, implying that the equivalent width is roughly constant through the eclipse. The light curves of this Doppler-shifted line intensity show clearly that the X-ray emissions from the relativistic jets are really modulated by the orbital motion. The eclipse fraction for the emission line at the center of 1987 May eclipse is about 50%, which is similar to the ratio of the line intensity in two spectra in Figure 4.4. For the observations 1988 May and 1989 May, the eclipse fractions of the line intensity are only 30% and 20% respectively, much smaller than the 50% fraction in 1987 May. The good agreement between the continuum light curve and the profile of emission line variation indicates that the emission region of the Doppler-shifted line is eclipsed during the present observations and supports the conclusion from the previous observations that a major part of the X-ray emission which is eclipsed originates from the relativistic jet.

4.4 Discussion

4.4.1 Is There An X-ray Eclipse - and What Is Eclipsed?

The present observations of the reductions in X-ray intensity at the binary phase of optical primary minimum are the direct confirmations of the *EXOSAT* observed eclipses (Stewart *et al.*, 1987; and Chapter 3 in this thesis) with more complete coverage. In addition to the light curves in coarse energy band, the information on the time evolution of the energy spectra is now also obtained, which allows further discussion on the geometry and nature of the X-ray

emitting region (see the following chapters). In the first place it is necessary to clarify the evidence supporting the interpretation of the events of the large amount drops in the X-ray intensity being eclipses by the optical star.

The temporal agreement of the flux reduction centres with the predicted epoch of optical primary minimum is a strong support that the events observed in 1987 May, 1988 May and 1989 May are connected with the epochs of conjunction between the optical star and compact object. The centres of the X-ray events, which defined as the mid-point of ingress (1987 May 19.6 and 1988 May 19.9) and egress (1987 May 22.0 and 1988 May 22.2-22.5) were 1987 May 20.8 and 1988 May 21.1 while the predicted optical minimums were at 1987 May 20.9 and 1988 May 21.1. Although it is difficult to determine these epochs for the observations made in 1989 May, it is obvious that around the predicted optical primary minimum 1989 May 9.3, the fluxes in the energy bands 5-9 keV, 9-18 keV are at low level. Simultaneous optical observations (Goranskii, private communication) from 1987 May 19 to May 21 are completely consistent with the long-term averaged optical light curve and justify the extrapolation of the ephemeris given by Kemp *et al.* (1986).

From the spectral behaviour it is clear that the reduction in flux is not caused by photoelectric absorption, for which the flux reduction would be expected to be much stronger at lower energies than that at high energies. The relatively constant line energy and width also preclude the possibility of reduction due to an ionized scattering media, which would cause further Compton broadening of the iron emission line during the reduction.

The softening of the energy spectrum with the decrease of intensity can be most easily interpreted as a partial eclipse of an X-ray source consisting of components with different temperatures among which harder component is obscured. If the temperature of the X-ray emitting material falls outward along the jet and the outer region of the jet with low temperature remains visible at the center of eclipse, the X-ray spectrum will become softer during the eclipse.

The time variation of the intensity of the emission line supports strongly the interpretation that the relativistic jet is indeed the eclipsed X-ray source, since the Doppler-shifted energy of the iron emission line is most naturally interpreted as, at least for a major fraction, being emitted from the relativistic jet. The remaining line intensity at the bottom of the eclipse indicates that the eclipse of the relativistic jet is not total.

One possible argument against eclipses is the presence of decline of X-ray intensity seen on May 22 1987 after the 'egress', which can be interpreted either as an occultation by some material (c.f. the disc bulge as in 'dip sources') or as an intrinsic variation in X-ray intensity (see the discussion below). If this kind of intensity reduction is possible at arbitrary phases, the episode on 1987 May 20 could also be caused similarly. However, the previous detections of flux minima coincident with the optical eclipse strongly argue against the flux reductions at this epoch being accidental.

As shown in Fig. 4.1-4.3, it is obvious that the shape of the X-ray eclipse is variable over the various jet precession phases. When the upper jet approaches the observer, the eclipse is deep with clear start and end epochs, while the jets change to edge-on, the eclipse becomes shallow. The variable eclipse configuration may be due to the occultation of the X-ray jets by the accretion disc.

4.4.2 Implication of the Intensity Drop at Post-eclipse Phase in 1987 May — Oscillation of the Accretion Disc?

X-ray source of SS 433 was found to be non-thermal with the *EINSTEIN* observations, while the *EXOSAT* and *TENMA* observations strongly suggested the X-ray radiation to be thermal in nature. When the simultaneous X-ray and radio flare was observed with *EINSTEIN* in 1979 October, the X-ray source was at low state with luminosity $\sim 50\%$ lower than those derived from the *EXOSAT* and *TENMA* observations, in which no flare events were observed. Coupling the *EINSTEIN*, *EXOSAT* and *TENMA* results with the simultaneous radio observations, Band (1988) found that all the *EXOSAT* and *TENMA* observations, and some of the *EINSTEIN* observations were made during the radio quiescent period over which the X-ray luminosity was at high state and the X-ray source was stable, while most of the *EINSTEIN* observations were carried out in the radio active phase at which the source was flaring and its luminosity was low. This correlation then makes Band suggest that two X-ray states, quiescent with high luminosity and active with low luminosity, may exist.

A multifrequency campaign to observe SS 433 was conducted during the period from 1987 May 17 to 1987 June 1 (Vermeulen, 1989), over which the *GINGA* observations were made. While the *GINGA* observations suggested that the X-ray source of SS 433 was stable and the luminosity was completely consistent with the *EXOSAT* results, the simultaneous radio

observations indicated that SS 433 was at its radio quiescent phase. At the very end of the *GINGA* observations when the X-ray source reached to its lowest state, the radio flare was found to switch on and a series of radio flaring events, each lasting several days, were observed. It is believed that the first of the series of flare observed after the end of *GINGA* observations was related to events in or very close to the core of SS 433 (Vermeulen, 1989). Before the onset of the radio flare, a dip in the total radio flux was observed and this dip was almost coincident with the second decrease of the X-ray intensity at 1988 May 22.0. Considering the correlated behavior in X-ray and radio bands, one may suggest that the second flux reduction seen by *GINGA* in 1987 May was a transition which connected the X-ray quiescent state to the active X-ray state.

Although the explanation of the X-ray intensity drop at post-eclipse phase is not clear, it is likely that the event is related to the variation of the internal physical condition of the accretion disc because the onset of the radio flare is correlated with the intensity decrease. The accretion disc could have suffered a perturbation and was expanding or ejecting material at around 1987 May 22.0 so that part of the X-ray and radio radiation regions was obscured, or because of a decrease of the mass supply rate from the optical companion star, the accreted mass in the accretion disc was insufficient to maintain the luminosity of the system and the stability of the disc.

Oscillation in a thick inner accretion disc is one of the possibilities which could produce the above phenomenon. It is known that most of the radiation power comes from the region of about five Schwarzschild radius of the disc. This part of the disc is unstable with respect to thermal and viscous perturbations when accretion rates are in the range $10^{-2} \leq (\dot{M}/\dot{M}_E) \leq 10^2$ (where \dot{M}_E is Eddington limit) (Abramowicz, Lasota & Xu 1986). Higher or lower accreting rates give steady discs, and when the accretion rate falls within the instability region, the disc experiences a quasiperiodic behavior, showing recurrent bursts, or switching between high and low states, or changing the ratio of thermal to non-thermal emission.

Observations of SS 433 suggest that SS 433 is a super-Eddington accreting system and the source is stable in most periods, which imply that the accretion rate must be $(\dot{M}/\dot{M}_E) \geq 10^2$, outside the instability region. If the mass supply rate from the companion star is higher than this value, the accretion disc will be stationary and thick. If, for some reason (not yet known), the accretion rate falls into the instability region, i.e., $(\dot{M}/\dot{M}_E) \leq 10^2$, the disc

becomes unstable and the source switches from quiescent to active states. At the same time, because of a shortage of fuel in the disc, the source gradually dims.

If this qualitative argument is right, the accretion rate of SS 433 must be not very far from $(\dot{M}/\dot{M}_E) \simeq 10^2$. Although the mass of the compact object is not certain, it is estimated to be in the range of $1 \sim 100 M_\odot$. With these values, the Eddington limit is $\dot{M}_E \sim 10^{-7} - 10^{-5} M_\odot \text{ y}^{-1}$, and the accretion rate of SS433 is then expected to be in the range of $\dot{M} \sim 10^{-5} - 10^{-3} M_\odot \text{ y}^{-1}$, which is completely consistent with the values derived from various observations and theoretical predictions of SS 433 (e.g. $\dot{M} \geq 10^{-5} M_\odot \text{ y}^{-1}$ by Calvani and Nobili 1981 and $\dot{M} > 2.5 \times 10^{-4} M_\odot \text{ y}^{-1}$ by Leibowitz 1984; and also from the X-ray observations, Stewart *et al.* 1987).

4.4.3 Implications of Variable Line Width — Again

During the *GINGA* observations, the evolution of the Doppler energy shifted line was monitored in details over the periods of three X-ray eclipses. As shown in Fig. 4.7(b), Fig. 4.8(b) and Fig. 4.9(b), the line width does not change during the eclipses, but is consistent with 1.2 keV, 0.66 keV and 0.55 keV respectively, indicating that the line width only varies with the precession of the jets on a 163 day period. When expressed in terms of coordinates of a cylindrical system with z along the jet axis, it means that the line width is only a function of the polar angle and independent of z and azimuthal angle.

As discussed in last chapter, Compton scattering is one of the possible mechanisms which can make the observed line width vary with the polar angle. The X-rays are produced with narrow emission lines in the jets, and then Compton scattered in a surrounding medium or possibly in the jets themselves, thereby giving broadened lines with various widths in different directions. According to the calculation by Pozdnyakov, Sobol and Sunyaev (1979), for electron temperature $T_e = 10 \text{ keV}$, an optical depth $\tau \sim 2$ is required and for $T_e = 1 \text{ keV}$ $\tau \sim 7$. An optical depth $\tau \sim 2$ corresponds to a column density $n_{eR} \sim 3 \times 10^{24} \text{ cm}^{-2}$ with respect to the Thomson scattering cross section.

From the spectral fitting the absorption column determined from low-energy cut-off is $< 1 \times 10^{22} \text{ cm}^{-2}$. The upper limit to the iron absorption column is dependent on the assumption on the continuum and the shape of the emission line, but a conservative estimate for an equivalent

hydrogen column density for solar abundances is 10^{23} H atoms cm^{-2} , which corresponds to $\tau \sim 0.07$. This is much smaller than the required optical depth for $T_e < 10$ keV when iron atoms are not fully ionized. On the other hand, if the scattering medium is hot and iron is fully ionized, the emission from the hot scattering medium is not negligible and the thermal emission from this scattering media itself is $L = 1.4 \times 10^{-27} T^{1/2} n_e^2 g_{\text{ff}} V$, where g_{ff} is the Gaunt factor. Substituting the volume $V = \pi r_j^2 l_j$ for a cylindrical geometry, where r_j and l_j are radius and length of the scattering medium along the jet, and using the column density for $\tau \sim 2$, $L > 10^{26} \times (\frac{T}{10^8 \text{K}})^{1/2} l_j$ is obtained. The length of the jet should have a similar dimension to the companion star or binary separation i.e., $\sim 10^{12}$ cm. The expected luminosity from the scattering medium is then at least 10^{38} erg s^{-1} , two order of magnitude larger than the actually observed.

Summarizing above discussion, if the electron temperature in scattering medium is sufficiently low that the iron is not ionized, the electron column density required for Compton broadening is larger than the upper limit obtained from the spectrum. If the electron temperature is sufficiently high that the iron atoms are completely ionized, more X-ray emission from the scattering medium is expected to have been observed.

It is also difficult to radiatively ionize the scattering medium. The UV radiation from the accretion disc is too soft to ionize oxygen or iron atoms. If the ionizing radiation is X-ray, its luminosity should be observed, since a large fraction would be scattered isotropically. The ionization parameter ξ (Kallman and McCray 1982) can be roughly estimated by assuming that the ionizing radiation has a luminosity close to the observed luminosity. When the jet is the source of the radiation, the ionization parameter ($\xi = L/(nr^2)$) is transformed to $\pi L/(nr l_j)$. From $L \sim 10^{36}$ erg s^{-1} , $n_e r \sim 3 \times 10^{24}$ cm^{-2} , and $l_j \sim 10^{12}$ cm, $\xi = 1$ is obtained, which is too low to fully ionized iron atoms, for which $\xi = 10^4$ is required. If the ionizing radiation is a collimated beam which is not directly observed, a scattered component, which would be more intense than the observed flux, should be still observed.

It is thus very difficult to have hot plasma (presumably continually reheated), or to keep the scattering medium ionized by X-ray irradiation unless the gas is photo-ionized at the very base of the jet near the compact object and then ejected around the relativistic jet.

However, it is possible that the iron lines are generated in the jets and scattered also by the material inside the jets. Here, the contradiction between the observed column density

and that required for broadening the line is no longer a real problem because the derived column density does not represent the actual column of the jets if the X-rays are produced everywhere in the jets, both along the jet axis and on the surface of the jet. When the electron temperature is sufficient high and the jet radius is reasonably large so that suitable optical depth could be achieved, Compton scattering mechanism would give an acceptable explanation to the 163 day modulation on the line width.

If, the jet cylinder is very thin and it could not provide required optical depth to make the Compton broadening possible, other scenarios, as suggested in last chapter, must be taken into considerations. Broadening of line emission from the jet is expected if the radial velocity of the source material has dispersion. This is possible if, either the jet has a large opening cone angle, or there is a dispersion in the bulk velocity within the jet. The narrow width of the optical emission line, consistent with an opening angle of 0.04 rad (Margon 1984), precludes this scenario in general. The dispersion in the bulk velocity might conflict less with the optical narrow line as the X-ray and optical emission region are completely separate considering their large difference in size. If the X-rays were emitted from the jet while being accelerated to the relativistic speed, different velocities could be observed in various stage of acceleration. Thus a broad emission line would be seen at the precession phases with large Doppler shift when the base of the jet could be looked deeply and the acceleration region could be more easily visible. However, the upper wing of the broad emission line extends up to 10 keV, implying a much faster component in the jet. This component would have to be decelerated before it reaches optical emission region, which would then require the release a huge amount of energy.

4.5 Summary

The X-ray intensity of SS 433 was observed with the *GINGA* X-ray satellite to reduce at 1987 May 19.60 and 1988 May 19.85 for a duration of ~ 2.4 days. In the 1989 May observations, although the configuration of the eclipse is not well constrained, an intensity variation is seen around the primary optical minimum phase. Since these episodes occurred in good agreement with the optically primary minima, similar to those previously observed by *EINSTEIN* and *EXOSAT* Observatory, they are most likely to be eclipses of an X-ray emitting region near the compact object by the companion star. The eclipse duration is thus determined with the

best-ever accuracy. The eclipse configuration is variable with the jet precession.

The X-ray spectra were measured throughout the eclipse episodes. The spectra are approximately described by a combination of a thin-thermal continuum and an intense broad emission line with its line centre located at the position consistent with Doppler shifted line energy predicted from the 'standard kinematic model'. As the total intensity changed with time, the continuum temperature and the line intensity changed, while the energy and the width of the line as well as the absorption column remained relatively constant. The 1987 May eclipse profile of the Doppler shifted line confirms the eclipse of the relativistic jet itself with a depth of $\sim 50\%$. Although both single and double line models may be allowed, a large line width (Gaussian ~ 1 keV) is required in either case. This is probably due to Comptonization. The variation of the line width with respect to the jet precession phase is consistent with the *EXOSAT* results.

A transition period from X-ray quiescent to active states may have been observed with *GINGA* between 1987 May 22.0 and 1988 May 23.0. If this interpretation is correct, it implies that the accretion rate of SS 433 is in the range of $10^{-5} \sim 10^{-3} M_{\odot} \text{ y}^{-1}$.

Chapter 5

The Geometric Parameters of SS 433

— constraints from the EXOSAT & GINGA observations

5.1 Introduction

A general picture has been established for SS 433 (ref. Margon 1984). It is a 13 day binary system which consists of a massive early-type companion star and a compact object surrounded by an accretion disc. In terms of the ‘standard’ kinematic model, a pair of well collimated jets are oppositely ejected from the vicinity of the accretion disc at a relativistic speed, and are precessing in the sky with 163 day period. From the observed photometric and spectroscopic characteristics of SS 433 together with the spatial structure of the diffuse X-ray lobes, the system parameters like the periods of the orbital motion and jet precession, the precession cone angle, the jet speed and the inclination of the binary orbit, are unambiguously determined, and various phenomena observed can be almost universally interpreted within the framework of this ‘standard’ kinematic model. However, other important parameters of the SS 433 system, such as the orbital separation, the mass of the companion star and the nature of the compact object etc, remain unclear in this general picture.

Estimating the parameters unspecified by the ‘standard’ kinematic model requires detailed information for each component of SS 433. Although various assumptions and approximations can be made for modelling the configuration and luminosity distribution of each system component, the methods applied for the estimation of these parameters are either to fit the

whole light curve with many free parameters (e.g. Leibowitz 1984) or to consider only certain aspects of the light curve such as the shape of the eclipse (e.g. Stewart *et al.* 1987). In the X-ray energy range, the strong modulation by the jet precession and the orbital motion of the X-ray properties of SS 433 found with the *EXOSAT* and *GINGA* observations (see Chapters 3&4) makes it clear that the energy shifted iron line and X-ray continuum emissions are associated with each other and come from the same region – the jets. Modelling the system geometry with the constraints from X-ray observations is therefore relatively easier and more accurate because the assumptions on the luminosity distributions on the surfaces of the companion star and accretion disc required for the optical modelling need not be made.

Considering the width and depth of the *EXOSAT* observed eclipse, Stewart *et al.* (1987) have modelled the system geometry of SS 433. Due to the incomplete coverage of the eclipse with *EXOSAT* and the inaccurate assumption on the shape of the companion star and accretion disc, the uncertainty of the estimated parameters was large. With the *GINGA* observations, three X-ray eclipses with much better sampling were obtained and the duration of the eclipses rather accurately determined. It then becomes possible to model SS 433 system with more reliability.

In this chapter, discussions on the geometry of SS 433 system are presented. Mathematics which can be generally employed to describe the system geometry in future numerical calculations is established in section 5.3 using assumptions and definitions made in section 5.2. Constraints on the geometrical parameters of SS 433 are derived in section 5.4 without specifying of the accretion disc shape. The comparison of the derived constraints on the system geometry from the X-ray observations with previous modelling results is made and the implications of these results are discussed in section 5.5. Accordingly, several possible models are suggested in section 5.6 in order to map physical parameters in the jets of SS 433 in chapter 6. Section 5.7 gives a summary of the discussion in this chapter.

5.2 Assumptions, Definitions and Constraints

The following assumptions and definitions are made in this chapter to set up a geometrical model of SS 433 and derive constraints for its parameters.

- 1 The system consists of a compact object with mass M_x , an optical companion star M_s , an accretion disc and a pair of well-collimated, anti-parallel jets. The mass ratio of the compact object and the companion star is assumed to be $q = M_x/M_s$.
- 2 The star M_s and compact object M_x are rotating around each other in a (nearly) circular orbit with a plane (roughly) orthogonal to the orbital angular momentum vector. The orbital separation is defined to be a and will be used as a unit of length in this chapter. The binary period is $P_b = 13^{\text{d}}.081 \pm 0^{\text{d}}.003$ as given by Kemp *et al.* (1986) and the orbital inclination $i = 78.82^\circ \pm 0.11^\circ$ is adopted from Margon (1984).
- 3 The companion is a ‘normal’ OB star which fills its Roche lobe and its shape is therefore approximated by an ellipsoid equipotential surface in the Roche model as given in Appendix B.
- 4 The normal of the accretion disc coincides with the jets’ instantaneous direction. The disc is precessing along with the jets in space around an axis parallel to the orbital angular momentum vector at the same angular velocity. The period of the precession is defined as P_p and $P_p = 162^{\text{d}}.5 \pm 0^{\text{d}}.25$ from Kemp *et al.* (1986) is adopted. The half precession cone angle $\alpha = 19.80^\circ \pm 0.18^\circ$ is taken from Margon (1984). The precession sense of jets and disc is opposite to the direction of the binary revolution (see Leibowitz 1984). In this chapter, the jets are assumed to precess clockwise and the star rotating counterclockwise about the compact object as viewed from the top of the orbital plane.
- 5 The size of the accretion disc must not be greater than that of the Roche lobe of the compact object.
- 6 The jet is approximated to be a cylinder with radius R_f and length L_j . If one assumes that the jets are formed inside the funnel of the thick accretion disc, R_f should be equal to the radius of the funnel exit from which the jet material are ejected at a relativistic speed v ; $v = 0.2601 \pm 0.0014 c$ from Margon (1984) is adopted.
- 7 The X-ray emission is from the jets and the eclipse located at around the optical primary minimum is due to the occultation of the relativistic jet by the normal star.

The assumption about the jet shape is from the arguments that the energy shifted line is possibly broadened by the Compton scattering (see Chapter 4) and the fact that the jet velocity dispersion is not very large. Assumption 7 is from the X-ray observation results presented in Chapter 3 & 4 in this thesis. Other assumptions above are based on the ‘standard’ kinematic model and used almost universally by most investigators (e.g. Leibowitz 1984; Antokhina & Cherepashchuk 1987).

For convenience sake in the following discussions, the jet above the orbital plane is called upper (or top) jet and the one below the orbital plane is named as lower (or bottom) jet.

The ephemeris adopted in this chapter is from Kemp *et al.* (1986), in which the following angles are defined,

$$\begin{aligned}
 j &= 90 - i \\
 \theta &= 2\pi \frac{(T - T_b)}{P_b} \\
 \psi &= 2\pi \frac{(T - T_p)}{P_p}
 \end{aligned}
 \tag{5.1}$$

where,

$$\begin{aligned}
 T_b &= JD2,440,003.434 \\
 &= MJD40002.934 \\
 T_p &= JD2,440,017.9 \\
 &= MJD40017.4
 \end{aligned}
 \tag{5.2}$$

T_b and T_p are so chosen that $\theta = 0$ implies the phase of primary optical minimum, i.e., the normal star crosses the line of sight and occults the compact object, and $\psi = \pi$ means a maximum blue-shifted line is observed, i.e., when the upper jet approaches the observer. T is the time in MJD.

Several Cartesian coordinate systems, called Sky System, System 1 and System 2, are used in this chapter and their definitions are given in Appendix A.

From the 1987 *GINGA* observation, the following constraints are derived,

- 1 The eclipse duration is $\sim 2.4 \pm 0.1$ days. The first contact time of eclipse is $T_1 = \text{MJD}46934.6$ and the fourth contact time $T_2 = \text{MJD}46937.0$ for the observations at precession phase 0.58. They are determined from the light curves of the continuum and the emission line.
- 2 The eclipse fraction is $\sim 0.5 \pm 0.1$ for the eclipse at the phase when the upper jet is approaching at observers, as determined from the light curve of the emission line.
- 3 At mid eclipse $T_m = \text{MJD}46935.8$, the star completely covers the base of the jet, but the top of the approaching jet is still visible.

The parameters to be determined in the following discussions are the mass ratio q , the masses M_x and M_s , the orbital separation a , the jet cylinder radius R_f and length L_j , the size of the companion star.

5.3 Mathematical Description of System Geometry

5.3.1 Coordinates of SS 433 in the Sky System

a). The Jets

The coordinates of upper jet axis in System 1 is

$$\begin{aligned}
 A &= L_j \\
 \theta_1 &= 0 \\
 \varphi_1 &= 0 \text{ or } 2\pi
 \end{aligned}
 \tag{5.3}$$

According to the transformation equation A.7 in Appendix A, the corresponding coordinates in the Sky System are

$$\begin{aligned}
x_j^u &= L_j \sin \alpha \cos \varphi_2 \\
y_j^u &= L_j(\sin \alpha \sin \varphi_2 \cos j - \cos \alpha \sin j) \\
z_j^u &= L_j(\sin \alpha \sin \varphi_2 \sin j + \cos \alpha \cos j)
\end{aligned} \tag{5.4}$$

When the energy separation of the Doppler-shifted lines becomes maximum, the upper jet points toward the observer and its x-component x_j^u should be equal to zero and y_j^u will become minus, therefore, $\varphi_2 = (2n+1)\pi + \frac{\pi}{2}$, ($n = 0, \pm 1, \pm 2 \dots$). At this phase, ψ equals ψ_0 ($\psi_0 = \pi$). With the assumption that the jets precess in the direction opposite to the star's, φ_2 becomes

$$\varphi_2 = (2n+1)\pi + \frac{\pi}{2} + (\psi_0 - \psi) \tag{5.5}$$

By substituting φ_2 in Equation (5.4) with (5.5), the coordinates of upper jet axis in Sky System (i.e., the sky plane) are obtained,

$$\begin{aligned}
x_j^u &= L_j \sin \alpha \sin \psi \\
y_j^u &= -L_j(\cos \alpha \sin j - \sin \alpha \cos \psi \cos j) \\
z_j^u &= L_j(\cos \alpha \cos j + \sin \alpha \cos \psi \sin j)
\end{aligned} \tag{5.6}$$

Because of the symmetry of jets, the lower jet axis has the coordinates $(-x_j^u, -y_j^u, -z_j^u)$.

The angle between projected jet axis in the sky and x-axis is given by

$$\tan \Theta = \frac{z_j^u}{x_j^u} = \frac{\cos \alpha \cos j + \sin \alpha \cos \psi \sin j}{\sin \alpha \sin \psi} \tag{5.7}$$

The outline of the jet cylindrical surface projection onto the sky plane can be described by two straight line equations, they are,

$$\begin{aligned}
z_l &= \tan \Theta x_l - R_f \sqrt{1 + \tan^2 \Theta} \\
z_r &= \tan \Theta x_r + R_f \sqrt{1 + \tan^2 \Theta}
\end{aligned} \tag{5.8}$$

where (x_l, z_l) are the coordinates of the jet cylinder projection on the left side of the cylinder axis and (x_r, z_r) for the right side projection of the cylinder.

b). The Accretion Disc

Using the circular cylindrical coordinates (R, ω, h) , the coordinates of any point on the accretion disc may be written in System 1 as

$$A = (R \cos \omega, R \sin \omega, h) \quad (5.9)$$

where $0 \leq R < Y_x$, $0 \leq \omega \leq 2\pi$, and $-Z_x < h < Z_x$, i.e., R and h are not larger than the Roche lobe Y_x , Z_x of the compact object.

It is easy to have the coordinates of the accretion disc in Sky System by using transformation relation A.7 and considering Equation (5.5). They are

$$\begin{aligned} x_d &= R(\cos \psi \sin \omega - \cos \alpha \sin \psi \cos \omega) + h \sin \alpha \sin \psi \\ y_d &= -R(\sin \psi \sin \omega \cos j + \sin \alpha \cos \omega \sin j + \cos \alpha \cos \psi \cos \omega \cos j) \\ &\quad -h(\cos \alpha \sin j - \sin \alpha \cos \psi \cos j) \\ z_d &= R(-\sin \psi \sin \omega \sin j + \sin \alpha \cos \omega \cos j - \cos \alpha \cos \psi \cos \omega \sin j) \\ &\quad +h(\cos \alpha \cos j + \sin \alpha \cos \psi \sin j) \end{aligned} \quad (5.10)$$

c). The Star

The coordinates of the star centre in System 2 are

$$\begin{aligned} x_s^2 &= a \cos \varphi_2 \\ y_s^2 &= a \sin \varphi_2 \\ z_s^2 &= 0 \end{aligned} \quad (5.11)$$

When $\varphi_2 = \frac{3}{2}\pi$, the star is crossing the line of sight and according to the definition of θ , θ should be zero. So, φ_2 can be replaced by θ as

$$\varphi_2 = \frac{3}{2}\pi + \theta \quad (5.12)$$

and the coordinates of the star centre in Sky System may be written

$$\begin{aligned} x_s &= a \sin \theta \\ y_s &= -a \cos \theta \cos j \\ z_s &= -a \cos \theta \sin j \end{aligned} \quad (5.13)$$

Around $\theta = 0$, the projected stellar disc on the sky plane can be well approximated with an ellipse of major semi-axis a_s , and minor b_s , that is

$$\frac{(x - x_s)^2}{a_s^2} + \frac{(z - z_s)^2}{b_s^2} = 1 \quad (5.14)$$

where a_s equals to the maximum extent Y_s of Roche lobe of the companion star in the Y direction and b_s , equals to the maximum extent Z_s along the Z-axis (see Appendix B for definition).

5.3.2 Eclipse Conditions

Eclipse by the accretion disc

Clearly, at any time, only that part of the accretion disc which is between the jets and the observer can cover the jets. Mathematically, this condition may be written

$$\begin{aligned} \frac{z_d}{x_d} &= \frac{z_j^u}{x_j^u} \\ y_d &= \min(y_d(\omega_1), y_d(\omega_2)) \end{aligned} \quad (5.15)$$

where ω_1 and ω_2 are two phase angles at which x_d and z_d can satisfy the condition $\frac{z_d}{x_d} = \frac{z_j^u}{x_j^u}$ in the above equation.

The following calculations give the values of ω_1 and ω_2 .

Case A: $x_j^y \neq 0$

When x_j^y is not equal to zero, from Equations (5.6), (5.10) and (5.15), a formula that may be used to calculate ω_1 and ω_2 in Case A is obtained, that is,

$$\tan \omega = \frac{\sin \psi}{\cos \alpha \cos \psi + \sin \alpha \tan j} \quad (5.16)$$

Case B: $x_j^y = 0$

When x_j^y equals zero, x_d must be zero and Equations (5.6) yields conditions

$$\begin{aligned} \sin \psi &= 0 \\ \cos \psi &= \pm 1 \end{aligned} \quad (5.17)$$

Substituting $\sin \psi$, $\cos \psi$ in Equation (5.10) with above values and considering $x_d = 0$, there follows

$$\sin \omega = 0 \quad (5.18)$$

Equations (5.16) and (5.18) yield two values of ω , i.e. ω_1 and ω_2 . The condition $y_d = \min(y_d(\omega_1), y_d(\omega_2))$ in Equation (5.15) may be used to choose a correct ω value that corresponds to the phase in which accretion disc eclipses jets.

Eclipse by the companion star

With assumption 7 in section 5.2, when an X-ray eclipse is observed, the companion star must be in between the observer and the jets and the z-component of its centre is less than zero, i.e.

$$z_s < 0 \quad (5.19)$$

The projections of jets in sky plane may be described by a general straight line equation, which is

$$z = sx + c \quad (5.20)$$

where

$$s = \tan \Theta \quad (5.21)$$

and

$$c = \begin{cases} -R_f \sqrt{1 + \tan^2 \Theta} & \text{for the jet left side} \\ 0 & \text{for the central jet axis} \\ R_f \sqrt{1 + \tan^2 \Theta} & \text{for the jet right side} \end{cases} \quad (5.22)$$

During the eclipse, the equation of the stellar disc and that of the jet projections must have common solutions,

$$\begin{aligned} z &= sx + c \\ \frac{(x-x_s)^2}{a_s^2} + \frac{(z-z_s)^2}{b_s^2} &= 1 \end{aligned} \quad (5.23)$$

and these equations give the coordinates of intersections between the star and the jets, they are

Case A: $\tan \Theta \neq \infty$

$$\begin{aligned} x_1 &= \frac{-[sa_s^2(c-z_s) - b_s^2 x_s] + a_s b_s \sqrt{b_s^2 + a_s^2 s^2 - (c-z_s + sx_s)^2}}{(b_s^2 + a_s^2 s^2)} \\ z_1 &= sx_1 \\ x_2 &= \frac{-[sa_s^2(c-z_s) - b_s^2 x_s] - a_s b_s \sqrt{b_s^2 + a_s^2 s^2 - (c-z_s + sx_s)^2}}{(b_s^2 + a_s^2 s^2)} \\ z_2 &= sx_2 \end{aligned} \quad (5.24)$$

Case B: $\tan \Theta = \infty$

$$\begin{aligned} x_{1,2} &= c \\ z_{1,2} &= z_s \pm \frac{b_s}{a_s} \sqrt{a_s^2 - (c - x_s)^2} \end{aligned} \quad (5.25)$$

Obviously, from Equations (5.19), (5.24) and (5.25), the conditions that an X-ray eclipse by the companion star can happen are

$$\begin{aligned}
 z_s &< 0 \\
 b_s^2 + a_s^2 s^2 - (c - z_s + s x_s)^2 &\geq 0 \text{ when } \tan \Theta \neq \infty \\
 a_s^2 - (c - x_s)^2 &\geq 0 \text{ when } \tan \Theta = \infty
 \end{aligned} \tag{5.26}$$

The time that the primary optical minimum occurs can be predicted by setting

$$\theta = n2\pi \tag{5.27}$$

and

$$T_0 = T_b + nP_b \tag{5.28}$$

where $n = 0, \pm 1, \pm 2, \pm 3, \dots$

With the ephemeris given by Kemp *et al.* (1986),

$$T_0 = MJD40002.934 + n \times (13.0811 \pm 0.003) \tag{5.29}$$

and from the formula of Gladyshev, Goranskii, and Cherepashchuk (1987):

$$T_0 = MJD46595.75 \pm 0.04 + n \times (13.08201 \pm 0.0007) \tag{5.30}$$

5.3.3 Doppler Effect in the Jets of SS 433

The wavelength of the Doppler shifted emission line arise from the relativistic motion of the emitting material in the jets of SS 433 can be expressed as (e.g. Milgrom 1981)

$$\lambda^{\pm} = \lambda_0(1 + z_g)\gamma(1 \pm \beta \cos \varphi) \quad (5.31)$$

where φ is the angle subtended to the line of sight by the jet axis along which the emitting material is approaching to the observers at $v = 0.26c$, λ_0 is the laboratory wavelength, z_g is the gravitational redshift which can be ignored in the case of SS 433, $\beta = v/c$ and $\gamma \equiv (1 - \beta^2)^{-1/2}$.

With $E = h\nu = hc/\lambda$, the Doppler shifted energy can be calculated by

$$E^{r/b} = \frac{E^0}{\gamma(1 \pm \beta \cos \varphi)} \quad (5.32)$$

where E^0 represents the rest photon energy and E^r , E^b are the observed Doppler red- and blue- shifted energies respectively.

According to the definition in Appendix A and Equation (5.6),

$$\cos \varphi = -y_j^u/L_j = \cos \alpha \sin j - \sin \alpha \cos \psi \cos j \quad (5.33)$$

and

$$E^{r/b} = \frac{E^0}{\gamma[1 \pm \beta(\cos \alpha \sin j - \sin \alpha \cos \psi \cos j)]} \quad (5.34)$$

While the material is moving along the jet axis at a relativistic speed, the Doppler boosting effect of radiation from the jet emitting material has to be considered. The boosting factor (or beaming factor) is (see e.g. Begelman, Blandford & Rees 1984)

$$\begin{aligned} B^{r/b} &= \left[\frac{1}{\gamma(1 \pm \beta \cos \varphi)} \right]^3 \\ &= \frac{1}{\gamma^3 [1 \pm \beta(\cos \alpha \sin j - \sin \alpha \cos \psi \cos j)]^3} \end{aligned} \quad (5.35)$$

The observed flux is then

$$F_{obs} = B^b F_B + B^r F_R \quad (5.36)$$

where F_B, F_R are the unbeamed fluxes from the approaching and receding jets respectively.

5.4 Constraints on the Parameters of the SS 433 Geometry

While the minimum flux was reached at around $T_m = \text{MJD}46935.8$ over the *GINGA* 1987 May observed X-ray eclipse, the stellar disc covered the base of approaching (upper) jet (constraint 3 in section 5.2). Conditions (5.26) must be satisfied,

$$F_m \equiv (b_s^2 + a_s^2 s_m^2) - (c_m - z_{sm} + s_m x_{sm})^2 \geq 0 \quad (5.37)$$

and the z-coordinate of intersection of the stellar disc rim and upper jet central axis must be greater than zero,

$$z_m^u = s_m x_m^u \geq 0 \quad (5.38)$$

Using Equation (5.24) and considering $c_m = 0$, (5.38) becomes

$$z_m^u = \frac{(s_m a_s^2 z_{sm} + b_s^2 x_{sm}) - a_s b_s \sqrt{b_s^2 + a_s^2 s_m^2 - (z_{sm} - s_m x_{sm})^2}}{(b_s^2 + a_s^2 s_m^2)} s_m \geq 0 \quad (5.39)$$

With the combination of (5.37) and (5.39), the upper limit of the mass ratio is derived,

$$q \leq 9.0 \quad (5.40)$$

which is independent of the assumptions on the shape of jets and accretion disc.

Also from constraint 3, i.e., the star cannot completely cover the approaching jet, the lower limit of the jet length is derived by using Equations (5.6) and (5.24),

$$L_j^{min} = \frac{(s_m a_s^2 z_{sm} + b_s^2 x_{sm}) - a_s b_s \sqrt{b_s^2 + a_s^2 s_m^2} - (z_{sm} - s_m x_{sm})^2}{(b_s^2 + a_s^2 s_m^2) \sin \alpha \sin \psi_m} \quad (5.41)$$

which is another model independent conclusion.

Constraint 2 indicates that the flux F_{min} at T_m is about 50% of F_{max} at T_1 , which gives the ratio of jet lengths visible outside and inside the eclipse assuming constant emissivity, i.e.,

$$\frac{F_{min}}{F_{max}} \simeq 0.5 \simeq \frac{L_j - L_j^{min}}{L_j - H_f} \quad (5.42)$$

where H_f is the height of the disc near the jet. With a simple calculation, the jet length is obtained,

$$L_j \simeq 2L_j^{min} - H_f \quad (5.43)$$

and the upper limit of the jet is

$$L_j^{max} = 2L_j^{min} \quad (5.44)$$

A critical jet length L_j^{crit} is introduced in the following. When $L_j^{crit} > L_j$, the receding jet is covered by the accretion disc and $L_j^{crit} < L_j$, the receding jet is visible.

According to Equation (5.10), the x-coordinate of the accretion disc which can cover the receding jet over the *GINGA* 1987 May observed eclipse is

$$\begin{aligned} x_d^l &= R(\cos \psi \sin \omega - \cos \alpha \sin \psi \cos \omega) + h \sin \alpha \sin \psi \\ &< Y_x(\cos \psi \sin \omega - \cos \alpha \sin \psi \cos \omega) - Z_x \sin \alpha \sin \psi \end{aligned} \quad (5.45)$$

and from Equation (5.6), the x-coordinate of the receding jet is

$$x_j^l = -L_j \sin \alpha \sin \psi \quad (5.46)$$

thus, the critical jet length can be defined as

$$L_j^{crit} = Z_x - \frac{\cos \psi \sin \omega - \cos \alpha \sin \psi \cos \omega}{\sin \alpha \sin \psi} Y_x \quad (5.47)$$

Plotting L_j^{min} , L_j^{max} and L_j^{crit} against mass ratio q in Fig. 5.1, the following model independent constraints can be derived:

- 1 **The mass ratio of SS 433 system cannot exceed $q \leq 9.0$, whatever the shapes of the jet and accretion disc are.**
- 2 **While q is greater than 0.566, the receding jet will be obscured by the accretion disc; while q is smaller than 0.174, the receding jet will be definitely visible.**
- 3 **The jet length would not exceed 0.486a if only one jet is seen, and should be greater than 0.350a if both jets are visible when $q < 0.566$.**

When the eclipse by the companion star happens, Conditions (5.26) are satisfied and the value range of parameter c can be derived from

$$(b_s^2 + a_s^2 s^2) - (c - z_s + s x_s)^2 \geq 0 \quad (5.48)$$

that is,

$$-\sqrt{b_s^2 + a_s^2 s^2} + z_s - s x_s \leq c \leq \sqrt{b_s^2 + a_s^2 s^2} + z_s - s x_s \quad (5.49)$$

When the eclipse started at T_1 , the stellar disc began to cover the left side jet and $c = -R_f \sqrt{1 + s_1^2}$, with Equation (5.49), the value range of R_f is

$$\frac{-\sqrt{b_s^2 + a_s^2 s_1^2} - z_{s1} + s_1 x_{s1}}{\sqrt{1 + s_1^2}} \leq R_f \leq \frac{\sqrt{b_s^2 + a_s^2 s_1^2} - z_{s1} + s_1 x_{s1}}{\sqrt{1 + s_1^2}} \quad (5.50)$$

At T_m , the stellar disc covered both sides of the upper jet, and there are,

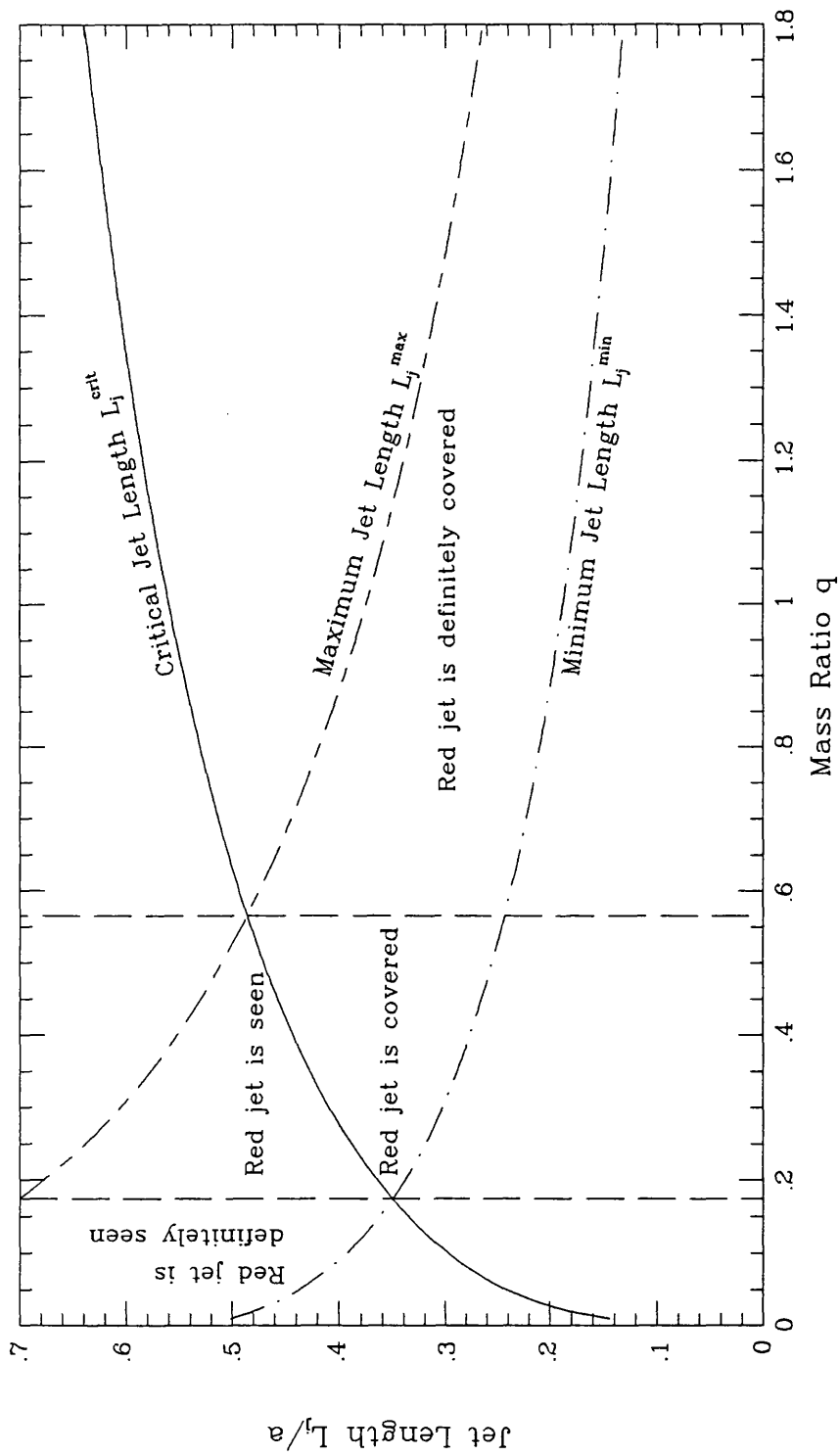


Figure 5.1: Constraints on SS 433 geometry: jet length L_j as a function of mass ratio q

$$\begin{aligned}
\frac{-\sqrt{b_s^2 + a_s^2 s_m^2} - z_{sm} + s_m x_{sm}}{\sqrt{1 + s_m^2}} &\leq R_f \leq \frac{\sqrt{b_s^2 + a_s^2 s_m^2} - z_{sm} + s_m x_{sm}}{\sqrt{1 + s_m^2}} \\
\frac{-\sqrt{b_s^2 + a_s^2 s_m^2} + z_{sm} - s_m x_{sm}}{\sqrt{1 + s_m^2}} &\leq R_f \leq \frac{\sqrt{b_s^2 + a_s^2 s_m^2} + z_{sm} - s_m x_{sm}}{\sqrt{1 + s_m^2}}
\end{aligned} \tag{5.51}$$

At the fourth contact of the eclipse, $T = T_2$, and the star only covered the jet right side. Let $c = R_f \sqrt{1 + s_1^2}$, Equation (5.49) yields

$$\frac{-\sqrt{b_s^2 + a_s^2 s_2^2} + z_{s2} - s_2 x_{s2}}{\sqrt{1 + s_2^2}} \leq R_f \leq \frac{\sqrt{b_s^2 + a_s^2 s_2^2} + z_{s2} - s_2 x_{s2}}{\sqrt{1 + s_2^2}} \tag{5.52}$$

With the mass ratio as abscissa, plotting the intersection of R_f values calculated from (5.50), (5.51) and (5.52) in Fig. 5.2, the following conclusions are obtained,

- 1 **When a cylindrical shape is assumed for the jets, the mass ratio cannot exceed 1.71.**
- 2 **If the assumption that the observed X-ray eclipse is only due to an occultation by the companion star itself is valid (but see the discussion below) and the receding jet is indeed not visible, the X-ray jet of SS 433 can no longer be regarded as a thin pencil shape, the width of the jet should be comparable with the jet length. A thin jet is possible only when the mass ratio is small and the receding jet is not covered by the accretion disc.**

In summary, the range of mass ratio can be divided into three groups: group A with $q < 0.174$ in which the receding jet is definitely visible; group B with mass ratio between 0.174 and 0.566, in which the receding jet may be covered by the accretion disc depending on the disc geometry; group C with mass ratio greater than 0.566 but smaller than 1.71 over which only the approaching jet is observed. Accordingly, the constraints on the system parameters are discussed in the following.

- 1). masses of the system components

Crampton's Doppler analysis of the 'stationary' HeII $\lambda 4686$ line indicates that its modulation

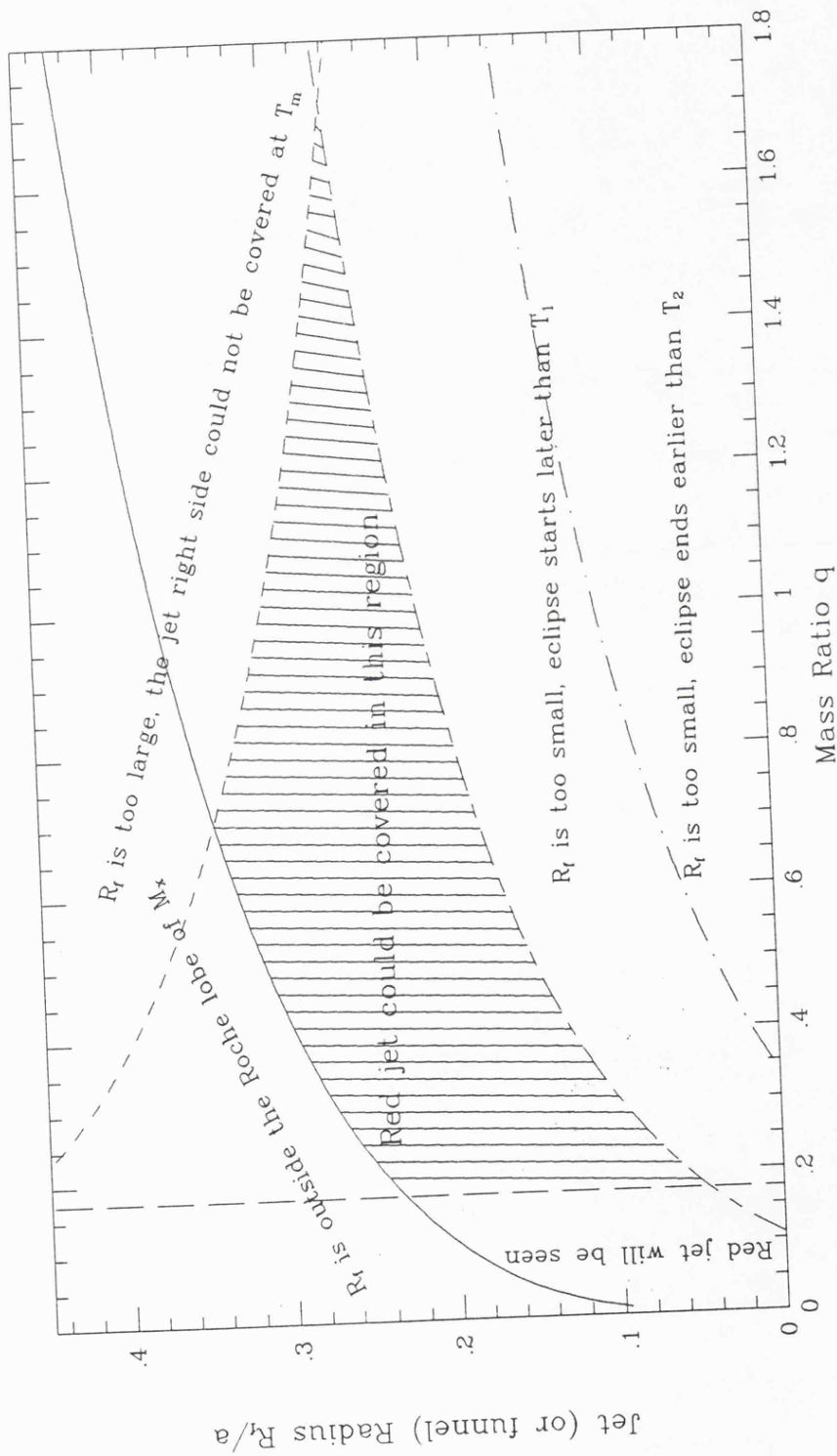


Figure 5.2: Constraints on SS 433 geometry: jet radius R_j as a function of mass ratio q

represents the orbital motion of the compact object. The projected velocity (K) equals 195 km s^{-1} with 150 km s^{-1} as a lower limit. The mass function (Crampton & Hutchings 1981) is then

$$M_s/(1+q)^2 = 10.6 M_\odot(4.8 M_\odot) \quad (5.53)$$

where the value in the brackets corresponds to $K = 150 \text{ km s}^{-1}$.

With the mass ratio in different groups, the mass M_x of the compact object and M_s of the companion star are obtained by using the mass function, i.e.,

for group A:

$$\begin{aligned} M_s &\leq 14.61 M_\odot(6.62 M_\odot) \\ M_x &\leq 2.54 M_\odot(1.15 M_\odot) \end{aligned} \quad (5.54)$$

for group B:

$$\begin{aligned} 14.61 M_\odot(6.62 M_\odot) &\leq M_s \leq 25.99 M_\odot(11.77 M_\odot) \\ 2.54 M_\odot(1.15 M_\odot) &\leq M_x \leq 14.71 M_\odot(6.66 M_\odot) \end{aligned} \quad (5.55)$$

for group C:

$$\begin{aligned} 25.99 M_\odot(11.77 M_\odot) &\leq M_s \leq 77.85 M_\odot(35.25 M_\odot) \\ 14.71 M_\odot(6.66 M_\odot) &\leq M_x \leq 133.12 M_\odot(60.28 M_\odot) \end{aligned} \quad (5.56)$$

2). the binary separation a

The Kepler's law gives a relation of the binary separation a and the binary period P .

$$4\pi^2 a^3 = G(M_x + M_s)M_\odot P^2 \quad (5.57)$$

For binary periods of the order of days like SS 433, the binary separation a can be expressed in the form of (see Frank, King & Raine 1985)

$$a = 2.9 \times 10^{11} M_x^{1/3} (1 + 1/q)^{1/3} P_{day}^{2/3} \text{ cm} \quad (5.58)$$

With the values of M_x and q derived above, the binary separation is

$$a \leq 4.15 \times 10^{12} \text{ cm} \text{ (} 3.19 \times 10^{12} \text{ cm)} \text{ (group A)} \quad (5.59)$$

$$4.15 \times 10^{12} \text{ cm} \text{ (} 3.19 \times 10^{12} \text{ cm)} \leq a \leq 5.54 \times 10^{12} \text{ cm} \text{ (} 4.25 \times 10^{12} \text{ cm)} \text{ (group B)} \quad (5.60)$$

$$5.54 \times 10^{12} \text{ cm} \text{ (} 4.25 \times 10^{12} \text{ cm)} \leq a \leq 9.58 \times 10^{12} \text{ cm} \text{ (} 7.36 \times 10^{12} \text{ cm)} \text{ (group C)} \quad (5.61)$$

3). the stellar radius

From the approximate formulae of Paczyński (1971), if a star fills its Roche lobe its shape is approximated by a sphere, the radius of this star will be

$$\frac{R_s}{a} = 0.38 - 0.20 \log q \quad (5.62)$$

with the mass ratio in different region and choosing suitable orbital separation, the stellar radius of SS 433 can be obtained by using the above formula.

4). the jet length and radius

The jet length L_j and radius R_f can be derived from Fig. 5.1-5.2, that is

for group A:

$$\begin{aligned} 0.350a < L_j < 1a \\ 0. < R_f < 0.233a \end{aligned} \quad (5.63)$$

for group B:

$$\begin{aligned} 0.243a < L_j < 0.701a \\ 0.046a < R_f < 0.323a \end{aligned} \tag{5.64}$$

for group C:

$$\begin{aligned} 0.137a < L_j < 0.486a \\ 0.161a < R_f < 0.342a \end{aligned} \tag{5.65}$$

5.5 Discussion

Constraints on the system geometry derived in the last section strongly depend on whether or not the receding jet is visible. Although the model fitting to the X-ray spectrum from *EXOSAT* and *GINGA* observations indicates that only one Doppler blue-shifted line (i.e., the one from the approaching jet) is needed, the possibility that the red-shifted line is submerged by the blue one still cannot be excluded. This uncertainty, therefore, makes the derived mass ratio region fairly large.

However, several important conclusions about the SS 433 system can still be made from the discussions in section 5.4. If the receding jet is indeed visible during the X-ray observations, the mass ratio would not exceed 0.566; if, on the other hand, the receding jet is actually covered by the accretion disc, the mass ratio would not be smaller than 0.174. With the assumptions made in section 5.2, it is concluded that in most cases, the radius of the jet can not be regarded as very small, instead, it should be comparable with the jet length, which indicates that the opening angle of the X-ray jet could be very large and the jet is very fat. The thin jet case, however, is possible only when the mass ratio is smaller than 0.174 if the assumption that the X-ray eclipse around the optical primary minimum is only due to the occultation of the X-ray jet by a companion star which fills its Roche lobe is valid.

Modelling the geometry of SS 433 has been previously done by several investigators using the optical light curve. Using the assumptions similar to those made in this chapter plus approximations on the configuration and surface brightness of both companion star and

accretion disc, Leibowitz (1984) fitted the whole optical light curve with 10 free parameters simultaneously. His results indicate that the mass ratio q is greater than 0.8 at the 95% confidence level and can be as high as 30 at the same confidence level. The calculations in the last section have excluded the possibility that mass ratio can be higher than 9.0 and strongly suggest it located in the range of $0 \sim 1.71$, which partially overlaps that of Leibowitz's results. However, the assumption of the cylinder shape for the jets used in the calculation in last section produces a very conservative estimate for the mass ratio. If a cone shape is assumed for the jets, the upper limit of the mass ratio would be smaller than 1.71. So, the region of the mass ratio derived from the calculation in this chapter should be regarded as more reliable than Leibowitz's.

Leibowitz found that the precession should be retrograde, so that the similarity between the predictions of the model and the observations can be achieved. The assumption on the relative directions between the companion star and jets made in this chapter are directly from Leibowitz's result. With the mathematics of the system geometry presented in section 5.3, it is easy to prove that the phase that the companion star maximally covers the jets is perfectly coincident with that of the optical primary minimum predicted from the ephemeris from the optical observations, and is well centered at the X-ray eclipse observed with *EXOSAT* and *GINGA*. Changing the moving direction of the companion star into the same direction as the jet precession would shift the phase of the X-ray eclipse centre to the position later than the predicted primary optical minimum. This confirms that the precession is indeed retrograde.

Antokhina and Cherepashchuk (1987) modeled the SS 433 geometry in a considerably more accurate way than Leibowitz's model. Instead of assuming a spherical shape for the companion star and cylindrical shape for the accretion disc, they used more accurate Roche lobe geometry to model the star and the disc. They also treated the surface brightnesses of the system components more accurately. With 6 independent parameters in their model to match the whole light curve, Antokhina and Cherepashchuk found that the normal star fills its Roche lobe and that the equatorial radius of the accretion disc was 'touching' the Roche lobe of the compact object. The lower limit of the mass ratio is 0.25 at the 99% confidence level. Although a mass ratio $q=0.4$ cannot be ruled out from the model fitting, they preferred the solution of $q=1.2$ so that the troubles in the interpretation of the observations can be avoided. Obviously, the mass ratio range derived in the last section is consistent with the results of Antokhina and Cherepashchuk.

However, contradictions exist between the optical observations and the logical consequences of the results from the geometrical model with constraints from the X-ray observations. Optical observations indicate that the line widths of the Doppler shifted lines such as $H\alpha$ correspond to several thousands kilometers per second, implying an upper limit for the opening angle of the jet of ~ 0.1 rad ($\sim 6^\circ$) (Zwitter *et al.* 1989). With the constraint on jet parameters from the X-ray observations, the jet with the opening angle compatible to the optical one is possible only in the case of small mass ratio. If the mass ratio of SS 433 system is not larger enough, the accretion disc would be completely covered by the companion star during the primary optical eclipse, which, in turn, contradicts the optical evidence that the accretion disc is only partially obscured by the companion star.

It is believed that the stationary emission line HeII $\lambda 4686$ is formed close to the compact object and its Doppler shifts represent the orbital motion of the compact object (Zwitter *et al.* 1989). At around the optical primary minimum, the intensity of HeII $\lambda 4686$ is just marginally lower, which implies that the formation region of HeII line never undergoes total eclipse and this line is formed in an extended region rather than in a well localized hot spot, possible candidates including corona or extended part of the accretion disc. This may suggest error in mass function.

There are two possibilities that can make the constraints on the SS 433 geometrical parameters derived in the last section compatible to the optical ones. If, for some reason, the companion star does not fill its Roche lobe and its size is smaller than its Roche lobe model, it will then not completely cover the accretion disc in the case of the thin jet with small mass ratio. With the consideration of high accretion rate of SS 433, it is difficult to imagine that the companion star does not fully fill its Roche lobe. The results of Antokhina and Cherepashchuk also suggest that the companion star does fill with its Roche lobe. The second possibility is that the jet is indeed thin with an opening angle consistent with the optical upper limit when the mass ratio is large, but the X-ray eclipse starts and ends at the occultation of the X-ray emitting region by the material flowing from the companion star, i.e. the assumption that the X-ray eclipse is simply due to the companion star may not be adequate. A dense stellar wind can indeed make the companion star look bigger than its Roche lobe. The mass loss rate in the stellar wind of the normal star is thought to be $\sim 10^{-7} - 10^{-5} M_\odot \text{ yr}^{-1}$ from infra-red measurements (Barlow & Cohen 1977). The line of sight column of this wind at $2R_s$ is then $\sim 10^{24} \text{ cm}^{-2}$, sufficient to cause a significant reduction in the X-ray intensity. The

non-observation of any extra soft X-ray absorption at ingress and egress, however, requires that the wind be highly ionized. However, it should be noted that the low value of N_{H} seen outside eclipse also requires that wind be highly ionized.

Despite these contraries, scenarios on a thin jet in the small mass ratio region or a fat jet in the high mass ratio region, with the companion star filling its Roche lobe as the main source acting to cover the X-ray jets, are still possible. Although the interpretation of the origin of the HeII $\lambda 4686$ is widely accepted, it leaves some observational results unexplained (Zwitter *et al.* 1989). If the HeII $\lambda 4686$ line indeed originates in the region close to the compact object, it should exhibit stronger precessional variations than the other stationary lines which are formed in the regions far from the central engine. However, no 163 day profile variation has been detected so far for the HeII $\lambda 4686$ other than other stationary emission lines.

Three geometric models are developed in the section which follows in order that the jet physical properties can be determined in chapter 6. Due to the difficulty in mathematics and the lack of theoretical models, fat jets are not considered.

5.6 Geometrical Models of SS 433

The configuration shown in Fig. 5.3 is assumed for the accretion disc of SS 433. It should be emphasized here that this configuration does not represent the reality of the disc but is equivalent to what is seen during the observations. The purpose of adopting this geometry is to make it mathematically simple to discuss the jet physical conditions and to decode information of the system geometry from the spectra obtained during the period of the eclipse. This idea is also applied to the configuration of the companion star derived below.

When viewed along the jet axis as in Fig. 5.3(b), the accretion disc has radius R_{d} , which is approximately equal to the Roche lobe Y_{x} (see Appendix B for definition) of the compact object (assumption from the results of Antokhina & Cherepashchuk, 1987). The jets are ejected in a region with radius R_{f} centered at the accretion disc. When viewed edge-on as displayed in Fig. 5.3(a), the cross section of the disc from radius R_{f} to R_{d} is a trapezium. The minimum thickness of the disc is H_{f} , which is near the jets at radius R_{f} . The maximum disc thickness is H_{d} , which is at the edge of the disc. Angle β_0 is a constant and satisfies the

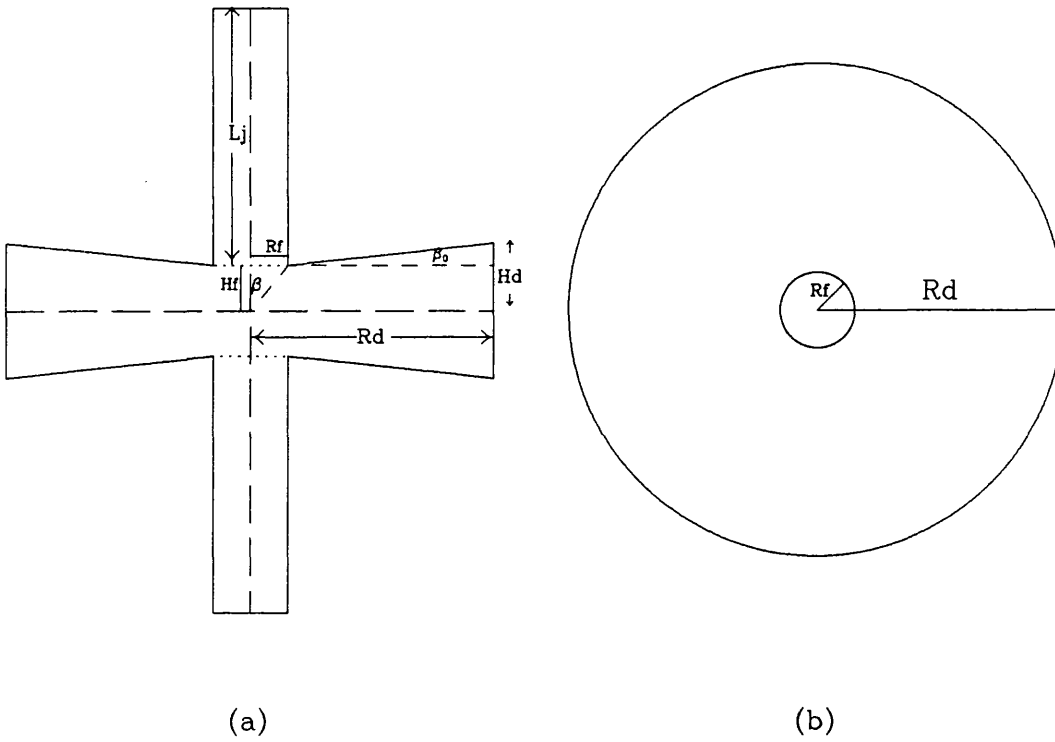


Figure 5.3: Configuration of the accretion disc of SS 433, (a) disc edge-on; (b) disc face-on

relationship of

$$\tan \beta_0 = \frac{H_d - H_f}{R_d - R_f} \quad (5.66)$$

angle β , the opening angle of the jets, satisfies

$$\tan \beta = \frac{R_f}{H_f} \quad (5.67)$$

Determination of H_d (or β_0) depends on whether the receding jet can be covered by the outermost disc when the jet axis is crossing the line of sight, and on the fact that the innermost part of the disc at the approaching jet side must not be obscured by the outer disc at the same time. In the case of high mass ratio when the receding jet is certainly occulted by the accretion disc, setting $\psi = 0$ and π , and using the mathematics in section 5.3, the following condition can be derived,

$$\begin{aligned}
L_j &\leq R_d \tan(\alpha - j) + H_d \\
\frac{H_d - H_f}{R_d - R_f} &\leq \tan(\alpha - j) \\
\text{or } \beta_0 &\leq (\alpha - j)
\end{aligned} \tag{5.68}$$

Three mass ratios, $q=0.11$, $q=0.4$ and 1.2 , are chosen to model SS 433 geometry. $q=0.11$ is for the case when the receding jet is definitely seen in the 1987 observation (see Fig. 5.1) and the compact object is a neutron star. The model with $q=1.2$ represents the case where the receding jet is definitely covered. The model with $q=0.4$ is selected to be intermediate between the above two extreme cases. Both $q=0.4$ and 1.2 suggest a black hole compact object. Choosing $q=0.4$ and 1.2 makes the results derived from the X-ray data easily comparable with those presented by Antokhina and Cherepashchuk (1987), and Leibowitz (1984) (e.g. $q=0.4, 1.2$ by Antokhina & Cherepashchuk; $q > 0.8$ by Leibowitz).

Three models for SS 433 are established in this section in terms of thin jet type models. For model of $q=0.11$, the size of the companion star is assumed to be equal to its Roche lobe and the eclipse happens because of the occultation by the edge of the stellar disc. For the thin jet models with $q=0.4, 1.2$, the eclipse of the X-ray jet by an oversized companion is considered. For simplicity, the star is equated to an ellipsoid with its minor axis along the orbital normal equal to its Roche lobe and its major axis on the orbital plane larger than its Roche lobe. The opening angle β for the thin jet models, however, is fixed at $\beta = 2^\circ$.

The following methods are used for calculating a self-consistent model:

- 1 For a given q , with the formula in Appendix B, the Roche lobe of the companion star and compact object can be determined; the jet minimum length L_j^{\min} can be calculated from equation (5.41).
- 2 With the assumption that the eclipse starts and ends both at the approaching jet and by setting the coordinates of the intersection between the stellar disc and the jet sides equal to those between the accretion disc inner part (or funnel) and the jet sides, R_f and H_f can be calculated if $q=0.11$ is assumed, or in the case of high mass ratio, a_s (the major semi-axis of the equivalent ellipse of the companion star and the accreting flow), R_f and H_f can be determined.

- 3 R_f and H_f should be tested to see if they are inside the Roche lobe of the compact object and if H_f is smaller than L_j^{\min} to assure the eclipse does happen.
- 4 With equation (5.43), the jet length L_j can be calculated.
- 5 For models with high mass ratio, H_d and β_0 can be determined within condition (5.68), and adjusted using the implications of the *GINGA* 1988 & 1989 results that in the phase of 1988 May, the disc cannot completely cover L_j^{\min} (otherwise no eclipse is observed in 1988 May) and the disc can almost obscure L_j^{\min} in 1989 May observations (because a shallow eclipse was observed.)

Self-consistent solutions for each of the three models are tabulated in table 5.1. The configurations of these models at the phases when the *GINGA* observations were made are illustrated in Appendix D.

5.7 Summary

Mathematics for the general description of the system geometry of SS 433 has been established in this chapter. With the constraints from the X-ray observations, it is concluded that the mass ratio of SS 433 will not be higher than 9.0. This conclusion is independent of the configurations of the jets and accretion disc. It is likely that the system mass ratio is in the range of $0.0 \sim 1.71$. When assuming that the size of the companion star is less than or equal to its Roche lobe, the jets can be no longer regarded as thin if the compact object is a black hole. Effects of the accretion flow and the stellar wind, which may make the companion star look bigger than its Roche lobe, have to be considered during modelling the X-ray eclipse if the jet configuration is assumed to be consistent with that from optical observations. Three thin jet type models which represent three different cases in Fig. 5.1, are suggested for the discussions in Chapter 6.

Table 5.1: Geometrical Models of SS 433

Model Type	Mass (M_{\odot})		Binary a ($\times 10^{12}$ cm)	Roche Lobe				Stellar Disc		Accretion Disc			Jet			
	M_x	M_s		Y_x	Z_x	Y_s	Z_s	a_s	b_s	R_d	H_d	H_f	R_f	L_j^{\min}	L_j	β
A: $q=0.11$	1.44	13.06	3.93	0.203	0.195	0.587	0.528	0.587	0.528	0.203	0.150	0.073	0.003	0.386	0.700	2°
B: $q=0.40$	8.31	20.78	4.95	0.295	0.283	0.462	0.433	0.701	0.433	0.295	0.240	0.129	0.005	0.276	0.423	2°
C: $q=1.20$	61.56	51.30	7.78	0.391	0.371	0.357	0.341	0.797	0.341	0.391	0.150	0.101	0.04	0.170	0.341	2°

Chapter 6

Physical Properties of the X-ray Jets in SS 433

6.1 Introduction

In Chapter 5 the discussions of the geometrical parameters of SS 433 were to some extent inconclusive due to insufficient information on whether or not the receding jet is visible in the observations made at around precession phase 0.6, the lack of the simultaneous optical observations and lack of knowledge of the structure of the companion star and accretion disc. Only the first and fourth contact times and the duration of the X-ray eclipse were used for modelling the geometrical parameters of SS 433. However, information on the geometry is almost certainly coupled in the profiles of variation of the intensity and spectra of SS 433 over the eclipse. The physical properties of the jets thus become crucial to help tighten up the parameter ranges of the system geometry and distinguish which geometrical model suggested in Chapter 5 is more consistent with the *GINGA* observations made in 1988 and 1989, and with results from the observations in other electromagnetic wave bands.

Discussions of the physical conditions of the SS 433 jets with the constraints derived from the X-ray observations are also very important for solving the problems of the origin, acceleration and evolution of the jets (and the jets associated with other astrophysical objects through their similarities). Although various theories, as introduced in Chapter 1, have been suggested for this problem, none of them can fully explain the observations of SS 433. The X-ray

observations with *EXOSAT* and *GINGA* strongly indicate that the X-ray radiation is from the very base of the SS 433 jets. Thus, modelling this part of the jets will provide a key, or at least a strong hint, for the solution of the problem of the jet's formation and evolution in the SS 433 system.

In this chapter, the jet is studied as a continuous fluid, having velocity \vec{v} , temperature T and density ρ defined at each point along the jet axis. The jet flow can be assumed to be stable in any local region along the jet axis and the temperature gradient in this region is regarded as very small so that thermal conduction can be ignored (the treatment of thermal conduction would require a detailed knowledge of the structure of any magnetic field). Under this assumption, the temperature and electron density, as functions of the jet coordinates, are derived in Section 6.2.1 using the laws of conservation of mass, momentum and energy. The integral constants in these functions are determined in Section 6.3 for each chosen jet region along the axis of the jet with the technique described in Section 6.2.2. Thus, a model independent temperature profile is derived for each suggested geometrical model. In Section 6.3.2, the model spectra and light curves corresponding to the phases of the *GINGA* observations are created by using the temperature and electron density profiles, and are compared with the observations. Further constraints on the geometrical models of SS 433 are derived in Section 6.4 by discussing the compatibility of the model calculations with the observations. In this section, the physical properties of the SS 433 jets are also discussed and the constraints on the jet formation mechanisms are suggested. A summary to the results derived in this chapter is given in Section 6.5.

6.2 Theory and Technique Details

6.2.1 Theory

A steady, one dimension flow with no thermal conduction is assumed for any small region of the jets in SS 433. By setting time derivatives equal to zero, the three conservation laws of mass, momentum and energy given in Appendix C (see Appendix C for the definitions of the symbols used here) then become

$$\nabla \cdot (\rho \vec{v}) = 0 \quad (6.1)$$

$$\rho \vec{v} \cdot \nabla \vec{v} = -\nabla P + \vec{f} \quad (6.2)$$

$$\nabla \cdot \left[\left(\frac{1}{2} \rho v^2 + \rho \varepsilon + P \right) \vec{v} \right] = \vec{f} \cdot \vec{v} - \nabla \cdot \vec{F}_{rad} \quad (6.3)$$

Substituting the first of these equations in the third implies

$$\rho \vec{v} \cdot \nabla \left(\frac{1}{2} v^2 + \varepsilon + P/\rho \right) = \vec{f} \cdot \vec{v} - \nabla \cdot \vec{F}_{rad} \quad (6.4)$$

while the Euler equation shows that

$$\vec{f} \cdot \vec{v} = \rho \vec{v} \cdot \nabla \left(\frac{1}{2} v^2 \right) + \vec{v} \cdot \nabla P \quad (6.5)$$

hence eliminating $\vec{f} \cdot \vec{v}$ from Equation (6.4) and considering Equation (C.9) give

$$\rho \vec{v} \cdot [\nabla \varepsilon + P \nabla (1/\rho)] = -C_1 T^{1/2} n_e^2 \quad (6.6)$$

Using the circular cylindrical coordinates (R, φ, z) , where z -axis is coincident with the jet ejection direction, and assuming that the variables v , T , ρ , only change along the z -direction, Equation (6.6) becomes

$$\rho v \frac{d\varepsilon}{dz} - \frac{Pv}{\rho} \frac{d\rho}{dz} = -C_1 T^{1/2} n_e^2 \quad (6.7)$$

Since the internal energy ε is given by Equation (C.5) and the relation of pressure P and ρ , T is expressed by the perfect gas law (C.2), Equation (6.7) may be written:

$$\frac{3}{2} \frac{k\rho v}{\mu m_H} \frac{dT}{dz} - \frac{kTv}{\mu m_H} \frac{d\rho}{dz} = -C_1 T^{1/2} n_e^2 \quad (6.8)$$

From Equation (6.1), the z derivative of ρ is

$$\frac{d\rho}{dz} = -\frac{\rho}{v} \frac{dv}{dz} \quad (6.9)$$

Assuming that the jet velocity, which equals to 0.26c, keeps constant along the z-direction, gives

$$\begin{aligned} \frac{d\rho}{dz} &= 0 \\ \rho &= \rho_0 = \text{constant} \end{aligned} \quad (6.10)$$

therefore, Equation (6.8) reduces to

$$\frac{3}{2} \frac{k\rho v}{\mu m_H} \frac{dT}{dz} = -C_1 T^{1/2} n_e^2 \quad (6.11)$$

For a fully ionized gas, the density may be approximated by

$$\rho \simeq m_H n_e \quad (6.12)$$

and Equation (6.11) becomes

$$\frac{3vk}{2\mu} \frac{dT}{dz} = -C_1 T^{1/2} n_e \quad (6.13)$$

This gives the temperature distribution along the jet

$$T^{1/2} = -\frac{\mu C_1 n_e}{3vk} z + C_0 \quad (6.14)$$

where C_0 is an integral constant and will be determined later from the observed spectra.

Integrating the emissivity given in Equation (C.8) over the jet volume, the photon spectrum of SS 433 is obtained,

$$\begin{aligned}
F(E, T) &= \frac{1}{4\pi d^2} \int 4.2 \times 10^{-15} E^{-1} T^{-1/2} n_e^2 e^{-E/T} \bar{g}_{ff} dV \\
&= \frac{4.2 \times 10^{-15} \pi R_j^2}{4\pi d^2} \int_{z_1}^{z_2} E^{-1} T^{-1/2} n_e^2 e^{-E/T} \bar{g}_{ff} dZ \\
&= 4.4 \times 10^{-60} R_j^2 \int_{z_1}^{z_2} E^{-1} T^{-1/2} n_e^2 e^{-E/T} \bar{g}_{ff} dZ \quad (\text{photons } s^{-1} \text{ cm}^{-2} \text{ keV}^{-1})
\end{aligned} \tag{6.15}$$

where $d \simeq 5 \text{ kpc} = 1.54 \times 10^{22} \text{ cm}$ is the distance of SS 433. By fitting the observed X-ray spectra with Equation (6.15), n_e & C_0 can be determined.

6.2.2 Technique Details

In this chapter, the jet properties are discussed within the frameworks of the three geometrical models listed in table 5.1. The X-ray spectra of SS 433 obtained over the period between the first contact time and the optical primary minimum in the 1987 May observations are adopted to derive the parameters n_e and C_0 in the jet region where Equation (6.14) is valid.

As shown in the previous chapters, the X-ray spectrum of SS 433 consists of two components, a thermal continuum which can be well approximated with a thermal bremsstrahlung, and a broadened Doppler shifted iron line. Both components originate in the same region — the jets. To simplify the problem, the X-ray continuum and emission line feature are considered independently, and their relationship is not modelled. In the following, the continuum spectrum of SS 433 is represented by the summary of (6.15) integrated over each small jet region and the emission line is approximated by a Gaussian profile.

Corresponding to the time at which each spectrum is obtained over the period of the eclipse, the length of the projected shadow of the companion star on the jet axis can be calculated for each given geometrical model. Thus, the jet is divided into several small regions (jet bins) along the jet axis according to the projected lengths calculated. The parameters n_e and C_0 in any small region are determined from fitting the X-ray spectrum generated in this region with (6.15) as the continuum. Constant C_1 in Equation (6.14) is small, meaning that for sufficiently small jet bins the temperature within each jet bin can be considered as constant.

To determine the contribution of the X-ray radiations for each small jet region, the following strategy is used. Suppose N number spectra are available over the period from the start of the X-ray eclipse to the minimum state of the flux. If these spectra are labeled 1, 2, ..., N in

the order of observational time, the jet regions should be numbered from the base to the top of the jet. For spectrum i , it must be the resultant of the X-ray emission from jet regions i , $i+1$, ..., N . Therefore, the X-ray emission produced in jet region i alone can be obtained by subtracting spectrum $i+1$ from spectrum i .

The determination of n_e and C_0 depends on the shape of the X-ray continuum which may be affected by the X-ray emission line during the spectral model fitting. To reduce this effect and to make it easy for the comparison of the results derived within different geometrical models, the ‘observed’ continuum in jet region i is kept unchanged for different geometrical models. This can be achieved by using the same parameters to specify the line features in the SS 433 spectrum. The line parameters used are derived from fitting the spectrum with a single bremsstrahlung as the continuum plus a neutral hydrogen absorption with column density fixed at $8 \times 10^{21} \text{ cm}^{-2}$, which is consistent with the results of most X-ray observations presented in this thesis.

The Doppler boosting factor is also included in the model fitting. Whenever the receding jet is possibly visible, the contributions from both jets are combined using Equation (5.36).

6.3 Results

6.3.1 Parameter Distribution along the X-ray Jets of SS 433

1) Model A

In this model, the receding jet should be visible during the observations and the observed X-ray emission includes the contributions from both jets. When the spectra are fitted with the method described above to determine n_e and C_0 , Equation (5.36) should be employed. However, including the radiation from the receding jet introduces excessive soft X-ray flux for the model spectrum and this effect makes the spectral fit not acceptable. Thus the parameter n_e and C_0 can not be well constrained in Model A. Fig. 6.1(a) shows the temperature and electron density distributions in which the temperature is so high that the line production may not be possible.

The case in which only approaching jet can contribute to the X-ray emission is also considered

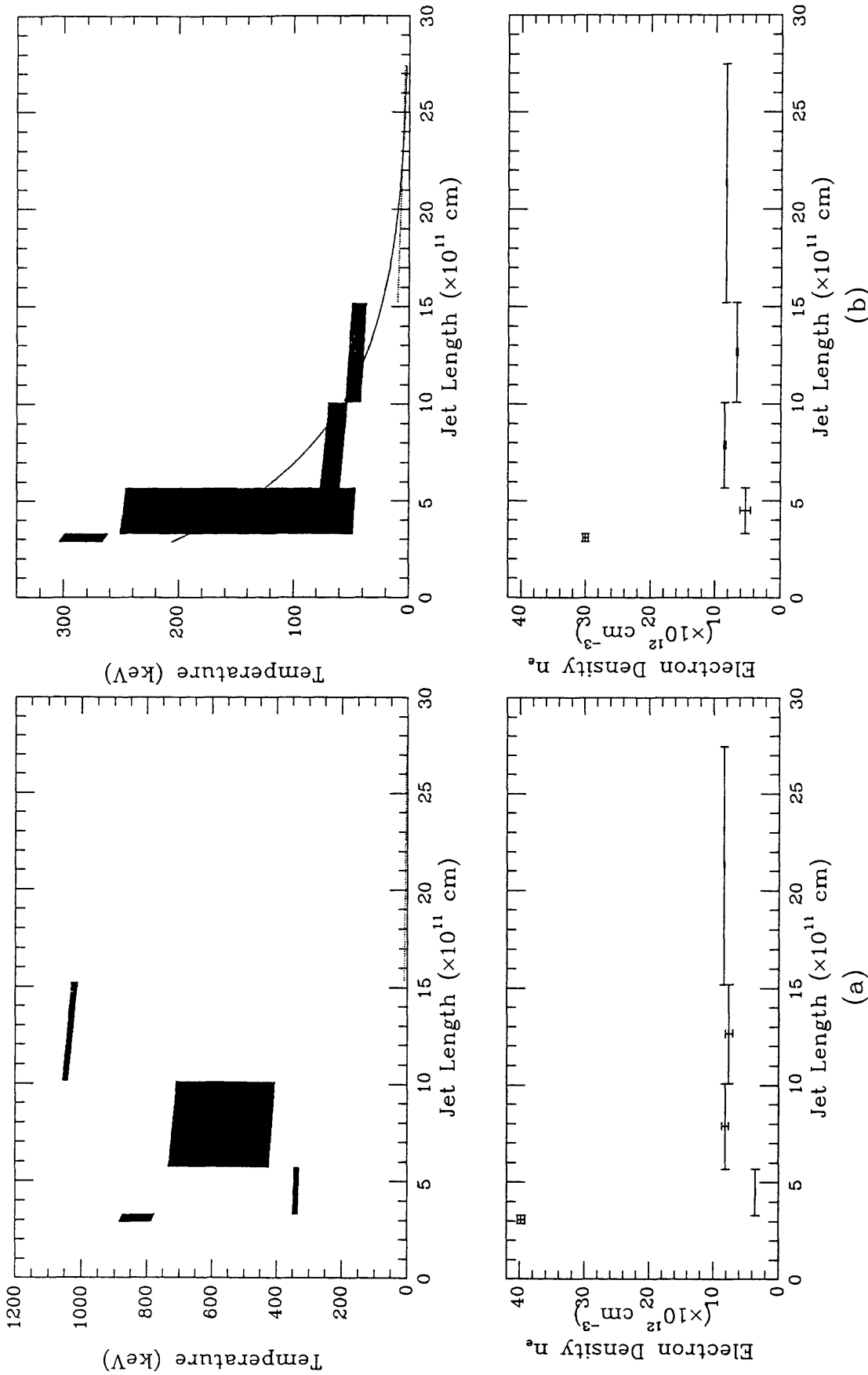


Figure 6.1: Temperature & electron density distributions along the jet axis (Model A, $q=0.11$). (a) X-ray emissions from both jets are considered; (b) only X-ray emissions from the approaching jet are considered.

here. While this is not physically realistic for symmetric jets it might apply if for some reason the jets are asymmetric. The chi square in the spectral model fit is much improved in this case but not as good as the following two models, B and C. The results are presented in Fig. 6.1(b) which shows the temperature roughly exponentially decreases along the jet axis.

The electron density in Model A ranges from $3.5 \sim 40 \times 10^{12} \text{ cm}^{-3}$, implying the mass loss rate along the two jets is

$$\begin{aligned} \dot{M} &= 2\pi R_f^2 m_H n_e v \\ &= 4.5 \times 10^{-7} \sim 5.2 \times 10^{-6} M_\odot/\text{yr} \end{aligned} \quad (6.16)$$

2) Model B

Model B represents the case in which the receding jet is possibly visible during the 1987 observations depending on the disc geometry. The geometrical parameters used here are such that the receding jet is visible before the start of the eclipse but it is not long enough to make any significant contribution to the observed X-rays. Besides, once the eclipse starts, the receding jet is quickly covered by the companion star. So, when the spectra are fitted to map the temperature and density distributions, the effect of the receding jet is ignored. In Model B, the Equation (6.15) can give an acceptable fit to every spectrum and parameters n_e and C_0 are very well determined.

The temperature and density profiles are plotted in Fig. 6.2. The errors cited in the figure corresponds to the 90 per cent level in the local spectral fit and have not included the contributions from other spectra. The temperature and electron density distributions can both be approximated by exponential functions. The temperature can be expressed as

$$T = 1400e^{-z/3.5 \times 10^{11}} \text{ (keV)} \quad (6.17)$$

and density

$$n_e = 15 \times 10^{12} e^{-z/9 \times 10^{11}} \text{ (cm}^{-3}\text{)} \quad (6.18)$$

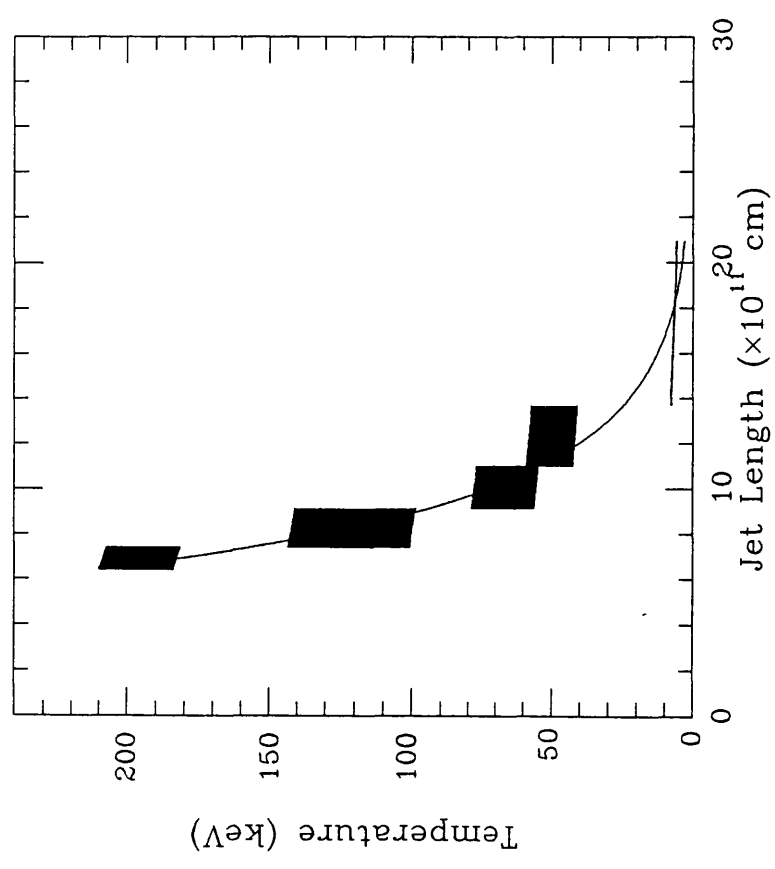
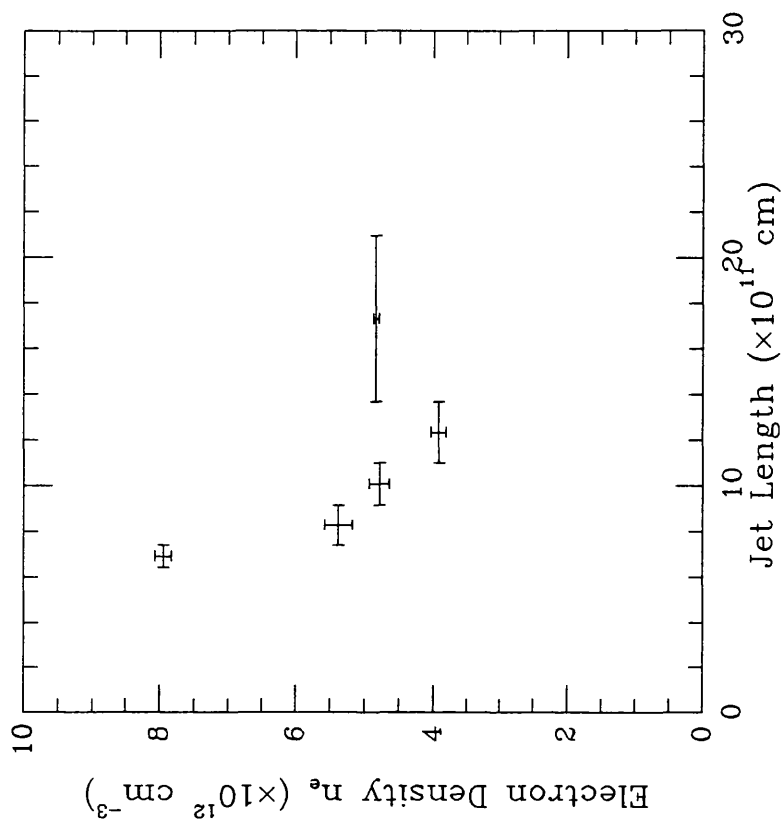


Figure 6.2: Temperature & electron density profiles for Model B ($q=0.4$), both temperature and electron density obey exponential distributions.

where z is in centimeters.

The mass loss rate is

$$\begin{aligned}\dot{M} &= 2\pi R_j^2 m_H n_e v \\ &= (2 \sim 4) \times 10^{-6} M_\odot / yr\end{aligned}\tag{6.19}$$

3) Model C

The receding jet is definitely covered by the accretion disc in Model C. The spectrum is well fitted by Equation (6.15) and no contribution from the receding jet is considered.

The temperature and density distributions along the jet axis are shown in Fig. 6.3. Similar to the results of Model B, the errors quoted in Fig. 6.3 only include those from local spectral fit. The profiles of the temperature and density in Model C can be also well fitted by exponential functions, i.e.,

the temperature:

$$T = 2000e^{-z/3.2 \times 10^{11}} \text{ (keV)}\tag{6.20}$$

and the electron density

$$n_e = 35 \times 10^{12} e^{-z/5.1 \times 10^{11}} \text{ (cm}^{-3}\text{)}\tag{6.21}$$

where z is in centimeters.

The mass loss rate along the jet axis in Model C is

$$\begin{aligned}\dot{M} &= 2\pi R_j^2 m_H n_e v \\ &= (2.6 \sim 6.3) \times 10^{-6} M_\odot / yr\end{aligned}\tag{6.22}$$

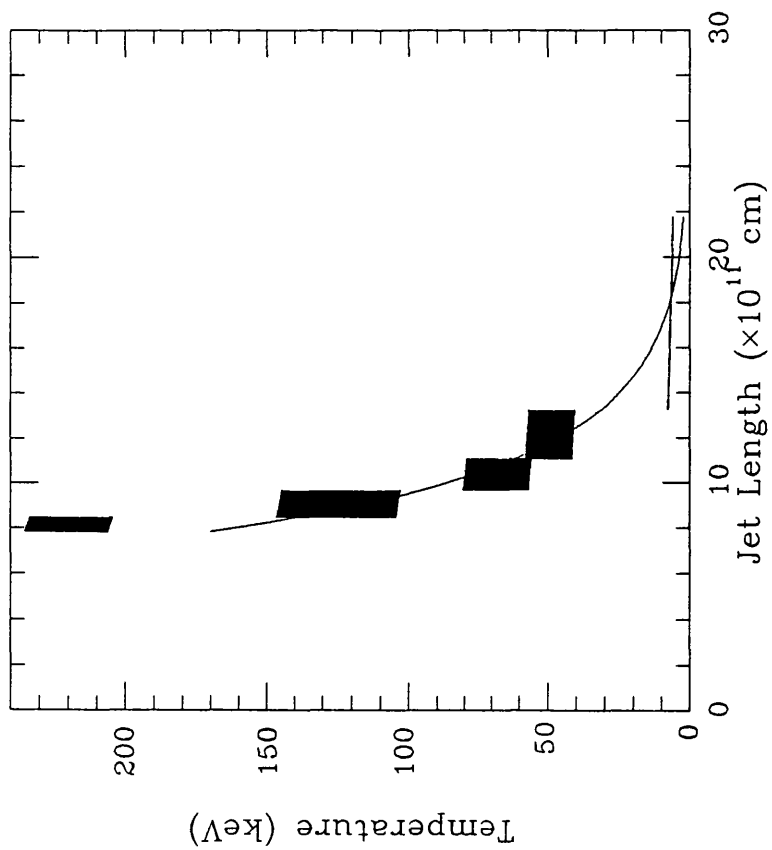
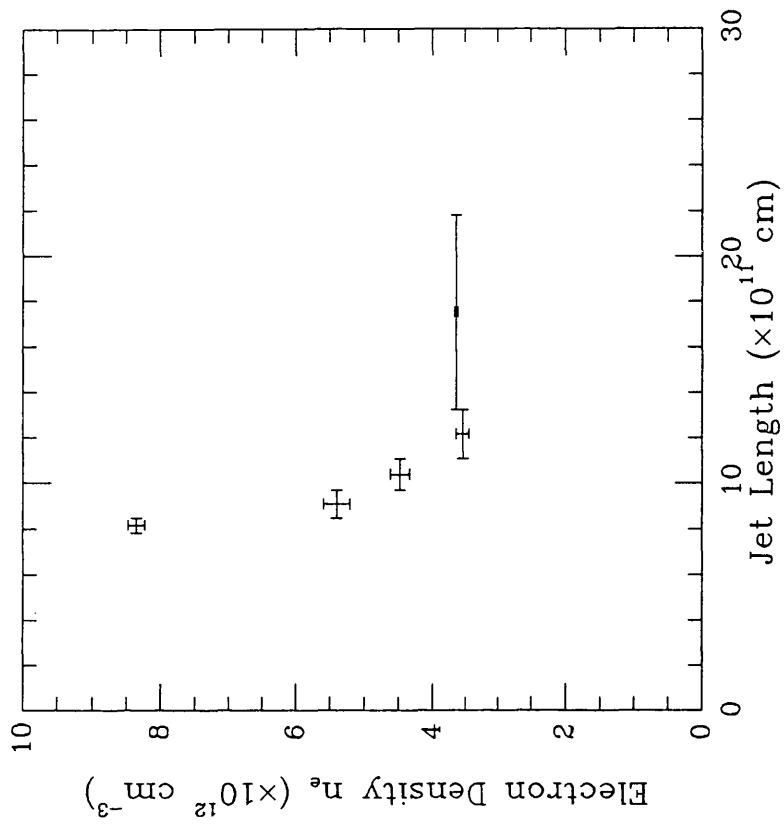


Figure 6.3: Temperature & electron density profiles, (Model C, $q=1.2$). These profiles can be fitted by an exponential function.

6.3.2 Comparisons with the Observations

1) the X-ray Spectrum

Several model spectra, corresponding to phases outside and inside the eclipses of the *GINGA* 1988 & 1989 observations, are created and displayed in Fig. 6.4 for Model A, in Fig. 6.5 for Model B and Fig. 6.6 for Model C. The solid lines represent the model spectra, the dashed lines are the model spectra normalized to the data points.

The temperature and electron density distributions along the jet axis of SS 433, as shown in Fig. 6.1(b), Fig. 6.2 and Fig. 6.3 were adopted to establish the model spectra. The system geometries presented in Chapter 5 are also used here and the Doppler boosting effects are included. The disc thickness H_d in each geometrical model is adjusted by making the predicted model spectrum close to the spectrum obtained inside the 1988 eclipse.

None of the model spectra can fit the observations. In general, the spectra inside the 1988 & 1989 eclipses are under-predicted while the spectra outside the eclipses are over-predicted by the models. Model B can give the closest fits to most observed spectra than other two models. Model C is better than Model A. Details about the percentages in which the model spectra should be increased or decreased to be normalized to the observations are listed in the captions of Fig. 6.4-6.6.

Although adjusting the disc thickness H_d can make each model spectrum close to the observation, no self-consistent solutions can be found for any of the three models.

2) the X-ray Light Curves

The model light curves are generated with the similar methods used for producing the model spectra, and are compared with the *GINGA* observations in 1987, 1988 and 1989. Fig. 6.7-6.9 corresponds to the results of Model A-C respectively. The solid lines in these figures are the model light curves.

The profiles of the temperature and electron density are derived from fitting the observed X-ray spectra over the 1987 eclipse. It is then not surprising that the generated light curves of Model A-C can reasonably well fit the data of 1987 observations except for part of the second intensity decrease, which may be due to the intrinsic variations of the X-ray sources.

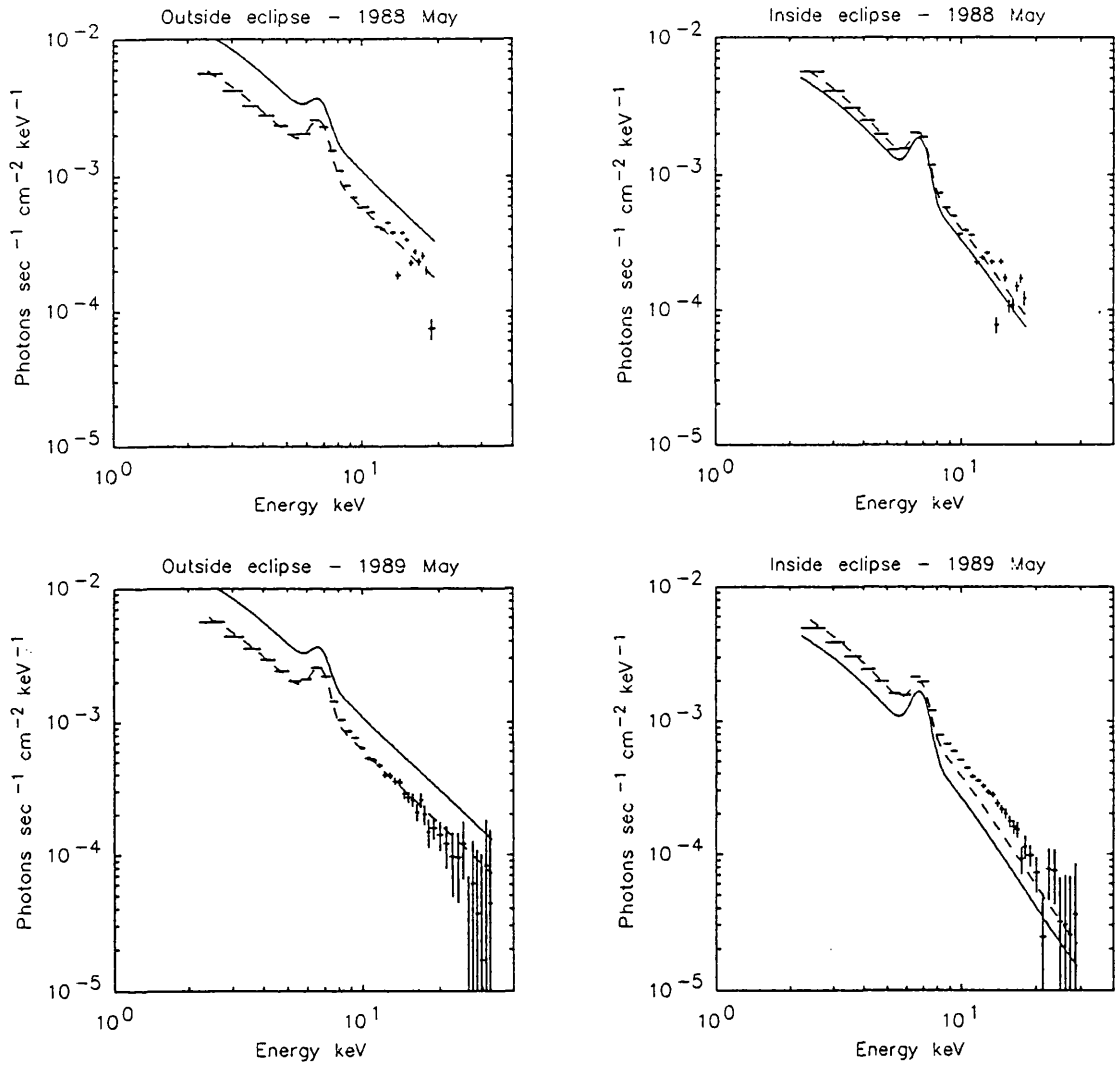


Figure 6.4: Comparisons of model spectra (solid line) with the observations (Model A, $q=0.11$). Spectra are under-predicted in the phase of inside eclipse with percentage of 21% (1988 May) and 44% (1989 May), and over-predicted in the period of outside eclipse of 47% (1988 May) and 44% (1989 May).

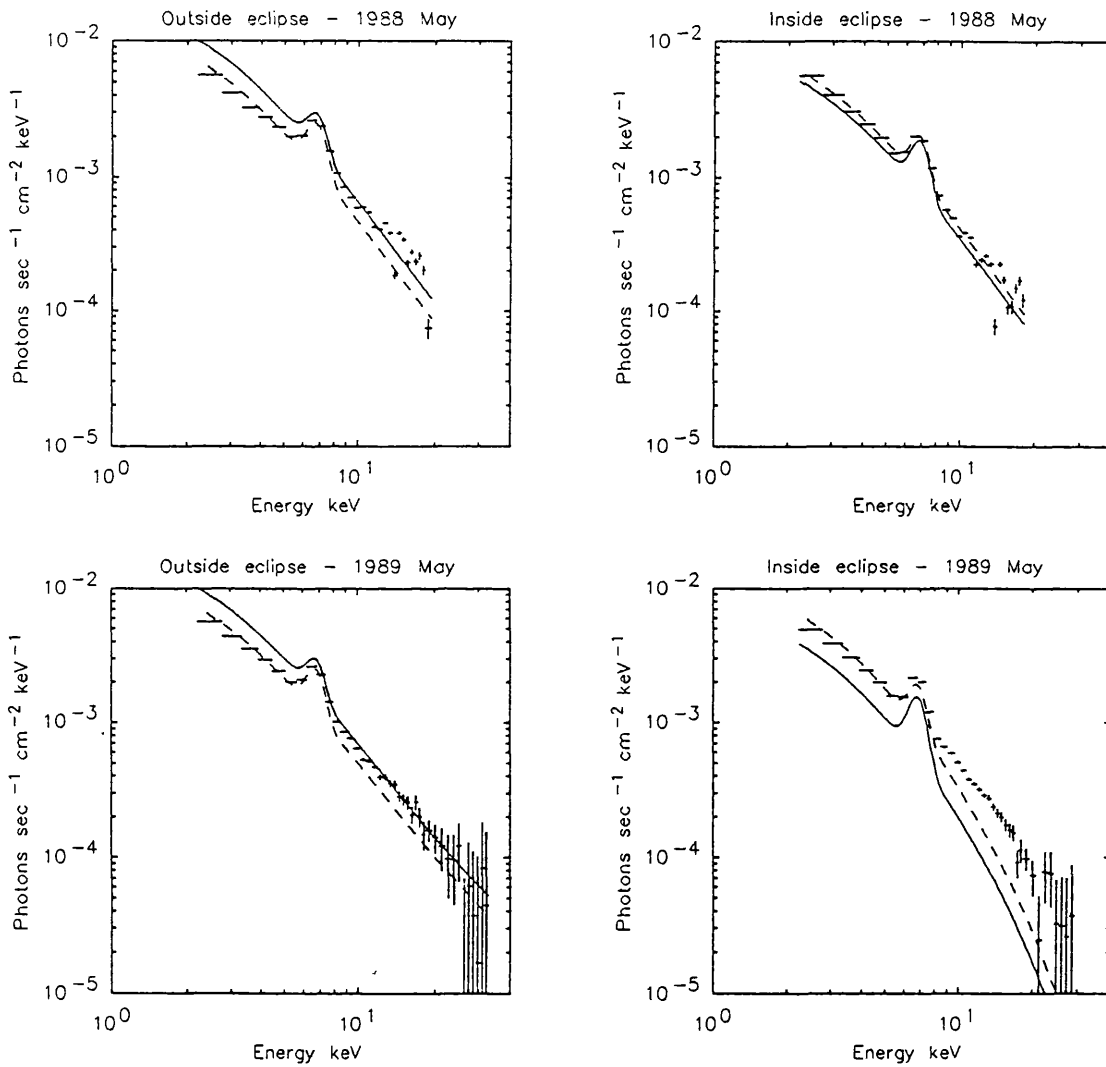


Figure 6.5: Comparisons of predicted spectra (solid line) from Model B ($q=0.4$) with the observations. The spectra inside eclipse are under-predicted of 19% (1988 May) and 66% (1989 May). For those outside eclipse of 1988 and 1989, they are over-predicted of 29%.

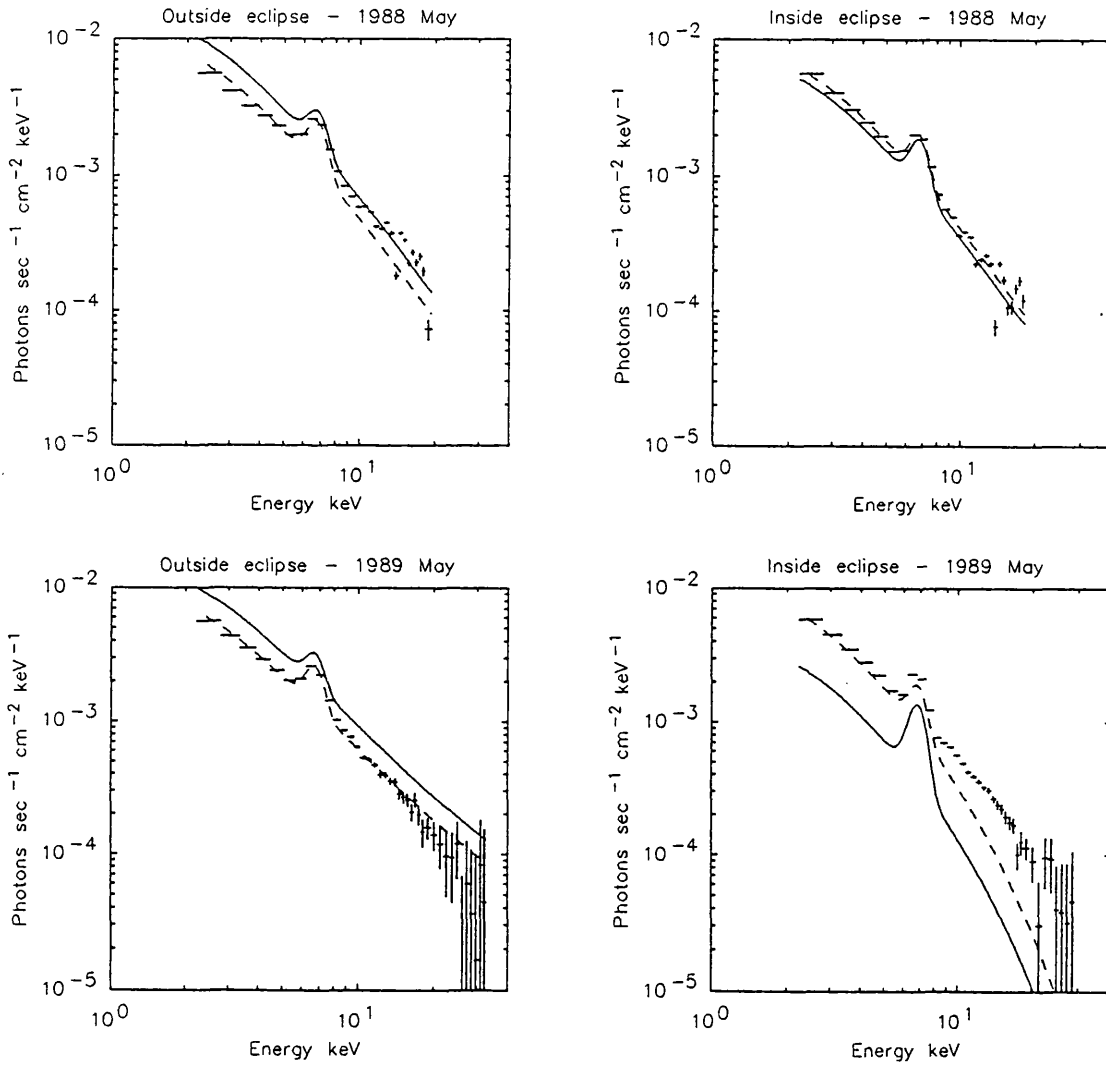


Figure 6.6: Comparisons of model spectra (solid line) with the observations (Model C, $q=1.2$). The spectra are under-predicted of 19% and 147% in the inside eclipse periods of 1988 May and 1989 May observations, and over-predicted of 30% (1988 May) and 33% (1989 May) in the phase of outside eclipse.

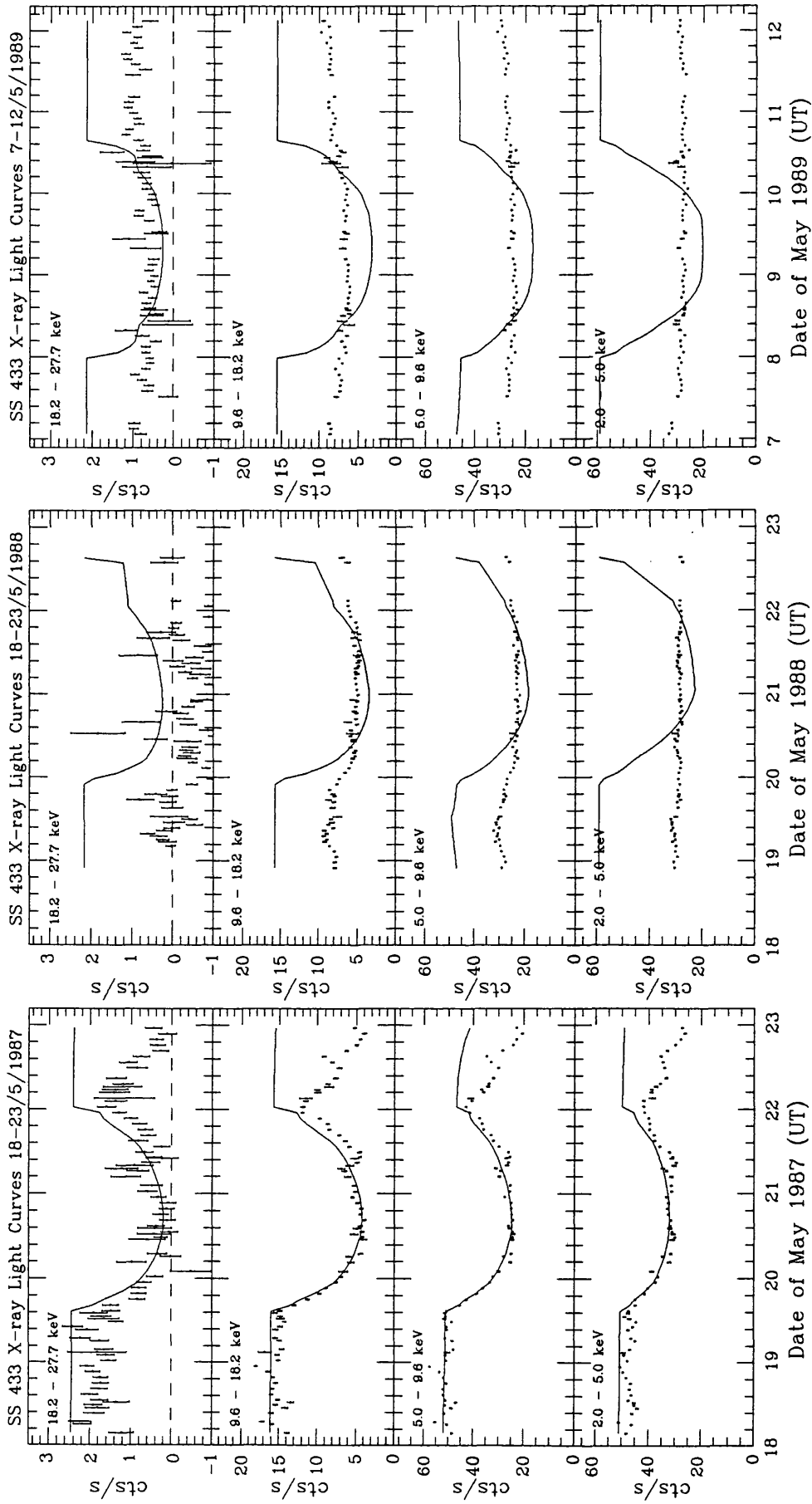


Figure 6.7: Model A ($q=0.11$). Comparisons of model light curves (solid lines) with the observations. Similar eclipse shape is produced for the light curves at different precession phases

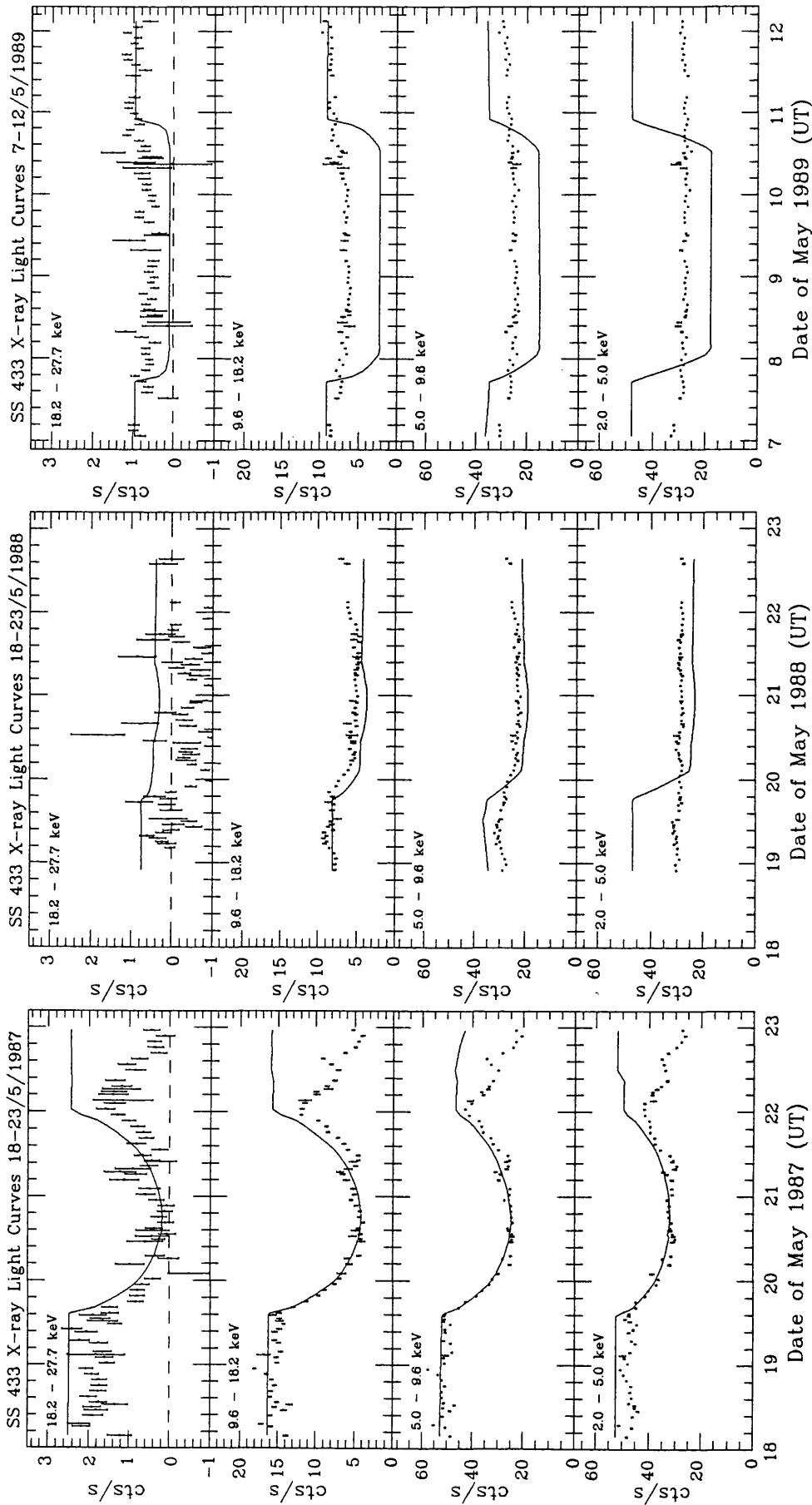


Figure 6.8: Model B ($q=0.4$). Comparisons of model light curves (solid lines) with the observations. The eclipse shape of the model light curves is variable, which is consistent with the observations.

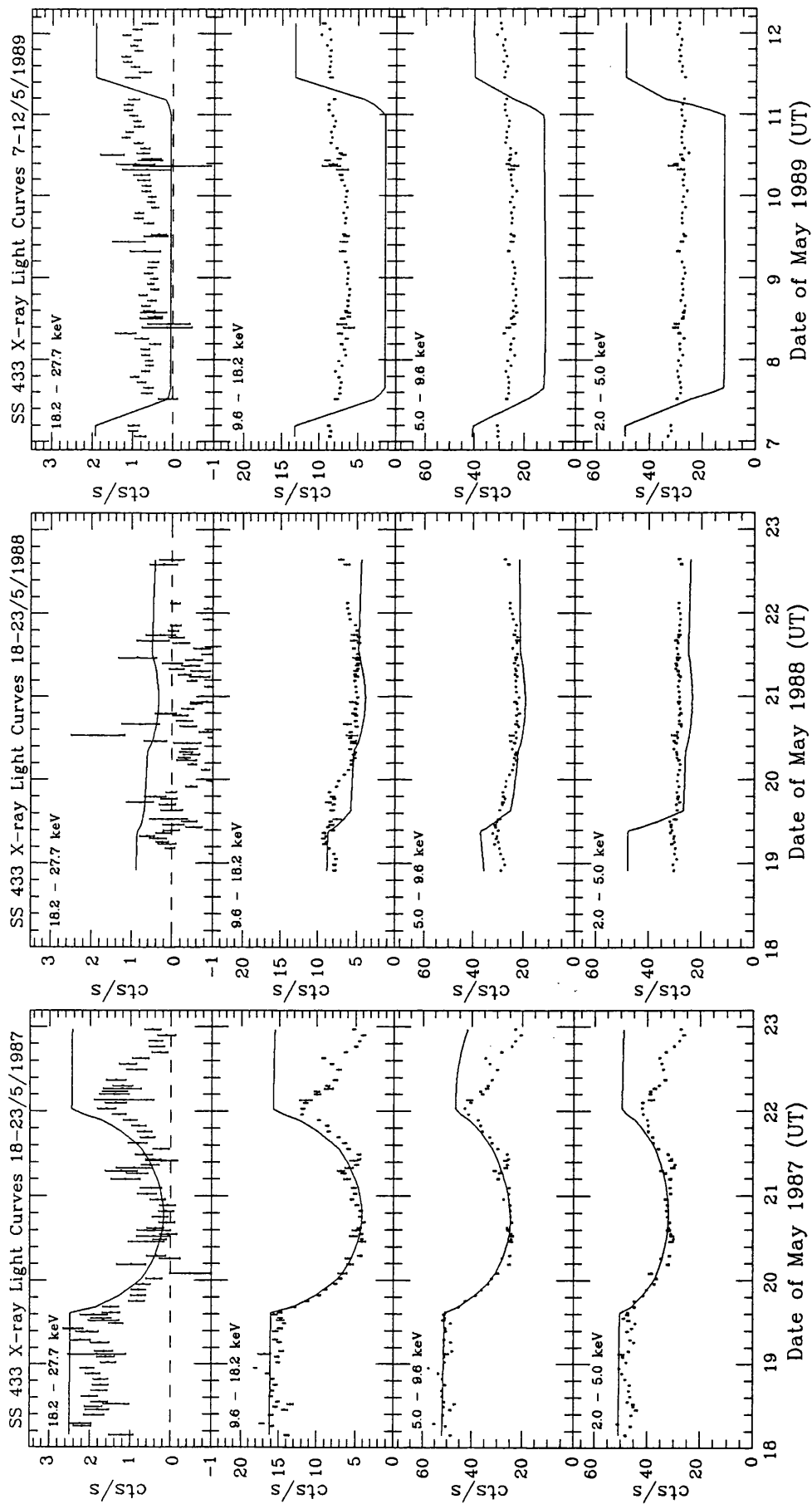


Figure 6.9: Model C ($q=1.2$). Comparisons of model light curves (solid lines) with the observations. The eclipse shape of the model light curves is set to be variable through adjusting the thickness of the accretion disc.

None of the models fit the observations in 1988 & 1989. For Model A, which has a big companion star and a small accretion disc, the model light curves have very similar shapes over the periods corresponding to the observed eclipses. It is almost impossible for Model A to generate light curves with highly variable eclipse shapes, as indicated by the results of three *GINGA* observed eclipses, via adjusting the thickness of the accretion disc.

In contrast, Model B and C have a small companion star and a big accretion disc. Although model light curves shown here do not fit the *GINGA* observations in 1988 & 1989 either, it is possible to make the generated model light curves more closely resemble the observations by carefully adjusting the disc and stellar extension geometry used. With a large accretion disc, it is clearly possible for Model B and C to have variable eclipse shapes by allowing the occultation of the X-ray source by the accretion disc. It is not attempted to derive a unique solution in this work because of the lack of theoretical models for the exact disc, stellar wind and accurate flow geometry.

6.4 Discussion

6.4.1 Geometrical Models of SS 433 — Further Discussion

The uncertainty on whether or not the receding jet was visible in the period of the *GINGA* 1987 observations has led to three possible regions for the mass ratio of the SS 433 system. As discussed in Chapter 5, a mass ratio $q < 0.174$ is the region when the receding jet should have been visible in the 1987 *GINGA* observations; while in the region of $0.174 < q < 0.566$, whether the receding jet was covered by the disc or not depends on the geometry of the accretion disc; when $q > 0.566$, the receding jet is definitely obscured by the accretion disc in the 1987 observations. Model A, B & C discussed in this chapter, represent the system geometries representative of these three possible mass regions.

The calculations in section 6.3 have shown that there are several problems with Model A. In this model, the contribution of the receding jet to the observed X-ray flux should be considered. However, the excessive soft X-ray radiations from the receding jet seriously distort the shape of the model spectrum and make it hard for the model to well fit the observations. On the other hand, the temperature derived for this model is so high that the

line production become very difficult. Model A also fails to produce a variable eclipse shape at different jet precession phase. Instead, as shown in Fig. 6.7, it gives very similar patterns for every eclipse. Therefore, Model A in which the compact object of the SS 433 system is of neutron star mass is not suitable to interpret the observations.

Model B and C give rather similar results. Although neither of them can provide acceptable fits to the X-ray light curves and spectra from the *GINGA* observations, it is possible for the Model with the mass ratio located in the region bracketed by Model B & C to self-consistently interpret the X-ray observations by carefully choosing a set of suitable geometrical parameters. The effect of the accretion flow has been naively considered in Model B and C by simply extending the semi-major axis of the ellipse disc of the companion star. Detailed modelling on the accretion flow or stellar wind is necessary to fully define the feature of SS 433. However, the characteristics of the accretion flow are largely unknown, and it is impossible at this stage to set up a detailed model for the accretion flow and the structure of the ionized stellar wind.

Due to the difficulty in mathematics and its unknown properties in the x, y directions, the fat jet model has not been considered in this chapter. This does not affect the discussion of the SS 433 component masses because the fat jet case is in any case only appropriate for high mass ratios.

6.4.2 Physical Properties of the SS 433 Jets

Temperature and electron density profiles have been derived for the models among three typical mass ratio regions. Comparing Fig. 6.1(b), Fig. 6.2 and Fig. 6.3, it is easy to see that the temperature profiles for the three models with rather different mass ratio are surprisingly similar. This similarity indicates that the determination of the temperature as a function of the jet coordinate is not sensitive to what geometrical parameters are adopted. Indeed, when parameters n_e & C_0 are derived from fitting the eclipse spectra, varying the geometrical size of the local jet bin does not change the value of C_0 , but slightly alters n_e and largely decreases (if the local jet bin becomes big) or increases (when the local jet bin is small) the normalization factor.

The relationship between the X-ray emission line and continuum has not been taken into

account during the calculations of jet temperature and density. This approximation may be justifiable because in each local jet region, the radiative loss due to the line production is much smaller than that of the bremsstrahlung. On the other hand, the drop of temperature caused by other cooling effects such as adiabatic expansion and Comptonization may be much larger than that by bremsstrahlung cooling (see the discussion below).

The basic simplifying assumption made in this chapter in the study of the jet plasma is that the particle distribution is thermal, i.e., the particles have a Maxwell-Boltzmann velocity distribution characterized by one single parameter alone, the temperature. The moving particles in the jet are assumed to instantaneously join the thermal distribution. This may not be the case in the actual situation, although the high derived densities suggest a relatively short equilibration time.

Combining the above arguments, it can be concluded that the temperature profiles shown in Fig. 6.2-6.3 do well describe the real situation along the jets of SS 433 and the electron density profiles in these figures also approximately represent the reality.

As in Fig. 6.2-6.3, the temperature of the jet plasma is in the range of 6-200 keV. With these values, the jet sound speed can be calculated as

$$\begin{aligned} C_s^{ad} &= \left(\frac{5P}{\rho}\right)^{1/2} = \left(\frac{5KT}{3\mu m_H}\right)^{1/2} \\ &\simeq (1 \sim 8) \times 10^8 \text{ cm/s} \end{aligned} \quad (6.23)$$

Comparing this speed with the bulk velocity of jet $V = 7.8 \times 10^9 \text{ cm/s}$ indicates that the X-ray jet of SS 433 is a highly supersonic plasma flow.

The jet plasma becomes rapidly cools along the jet axis. Assuming that at the base of the X-ray jet, the highest temperature is $\sim 200 \text{ keV}$ and the electron density $\sim 8 \times 10^{12} \text{ cm}^{-3}$, the bremsstrahlung cooling time is (see Tucker P207)

$$\begin{aligned} t_{ff} &= 3n_eKT/j(T) \\ &= 6 \times 10^{14}T^{1/2}/n_e \\ &\simeq 1000 \text{ sec} \end{aligned} \quad (6.24)$$

which is about ten times longer than the jet flow time $t_{flow} = L_j/V \simeq 100 \text{ sec}$.

This calculation suggests that the radiative losses alone are insufficient to cool the jet plasma. Other effects such as adiabatic expansion, or Compton cooling by UV photons from disc and star must be considered and may dominate the cooling of the jet plasma. In fact, the decrement of the electron density n_e along the jet axis (see Fig. 6.2-6.3) may also imply the slightly transverse expansion of the jet plasma when moving outward. The above conclusion depends on the value of the jet filling factor f . Here f is assumed to be ~ 1 . This may be close to the reality of the X-ray jets according to the following discussion.

The mass loss rate of SS 433 via the jet flow is $4 \times 10^{-6} M_{\odot} \text{ yr}^{-1}$ for Model B and $6.3 \times 10^{-6} M_{\odot} \text{ yr}^{-1}$ for Model C. This gives Model B a kinetic luminosity of $2 \times 10^{40} \text{ erg s}^{-1}$ and $3 \times 10^{40} \text{ erg s}^{-1}$ for Model C. These kinetic luminosities are significantly higher than their respective Eddington limits, $1 \times 10^{39} \text{ erg s}^{-1}$ for Model B with $M_x \simeq 8 M_{\odot}$ and $8 \times 10^{39} \text{ erg s}^{-1}$ for Model C with $M_x \simeq 62 M_{\odot}$. This conclusion is completely consistent with those drawn from the properties of the Doppler-shifted optical lines (e.g. Milgrom 1981; Begelman *et al.* 1980), the X-ray lobes (Watson *et al.* 1983), or the supernova remnant W50 surrounding SS 433 (e.g., Zealey, Dopita & Malin 1980).

The jet optical line regions are located in a distance of $10^{13} \sim 10^{15}$ cm from the compact object. Optical observations indicate the radiating matter in these regions has a temperature of $\sim 10^4$ K, as no highly excited lines of HeII and CIII/NIII are seen (Shaham 1981). Extrapolations of the temperature functions expressed in Equation (6.17) and (6.20) into the jet optical region fail to match the results from the optical observations. The extrapolated temperature is much lower than 10^4 K, which implies that when the jet plasma transit from the X-ray region to the optical region, the plasma cooling is slowing down. Photoionization and mechanical heating are two possible mechanisms which can stop the cooling of the jet plasma. From the hot X-ray jet to the cold optical region, energy can be transferred through photoionization by X-rays or thermal conduction. A large amount of kinetic energy is stored in the jets as indicated by the above calculations. In principle, only a small fraction of this energy is sufficient to stop the cooling of the jet plasma and sustain the optical emission.

The optical jets are clumpy and the optically radiating material is confined in individual blobs (e.g. Kopylov *et al.* 1986). This idea is supported by the irregular fluctuations of the observed Doppler shifts and limits on the overall energy output acceptable for a stellar object. Both theoretical and observational arguments indicate that a filling factor $f \ll 1$ is required

for the jet optical emitting region (see, e.g. Zwitter *et al.* 1989). It is hard from the current calculations to distinguish if the plasma in the X-ray region, like its optical partner, stays in the blob state. When the spectra are fitted to derive the jet temperature and density profiles, the normalization factor is fixed at one, which implicitly assumes that the filling factor of the X-ray jet is close to one.

The formation of blobs in the jets may be due to variations in the mass ejection rate on time-scales longer than the X-ray jet transit time t_{flow} , or thermal instability as suggested by Davidson and McCray (1980) and investigated in detail by Bodo *et al.* (1985), Brinkmann *et al.* (1988). In the first case, the filling factor of the X-ray jet should be close to one. If thermal instability does occur in the jet X-ray region, the blobs would not be efficiently formed during the X-ray jet transit time. This is suggested by $C_s^{\text{ad}} t_{\text{flow}} \sim 10^{10} \text{ cm} \sim R_f$ because the scale of the perturbation must not be greater than the sound travelling distance. Therefore, it may be concluded that the filling factor of the X-ray jet is close to one and the jet plasma can be regarded as continuous flow.

6.4.3 Jet Acceleration Mechanisms

As discussed in Chapter one, supersonic collimated material jets have recently been observed in a wide range of celestial objects from powerful extragalactic sources to galactic objects such as SS 433 and newborn stars. The jets of SS 433 display somewhat different features from the extragalactic ones in that they are only mildly relativistic, with $v=0.26c$, which has remained remarkably constant to $\delta v/v < 1\%$ (Margon 1981; Katz & Piran 1982) since the discovery of the moving lines. This constancy and uniformity have been maintained over a number of cycles of the 163 day period, many binary orbit periods, and an extremely large number of transit times (i.e., the time it takes a fluid element to travel down the length of the jet and out of the optical emission-line region). This constancy of the velocity places a powerful constraint on all models for the origin of the jets.

Among those mechanisms for the interpretation of the collimation and acceleration of astrophysical jets, radiative acceleration mechanisms are widely discussed for the jets of SS 433. The Line locking mechanism has the advantage of explaining the value, constancy and uniformity of the observed jet velocity, however, it requires low temperature ($T \sim 10^4 \text{ K}$) to avoid having H and He completely ionized. This requirement is basically ruled out by the

X-ray observations presented in this thesis. Line locking in the Fe Lyman-alpha line, which may work at X-ray temperatures, requires a very large Fe abundance in the jets. This is not allowed by the *EXOSAT* and *GINGA* observations which indicate that the Fe emission has an equivalent width close to the expected value for material with normal cosmic abundances. The Line locking mechanism also requires the jet gas be highly clumped so that an efficient acceleration can be achieved. This is the case in the optical emission regions but not in the X-ray regions as discussed above.

Acceleration by radiation pressure in the funnels of a thick accretion disc is the most promising mechanism to explain the formation of the SS 433 jets. Based on the suggestion by Lynden-Bell (1978), the model has been developed for optically thin jet cases (Sikora & Wilson 1981; Bodo *et al.* 1985) and thick ones (Fukue, 1982, 1983, 1987; Calvani & Nobili 1983; Nobili *et al.* 1985). In the case of SS 433, the jets are probably closer to the optically thick regime, as suggested by the value of the jet density from observations. In fact, the optically thick jets are more efficient in transferring momentum from the radiation field to the matter. In the scenario of this model, the jet flow in the funnels is accelerated hydrodynamically through the sonic point like a stellar wind until a relativistic asymptotic velocity is achieved. The funnel's opening angle provides the narrow jet's collimation angle, as required by observations. The energies stored initially as thermal, radiative, rotational, and/or magnetic forms are converted into the final kinetic energy of jets. After exiting the funnels, the jets move ballistically with a negligible expansion, even without pressure confinement by an external medium, due to their high Mach number (~ 60).

The results derived in this chapter are completely compatible with the above scheme. The jet flow becomes highly supersonic before exiting the funnel. This will maintain the constancy and uniformity of the jet velocity over a large number of transit times. The derived jet density also indicates that the jets are optically thick. It is of more interest that both temperature and density exponentially distribute along the jet axis. This is completely consistent with the theoretical predictions shown in Fig. 2-3 of Fukue's paper (Fukue, 1987) in which the characteristics of the SS 433 jets are discussed within the framework of the funnel acceleration theory.

6.5 Summary

The physical properties of SS 433 jets have been discussed in this chapter within three possible geometrical models for SS 433 by directly mapping the temperature and electron density distributions along the jet axis. The derived temperature and density profiles from the 1987 *GINGA* observations cannot be extrapolated to fit the observations made in 1988 & 1989. This is mainly due to the uncertainty of the geometrical parameters adopted for the discussions. Fortunately, the measured temperature and density profiles are not highly sensitive to the geometrical models assumed, therefore, several conclusions can be drawn from these discussions.

Geometrical models with a neutron star as the compact object are not adequate in explaining the X-ray observations. The mass ratio of the SS 433 system is thus limited in the range of $0.174 < q < 1.7$ in which the compact object is a black hole (if the K velocity is correct). It is possible to choose a set of geometrical parameters inside this mass ratio region to self-consistently explain the observations made with *EXOSAT* and *GINGA* satellites. The X-ray properties of SS 433 are determined by three geometrical effects, eclipse by the companion star and its wind/accretion flow, eclipse by the accretion disc and the jet precession.

The X-ray jets of SS 433 are a continuous, supersonic plasma flow with Mach number high enough to maintain the constancy and uniformity of the jet velocity. The temperature and density profiles obey an exponential function, which is consistent with the theoretical calculations by assuming the adiabatic expansion of jets once exiting the funnel by Fukue (1987). The jet material is rapidly cooling down outward along the flow. However the radiative losses may not be the main cooling effects as suggested by the ratio of the bremsstrahlung cooling time and the X-ray jet flow transit time. Adiabatic expansion may dominate the plasma cooling of the jets. This is supported by the similarities between the measured temperature profile and Fukue's theoretical predictions. In the transient region of the X-ray and optical emitting jets, the jet cooling is slowed down. Photoionization and mechanical heating may be two possible candidates which can reheat the jet plasma. The kinetic luminosity of jets is largely higher than the Eddington limit for a $1.4M_{\odot}$ object, which is consistent with the conclusions from observations in other energy bands and theoretical arguments.

The most promising mechanism for the collimation and acceleration of the SS 433 jets is the

theory of the jet acceleration inside the funnels of a thick accretion disc. The results derived in this chapter are completely consistent with the predictions of this model and therefore provide strong support to this theory.

Chapter 7

The Variable X-ray Absorption and Soft X-ray Excess of the QSO MR 2251 – 178

7.1 Introduction

MR 2251 – 178 is a low-redshift QSO which lies in the nucleus of a galaxy having a gaseous component of high ionization, high temperature ($T = 3 \times 10^4$ K) and relatively low metal abundance and is surrounded by a giant HII envelope observed in [O III] emission (Bergeron *et al.* 1983). It lies in the outskirts of a cluster of approximately 50 galaxies (Phillips 1980). Radio data show MR 2251 – 178 to be a weak, pointlike source of emission (Ricker *et al.* 1978) and the infrared colours are typical for low-luminosity QSOs (Glass 1981; Hyland & Allen 1982; Neugebauer *et al.* 1982; McAlary *et al.* 1983). Spectrophotometry of MR 2251 – 178 (Canizares *et al.* 1978) shows a typical optical spectrum for a low-redshift QSO although the FWZI of $H\alpha$ (23000 km s^{-1}) is extreme. It has been observed to vary optically by at least two magnitudes on time-scales from one month to about one year (Ricker *et al.* 1979). A weak and variable $\text{Ly}\alpha$ absorption line, with equivalent width $\leq 1 \text{ \AA}$, observed by *IUE* (Ulrich 1988) is suggested to arise in gas in the vicinity of the active nucleus.

As a relatively bright X-ray source, the QSO MR 2251 – 178 was first discovered in the

ARIEL V survey (Cooke *et al.* 1978) and was subsequently identified with the QSO by Ricker *et al.* (1978) from observations with *SAS-3*. The *SAS-3* measurement reports a flux in the 2-10 keV band of $2.5 \pm 0.4 \times 10^{-11}$ erg cm⁻² s⁻¹ (Ricker *et al.* 1978) and the 3A catalogue (McHardy *et al.* 1981) a mean flux of $3.7 \pm 0.5 \times 10^{-11}$ erg cm⁻² s⁻¹. At a redshift of $z = 0.0638 \pm 0.0015$ (Canizares *et al.* 1978), this implies a 2-10 keV luminosity of $\sim 10^{45}$ erg s⁻¹ ($H_0 = 50$ km s⁻¹ mpc⁻¹). Variability of the X-ray flux by a factor of about 10 was suggested by Cooke *et al.* (1978) but not confirmed in a subsequent, more detailed, analysis of the *ARIEL V* data by Marshall, Warwick & Pounds (1981).

The X-ray spectrum of MR 2251 – 178 was first obtained by Halpern (1984) in 2 observations with the *EINSTEIN* MPC (2-10 keV). For an assumed power-law spectrum with low energy absorption he found photon indices of 1.52 ± 0.17 and $1.72(+0.35, -0.30)$. A large variation in absorbing column density was observed, with N_H changing from less than 5×10^{21} cm⁻² to $23 \pm 12 \times 10^{21}$ cm⁻² over the 1 yr interval between the observations. An excess soft X-ray flux below 1 keV was inferred in the latter observation from the simultaneous measurement with the *EINSTEIN* HRI.

Intrinsic absorption is found to be common, particularly in low X-ray luminosity AGN (Reichert *et al.* 1985) and the *EXOSAT* spectral survey has detected absorbing columns in the range of $10^{21} - 10^{23}$ cm⁻² in 18 of 35 emission line AGN (Turner & Pounds 1989). MR 2251 – 178 is the highest luminosity object in which low energy absorption has been confidently detected. In several cases, including NGC 4151 (Yaqoob, Warwick & Pounds 1989) and ESO 103-G35 (Warwick, Pounds & Turner 1988) this absorption is found to be variable. Excess flux, below ~ 1 keV is also found in ~ 30 per cent of the sources in the *EXOSAT* spectra survey sample.

Three models have been proposed to explain column density variations and excess fluxes below 2-3 keV:

(1) *A complex spectrum model.* The X-ray spectrum includes a separate emission component dominant below 1 keV (e.g. Mkn 335; Pounds *et al.* 1986).

(2) *The leaky cold absorber model.* The variable absorption is caused by the random passage of cold clouds across the line of sight to the X-ray emitting region (e.g. NGC 4151; Holt *et al.* 1980).

(3) *The warm absorber model.* Changes of the ionization structure of the absorbing material around the central source cause the changes in the X-ray absorption (e.g. this source; Halpern 1984).

To further examine the X-ray spectrum and variability of MR 2251 – 178, particularly interesting because of its high luminosity, a series of *EXOSAT* observations were carried out over the period 1983 October - 1984 December. In this chapter the results of these observations are presented and it is shown that they can be best explained by the ‘warm absorber’ model. The observations and data reduction are introduced in section 7.2 and the results are presented in section 7.3. Model calculation results are given in section 7.4 and the implications of these results are discussed in section 7.5. The conclusion is drawn in section 7.6.

7.2 EXOSAT Observations

MR 2251 – 178 was monitored by *EXOSAT* over the period 1983 October to 1984 December in 15 separate observations. The observing log is given in Table 7.1. Data were obtained in the energy range 0.03-2 keV using the *EXOSAT* low-energy (LE) telescope(s) (de Korte *et al.* 1981) and in the range 1-10 keV using the medium-energy (ME) detector array (Turner, Smith & Zimmermann 1981).

Count rates for the LE observations were extracted from a 100×100 arcsec² cell centered on the source and the background count rates from adjacent source-free regions subtracted. Count-rate corrections for mirror vignetting, dead-time and scattering due to the instrumental response were also applied. The ME count rates refer to the full on-source half-array after subtraction of background count rates obtained either from stable slew data, from before or after each observation, or from stable offset half-array data with the appropriate ‘difference spectrum’ correction (Parmar & Izzo 1986).

Spectra from the argon chambers of the ME detectors were obtained by correcting background and dead-time. Spectral fits are performed on the ME spectra and on the combined LE and ME measurements for each observation. This was carried out by comparing spectral data with the convolution of the instrument response function and input spectra of the form

Table 7.1: Observing log for MR 2251 – 178 (times in UT)

No.	Start	End	Instrument		Exposure (secs)
1	279/83 12:22 (MJD45613.52)	280/83 12:26	ME Array	(H2 on, H1 on)	81550
			3LX	(Telescope 1,2)	37740
			AL/P	(Telescope 2)	22200
			BOR	(Telescope 2)	31980
2	288/83 21:25 (MJD45622.89)	289/83 00:47	ME Array	(H1 on)	11740
			3LX	(Telescope 2)	10740
3	300/83 15:16 (MJD45634.64)	300/83 21:20	ME Array	(H1 on)	20600
			3LX	(Telescope 1)	10380
			AL/P	(Telescope 2)	20220
4	310/83 18:03 (MJD45644.75)	310/83 20:29	ME Array	(H2 on, H1 on)	8280
			3LX	(Telescope 1)	3540
			AL/P	(Telescope 1)	3330
5	321/83 04:10 (MJD45655.17)	321/83 05:59	ME Array	(H1 on)	6370
			3LX	(Telescope 1)	6240
6	331/83 15:07 (MJD45665.63)	332/83 15:51	ME Array	(H1 on)	29870
			3LX	(Telescope 1)	17278
			BOR	(Telescope 1)	9968
7	343/83 05:22 (MJD45677.22)	343/83 06:50	ME Array	(H2 on)	11100
			3LX	(Telescope 1)	5220
			AL/P	(Telescope 1)	2640
8	352/83 07:45 (MJD45686.32)	352/83 09:38	ME Array	(H2 on)	6320
			3LX	(Telescope 1)	3960
			AL/P	(Telescope 1)	2640
9	361/83 19:28 (MJD45695.81)	361/83 20:59	ME Array	(H2 on)	4100
			3LX	(Telescope 1)	3840
			AL/P	(Telescope 1)	780
10	191/84 23:59 (MJD45891.00)	192/84 03:16	ME Array	(H1 on, H2 on)	9960
			3LX	(Telescope 1)	1560
			AL/P	(Telescope 1)	2580
			BOR	(Telescope 1)	4080
11	292/84 19:07 (MJD45991.80)	293/84 04:14	ME Array	(H1 on, H2 on)	30920
			3LX	(Telescope 1)	4855
			AL/P	(Telescope 1)	7551
			BOR	(Telescope 1)	4749
12	307/84 02:59 (MJD46006.13)	307/84 10:13	ME Array	(H1 on, H2 on)	24310
			3LX	(Telescope 1)	11940
			AL/P	(Telescope 1)	5640
			BOR	(Telescope 1)	3720
13	316/84 02:14 (MJD46015.09)	316/84 10:27	ME Array	(H2 on, H1 on)	28670
			3LX	(Telescope 1)	10740
			AL/P	(Telescope 1)	16169
14	325/84 12:37 (MJD46024.53)	325/84 18:55	ME Array	(H2 on, H1 on)	21190
			3LX	(Telescope 1)	10240
			AL/P	(Telescope 1)	4380
			BOR	(Telescope 1)	5280
15	332/84 11:40 (MJD46031.48)	332/84 18:29	ME Array	(H2 on, H1 on)	23910
			3LX	(Telescope 1)	9880
			AL/P	(Telescope 1)	4740
			BOR	(Telescope 1)	8940

Table 7.2: Count rates observed from MR 2251 – 178

Day	3LX (ct s ⁻¹)	AL/P (ct s ⁻¹)	BOR (ct s ⁻¹)	ME (2-6 keV) (ct s ⁻¹ detector ⁻¹)
279/83	0.030 ± 0.002	0.020 ± 0.001	0.006 ± 0.001	0.509 ± 0.004
288/83	0.031 ± 0.002			0.508 ± 0.010
300/83	0.030 ± 0.002	0.015 ± 0.001		0.424 ± 0.010
310/83	0.027 ± 0.004	0.015 ± 0.003		0.489 ± 0.015
321/83	0.024 ± 0.003			0.428 ± 0.010
331/83	0.017 ± 0.002		0.004 ± 0.002	0.398 ± 0.007
343/83	0.030 ± 0.012			0.514 ± 0.012
352/83	0.022 ± 0.004	0.019 ± 0.004		0.535 ± 0.016
361/83	0.027 ± 0.005	0.020 ± 0.011		0.520 ± 0.017
192/84	0.029 ± 0.006	0.027 ± 0.005	0.002 ± 0.003	0.532 ± 0.012
292/84	0.007 ± 0.003	0.005 ± 0.002	0.004 ± 0.003	0.285 ± 0.008
307/84	0.010 ± 0.002	0.004 ± 0.002	0.003 ± 0.003	0.344 ± 0.008
316/84	0.012 ± 0.002	0.009 ± 0.001		0.368 ± 0.008
325/84	0.017 ± 0.002	0.010 ± 0.003	0.007 ± 0.003	0.498 ± 0.009
332/84	0.015 ± 0.003	0.004 ± 0.004	0.005 ± 0.002	0.447 ± 0.009

$$N(E) = AE^{-\Gamma} e^{-N_H \sigma(E)} \text{ photon cm}^{-2} \text{ s}^{-1} \text{ keV}^{-1} \quad (7.1)$$

where Γ is the photon number index, N_H is the equivalent hydrogen column density which characterizes the effective absorption of cold gas with solar abundance and $\sigma(E)$ is the corresponding absorption cross-section (Morrison & McCammon 1983).

7.3 Results

No evidence for extended emission was detected in the LE. The upper limit is consistent with the luminosities of $10^{42} - 10^{43}$ and temperatures of $\sim 2-3$ keV found for nearby clusters of similar richness (Kriss, Cioffi & Canizares 1983; Edge & Stewart, in preparation), and implies that the X-ray emission discussed here comes solely from the active nucleus.

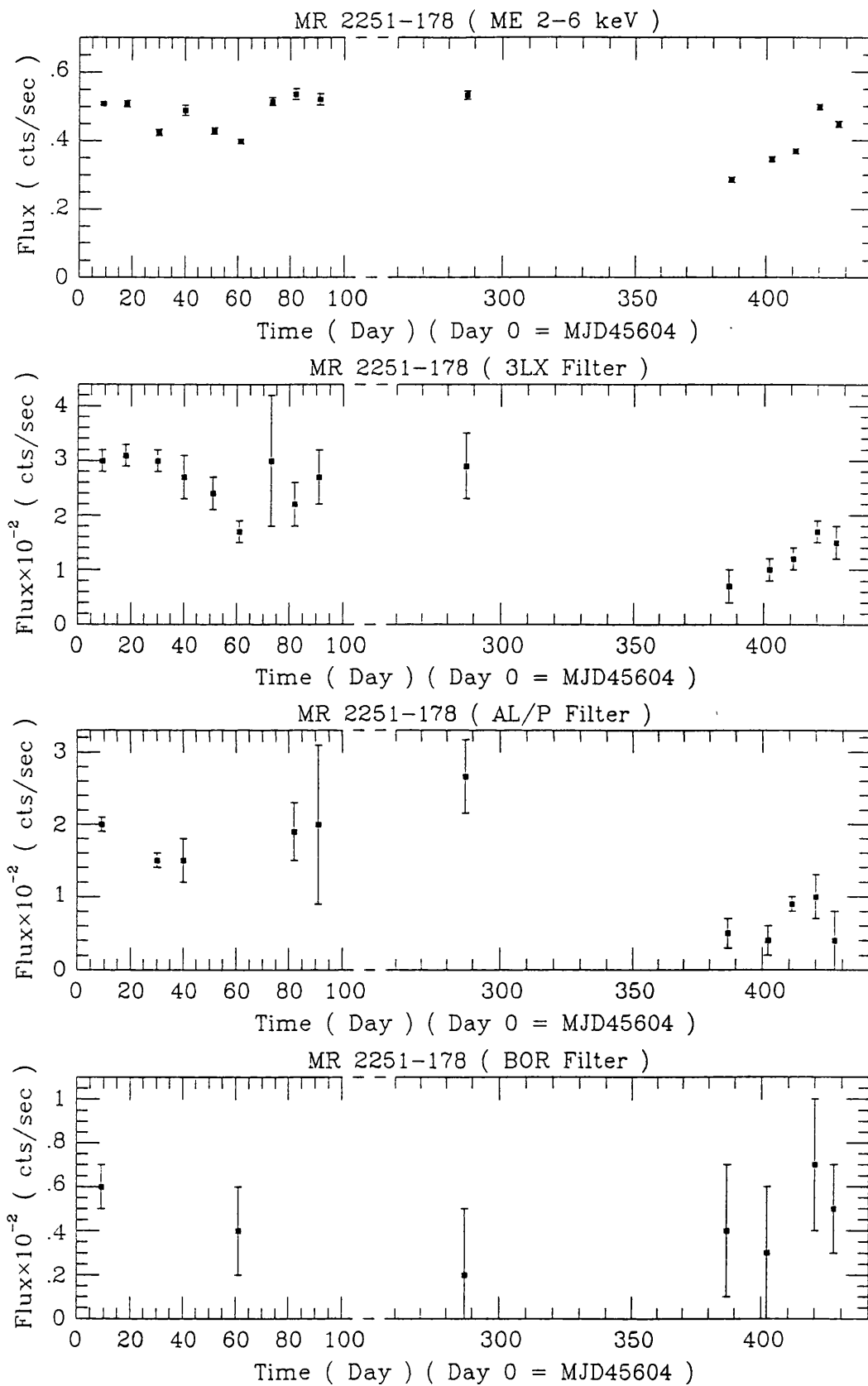


Figure 7.1: X-ray light curves of MR 2251 - 178. From the top, in the 2-6 keV Medium Energy band, in the LE telescope with thin Lexan filter, LE with aluminium + parylene filter and LE boron filter.

7.3.1 Intensity Variability

Table 7.2 lists the count rates observed from MR 2251 – 178 and Fig 7.1 shows the ME and LE light curves. Intensity variability can be seen over the period of the observations, with significant changes in the ME count rate over periods of ~ 10 d, not untypical for an AGN of this luminosity (e.g. Barr & Mushotsky 1986). The ME and LE fluxes are moderately well correlated but the variability in the LE has a larger amplitude. While the ME intensity

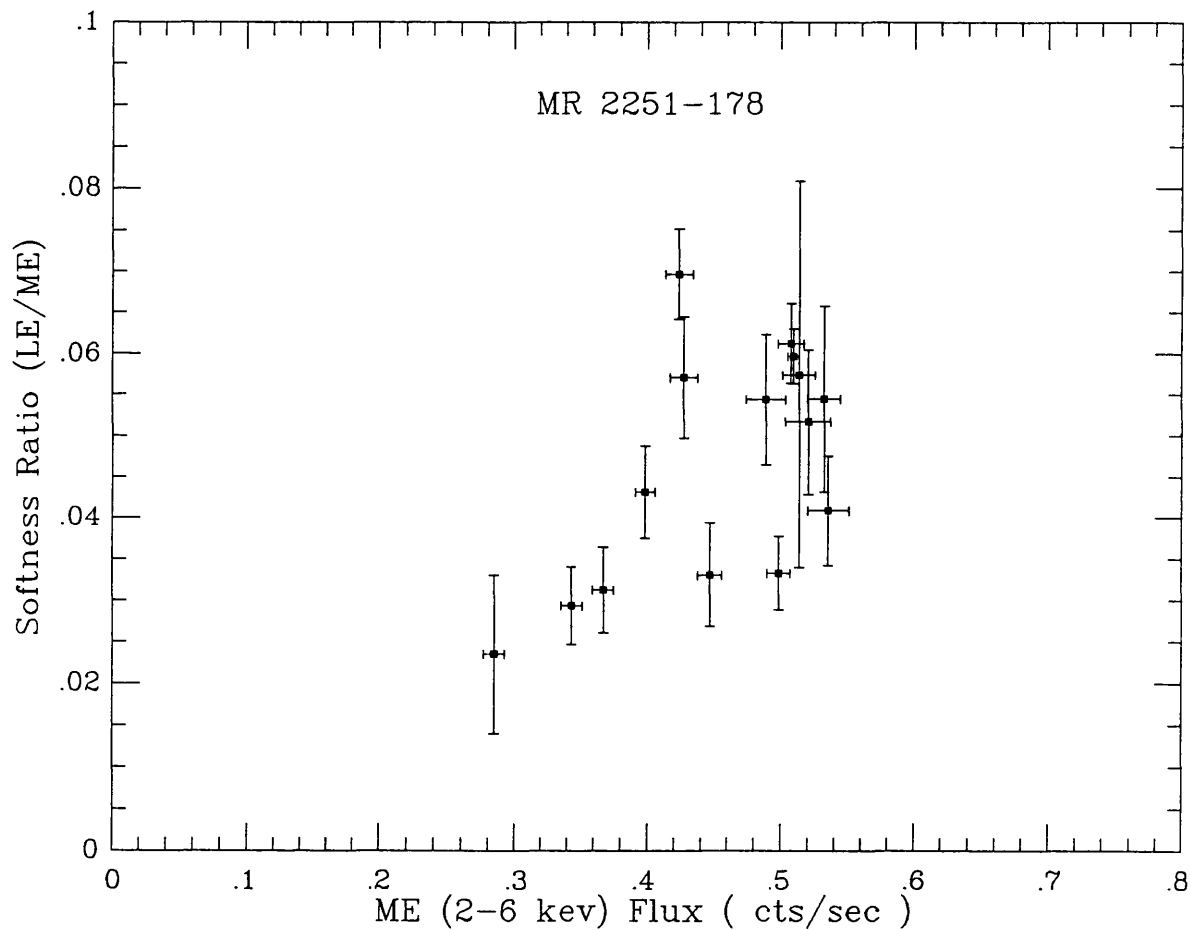


Figure 7.2: The ratio of the thin Lexan to the 2-6 keV ME count rates as a function of the ME count rate

changes by a factor of about 2, the LE (3LX filter) varies by a factor of about 5. Fig 7.2 shows the ratio of the LE (3LX filter) count rates to those measured in the ME detector as a function of the ME count rate. A trend can be seen in that, at higher flux levels, this ratio is highest.

7.3.2 X-ray Spectrum

Table 7.3 gives the spectral fit details. Spectral fits to the ME data and to the combined ME+LE data with all parameters free yield values of the photon index Γ consistent, within the errors, with a constant $\Gamma \sim 1.7$ (Fig 7.3). The values derived for reduced χ^2 indicate however that a simple power-law spectral form with absorption from neutral material is an inadequate description of the source spectrum.

The equivalent hydrogen column density N_{H} derived from fitted ME (2-10 keV) data varies from a value consistent with the line-of-sight column through the Galaxy of $6 \times 10^{20} \text{ cm}^{-2}$ (Elvis, Lockman & Wilkes 1989) to about $1.7 \pm 0.6 \times 10^{22} \text{ cm}^{-2}$, (the error corresponds to the 90 per cent level for 2 parameters of interest). This range is similar to that found by Halpern (1984) using the *EINSTEIN* MPC data. Column densities derived from the spectral fits with the combined LE and ME data are, however, an order of magnitude smaller than those derived from the ME spectral fits, implying that there is a soft X-ray excess below 1 keV.

Fig 7.4 shows two examples of the measured MR 2251 – 178 count spectra, one obtained on 1984 October 18 when the minimum X-ray flux occurred and the other on the 1983 October 6 when the source was bright. Extrapolating the best spectral fit found in the 2-10 keV band reveals a significant excess at low energies for the 1983 data.

7.3.3 Variability of X-ray Absorption

Because the underlying spectral slope did not change significantly during the *EXOSAT* observations, further spectral fits with Γ fixed at the value of 1.70, which is consistent with both the mean value determined here of 1.64 ± 0.08 and the average value found for the *EXOSAT* spectral survey objects, were made to both the ME and the combined LE-ME spectra, to better determine the relationship between the absorbing column density and the source luminosity. The derived column densities for both data sets are shown as a function of flux in Fig 7.5. The correlation between column density and luminosity is clear. As the source flux increases the derived absorbing column density decreases. The difference in the absorbing column density derived from fitting the ME spectra and the combined ME+LE spectra, which is a measure of the ‘soft excess’ also increases.

Table 7.3: Spectral fit details for MR 2251 – 178

Day	Instruments	Spectral fit with floating parameters			Spectral fit with fixed photon index(1.70)		
		Photon Index	Column Density (10^{21} cm^{-2})	Reduced χ^2 (d.o.f)	Column Density (10^{21} cm^{-2})	2-10 keV Flux ($10^{-11} \text{ ergs cm}^{-2} \text{ sec}^{-1}$)	Reduced χ^2 (d.o.f)
279/83	ME	$1.77^{+0.15}_{-0.11}$	$4.5^{+4.2}_{-2.9}$	1.71(32)	$2.9^{+0.7}_{-0.6}$	2.99	1.69(34)
	ME+LE	$1.63^{+0.06}_{-0.06}$	$0.6^{+0.2}_{-0.2}$	2.49(35)	$0.8^{+0.1}_{-0.1}$	2.94	2.65(37)
288/83	ME	$1.57^{+0.20}_{-0.12}$	$0.0^{+5.2}_{-0.0}$	1.39(32)	$2.6^{+1.5}_{-1.4}$	3.02	1.40(34)
	ME+LE	$1.59^{+0.12}_{-0.09}$	$0.6^{+0.4}_{-0.1}$	1.36(33)	$0.8^{+0.2}_{-0.1}$	2.99	1.42(35)
300/83	ME	$1.89^{+0.39}_{-0.24}$	$9.4^{+11.4}_{-9.4}$	1.02(27)	$4.5^{+1.9}_{-1.8}$	2.72	0.99(29)
	ME+LE	$1.57^{+0.17}_{-0.17}$	$0.6^{+0.5}_{-0.3}$	1.65(29)	$0.9^{+0.2}_{-0.1}$	2.66	1.67(31)
310/83	ME	$2.13^{+0.58}_{-0.49}$	$16.7^{+12.2}_{-1.8}$	1.34(26)	$5.2^{+2.5}_{-2.3}$	2.88	1.42(28)
	ME+LE	$1.63^{+0.19}_{-0.15}$	$0.7^{+0.7}_{-0.5}$	1.58(28)	$0.9^{+0.4}_{-0.2}$	2.79	1.51(30)
321/83	ME	$2.00^{+0.41}_{-0.26}$	$16.8^{+13.2}_{-11.9}$	1.15(31)	$8.2^{+2.1}_{-2.0}$	2.67	1.19(33)
	ME+LE	$1.52^{+0.14}_{-0.12}$	$0.5^{+0.5}_{-0.3}$	1.50(32)	$0.8^{+0.4}_{-0.2}$	2.56	1.68(34)
331/83	ME	$1.55^{+0.28}_{-0.14}$	$1.6^{+8.4}_{-1.6}$	1.59(30)	$5.5^{+1.6}_{-1.5}$	2.37	1.55(32)
	ME+LE	$1.60^{+0.11}_{-0.12}$	$1.6^{+0.4}_{-0.3}$	1.76(32)	$1.2^{+0.5}_{-0.3}$	2.32	1.78(34)
343/83	ME	$1.58^{+0.35}_{-0.18}$	$1.7^{+10.0}_{-1.7}$	0.98(35)	$4.7^{+1.9}_{-1.8}$	3.07	0.95(37)
	ME+LE	$1.55^{+0.16}_{-0.16}$	$0.9^{+0.7}_{-0.5}$	1.01(37)	$1.3^{+0.4}_{-0.3}$	3.00	1.12(39)
352/83	ME	$1.55^{+0.43}_{-0.18}$	$0.0^{+11.9}_{-0.0}$	1.08(35)	$3.7^{+2.3}_{-2.1}$	3.22	1.04(37)
	ME+LE	$1.59^{+0.18}_{-0.15}$	$0.8^{+0.8}_{-0.5}$	1.03(37)	$1.1^{+0.4}_{-0.3}$	3.17	1.04(39)

Table 7.3: Spectral fit details for MR 2251 – 178 (continued)

Day	Instruments	Spectral fit with floating parameters			Spectral fit with fixed photon index(1.70)		
		Photon Index	Column Density (10^{21} cm $^{-2}$)	Reduced χ^2 (d.o.f)	Column Density (10^{21} cm $^{-2}$)	2-10 keV Flux (10^{-11} ergs cm $^{-2}$ sec $^{-1}$)	Reduced χ^2 (d.o.f)
361/83	ME	$1.46^{+0.26}_{-0.20}$	$0.0^{+5.4}_{-0.0}$	1.17(33)	$4.3^{+2.7}_{-2.4}$	3.11	1.26(35)
	ME+LE	$1.47^{+0.21}_{-0.17}$	$0.4^{+0.6}_{-0.3}$	1.12(35)	$0.8^{+0.5}_{-0.3}$	3.04	1.25(37)
192/84	ME	$1.57^{+0.53}_{-0.23}$	$1.1^{+15.6}_{-1.1}$	0.86(31)	$4.5^{+2.9}_{-2.6}$	3.27	0.82(33)
	ME+LE	$1.63^{+0.18}_{-0.19}$	$1.0^{+0.5}_{-0.4}$	1.08(34)	$0.8^{+0.5}_{-0.3}$	3.19	1.02(36)
292/84	ME	$1.31^{+0.37}_{-0.20}$	$3.0^{+12.0}_{-3.0}$	1.28(33)	$14.4^{+2.6}_{-2.5}$	1.86	1.40(35)
	ME+LE	$1.26^{+0.18}_{-0.16}$	$1.0^{+3.3}_{-0.4}$	1.18(36)	$13.2^{+2.6}_{-2.5}$	1.85	1.55(38)
307/84	ME	$1.67^{+0.36}_{-0.33}$	$9.7^{+11.1}_{-9.7}$	0.77(33)	$10.5^{+2.1}_{-2.0}$	2.18	0.73(35)
	ME+LE	$1.42^{+0.17}_{-0.13}$	$1.4^{+1.9}_{-0.8}$	0.93(36)	$4.3^{+2.1}_{-1.5}$	2.11	1.28(38)
316/84	ME	$1.36^{+0.20}_{-0.17}$	$0.0^{+4.4}_{-0.0}$	1.11(33)	$7.1^{+2.3}_{-2.1}$	2.43	1.41(35)
	ME+LE	$1.38^{+0.18}_{-0.13}$	$0.9^{+0.8}_{-0.6}$	1.07(35)	$2.1^{+0.6}_{-0.4}$	2.37	1.51(37)
325/84	ME	$1.63^{+0.38}_{-0.22}$	$3.0^{+10.9}_{-3.0}$	0.99(35)	$4.7^{+2.0}_{-1.9}$	3.12	0.94(37)
	ME+LE	$1.59^{+0.17}_{-0.13}$	$1.4^{+1.0}_{-0.8}$	0.93(38)	$1.9^{+0.5}_{-0.4}$	3.08	0.96(40)
332/84	ME	$1.51^{+0.31}_{-0.17}$	$2.0^{+9.1}_{-2.0}$	0.87(37)	$6.9^{+1.7}_{-1.6}$	2.74	0.89(39)
	ME+LE	$1.49^{+0.15}_{-0.12}$	$1.3^{+1.8}_{-0.7}$	0.87(37)	$3.1^{+1.5}_{-1.1}$	2.69	1.11(42)

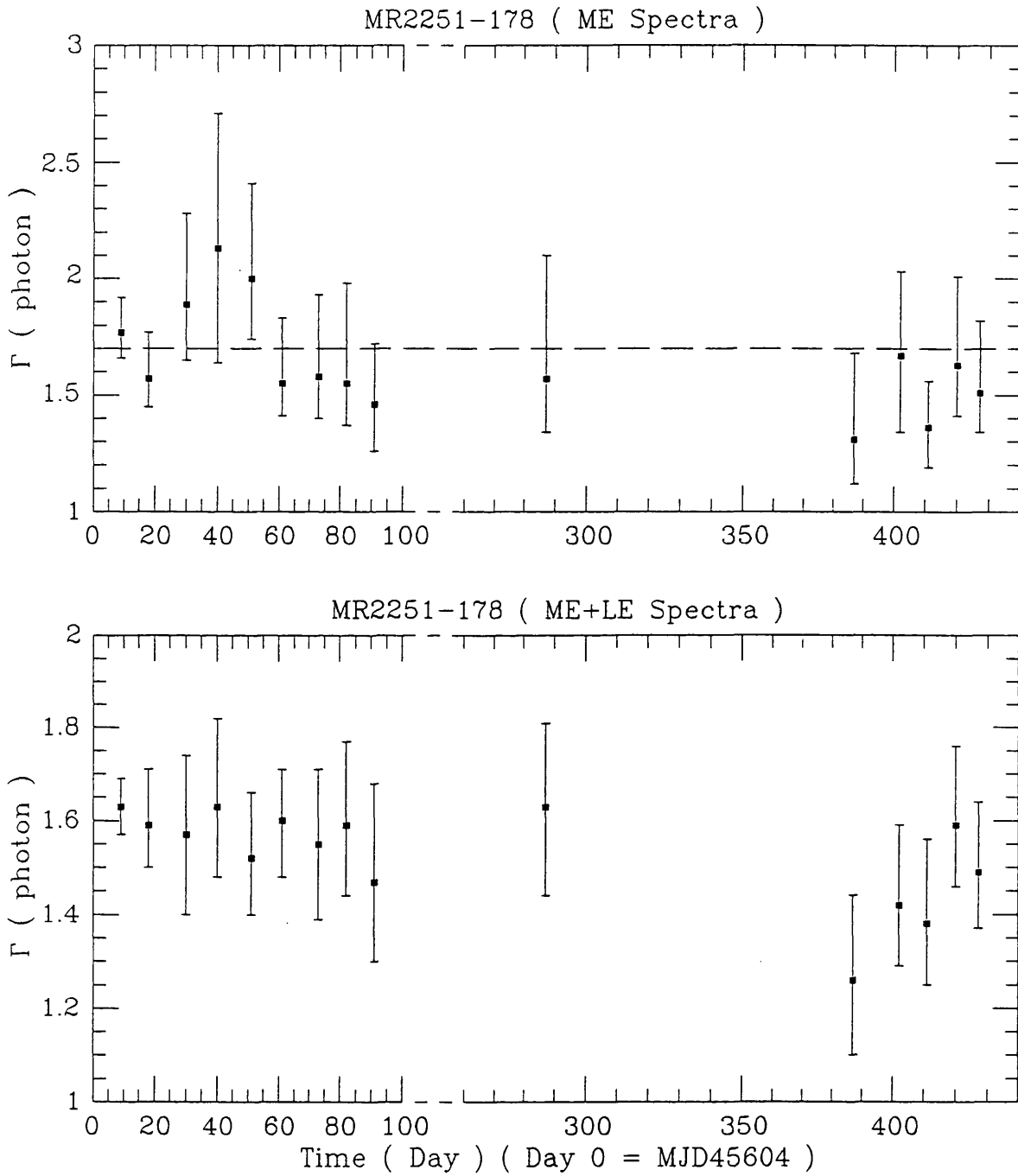


Figure 7.3: The spectra photon index Γ as measured from (top) and ME data alone and (below) the ME and LE data combined. The first are for both column density and Γ as free parameters. The dashed line shows the average AGN spectral slope of 1.70.

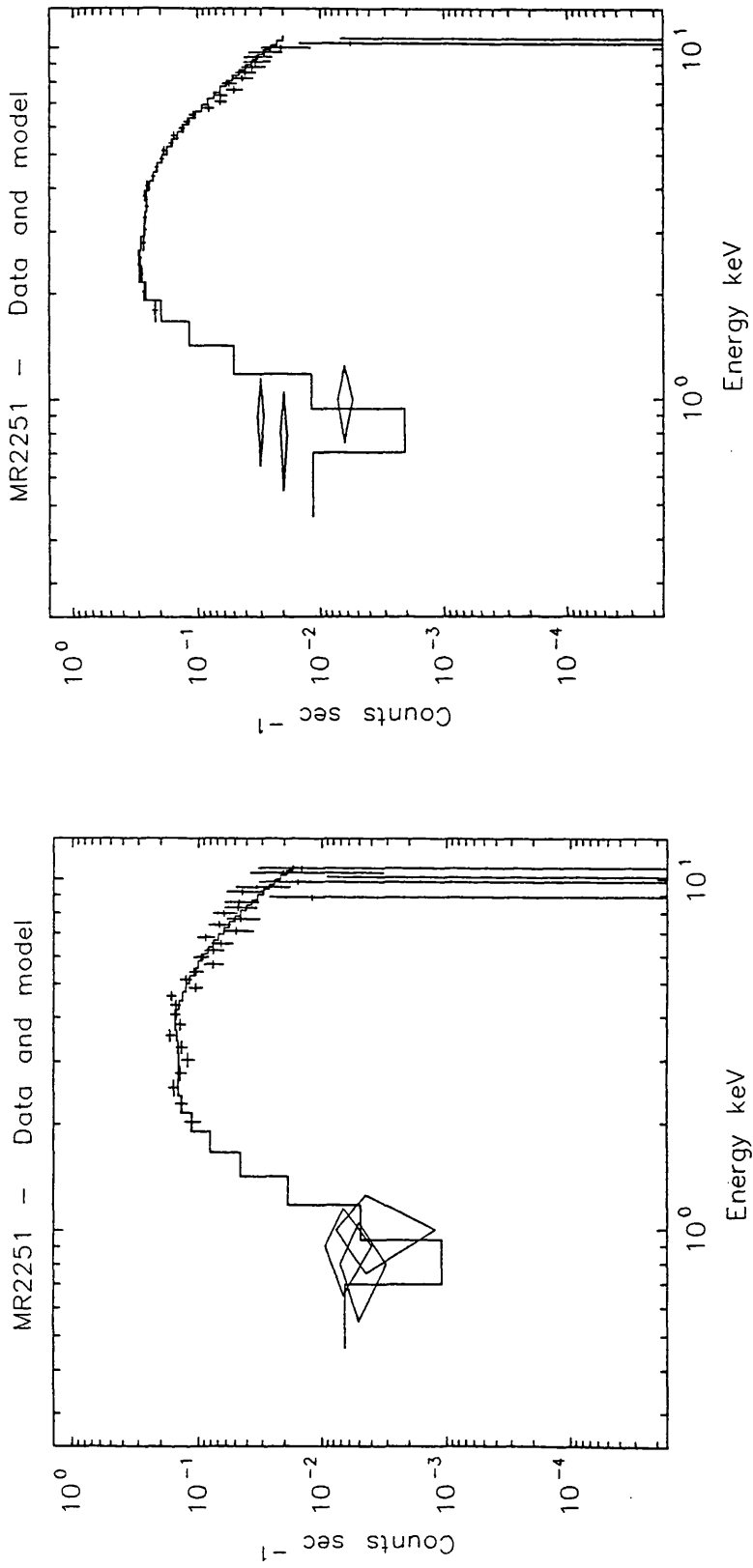


Figure 7.4: Examples of spectral fits. Left: At flux minimum on 1984 October 18. Right: At flux maximum on 1983 October 6. Note the soft excess in the high-flux spectrum.

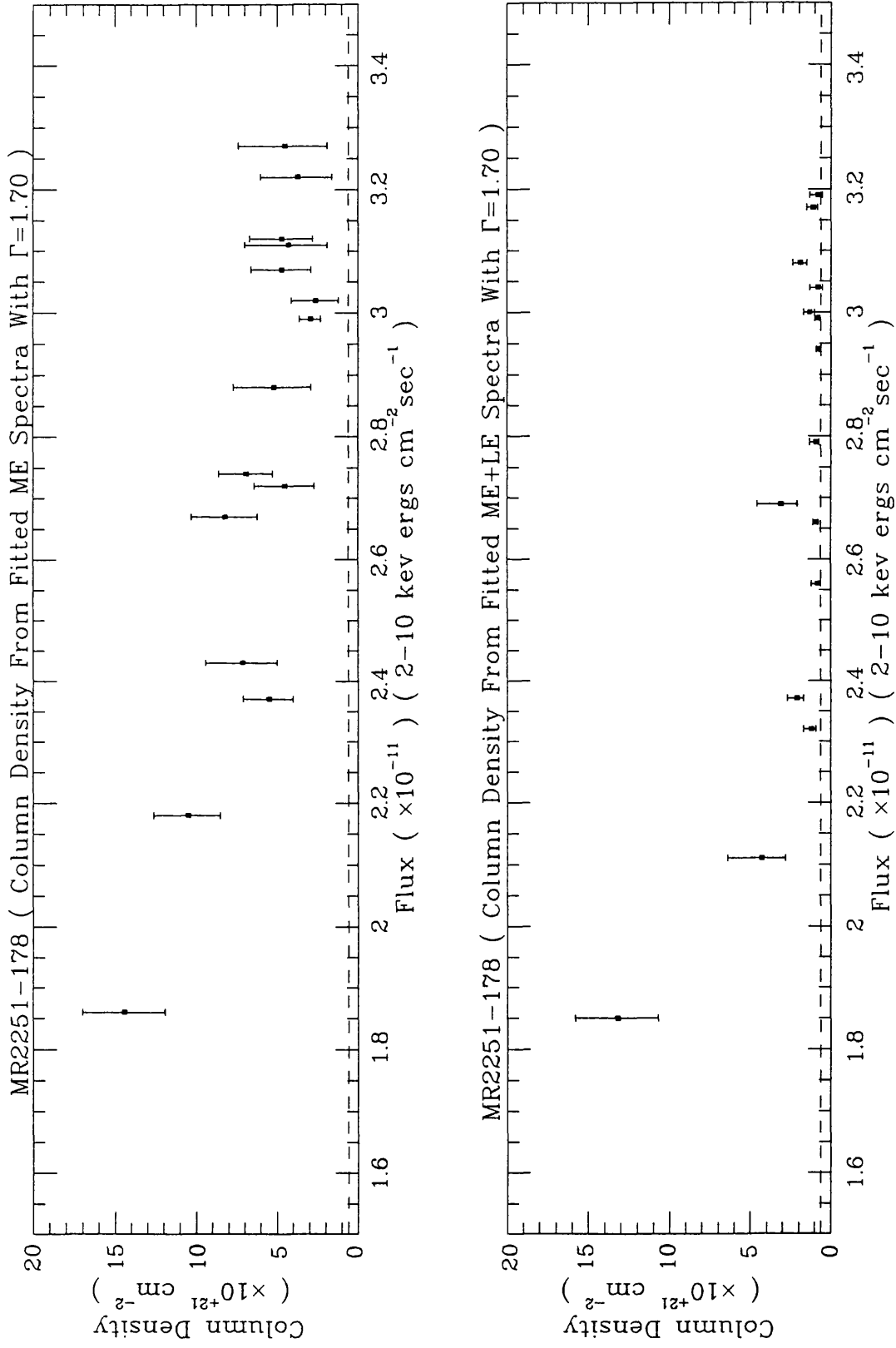


Figure 7.5: Derived column densities as a function of 2-10 keV flux with Γ fixed at 1.70. Top: ME data. Bottom: ME and LE data.

7.4 Models

7.4.1 Two Emission Component Model

Several Seyfert galaxies have been found which exhibit a soft excess at energies below 1 keV (e.g. Arnaud *et al.* 1985; Pounds *et al.* 1986), commonly attributed to emission from the hot, innermost regions of the accretion disc around the central source. A good fit to the X-ray spectra of these objects can generally be obtained by including a second component, either a steep power-law or bremsstrahlung with $kT \sim 0.2$ keV being superimposed on the canonical power law AGN spectrum. However, a complex spectrum with two power-law components fails to give good fits to the observed spectra of MR 2251–178, unless both the normalizations and the power-law index of the second component are allowed to vary independently. The two component model also fails to explain simultaneously the soft excess *and* the variable absorption observed and as it is an *ad hoc* model with more complexity than the other models discussed below it is not considered further.

7.4.2 Leaky Cold Absorber

A partial-covering model, such as those used to explain the spectrum of NGC 4151 (Holt *et al.* 1980) can be used to fit the observed spectra with reasonable success. With the model suggested by Holt *et al.*, where the variability in column density is caused by random motion of clouds into and out of the line-of-sight, a correlation between the apparent column density, soft X-ray excess and high-energy flux would not be expected, however, particularly as the observed column is too small to influence the spectrum above ~ 4 keV.

7.4.3 Warm Absorber

The warm absorber model (suggested to apply to MR 2251 – 178 by Halpern, 1984) can evidently explain the inverse relationship between column density and source flux, at least in a qualitative manner. As the flux from the central source increases, the material around the source becomes ionized and more transparent. More soft X-rays can then escape, producing a soft X-ray excess and a reduced column density. In particular, if the ionization parameter

at the absorbing material is close to the value at which helium and other light elements up to oxygen become ionized, then quite small changes in the source flux can be sufficient to radically alter the opacity of the material at energies between 0.1 and 1 keV, the energy range over which the *EXOSAT* LE telescopes were most sensitive.

An appropriate photo-ionization code have been used to investigate in more detail the parameter space over which an AGN spectrum would respond in the manner observed for MR 2251 – 178.

1) The Computing Programme

The calculations were performed using the CLOUDY computer programme which was developed by Ferland (e.g. Ferland & Truran 1981) to generate realistic models of photo-ionized nebulae. The programme explicitly includes X-ray interactions with the material. Once the ionizing continuum and nebular characteristics are specified, the physical conditions in a photo-ionized nebula can be computed. The nebula is divided into a large number of spherically symmetric, optically thin zones and the ionizing continuum is then attenuated by the photoelectric opacity of each zone. The emergent spectra are then fitted, in the same way as fitting the observed data, to determine values of N_H .

2) The Incident Ionizing Continuum

The ionizing continuum of MR 2251–178 was approximated by a single power law with photon index of 1.70. A range of luminosities scaled to the minimum and the maximum unabsorbed luminosities in the 2-10 keV band was adopted. For simplicity, and because there is no observational evidence for its existence or luminosity in MR 2251 – 178, a contribution to the ionizing continuum from the XUV ‘bump’ observed in some AGN spectra and attributed to disc emission have not been considered. Examples are shown in Fig 7.6(a)-(b) for the incident/emergent spectra in the cases of low and high ionization parameters.

3) The Absorbing Material

The aim was to seek appropriate ranges for the ionization parameter U , where

$$U = \frac{Q}{4\pi r^2 n_e c} \quad (7.2)$$

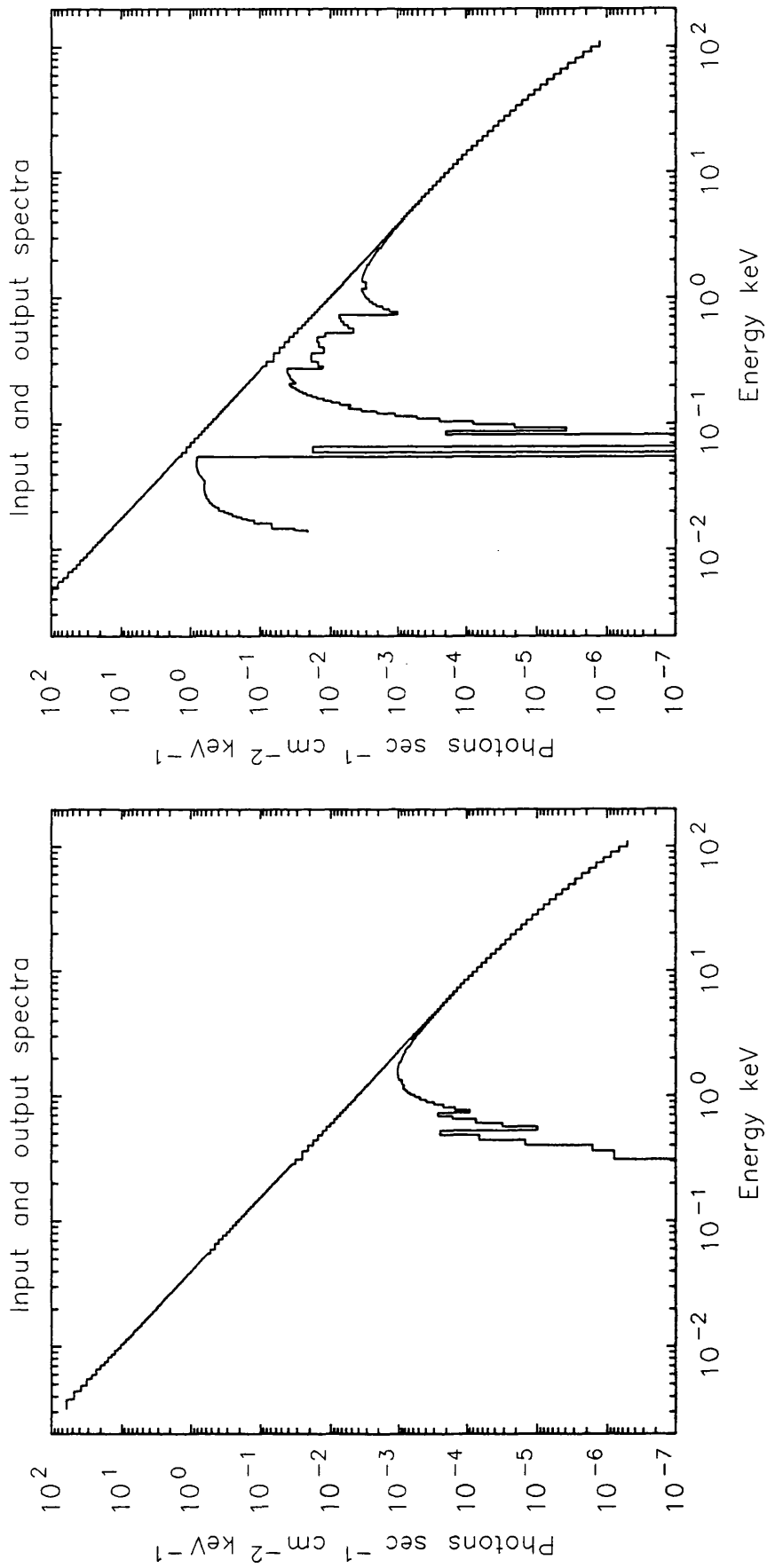


Figure 7.6: Examples of the input and transmitted spectra through the absorbing material at different values of ionization parameter.

such that, for a range in luminosity of a factor of ~ 2 the changes in opacity are sufficient to mimic the observed results. Q is the number of ionizing photons integrated over the energy range 13 eV – 100 keV. Only the continuum spectral distribution over the energy range of ~ 1 -10 keV is known. It is assumed for simplicity that $\Gamma = 1.7$ is appropriate for the entire ionizing continuum, and thus the measured flux can be used as a direct estimate of Q . The critical unknown variables are then the density of the absorbing material, n_e , and its distance from the central source, r . c is the speed of light.

One natural model for the absorbing material is that appropriate for a ‘standard’ BLR cloud (e.g. Kwan & Krolik 1981; Ferland & Mushotzky 1982), with column density $N_H \sim 10^{22 \pm 1} \text{ cm}^{-2}$, cloud density $n_e \sim 10^{9.5 \pm 0.5} \text{ cm}^{-3}$ and distance from the continuum source, $r \sim 5 \times 10^{17} \text{ cm}$, giving an ionization parameter $\text{LOG}(U) \sim -2 \pm 1$. Fig 7.7(a) illustrates the results for this model over the observed flux range. While there is reasonable agreement between the observed and predicted column densities at the highest luminosities the rate of variation is smaller than that observed.

The element which dominates the opacity near 1 keV is oxygen. The ionization parameter at which the K shell electrons are stripped is therefore likely to be appropriate. Fig 7.8 shows the fraction of oxygen in ionization states VI–IX (fully ionized). It can be seen that at $\log(U) \sim 0$ over 50 per cent of the oxygen has a filled K shell. However, as the ionization parameter increases both K shell electrons are rapidly removed, so that by a value of $\text{Log}(U) = 0.25$, oxygen is almost fully ionized. It is therefore required that $\text{Log}(U)$ is around this value if the warm absorber model is to explain the results for MR 2251 – 178.

This ionization parameter is higher than that appropriate for material in the canonical BLR. As the density of the material and its radius are strongly coupled in the calculation of the ionization parameter, the time-scale of variability of MR 2251 – 178 has been used as an indication that the material is closer to the continuum source, rather than being more diffuse. Accordingly a second case where the material is at a radius $r = 3 \times 10^{16} \text{ cm}$ has been modeled. As can be seen from Fig 7.7(b) this does indeed give a range of apparent column densities in better agreement with that observed. It is noted that the total amount of material involved is a few $\times 10^{23} \text{ cm}^{-2}$, substantially higher than the diffuse envelope of optical emission-line gas observed at larger radii from MR 2251 – 178.

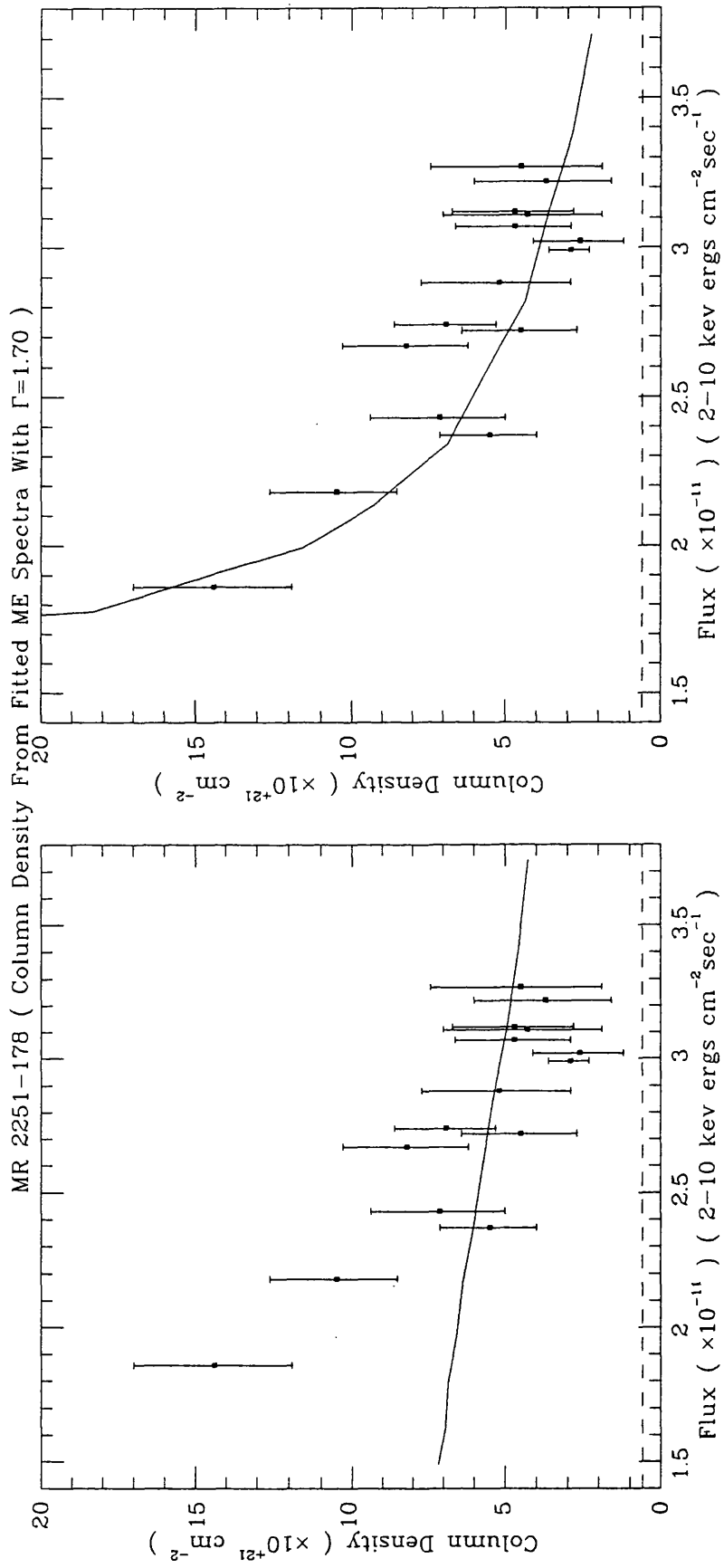


Figure 7.7: The 'effective' column density seen in the ME band as a function of 2-10 keV band as a function of 2-10 keV band for the two cases discussed in the text.

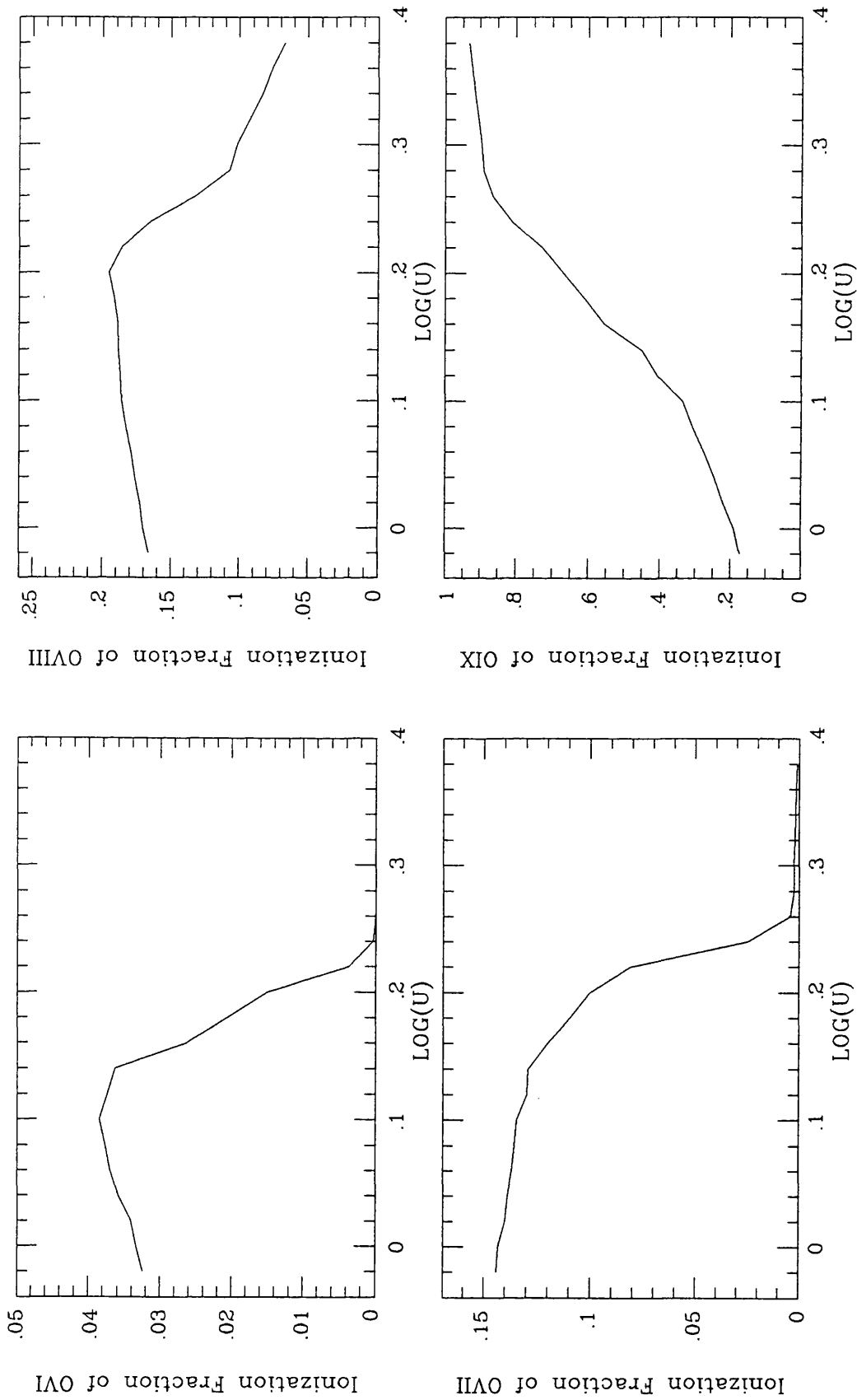


Figure 7.8: Fraction of oxygen in ionization states VI-IX as a function of ionization parameter.

Over the ionization parameter range investigated here it would be expected that the K shells of the high Z elements, particularly iron, would be filled. The low statistics of the short *EXOSAT* observations of MR 2251 – 178 meant only an upper limit of $\sim 10^{24} \text{ cm}^{-2}$ could be obtained for any solar abundance column absorbing at $\sim 7 \text{ keV}$. For the longest observation (day 279, 1983), however, examination of the residuals from the power-law fit did show evidence for a reduction in flux at $\sim 7 \text{ keV}$ (Fig 7.9(a)). Accordingly a further fit to the ME spectrum with additional absorption due to the K-edge of iron was attempted. The best fit column density was $300_{-100}^{+200} \times 10^{21} \text{ cm}^{-2}$, consistent with the total column required to produce the photo-ionized absorption at lower energies. The improvement in the fit with the inclusion of the K-edge opacity is significant (Fig 7.9(b)) with the reduced χ^2_{ν} falling from 1.6 to 0.9. The effective energy of the edge, $7.1 \pm 0.5 \text{ keV}$, is poorly constrained. It is, however, consistent with the majority of iron being in the form of $\sim \text{Fe XV}$, only slightly lower than the $\sim \text{Fe XVIII-XX}$ expected for the ionization parameter appropriate for the flux level of this observation. The upper limit to the strength of a 6.4 keV iron fluorescence line of 200 eV is not strong enough to place any limits on the geometry of the absorbing material.

7.5 Discussion

Evidence is accumulating for significant amounts of ‘cold’ material close to, or perhaps within, the central continuum source of many AGN. The soft emission components found in the X-ray spectra of many AGN in the *EXOSAT* spectral survey (Turner & Pounds 1989) may well be thermal radiation from material with a temperature $\sim 10^6 \text{ K}$. Recent reports of iron absorption features in several Seyfert galaxies (Nandra *et al.* 1989; Pounds *et al.* 1989; Matsuoka *et al.* 1989) suggest significant columns of material with $N_H \sim 10^{23}$, similar to the column found here for MR 2251 – 178. Similar results to those reported here have been found for the location and ionization of material around NGC 4151 (Yaqoob, Warwick & Pounds 1989).

MR 2251 – 178 is, by far, the highest luminosity object in which such material has yet been detected and suggests that this matter is a common feature of AGN, as recently suggested from a theoretical standpoint by Ferland & Rees (1988) and Lightman & White (1988). If MR 2251 – 178 is a black hole radiating at the Eddington limit then it would have a mass of $\sim 10^7 M_{\odot}$. At 10-100 Schwarzschild radii the ionization parameter deduced above would

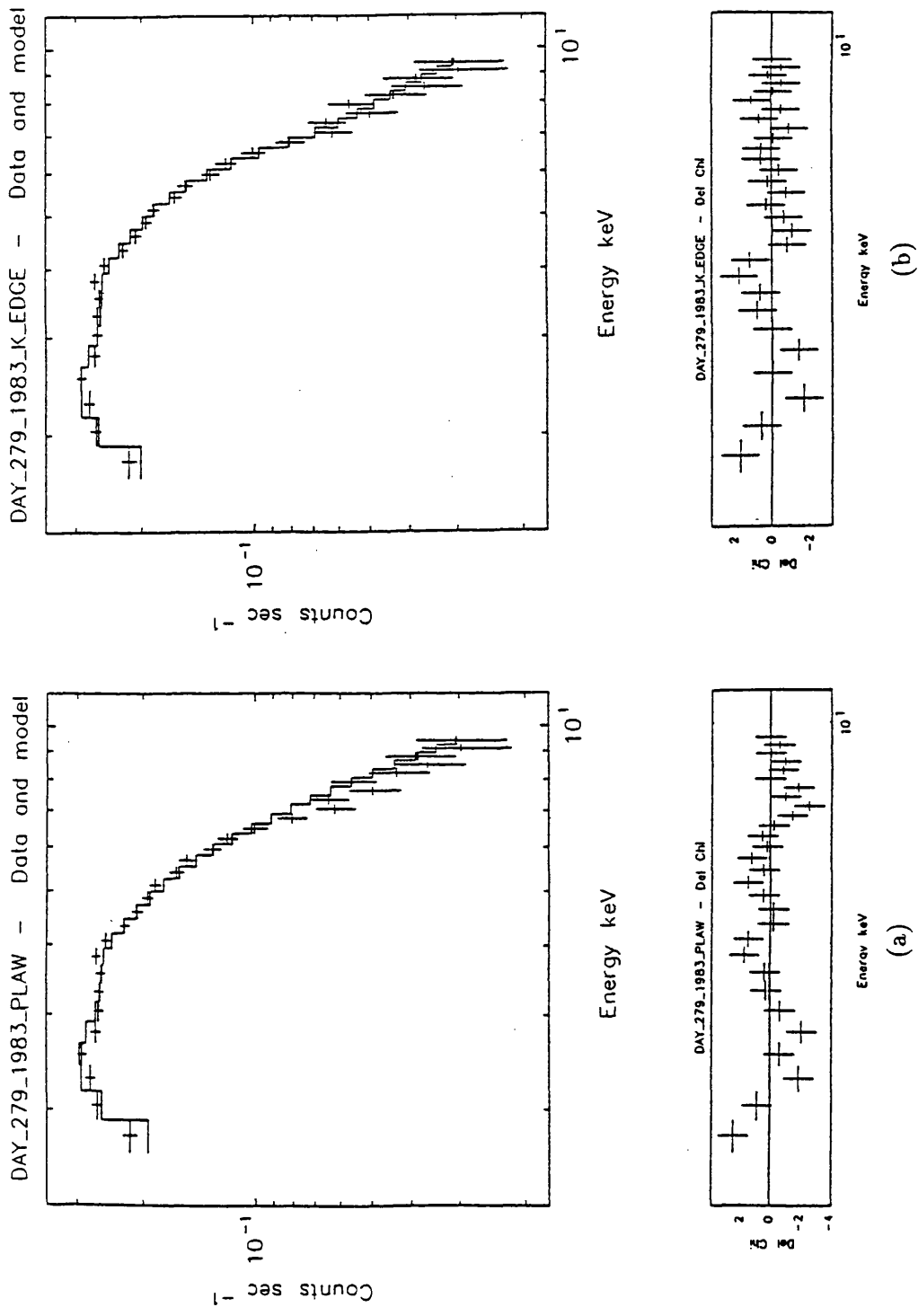


Figure 7.9: (a) Simple power-law and cold absorption fit to the ME data of day 279, 1983 and the residuals. (b) As (a) but with the inclusion of additional absorption from the ion K-edge. Note the improvement in the fit between 7 and 10 keV.

require the material to have a density of $\sim 10^{13} - 10^{14} \text{ cm}^{-3}$, very similar to that suggested by Guilbert & Rees (1988), to be responsible for the production of the XUV bump through reprocessing of the non-thermal continuum radiation.

7.6 Conclusions

MR 2251 – 178 was monitored on 15 observations over the period from 1983 October to 1984 December with the *EXOSAT* Satellite. Significant intensity variability was observed by both the *EXOSAT* LE and ME telescopes. The variations of ME and LE fluxes are moderately well correlated although there is an excess emission in soft X-ray band below 1 keV. The X-ray spectrum of MR 2251 – 178 can be described with a single power-law spectral form in which the photon index is consistent with the canonical value 1.70. A variation in absorbing column density is found and there are correlations between the soft X-ray excess, column density variability and source luminosity.

The behaviour observed in MR 2251 – 178 can be explained by a model in which the absorbing material is partially ionized by the flux from the central source. Varying degrees of photo-ionization caused by intrinsic luminosity variations of the source give rise to both the soft X-ray excess seen in the LE at times of high luminosity and to the variations in absorbing column density inferred from the spectrum above 1 keV. The amount and location of the absorbing material is similar to that inferred for a number of Seyfert galaxies, but on this occasion in an object of much higher luminosity.

Chapter 8

Conclusions

8.1 Introduction

In this thesis, two rather different objects, the galactic binary source SS 433 and the QSO MR 2251 – 178, have been studied. In Chapter 3 & 4, results of the X-ray observations of SS 433 with the *EXOSAT* and *GINGA* satellites were presented. These have revealed many characteristics of the X-ray spectrum and the time variability of SS 433. Based on the *EXOSAT* and *GINGA* observations, some constraints on the system geometry were derived in Chapter 5 and the physical properties of SS 433 jets discussed in Chapter 6. The results of the *EXOSAT* observations of MR 2251 – 178 were reported in Chapter 7, and a photoionization model adopted in explaining the variable absorption and soft excess in the X-ray spectrum of the QSO MR 2251 – 178.

Here in the final chapter of this thesis, the work on the X-ray observations of SS 433 and MR 2251 – 178 is summarized (Section 8.2). The problems left by the current study on SS 433 and MR 2251 – 178 are reviewed in Section 8.3 and future work required on these two objects are suggested. In Section 8.4, the relevance of SS 433 to the understanding of astrophysical jets and active galactic nuclei is discussed.

8.2 Summary of the Work Reported in This Thesis

8.2.1 SS 433

1) The X-ray Observations

SS 433 was intensively monitored by both the *EXOSAT* and *GINGA* satellites. In the period of 1983 October-1985 October, a total of 15 separate observations was made over the various phases of jet precession and orbital motion of SS 433 using the LE telescopes, ME detectors and the Gas Scintillation Proportional Counter aboard the *EXOSAT* observatory with a total effective exposure time of ~ 9 days. Three *GINGA* observations of SS 433, each centered at the primary optical minimum and lasted for ~ 5 days, were made in 1987 May, 1988 May and 1989 May with the *GINGA* Large Area Counter. Except for the *EXOSAT* GSPC data, all these data have been carefully analyzed and the results have been reported in Chapter 3 (for *EXOSAT* observations) and Chapter 4 (for *GINGA* observations) of this thesis. The theoretical modelling of the system geometry and the physical properties of the X-ray jets is based on these observations.

Many features of SS 433 are revealed in the *EXOSAT* and *GINGA* observations. Both the X-ray intensity and spectrum are found to vary over the periods of the jet precession and orbital motions.

Over the 163 day jet precession phase of SS 433, the X-ray source is at its highest luminosity when the top jet approaches the observer and the jet axis is in the line of sight, and reaches its lowest luminosity when the jets change from edge-on to the lower jet approaching the observer. Up to a 50% intensity decrease can be seen in each energy channel while the source changes from high to low luminosity.

An X-ray eclipse by the companion star was observed five times by the *EXOSAT* and *GINGA* satellites. The eclipses occurred at the phase of the primary optical minimum and were at jet precession phases of 0.0, 0.06, 0.58, 0.62, 0.83 respectively. The simultaneous optical monitoring of SS 433 over one binary cycle at jet precession phase around 0.6 together with *EXOSAT* clearly showed that the X-ray eclipse was completely coincident with the primary optical luminosity drop. The *GINGA* observations represent the three best sampled eclipses. These observations show that the configuration of the eclipse is variable over the jet precession

phase.

The X-ray spectrum of SS 433 consists of an underlying thermal continuum and a broad emission line feature. The spectrum can be approximately described by a combination of a thin-thermal bremsstrahlung as the continuum, a Gaussian profile for the line feature and neutral hydrogen absorption. Modulation of both the jet precession and orbital motion on the X-ray spectrum are found from the *EXOSAT* and *GINGA* observations.

Over the 163 day jet precession phase, the bremsstrahlung temperature varies from $16.34_{-1.35}^{+1.72}$ keV at phase 0.0 when the source is at low luminosity to $25.54_{-0.78}^{+1.03}$ keV at phase 0.58 when the source is bright. All parameters, which describe the X-ray emission line feature, vary with the precession of jets. The Doppler energy shift profile of the X-ray iron line is completely consistent with the prediction from the ‘standard kinematic model’, suggesting that the X-ray emission line comes from the jets. The line flux changes following the variation of the X-ray continuum over 163 day cycle, implying that the equivalent width of the line stays roughly constant and the X-ray continuum is associated with the line emission. The line width becomes widest when the line energy is maximally Doppler blue-shifted and narrow when the line energy is least Doppler-shifted. Large variations of the bremsstrahlung temperature and the line flux are observed over the 13 day binary cycle. The line energy and width, however, stay fairly constant. The equivalent width of the line is also constant over the eclipse, again indicating that the X-ray line and continuum are from the same regions.

There is no obvious modulation on the equivalent neutral hydrogen absorbing column density by the jet precession and binary motion. It is consistent with $8 \times 10^{21} \text{ cm}^{-2}$, lower than the value derived from the optical observations. This may suggest that the soft X-ray excess might present in the X-ray spectrum of SS 433.

A possible transition period from X-ray quiescent to active states may have been observed between 1987 May 22.0-23.0 with *GINGA*, possibly implying that the accretion rate of SS 433 is in the range of $10^{-5} \sim 10^{-3} M_{\odot} \text{ y}^{-1}$.

2) Geometrical Models

Based on the concepts of ‘standard kinematic model’, a general mathematical description of the system geometry is presented in this thesis. Detailed discussion of the configuration and

parameters of the SS 433 geometry are carried out using this mathematics.

The uncertainty of the visibility of the receding jet leads to the discussion of the system geometry in three mass ratio regions, $q < 0.174$, where the compact object is a neutron star and the receding jet is definitely visible; $0.174 < q < 0.566$, in which whether the receding jet is visible or not depends on the disc geometry; and $0.566 < q < 1.7$, where the receding jet is definitely covered by the accretion disc. The discussions in Chapter 6 indicate that geometrical models with a neutron star as the compact object are not adequate in explaining the X-ray observations. The mass ratio of the SS 433 system is therefore limited in the range of $0.174 < q < 1.7$ in which the compact object is a black hole, if the K-velocity measured by Crampton and Hutching (1981) is correct.

Unless occultations of the X-ray regions by the accretion flow, or by the stellar wind of the normal companion are considered, the jet can not be regarded as thin. A fat jet would require a new mechanism for the large scale acceleration of jets.

3) Jet's Physical Properties

Model independent profiles of the temperature and electron density of jets are directly derived from the *GINGA* observations in this thesis. These profiles put strong constraints on the jet properties and jet formation mechanisms.

The results suggest that the X-ray radiating material are continuous supersonic plasma flow ejected from the funnels of the thick accretion disc. After exiting from the funnels, the jet's plasma cools rapidly due to adiabatic expansion, Compton scattering and radiation losses. In the transit region between the X-ray and optical emitting jets, the jets are re-heated by photo-ionization and mechanical heating so that the jet cooling is slowed down.

4) General Picture of SS 433

A general scenario of the galactic binary source SS 433 becomes gradually clear through the work of this thesis. The binary consists of a massive companion star and a black hole surrounded by a supercritical thick accretion disc, from whose funnels two opposite, well collimated jets are generated. Both X-ray continuum and line emissions originate in the jets and are thermal in nature. The X-ray properties of SS 433 are greatly modulated by the relativistic motion of the jet material, the jet precession and orbital motion.

8.2.2 QSO MR 2251 – 178

MR 2251–178 was monitored over the period of 1983 October-1984 December in a programme of 15 *EXOSAT* observations. In this period, the hard X-ray flux varied by factor of 2. While there is an overall correlation between the ME(2-10 keV) and LE(0.1-2 keV) fluxes the pattern of variability is such that it can not be described by simple intensity, absorption or slope variations. The source spectrum also shows, when bright, an excess at soft energies above that which would be predicted by extrapolating the power-law and absorption found from the ME spectrum.

It is found that it is possible to explain all the observed features by adopting the ‘warm’ absorber model in which the absorbing material is partially ionized by the flux of extreme ultra-violet and X-ray photons from the central continuum source. The opacity profile of the absorbing material is then a function of the source luminosity. Using a photo-ionization code and adopting appropriate parameters for MR2251-178, it is found that the observed correlation of opacity with source luminosity can be reproduced.

The preferred location of the absorbing material is close to the central continuum source. The recent evidence for ‘cool’ material in the very centre of Seyfert galaxies is thus extended to include an object of significantly higher luminosity.

8.3 Future Prospects

8.3.1 Future Observations of SS 433 & MR 2251 – 178

1) SS 433

Two main uncertainties exist in the X-ray data obtained with *EXOSAT* and *GINGA* satellites. The first one is on the structure of the X-ray iron lines; the second is on the nature of the soft X-ray emissions.

The constraints on the geometry of SS 433 strongly depend on the ratio of the emission lines from the approaching and receding jets. Whether or not there is a signature of the Doppler red-shifted line in the X-ray spectrum of SS 433 during the *GINGA* 1987 May observations

leaves the system mass ratio and geometrical parameters uncertain. Observations with better energy resolutions around 7 keV in the future will be crucial in distinguishing the nature of the compact object and to determine the geometrical parameters of SS 433. In addition, a clear picture on the X-ray iron line will be important in fully determining the physical conditions in the jets of SS 433.

The behaviour of the soft X-ray emissions from SS 433 is largely unknown. Although the *EXOSAT* telescope made observations over several cycles of the jet precession, the *EXOSAT* filter data were insufficient to accurately characterize the spectrum of SS 433 between 0.1-2 keV. Observations presented in this thesis indicate a soft X-ray excess may exist in the X-ray spectrum and this affects the determination of the nature of the ME spectrum of SS 433. In the *GINGA* observations made in 1988 and 1989 May, the soft X-ray flux remains fairly constant over the eclipse, which is difficult to completely understand. Future investigations in the soft X-ray emissions from the central objects and the lobes of SS 433 are necessary to understand the nature of the X-ray radiations and the interaction of the jets with the ambient medium.

2) MR 2251 – 178

Evidence for the cold absorption of the iron K-edge is found in the spectrum of MR 2251 – 178. However, due to the poor statistics of the data, the column density and the effective energy of the edge are poorly constrained. From the results of the *EXOSAT* observations, it is not possible to accurately locate the ionized material, which is responsible for the absorption of the soft X-ray flux. Observations using an instrument with a good resolution around 7 keV are important to determine the intrinsic continuum of the QSO and understand the physical conditions of MR 2251 – 178. Observations over the soft X-ray energy band will determine the characteristics of the soft X-ray spectrum of MR 2251 – 178 and provide information about the accurate location and physical conditions of the ionized cloud.

3) Possible Facilities for the Future Observations

In summary, studies of both SS 433 and MR 2251 – 178 require further observations with good energy resolution at around 7 keV and covering the energy band below 2 keV. The X-ray satellites *ROSAT* and *SPECTRUM-X* are two facilities which satisfy these requirements.

ROSAT, the German X-ray satellite, is currently scheduled for launch in March 1990. Its general objects are to perform an all-sky in the X-ray and XUV bands and to conduct pointing observations. The payload of the satellite contains the German X-ray Telescope (XRT), which operates in the soft X-ray band (0.1-2 keV), and the UK Wide Field Camera (WFC), which operates in the XUV band (0.02-0.2 keV). It is hoped that *ROSAT* observations of SS 433 & MR 2251 – 178 will provide valuable information on the nature of these two objects over the energy band which is largely unknown.

The USSR X-ray satellite *SPECTRUM-X* is due for launch in 1993. The combined response of this project extends over the range of 20 eV-100 keV. The Joint European X-ray Telescope, JET-X, is one of the core instruments aboard the satellite and covers energy band of 0.15-10 keV. The spatial resolution of JET-X is 30 arcsecond or better. The telescope is designed with particular emphasis on high sensitivity and spectral resolution ($\frac{E}{\Delta E} \geq 50$) around the 7 keV Fe-line complex, which is well suited to study the spectral features of SS 433 and MR 2251 – 178.

8.3.2 Future Theoretical Modelling of SS 433

1) Geometrical Modelling

Although the future observations will provide important information about the system geometry, it is theoretically possible, by using the current *EXOSAT* and *GINGA* data, to establish a self-consistent geometrical model for SS 433. To do this work, a detailed study on the structure of the companion star, the effects of the stellar wind and the structure of the accretion flow is necessary. Once a good understanding of these problems is reached, the system parameters, such as the mass ratio, the sizes of the companion star and accretion disc, the dimensions of jets etc, can be obtained by fitting the X-ray light curves over each energy channel. A good understanding of the physical conditions in the jets of SS 433 may be necessary. However, the temperature and electron density profiles to a good approximation can be assumed to be an exponential function.

2) Physical Modelling

The approximation of the X-ray iron line with a Gaussian profile is not fully adequate.

Searching for a good model to describe the line profile is necessary. If the line broadening is due to the X-ray line photons scattered by high energy electrons, the broadened line profile can be regarded as two power laws with different index. In fact, the X-ray spectrum of SS 433 from the *GINGA* observations has been fitted by a combination of a bremsstrahlung and two power law located around the predicted iron line energy. The model can achieve a considerable reduction in the χ^2 and better fit to the line feature. A detailed physical model in which the X-ray lines are broadened due to the Compton scattering should be developed. This will be important in explaining the 163 day modulation of the line width and understanding the physical conditions inside the SS 433 jets. At the same time the relationship of the X-ray continuum and line radiations in the jets of SS 433 must be modeled.

Detailed physical processes involved in the jets of SS 433 should be investigated in the future. The temperature profile derived in this thesis can be regarded as a basis for this modelling.

8.4 SS 433, Astrophysical Jets and AGN

As shown in chapter one, well-collimated, jet-like outflows are widely observed from extragalactic objects to galactic sources. Although there are important differences among the jets from SS 433, newborn stars and active galactic nuclei, their structural analogies suggest that similar hydrodynamic phenomena may underlie the dynamics of the flow over a wide range of spatial scales.

The jets in SS 433 and extragalactic objects are both well-collimated plasma, moving at relativistic velocity. Radio observations indicate that the radio jets of SS 433 are twisted due to the precession of the direction of ejection, which may explain some similarly shaped extragalactic sources. Furthermore, the jets of SS 433 extend over an enormous range of length scales. Their interaction with the ambient medium and with W50 produce some phenomena which may also occur in the broad and narrow line regions of active galactic nuclei and in their outer radio lobes. In the X-ray energy range, although the SS 433 spectrum turns out to be thermal, it is of interesting to point out that when the continuum is fitted with a power-law model, the photon index varies in the range of $1.4 \sim 2.0$, very similar to the case of an AGN spectrum. Jets similar to those in SS 433 could thus be the intrinsic radiation source in AGN.

Of more important is that similar physics is involved in the acceleration, initial collimation of jets of SS 433 and AGN. The jets originate in the funnels of a thick accretion disc, as a result of the accretion of material onto a compact object. The configuration of such a thick accretion disc with two narrow funnels along its rotation axis can be obtained both for supercritical accretion rates, leading to dense, radiation supported bright discs (Calvani and Nobili, 1983), and subcritical accretion rates, leading to tenuous, cool, ion-pressure-supported discs (Rees *et al.* 1982). In latter case, matter can be accelerated inside the funnels by electromagnetic processes and only non-thermal radiations are generated.

The close distance of SS 433 offers a chance to study this galactic binary in much greater details than distant AGN. The modulations on the radio, optical and X-ray properties of SS 433 by its 163 day precession and 13 day orbital periods make it possible to derive strong constraints on the binary system, its jets and finally, its central engine so that the physics involved in SS 433 and AGN can be understood. Studying of SS 433, as a scaled-down version of active galactic nuclei, will therefore help us in gaining an insight in AGN phenomena which, to some extent, are still mysterious.

Appendix A

Transformation of Coordinate Systems Used for Analysis of SS 433

A.1 Coordinate System in the Plane of Sky

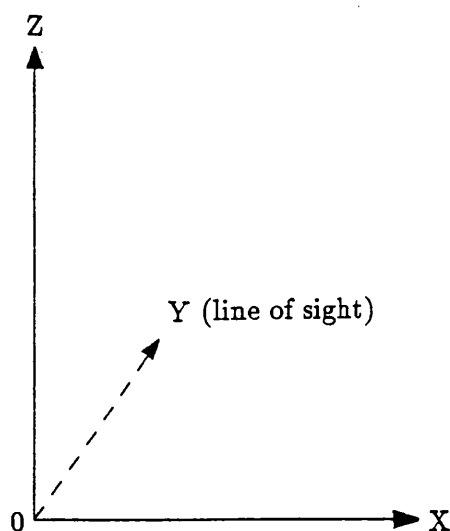


Figure A.1: Sky System

A cartesian coordinate system (called the Sky System, hereafter) in the plane of sky can be defined to quantitatively describe the motion of SS 433. As shown in Fig A.1, the origin of the coordinates is chosen to be the compact object, the x-z plane represents the sky plane,

and the y-axis is the line of sight.

A.2 Coordinate System Centered on the Accretion Disc

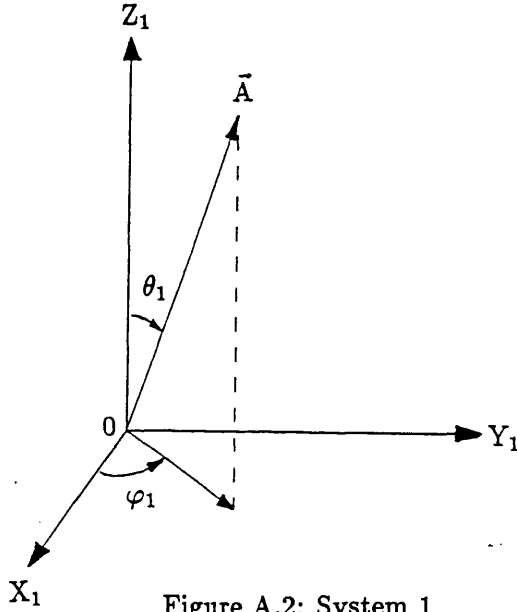


Figure A.2: System 1

As shown in Fig A.2, consider a right-handed coordinate system (x_1, y_1, z_1) with its origin at the centre of the compact object of SS 433, the x_1 - y_1 plane on the accretion disc and the z_1 -axis along the direction of the upper jet. If \hat{x}_1 , \hat{y}_1 , and \hat{z}_1 are defined as the unit base vectors, an arbitrary vector \vec{A} in this system, called System 1, thereafter, may be written

$$\vec{A} = (A \sin \theta_1 \cos \varphi_1, A \sin \theta_1 \sin \varphi_1, A \cos \theta_1) \quad (\text{A.1})$$

where the ranges of values of the radial distance A , the polar angle θ_1 and the azimuth angle φ_1 are $0 \leq A < \infty$, $0 \leq \theta_1 \leq \pi$, and $0 \leq \varphi_1 \leq 2\pi$ and are shown in Fig A.2.

A.3 Coordinate System Centered on the Orbital Plane

Similar to the definition of System 1, another right-handed coordinate system (called System 2, hereafter) is set up on the orbital plane and illustrated in Fig A.3. Here the centre of compact object is still taken as the origin, the orbital plane is assumed as the x_2 - y_2 plane,

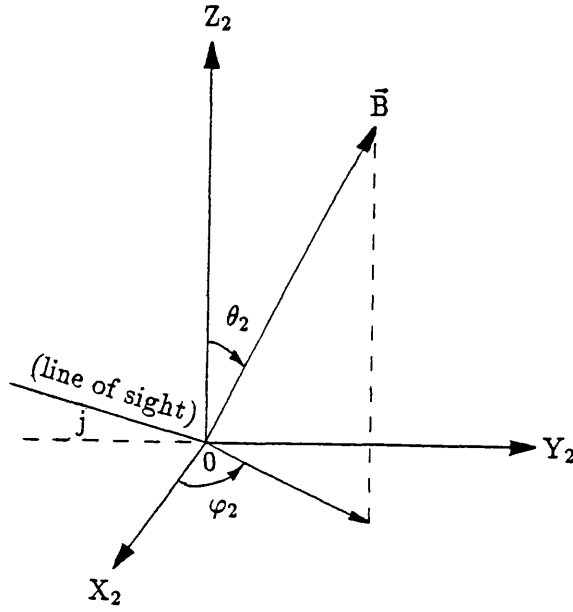


Figure A.3: System 2

and the orbital angular momentum vector as the z_2 -axis direction. For simplicity, it is assumed that the line of sight is perpendicular to the x_2 -axis, i.e., inside the y_2 - z_2 plane.

By the choice of definitions of θ_2 , the polar angle, and φ_2 , the azimuth angle, a vector \vec{B} in System 2 is

$$\vec{B} = (B \sin \theta_2 \cos \varphi_2, B \sin \theta_2 \sin \varphi_2, B \cos \theta_2) \quad (\text{A.2})$$

where B is the radial distance.

A.4 Transformation of System 1 To System 2

To a very good approximation, the jets and accretion disc only precess around the orbital angular momentum vector, i.e. the z_2 -axis. Therefore, it is adequate to fix the y_1 -axis of System 1 in the x_2 - y_2 plane of System 2. If φ_2 is defined as the angle subtended by the projected z_1 in the x_2 - y_2 plane to x_2 -axis and α , as the angle between z_1 -axis and z_2 -axis, i.e., the half precession cone angle of the jets, then in the System 2, the unit base vector \hat{x}_1 , \hat{y}_1 , \hat{z}_1 of System 1 may be written

$$\begin{aligned}
\hat{x}_1 &= (-\cos \alpha \cos \varphi_2, -\cos \alpha \sin \varphi_2, \sin \alpha) \\
\hat{y}_1 &= (\sin \varphi_2, -\cos \varphi_2, 0) \\
\hat{z}_1 &= (\sin \alpha \cos \varphi_2, \sin \alpha \sin \varphi_2, \cos \alpha)
\end{aligned} \tag{A.3}$$

and the vector \vec{A} becomes

$$\vec{A} = \begin{pmatrix} A \sin \theta_1 \cos \varphi_1 & A \sin \theta_1 \sin \varphi_1 & A \cos \theta_1 \\ -\cos \alpha \cos \varphi_2 & -\cos \alpha \sin \varphi_2 & \sin \alpha \\ \sin \varphi_2 & -\cos \varphi_2 & 0 \\ \sin \alpha \cos \varphi_2 & \sin \alpha \sin \varphi_2 & \cos \alpha \end{pmatrix} \begin{pmatrix} \hat{x}_2 \\ \hat{y}_2 \\ \hat{z}_2 \end{pmatrix} \tag{A.4}$$

where $\hat{x}_2, \hat{y}_2, \hat{z}_2$ are the unit base vectors of System 2.

A.5 Expressions of Vectors \vec{A} and \vec{B} in Sky System

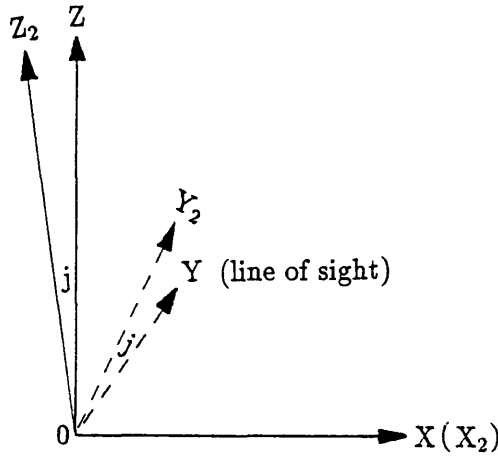


Figure A.4: System 2 to Sky System

The Sky System may easily be obtained by rotating the coordinate axes y_2 and z_2 of System 2 about the x_2 -axis clockwise through an angle j .

As illustrated in Fig A.4, the unit base vectors of System 2 may be written in Sky System as

$$\begin{aligned}
\hat{x}_2 &= (1, 0, 0) \\
\hat{y}_2 &= (0, \cos j, \sin j) \\
\hat{z}_2 &= (0, -\sin j, \cos j)
\end{aligned} \tag{A.5}$$

So, it is convenient to write vector \vec{B} of System 2 in the unit base vector $\hat{x}, \hat{y}, \hat{z}$ of Sky System like

$$\vec{B} = \begin{pmatrix} B \sin \theta_2 \cos \varphi_2 & B \sin \theta_2 \sin \varphi_2 & B \cos \theta_2 \end{pmatrix} \begin{pmatrix} 1 & 0 & 0 \\ 0 & \cos j & \sin j \\ 0 & -\sin j & \cos j \end{pmatrix} \begin{pmatrix} \hat{x} \\ \hat{y} \\ \hat{z} \end{pmatrix} \tag{A.6}$$

Combining Equations (A.4) and (A.5), vector \vec{A} of System 1 may be written

$$\vec{A} = \begin{pmatrix} A \sin \theta_1 \cos \varphi_1 & A \sin \theta_1 \sin \varphi_1 & A \cos \theta_1 \\ -\cos \alpha \cos \varphi_2 & -\cos \alpha \sin \varphi_2 & \sin \alpha \\ \sin \varphi_2 & -\cos \varphi_2 & 0 \\ \sin \alpha \cos \varphi_2 & \sin \alpha \sin \varphi_2 & \cos \alpha \end{pmatrix} \begin{pmatrix} 1 & 0 & 0 \\ 0 & \cos j & \sin j \\ 0 & -\sin j & \cos j \end{pmatrix} \begin{pmatrix} \hat{x} \\ \hat{y} \\ \hat{z} \end{pmatrix} \tag{A.7}$$

Appendix B

Calculation of the Roche Lobe of a Binary System

Consider a binary system with a compact object of mass M_x and a companion star of mass M_s , and set up a Cartesian coordinate system with its origin at M_x , X-axis along the line of centres of M_x and M_s , Z-axis along the vector of the orbital angular momentum, the total potential of a binary system in the Roche approximation can be expressed as (e.g. Pringle 1985)

$$\Phi = -\frac{GM_x}{(x^2 + y^2 + z^2)^{\frac{1}{2}}} - \frac{GM_s}{[(x - a)^2 + y^2 + z^2]^{\frac{1}{2}}} - \frac{1}{2}\Omega^2[(x - \mu a)^2 + y^2] \quad (\text{B.1})$$

where G is the Gravitational constant, a and Ω are the orbital separation and angular speed, $\mu = M_s/(M_x + M_s)$.

The coordinate of the Lagrangian points can be calculated from

$$\begin{aligned} \frac{\partial \Phi}{\partial x} &= 0 \\ y &= z = 0 \end{aligned} \quad (\text{B.2})$$

From Kepler's law, the binary period is

$$P_b = 2\pi \sqrt{\frac{a^3}{G(M_x + M_s)}} \quad (\text{B.3})$$

and angular speed Ω becomes

$$\Omega = \frac{2\pi}{P_b} = \left[\frac{a^3}{G(M_x + M_s)} \right]^{-\frac{1}{2}} \quad (\text{B.4})$$

With the definition of mass ratio $q = M_x/M_s$ and using formula (B.4), equations (B.2) yield a relation for the inner Lagrangian point X_L and mass ratio q ,

$$q(X_L^3 - 1)(X_L - 1)^2 + X_L^2[(X_L - 1)^3 + 1] = 0 \quad (\text{B.5})$$

where the orbital separation a is taken as the unit distance and $0 \leq X_L \leq 1$.

The Roche potential as a function of the inner Lagrangian point X_L can be written as

$$\begin{aligned} \Phi_L &= \frac{1}{GM_s} \left[-\frac{q}{X_L} - \frac{1}{1-X_L} - \frac{1+q}{2} \left(X_L - \frac{1}{1+q} \right)^2 \right] \\ &= \frac{1}{GM_s} \Phi'_L \end{aligned} \quad (\text{B.6})$$

where

$$\Phi'_L \equiv -\frac{q}{X_L} - \frac{1}{1-X_L} - \frac{1+q}{2} \left(X_L - \frac{1}{1+q} \right)^2 \quad (\text{B.7})$$

Combining formula (B.1) and (B.6), the equation of the Roche lobe of the binary system is obtained in the form of

$$-\frac{q}{(x^2 + y^2 + z^2)^{\frac{1}{2}}} - \frac{1}{[(x-a)^2 + y^2 + z^2]^{\frac{1}{2}}} - \frac{(1+q)}{2} \left[\left(x - \frac{1}{1+q} \right)^2 + y^2 \right] = \Phi'_L \quad (\text{B.8})$$

Let $x = z = 0$ in (B.8) and define $A \equiv \frac{1}{2(1+q)} + \Phi'_L$, the maximum extent of the Roche lobe of the compact object M_x in the Y direction can be calculated from the following formula

$$(AY_x + q)(1 + Y_x^2)^{\frac{1}{2}} + Y_x + \frac{1+q}{2}Y_x^3(1 + Y_x^2)^{\frac{1}{2}} = 0 \quad (\text{B.9})$$

Taking $x = y = 0$, Equation (B.8) gives a relation for the mass ratio q and the maximum extent of the Roche lobe of M_x in the Z direction as

$$(AZ_x + q)(1 + Z_x^2)^{\frac{1}{2}} + Z_x = 0 \quad (\text{B.10})$$

Similarly, by taking $x = 1, z = 0$ and $x = 1, y = 0$ in (B.8) and defining $B \equiv \frac{q^2}{2(1+q)} + \Phi'_L$, the equations used to calculate the maximum extents of the Roche lobe of the companion star M_s in the Y and Z directions are obtained,

$$(BY_s + 1)(1 + Y_s^2)^{\frac{1}{2}} + qY_s + \frac{1+q}{2}Y_s^3(1 + Y_s^2)^{\frac{1}{2}} = 0 \quad (\text{B.11})$$

$$(BZ_s + 1)(1 + Z_s^2)^{\frac{1}{2}} + qZ_s = 0 \quad (\text{B.12})$$

The values of X_L , $1 - X_L$ (inner Lagrangian point for M_s), Y_x , Y_s , Z_x , Z_s for different mass ratios q are tabulated in table B.1.

table B.1 Values of Roche lobe as a function of q

q	X_L	Y_x	Z_x	$1 - X_L$	Y_s	Z_s	$1/q$
0.00	0.000000	0.000000	0.000000	1.000000	1.000000	0.666667	∞
0.01	0.141475	0.096129	0.092304	0.858525	0.777774	0.628678	100.00
0.02	0.175443	0.119901	0.115210	0.824557	0.730678	0.609775	50.00
0.03	0.198521	0.136252	0.130973	0.801479	0.699934	0.595306	33.33
0.04	0.216440	0.149071	0.143332	0.783560	0.676735	0.583293	25.00
0.05	0.231255	0.159756	0.153633	0.768745	0.657986	0.572912	20.00
0.06	0.243963	0.168990	0.162531	0.756037	0.642205	0.563717	16.67
0.07	0.255135	0.177161	0.170403	0.744865	0.628557	0.555436	14.29
0.08	0.265130	0.184516	0.177486	0.734870	0.616523	0.547887	12.50
0.09	0.274190	0.191220	0.183939	0.725810	0.605754	0.540940	11.11
0.10	0.282487	0.197393	0.189877	0.717513	0.596008	0.534499	10.00
0.11	0.290148	0.203121	0.195384	0.709852	0.587105	0.528490	9.09
0.12	0.297270	0.208471	0.200525	0.702730	0.578911	0.522857	8.33
0.13	0.303928	0.213495	0.205349	0.696072	0.571320	0.517552	7.69
0.14	0.310182	0.218234	0.209898	0.689818	0.564252	0.512538	7.14
0.15	0.316080	0.222723	0.214203	0.683920	0.557638	0.507783	6.67
0.16	0.321664	0.226989	0.218292	0.678336	0.551424	0.503262	6.25
0.17	0.326966	0.231055	0.222187	0.673034	0.545566	0.498952	5.88
0.18	0.332014	0.234942	0.225907	0.667986	0.540025	0.494834	5.56
0.19	0.336834	0.238665	0.229469	0.663166	0.534770	0.490892	5.26
0.20	0.341444	0.242240	0.232886	0.658556	0.529773	0.487110	5.00
0.25	0.361924	0.258267	0.248176	0.638076	0.507932	0.470218	4.00
0.30	0.379133	0.271935	0.261169	0.620867	0.490014	0.455942	3.33
0.35	0.393986	0.283886	0.272490	0.606014	0.474855	0.443589	2.86
0.40	0.407052	0.294526	0.282532	0.592948	0.461746	0.432715	2.50
0.45	0.418717	0.304127	0.291562	0.581283	0.450217	0.423013	2.22
0.50	0.429248	0.312882	0.299768	0.570752	0.439944	0.414265	2.00
0.55	0.438845	0.320934	0.307288	0.561155	0.430694	0.406307	1.82
0.60	0.447657	0.328392	0.314229	0.552343	0.422290	0.399016	1.67
0.65	0.455800	0.335339	0.320674	0.544200	0.414599	0.392293	1.54
0.70	0.463366	0.341844	0.326687	0.536634	0.407516	0.386061	1.43
0.75	0.470429	0.347960	0.332321	0.529571	0.400959	0.380258	1.33
0.80	0.477050	0.353732	0.337622	0.522950	0.394858	0.374831	1.25
0.85	0.483278	0.359197	0.342625	0.516722	0.389159	0.369739	1.18
0.90	0.489156	0.364388	0.347360	0.510844	0.383816	0.364944	1.11
0.95	0.494720	0.369330	0.351855	0.505280	0.378789	0.360417	1.05
1.00	0.500000	0.374046	0.356131	0.500000	0.374046	0.356131	1.00

Appendix C

Hydrodynamic Equations

With the definitions of \vec{v} , ρ , T as functions of position, \vec{r} , and time, t , conservation of mass is described by the continuity equation:

$$\frac{\partial \rho}{\partial t} + \nabla \cdot (\rho \vec{v}) = 0 \quad (\text{C.1})$$

Because of the thermal motion of its particles the gas has a pressure, P , at each point. For most astrophysical gases, the equation of state of the perfect gas can be used to relate this pressure to the density and temperature, that is:

$$P = \rho k T / \mu m_H \quad (\text{C.2})$$

where $k = 1.60 \times 10^{-9} \text{ erg/keV}$ is Boltzmann constant, $m_H \sim m_p$ is the mass of the hydrogen atom and μ is the mean molecular weight, which equals to 1 for neutral hydrogen, $\frac{1}{2}$ for fully ionized hydrogen, and something in between for a mixture of gases with cosmic abundances, depending on the ionization state.

If the force density, \vec{f} , represents unspecified forces (other than gas pressure) acting on the gases, conservation of momentum for each gas element then the Euler equation gives:

$$\rho \frac{\partial \vec{v}}{\partial t} + \rho \vec{v} \cdot \nabla \vec{v} = -\nabla P + \vec{f} \quad (\text{C.3})$$

The energy conservation law for the gas may be written:

$$\frac{\partial}{\partial t} \left(\frac{1}{2} \rho v^2 + \rho \epsilon \right) + \nabla \cdot \left[\left(\frac{1}{2} \rho v^2 + \rho \epsilon + P \right) \vec{v} \right] = \vec{f} \cdot \vec{v} - \nabla \cdot \vec{F}_{rad} - \nabla \cdot \vec{q} \quad (\text{C.4})$$

where ϵ is the internal energy per unit mass, which depends on the temperature T of the gas, \vec{F}_{rad} is the radiative flux vector, and \vec{q} is the conductive flux of heat.

For a monatomic gas, the internal energy is

$$\epsilon = \frac{3}{2} kT / \mu m_H \quad (\text{C.5})$$

In reality, cosmic gases are not quite monatomic but in practice Equation (C.5) is usually a good approximation.

The term $-\nabla \cdot \vec{F}_{rad}$ in the energy equation gives the rate at which radiant energy is being lost by emission, or gained by absorption, by unit volume of the gas. In the case of thin jet where the gas may be assumed to be optically thin and radiation escapes freely once produced in the gas, the radiative losses $-\nabla \cdot \vec{F}_{rad}$ can be approximated quite simply,

$$-\nabla \cdot \vec{F}_{rad} = - \int j_E dE \quad (\text{C.6})$$

where j_E ($\text{erg s}^{-1} \text{cm}^{-3} \text{keV}^{-1}$) is the emissivity of the gas and E represents photon energy in keV. If thermal bremsstrahlung is assumed in the hot gas radiation, the emissivity (see Tucker, P₂₀₂₋₂₀₆, here frequency $\nu \rightarrow E(\text{keV})$, $T(\text{k}) \rightarrow T(\text{keV})$) is

$$\begin{aligned} j_E(E, T) &= 4.8 \times 10^{-24} T^{-1/2} Z^2 n_e n_z e^{-E/T} \bar{g}_{ff} \quad (\text{erg s}^{-1} \text{cm}^{-3} \text{keV}^{-1}) \\ &= 3.0 \times 10^{-15} E^{-1} T^{-1/2} Z^2 n_e n_z e^{-E/T} \bar{g}_{ff} \quad (\text{photons s}^{-1} \text{cm}^{-3} \text{keV}^{-1}) \end{aligned} \quad (\text{C.7})$$

where $\bar{g}_{ff}(E, T)$ is a velocity averaged Gaunt factor, n_e, n_z are electron and ion densities, and Z is ion charge number.

For a fully ionized gas (temperature above 0.01 keV, roughly) with cosmic abundances, $\Sigma Z^2 n_e n_z = 1.4 n_e^2$, the thermal bremsstrahlung emissivity may be written

$$\begin{aligned}
j_E(E, T) &= 6.8 \times 10^{-24} T^{-1/2} n_e^2 e^{-E/T} \bar{g}_{ff} \quad (\text{erg s}^{-1} \text{ cm}^{-3} \text{ keV}^{-1}) \\
&= 4.2 \times 10^{-15} E^{-1} T^{-1/2} n_e^2 e^{-E/T} \bar{g}_{ff} \quad (\text{photons s}^{-1} \text{ cm}^{-3} \text{ keV}^{-1})
\end{aligned} \tag{C.8}$$

Since the temperature in the X-ray jet of SS 433 is much higher than 0.01 keV, the radiative losses in the jet may be obtained by integrating Equation (C.8) over all frequencies, thus

$$\begin{aligned}
-\nabla \cdot \vec{F}_{rad} &= -\int j_E dE \\
&= 6.8 \times 10^{-24} T^{1/2} n_e^2 g_{ff}(T) \\
&\simeq -8.1 \times 10^{-24} T^{1/2} n_e^2 \quad (\text{when } T > 0.1 \text{ keV, } g_{ff} = 1.2 \pm 0.1) \\
&= -C_1 T^{1/2} n_e^2 \quad (\text{erg s}^{-1} \text{ cm}^{-3})
\end{aligned} \tag{C.9}$$

where

$$C_1 \equiv 8.1 \times 10^{-24} \tag{C.10}$$

The thermal conduction flux, \vec{q} , which measures the rate of thermal energy transport by the gas particle random motions, is proportional to the temperature gradient ∇T . In many cases, ∇T is small enough that this term can be omitted from energy equation.

Appendix D

Configurations of Three Suggested Geometrical Models of SS 433

The configurations of the three self-consistent geometrical models of SS 433, suggested in Chapter 5 (see table 5.1 for detailed parameters of the models), are illustrated graphically in this Appendix. The configurations of each model are shown for the binary phases of before, at and after the primary optical minimum at the jet precession phases when the upper jet approaches the observer (1987 May), the jets are edge-on (1988 May) and the lower jet points to the observer (1989 May). The orbital separation a is used here as the unit of length.

Model A represents the case where the mass ratio of SS 433 is 0.11 and the compact object is a neutron star. Fig. D.1-D3 give the configurations of the star, disc and jets in the eclipses of 1987 May, 1988 May and 1989 May. The size of the star is that of the Roche lobe. Fig. D.4 gives the projections of the star and disc on the jet axis.

Model B & C are the cases where a black hole is suggested for the compact object. The configurations are plotted in Fig. D.5-D.8 for Model B with mass ratio $q=0.4$, and in Fig. D.9-D.12 for Model C with $q=1.2$. The effects of the stellar wind and accretion flow are considered in these two models when modelling the companion star, and the companion star therefore looks bigger than its Roche lobe.

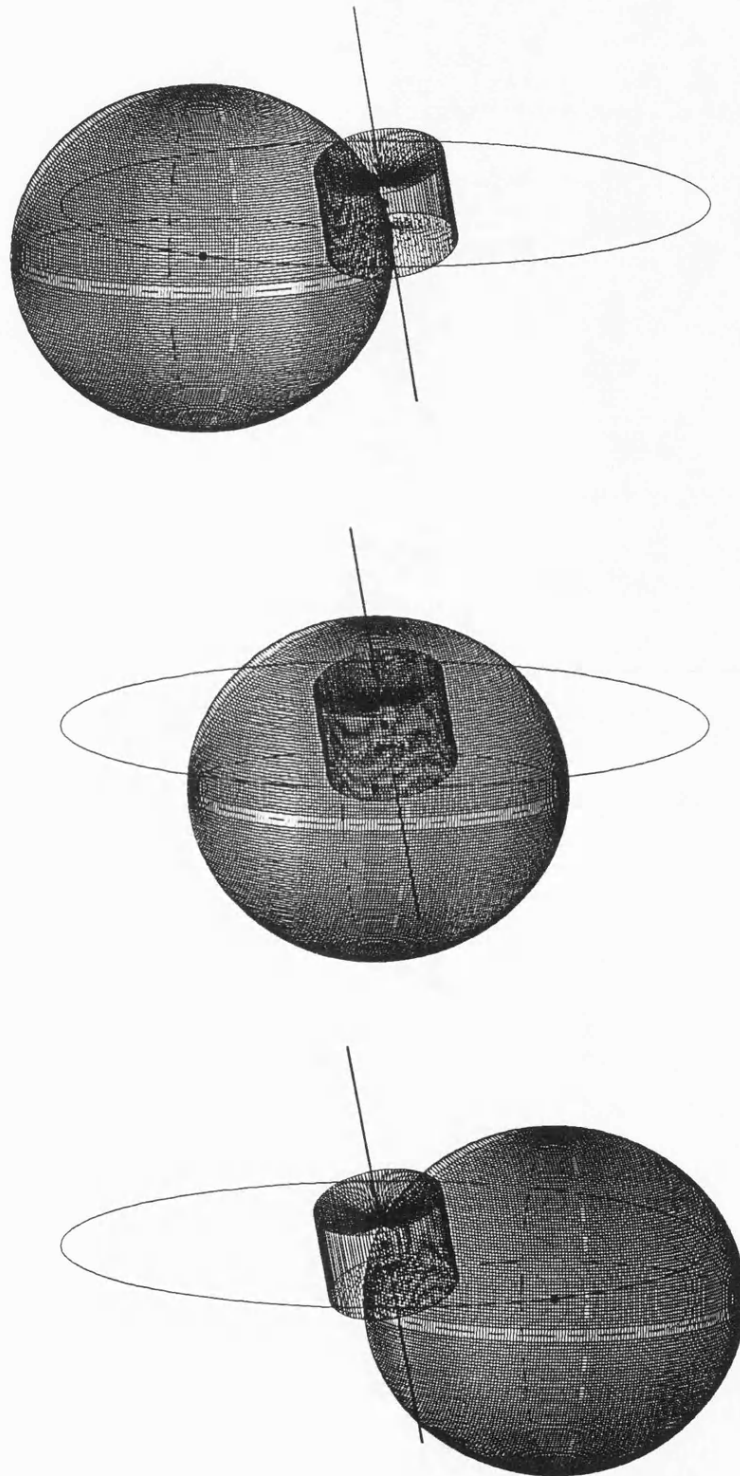


Figure D.1: Configurations of Model A ($q=0.11$) in 1987 May (jet precession phase = 0.58). Top: at binary phase 0.90; Mid: at 0.99; Bottom: at 1.08. The size of the star equals its Roche lobe.

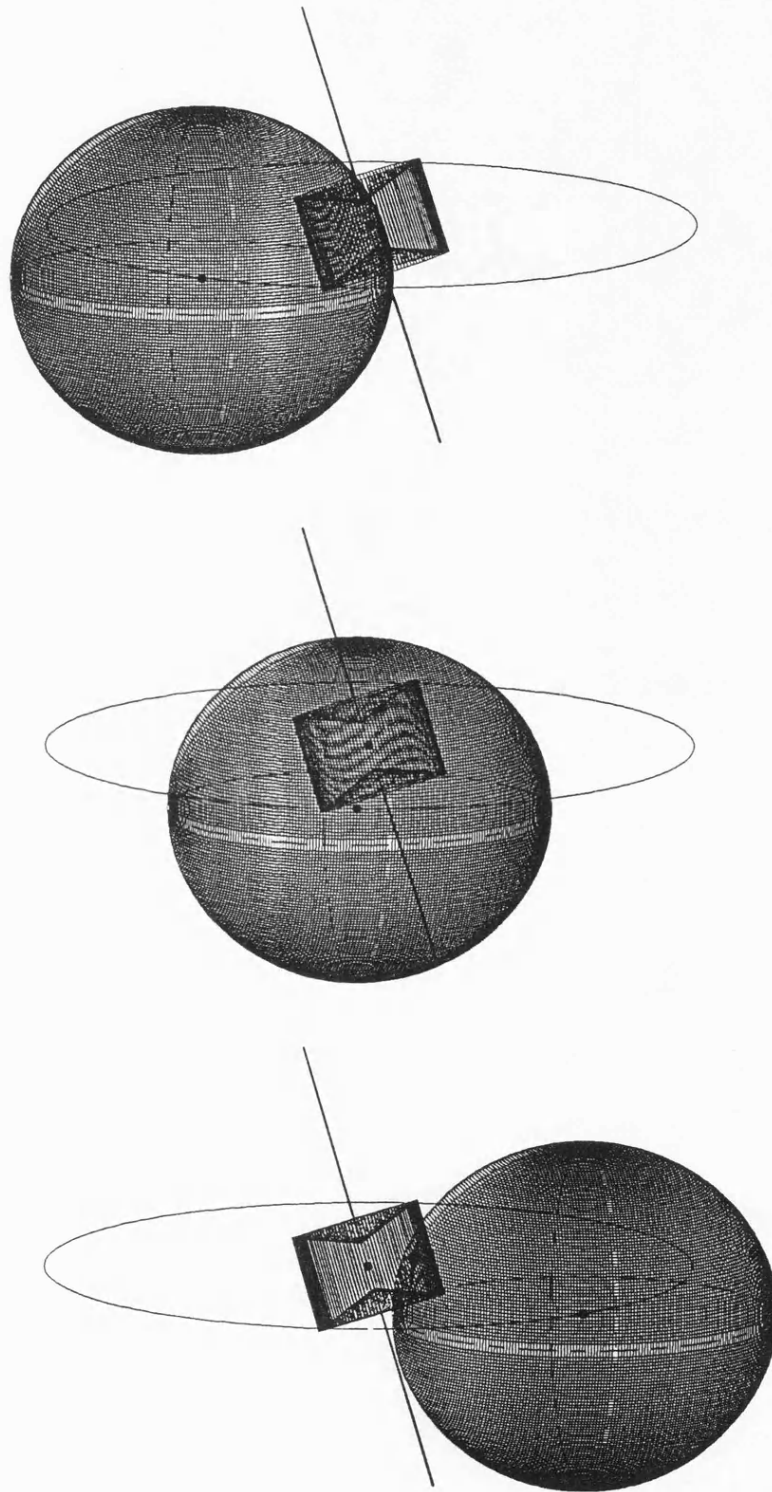


Figure D.2: Configurations of Model A ($q=0.11$) in 1988 May (jet precession phase: 0.83). Top: at binary phase 0.91; Mid: at 0.99; Bottom: at 1.12. The size of the star equals its Roche lobe.

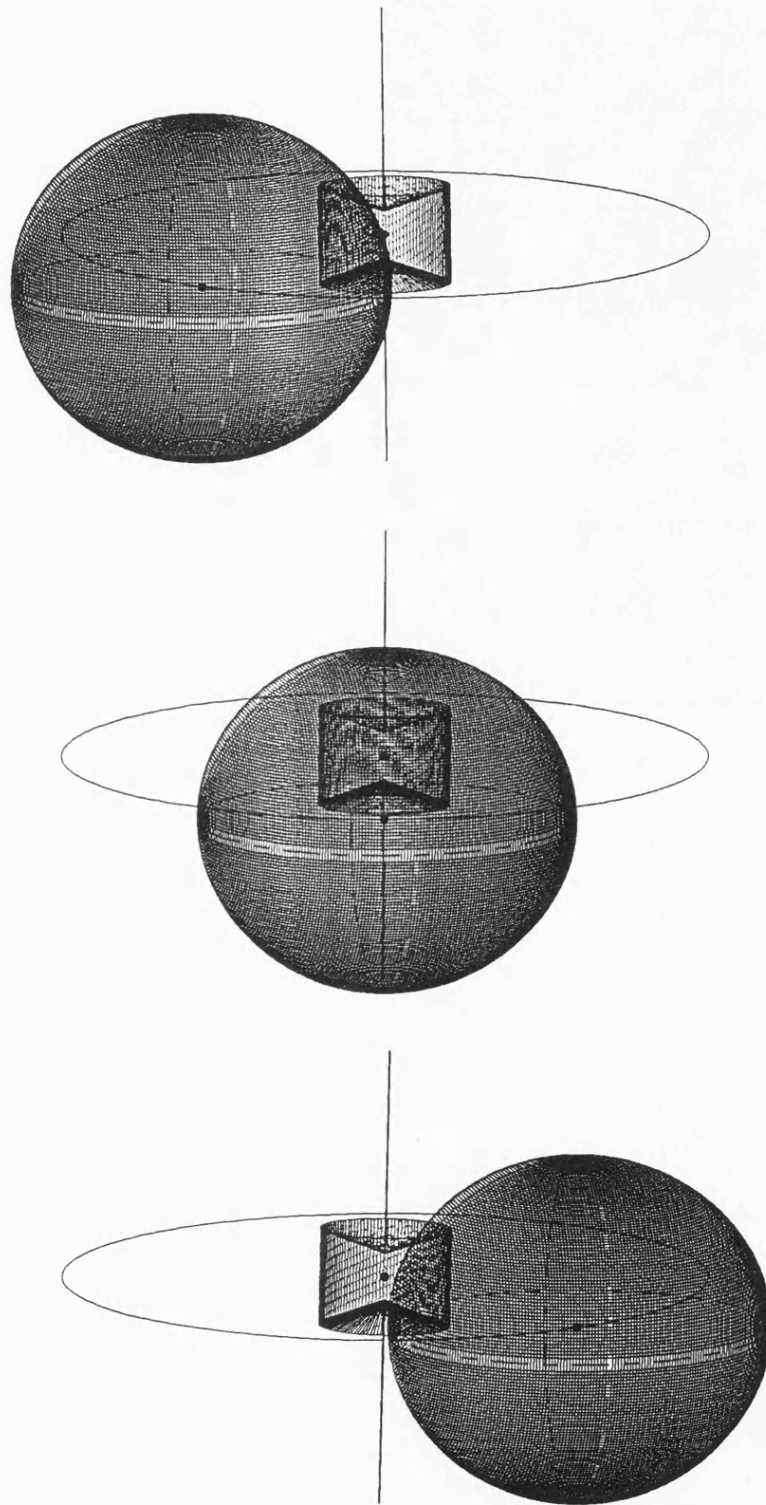


Figure D.3: Configurations of Model A ($q=0.11$) in 1989 May (jet precession phase: 1.0). Top: at binary phase 0.90; Mid: at 1.00; Bottom: at 1.10. The size of the star equals its Roche lobe.

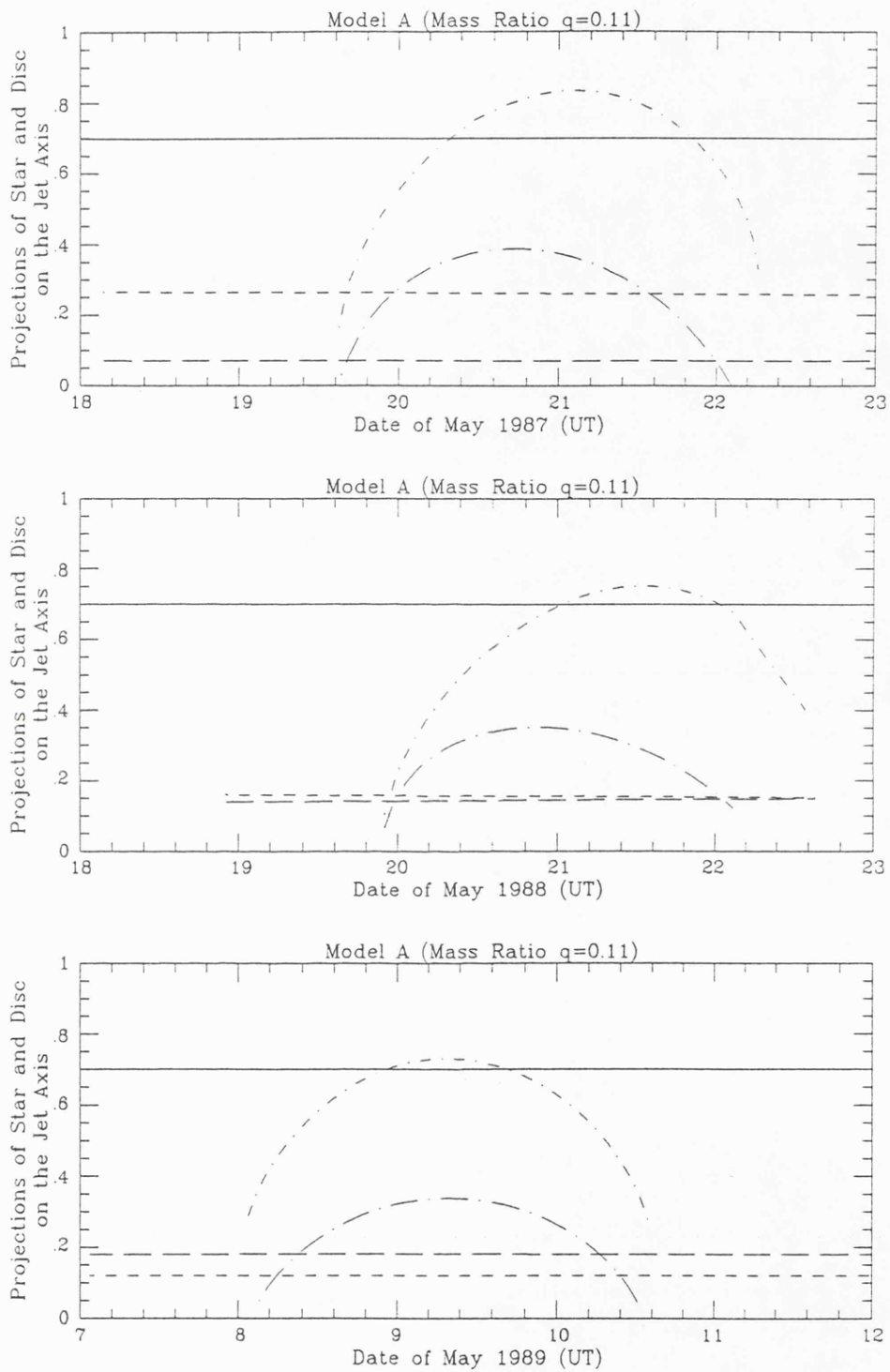


Figure D.4: Projections of the star and the accretion disc onto the jet axis. Model A, $q=0.11$. Here the solid line represents the jet length, the dot-long-dash line is the projection of the star on the top jet and the dot-short-dash line, the star projection on the bottom jet. The long-dash and the short-dash lines indicate the projections of the accretion disc onto the top and bottom jet respectively.

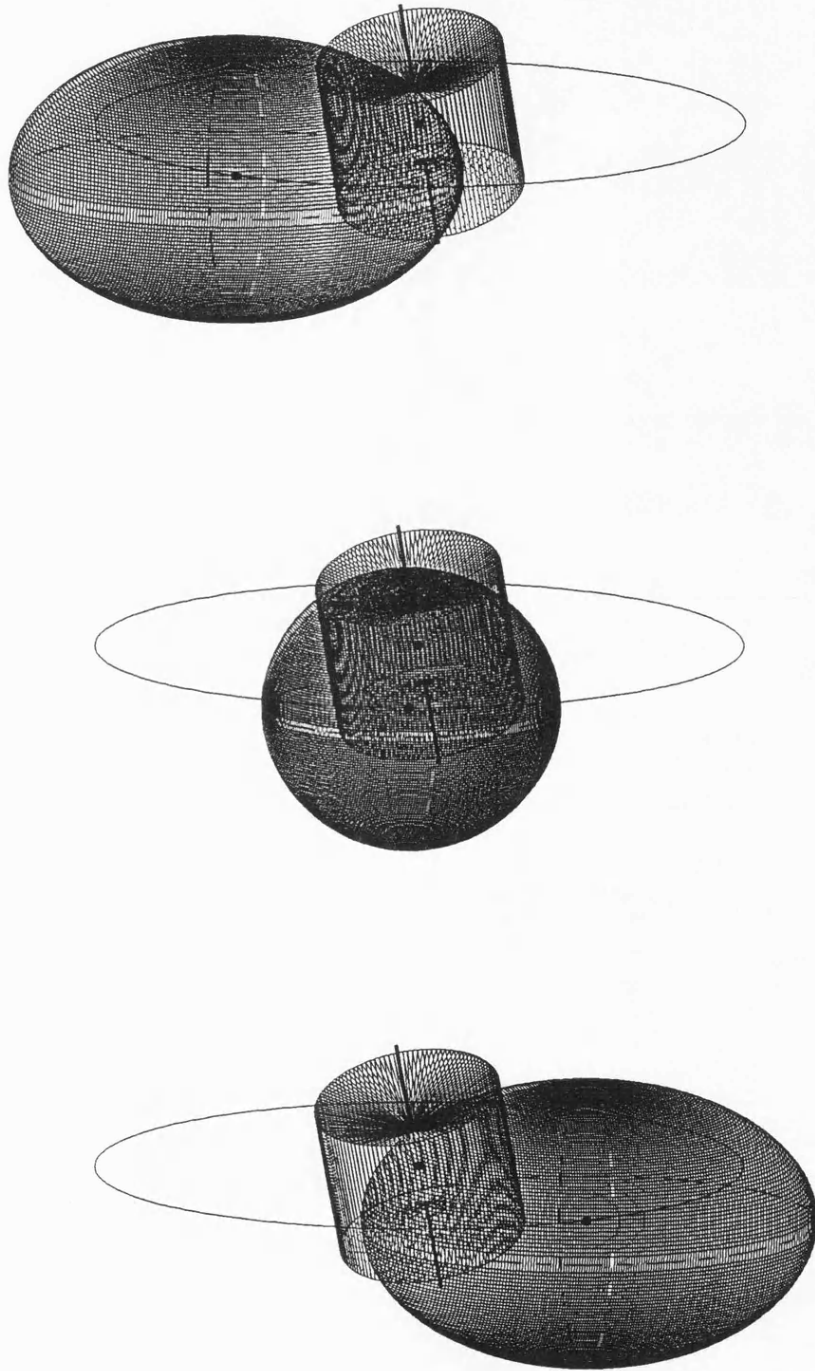


Figure D.5: Configurations of Model B with $q=0.40$ in 1987 May (jet precession phase: 0.58). Top: at binary phase 0.90; Mid: at 0.99; Bottom: at 1.08. The effects of the stellar wind and accretion flow make the star appear bigger than its Roche lobe.

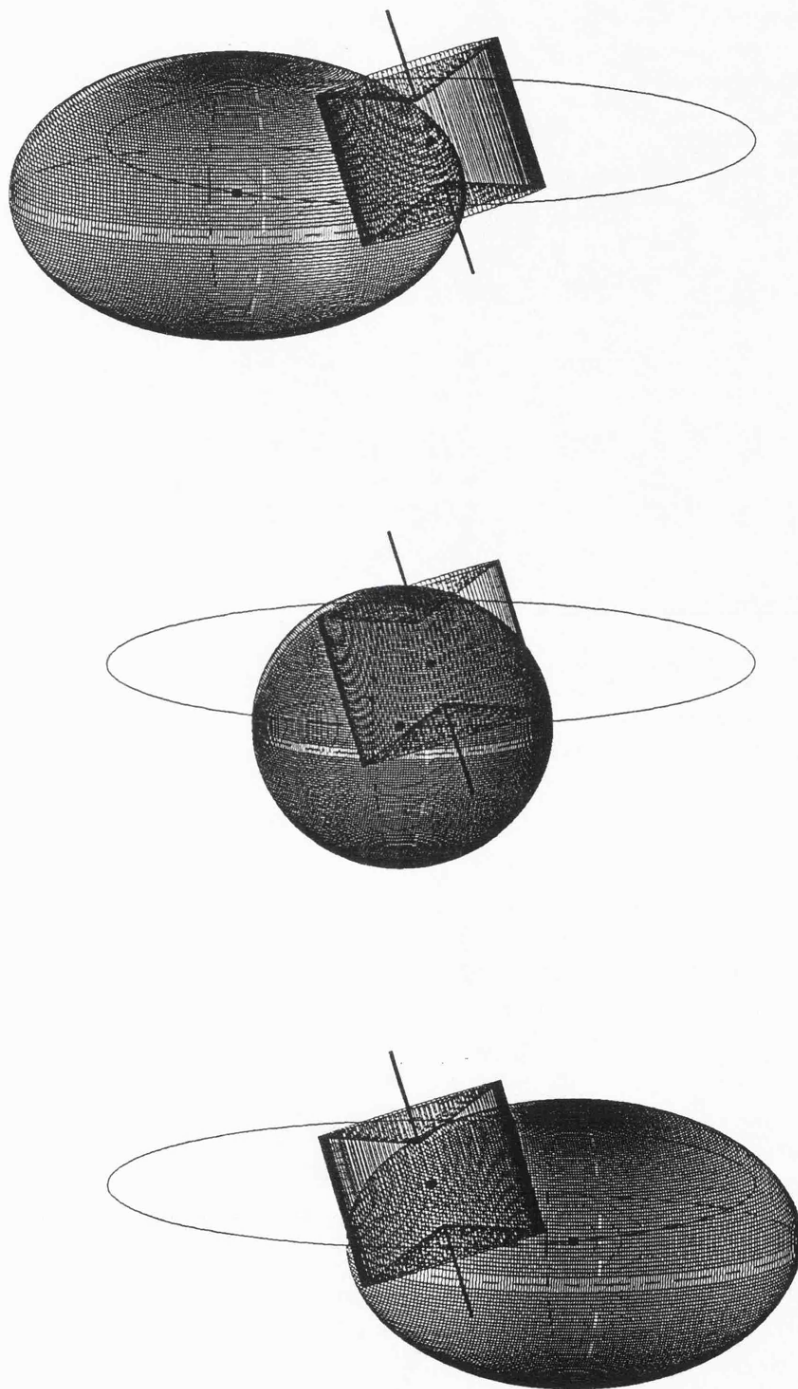


Figure D.6: Configurations of Model B with $q=0.40$ in 1988 May (jet precession phase: 0.83). Top: at binary phase 0.90; Mid: at 0.99; Bottom: at 1.07. The effects of the stellar wind and accretion flow make the star appear bigger than its Roche lobe.

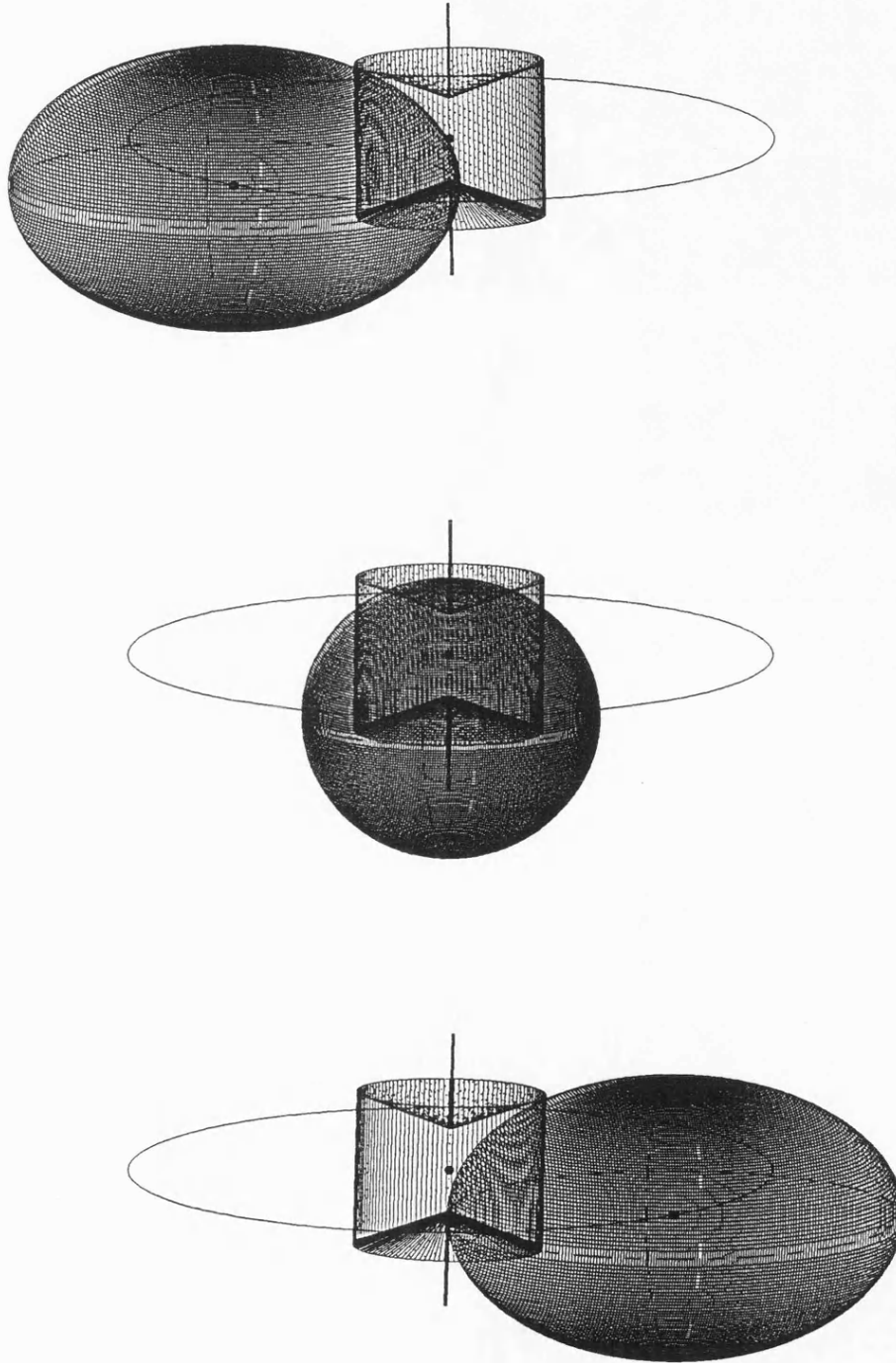


Figure D.7: Configurations of Model B with $q=0.40$ in 1989 May (jet precession phase: 1.0). Top: at binary phase 0.88; Mid: at 1.00; Bottom: at 1.12. The effects of the stellar wind and accretion flow make the star appear bigger than its Roche lobe.

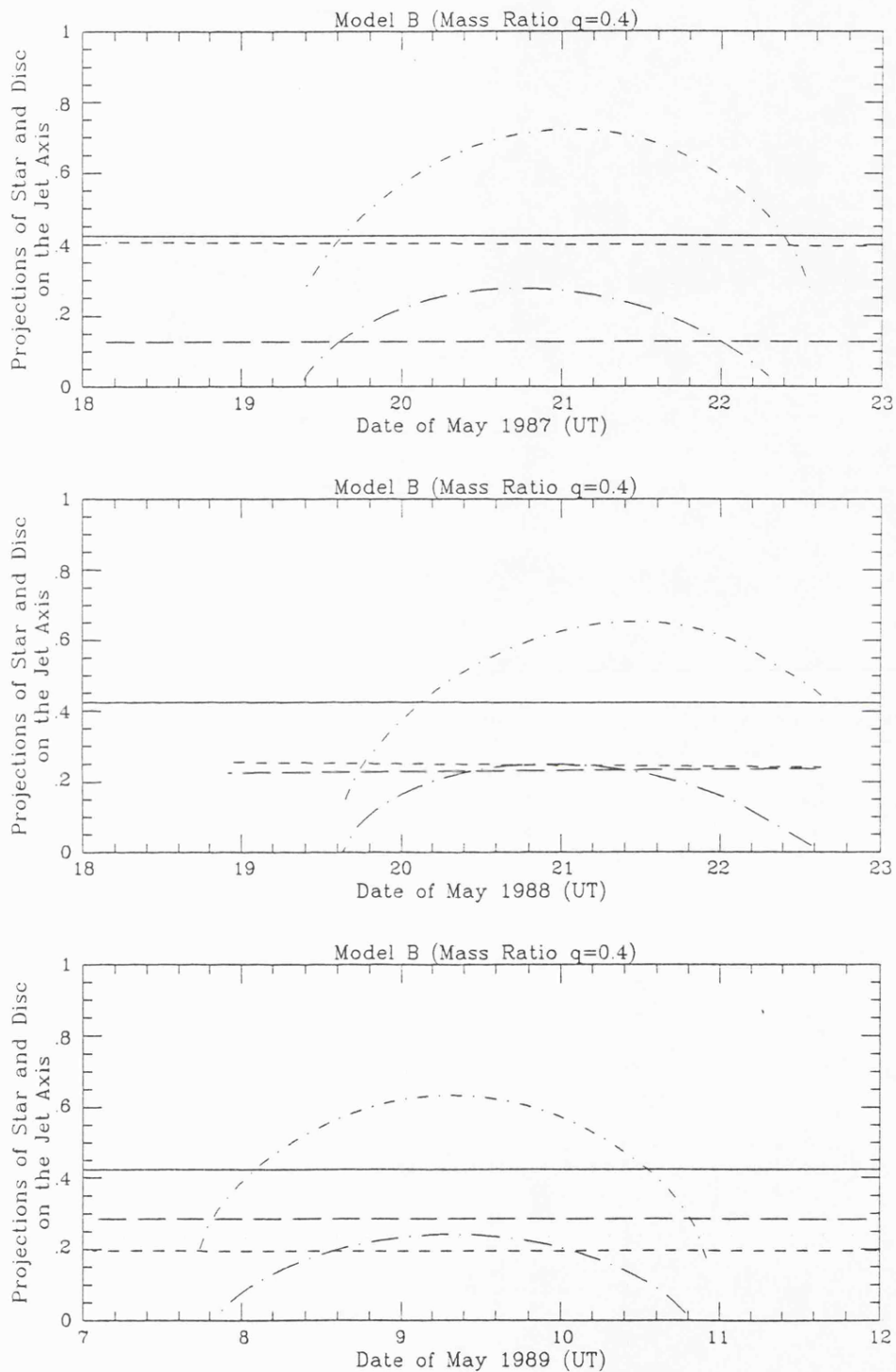


Figure D.8: Projections of the star and the accretion disc onto the jet axis. Model B, $q=0.40$. Here the solid line represents the jet length, the dot-long-dash line is the projection of the star on the top jet and the dot-short-dash line, the star projection on the bottom jet. The long-dash and the short-dash lines indicate the projections of the accretion disc onto the top and bottom jet respectively.

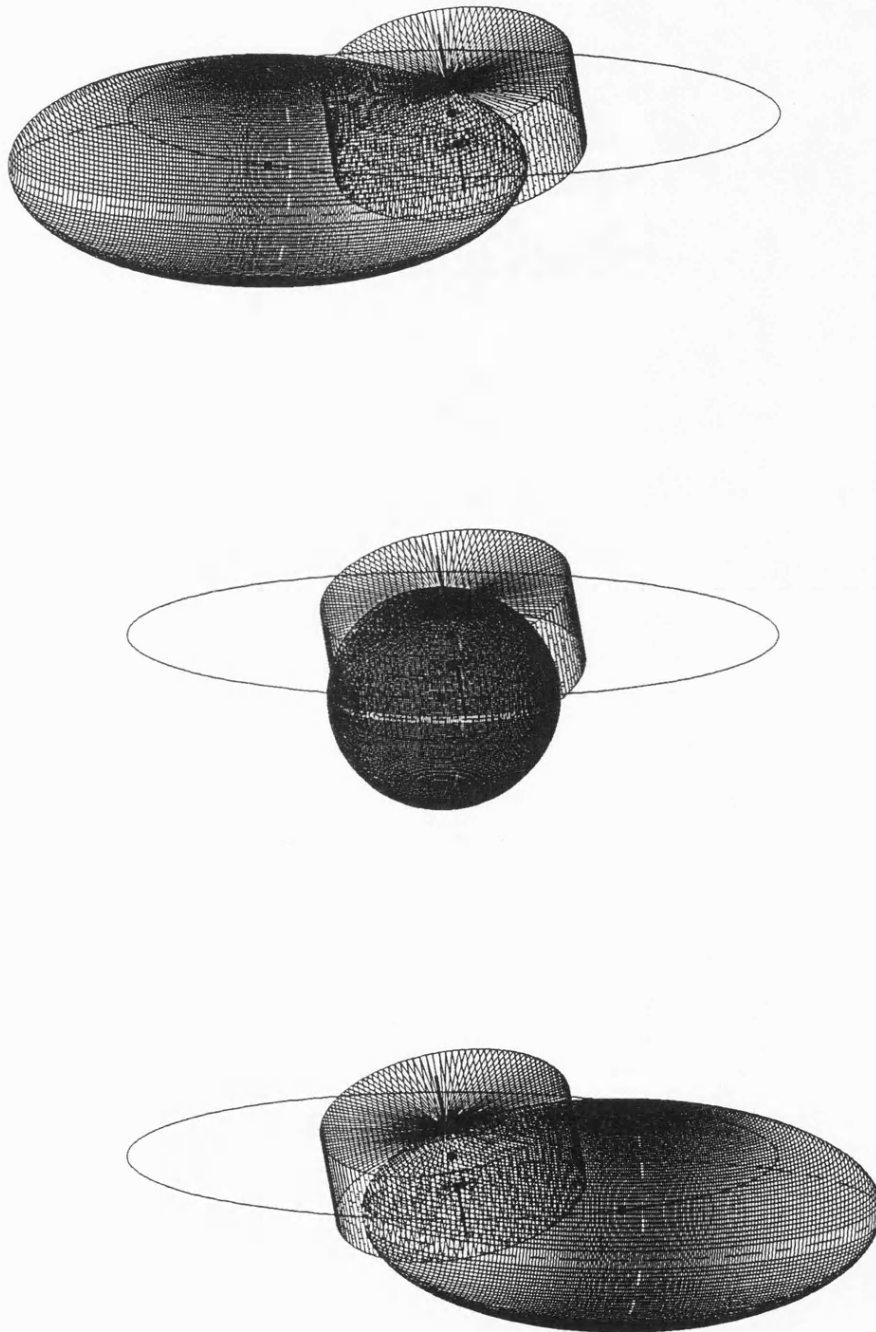


Figure D.9: Configurations of Model C with $q=1.20$ in 1987 May (jet precession phase: 0.58). Top: at binary phase 0.90; Mid: at 0.99; Bottom: at 1.08. The effects of the stellar wind and accretion flow make the star appear much bigger than its Roche lobe.

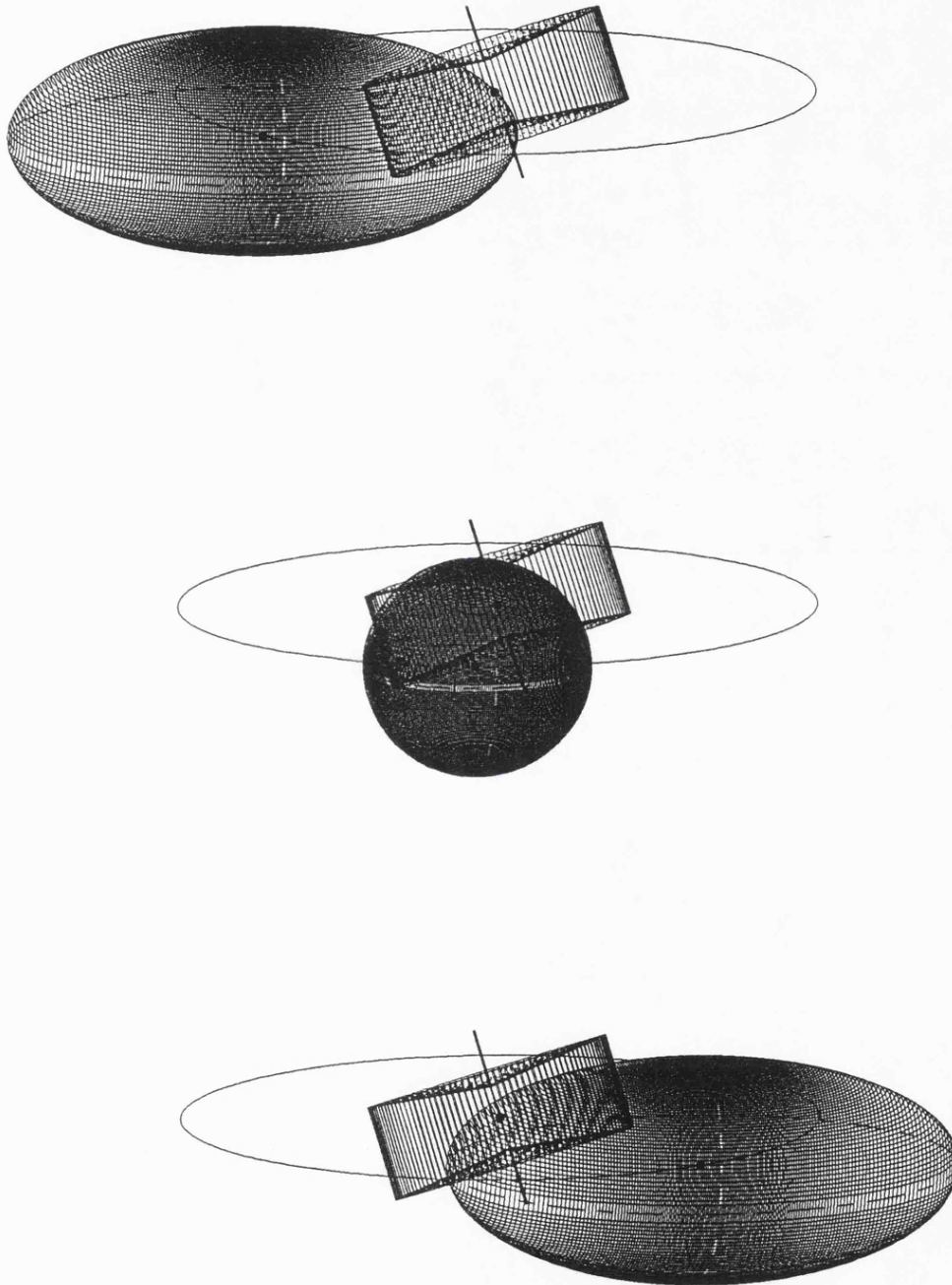


Figure D.10: Configurations of Model C with $q=1.20$ in 1988 May (jet precession phase: 0.83). Top: at binary phase 0.87; Mid: at 0.99; Bottom: at 1.11. The effects of the stellar wind and accretion flow make the star appear much bigger than its Roche lobe.

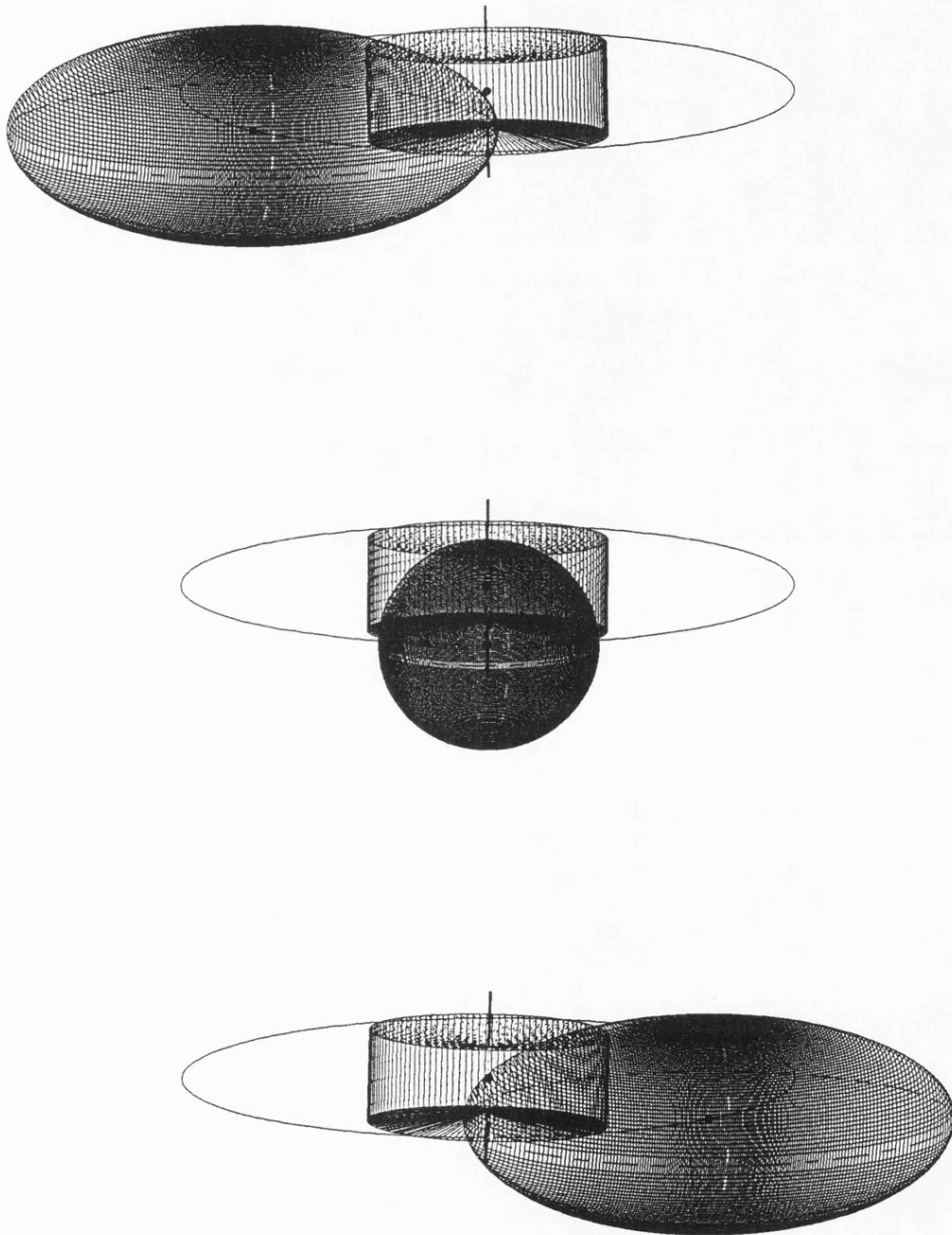


Figure D.11: Configurations of Model C with $q=1.20$ in 1989 May (jet precession phase: 1.0). Top: at binary phase 0.86; Mid: at 1.00; Bottom: at 1.13. The effects of the stellar wind and accretion flow make the star appear much bigger than its Roche lobe.

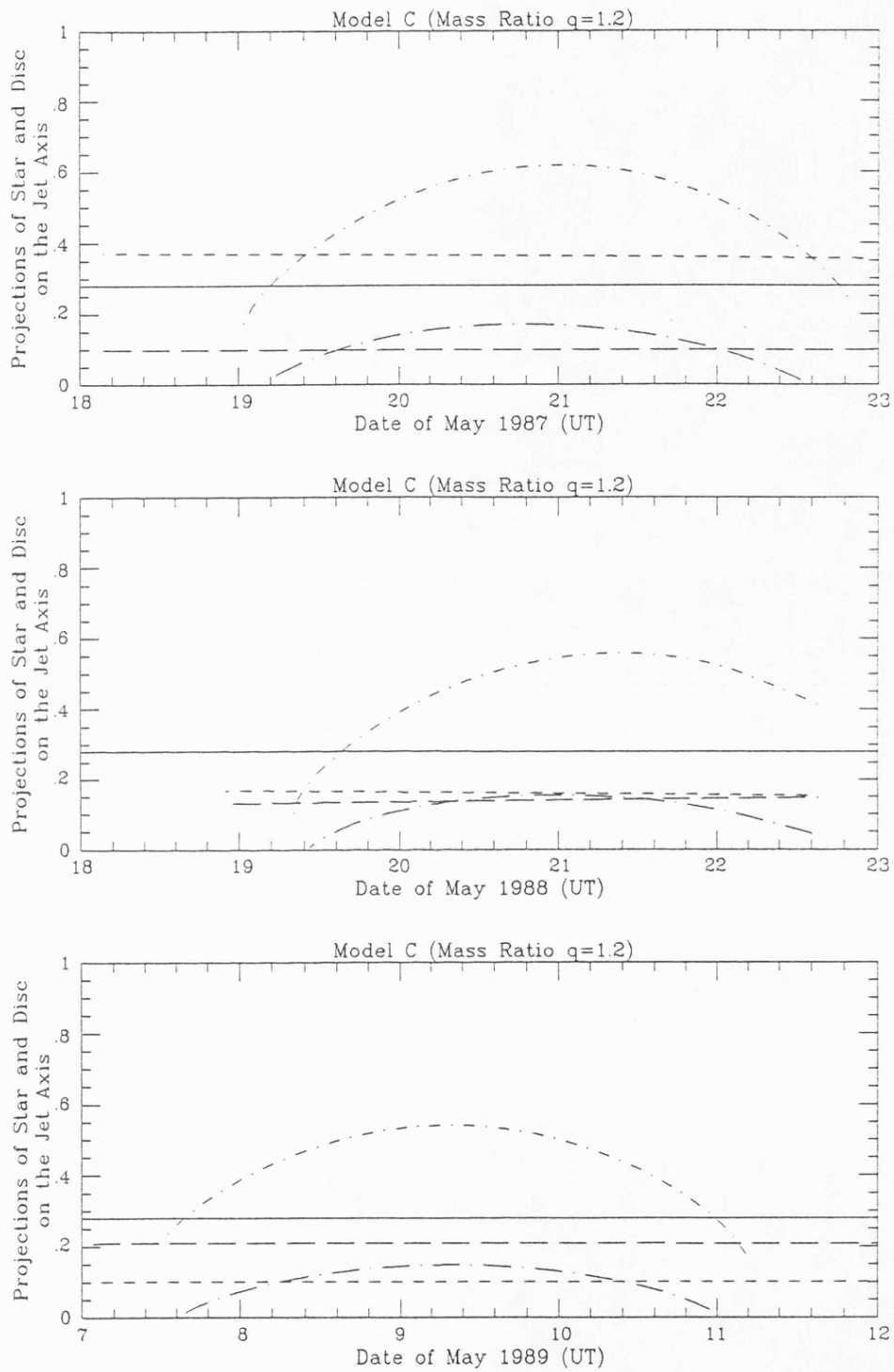


Figure D.12: Projections of the star and the accretion disc onto the jet axis. Model C, $q=1.20$. Here the solid line represents the jet length, the dot-long-dash line is the projection of the star on the top jet and the dot-short-dash line, the star projection on the bottom jet. The long-dash and the short-dash lines indicate the projections of the accretion disc onto the top and bottom jet respectively.

References

The following abbreviations for names of journals have been used in this thesis:

<i>Ann. Rev. Astron. Astrophys.</i>	Annual Reviews of Astronomy and Astrophysics
<i>Ap. Space Sci.</i>	Astrophysics and Space Science
<i>Astrophys. J.</i>	The Astrophysical Journal
<i>Astrophys. J. Suppl.</i>	The Astrophysical Journal Supplement Series
<i>Astrophys. J. (Letters)</i>	The Astrophysical Journal Letters
<i>Astrophys. Lett.</i>	Astrophysical Letters and Communications
<i>Astron. J.</i>	The Astronomical Journal
<i>Astron. Astrophys.</i>	Astronomy and Astrophysics
<i>Bull. American Astron. Soc.</i>	Bulletin of the American Astronomical Society
<i>Mon. Not. R. astr. Soc.</i>	Monthly Notices of the Royal Astronomical Society
<i>Phys. Scr.</i>	Physica Scripta
<i>Publ. Astron. Soc. Japan</i>	Publications of the Astronomical Society of Japan
<i>Publ. Astron. Soc. Pacific</i>	Publications of the Astronomical Society of the Pacific
<i>Rev. Mod. Physics</i>	Reviews of Modern Physics
<i>Sov. Astron.</i>	Soviet Astronomy
<i>Space Sci. Rev.</i>	Space Science Reviews
<i>Vista Astron.</i>	Vistas in Astronomy

- Abell, G.O., & Margon, B. 1979. *Nature*, **279**, 701.
- Abramowicz, M.A., & Sharp, N.A., 1983. *Ap. Space Sci.*, **96**, 431.
- Abramowicz, M.A., Lasota, J.P., & Xu, C., 1986. In: *Quasars*, eds Swarap, G., & Kapahi, V.K.
- Anderson, S.F., Margon, B., & Grandi, S.A., 1983. *Astrophys. J.*, **269**, 605.
- Antokhina, E.A., & Cherepashchuk, A.M., 1987. *Sov. Astron.*, **31**, 295.
- Arnaud, K.A., Branduardi-Raymond, G., Culhane, J.L., Fabian, A.C., Hazard, C., McGlynn, T.A., Shafer, R.A., Tennant, A.F., & Ward, M.J., 1985, *Mon. Not. R. astr. Soc.*, **217**, 105.
- Band, D.L., 1986. *Bull. American Astron. Soc.*, **18**, 949.
- Band, D.L., 1988. preprint.
- Band, D.L., & Grindlay, J.E., 1984. *Astrophys. J.*, **285**, 702.
- Band, D.L., & Grindlay, J.E., 1985. *Astrophys. J.*, **298**, 128.
- Bar, P., & Mushotzky, R.F., 1986. *Nature*, **320**, 421.
- Barlow, M.J., & Cohen, M., 1977. *Astrophys. J.*, **213**, 737.
- Begelman, M.C., Blandford, R.D., & Rees, M.J., 1984. *Rev. Mod. Phys.*, **56**, 255.
- Begelman, M.C., Sarazin, C.L., Hatchett, S.P., McKee, C.F., & Arons, I., 1980. *Astrophys. J.*, **238**, 722.
- Benvenuti, P., 1979. *IAUC*, 3370.
- Bergeron, J., Boksenberg, A., Dennefeld, M., & Tarenghi, M., 1983. *Mon. Not. R. astr. Soc.*, **202**, 125.
- Blandford, R.D., 1986. In: *Radiation Hydrodynamics in Stars and Compact Objects*, p.387 eds Mihalas, D. & Winkler, K.-H.A., (Springer-Verlag).
- Blandford, R.D., & Rees, M.J., 1974. *Mon. Not. R. astr. Soc.*, **169**, 395.
- Bodo, G., Ferrari, A., Massaglia, S., & Tsinganos, K., 1985. *Astron. Astrophys.*, **149**, 246.
- Bridle, A.H., & Perley, R.A., 1984. *Ann. Rev. Astron. Astrophys.*, **22**, 319.
- Brinkmann, W., Fink, H.H., Massaglia, S., Bodo, G., & Ferrari, A., 1988. *Astron. Astrophys.*, **196**, 313.

- Calvani, M., & Nobili, L., 1981. *Ap. Space Sci.*, **79**, 387.
- Calvani, M., & Nobili, L., 1983. In: *Astrophysical Jets*, p.189, eds Ferrari, A., & Pacholczyk, A.G., (Reidel, Dordrecht)
- Canizares, C.R., McClintock, J.E., & Ricker, G.R., 1978. *Astrophys. J. (Letters)*, **226**, L1.
- Clark, T.A., & Milone, E.F., 1981. *Publ. Astron. Soc. Pacific*, **93**, 338.
- Cooke, B.A., Ricketts, M.J., Maccacaro, T., Pye, J.P., Elvis, M., Watson, M.G., Griffiths, R.E., Pounds, K.A., McHardy, I., Maccagni, D., Seward, F.D., Page, C.G., & Turnur, M.J.L., 1978. *Mon. Not. R. astr. Soc.*, **182**, 489.
- Crampton, D., & Hutchings, J.B., 1981. *Vista Astron.*, **25**, 13.
- Crampton, D., & Hutchings, J.B., 1981. *Astrophys. J.*, **251**, 604.
- Davidson, K., & McCray, R., 1980. *Astrophys. J.*, **241**, 1082.
- de Korte, P.A.J., Bleeker, J.A.M., den Boggende A.J.F., Branduardi-Raymont, G., Brinkman, A.C., Culhane, J.L., Gronenschild, E., Mason, I., & McKechnie, S.P., 1981. *Space Sci. Rev.*, **30**, 495.
- Dopita, M.A., & Cherepashchuk, A.M., 1981. *Vista Astron.*, **25**, 51.
- Dreher, J.W., & Feigelson, E.D., 1984. *Nature*, **308**, 43.
- Elvis, M., Lockman, F.J., & Wilkes, B.J., 1989. *Astron. J.*, in press.
- EXOSAT Observers Guide II, ESA.
- Falomo, R., Buksenberg, A., Tanzi, E.G., Tarengki, M., & Treves, A., 1987. *Mon. Not. R. astr. Soc.*, **224**, 323.
- Ferland, G.J., & Mushotzky, R.F., 1982. *NASA Tech. Memo. No. 83945*
- Ferland, G.J., & Rees, M.J., 1988. *Astrophys. J.*, **332**, 141.
- Ferland, G.J., & Truran, J.W., 1981. *Astrophys. J.*, **244**, 1022.
- Fesen, R.A., & Gull, T.R., 1986. *Astrophys. J.*, **306**, 259.
- Forman, W., Jones, C., Cominsky, L., Julien, P. Murray, S., Peters, G., Tananbaum, H., & Giacconi, R., 1978. *Astrophys. J. Suppl.*, **38**, 357.
- Frank, J., King, A.R., & Raine, D.J., 1985. *Accretion power in astrophysics*, The University of Cambridge Press.
- Fukue, J., 1982. *Publ. Astron. Soc. Japan*, **34**, 163.

- Fukue, J., 1983. *Publ. Astron. Soc. Japan*, **35**, 539.
- Fukue, J., 1987. *Publ. Astron. Soc. Japan*, **39**, 679.
- Gaskell, C.M., 1987. In: *Astrophysical Jets and Their Engines*, p.29, eds Kundt, W., (Reidel, Dordrecht).
- Giacconi, R., 1980. In: *X-Ray Astronomy*, eds Giacconi, R., & Setti, G., (Reidel, Dordrecht).
- Gilmore, W.S., & Seaquist, E.R., 1980. *Astron. J.*, **85**, 1486.
- Gilmore, W.S., Seaquist, E.R., Stocke, J.T., & Crane, P.C., 1981. *Astron. J.*, **86**, 864.
- Glandyshev, S.A., Goranskii, V.P., & Cherepashchuk, A.M., 1987. *Sov. Astron.*, **31**, 541.
- Glass, I.S., 1981. *Mon. Not. R. astr. Soc.*, **194**, 795.
- Goranskii, V.P., 1987, Private Communication.
- Gorenstein, P., 1975. *Astrophys. J.*, **198**, 95.
- Grindlay, J.E., Band, D., Seward, F., Leahy, D., Weisskopf, M.C., & Marshall, F.E., 1984. *Astrophys. J.*, **277**, 286.
- Guilbert, P.W., & Rees, M.J., 1988. *Mon. Not. R. astr. Soc.*, **233**, 475.
- Halpern, J.P., 1984. *Astrophys. J.*, **281**, 90.
- Hayashida, K., Inoue, H., Koyama, K., Awaki, H., Takano, S., Tawara, Y., Williams, O.R., Denby, M., Stewart, G.C., Turner, M.J.L., Makishima, K., & Ohashi, T., 1989. *Publ. Astron. Soc. Japan*, **41**, 373.
- Hjellming, R.M., & Johnston, K.J., 1981a. *Nature*, **290**, 100.
- Hjellming, R.M., & Johnston, K.J., 1981b. *Astrophys. J. (Letters)*, **246**, L141.
- Hjellming, R.M., & Johnston, K.J., 1985. In: *Radio Stars*, p.309, eds Hjellming, R.M., & Gibson, D.M., (Reidel, Dordrecht).
- Holt, S.S., Mushotzky, R.F., Becker, R.H., Boldt, E.A., Serlemitsos, P.J., Szymkowiak, A.E. & White, N.E., 1980. *Astrophys. J.*, **241**, L13.
- Hyland, A.R., & Allen, D.A., 1982. *Mon. Not. R. astr. Soc.*, **199**, 943.
- Ikeuchi, S., 1988. In: *Physics of Neutron Stars and Black Holes*, p.345, eds Tanaka, Y., Universal Academy Press, Tokyo.
- Johnston, K.J., Santini, N.J., Spencer, J.H., Klepczynski, W.J., Kaplan, G.H., Josties,

- F.J., Angerhofer, P.E., Florkowski, D.R., & Matsukis, D.N., 1981. *Astron. J.*, **86**, 1377.
- Johnston, K.J., Geldzahler, B.J., Spencer, J.H., Waltman, E.B., Klepczynski, W.J., Josties, F.J., Angerhofer, P.E., Florkowski, D.R., McCarthy, D.D., & Matsukis, D.N., 1984. *Astron. J.*, **89**, 509.
- Kallman, T.R., & McCray, R., 1982. *Astrophys. J. Suppl.*, **50**, 263.
- Katz, J.I., 1980. *Astrophys. J. (Letters)*, **236**, L127.
- Katz, J.I., Anderson, S.F., Margon, B., & Grandi, S.A., 1982. *Astrophys. J.*, **260**, 780.
- Katz, J.I., & Piran, T., 1982. *Astrophys. Lett.*, **23**, 11.
- Kemp, J.C., Henson, G.D., Kraus, D.J., Carrol, L.C., Beardsley, I.S., Takagishi, K., Jugaku, J., Matsuoka, M., Leibowitz, E.M., Mazeh, T., & Mendelson, H., 1986. *Astrophys. J.*, **305**, 805.
- Kodaira, K., & Lenzen, R., 1983. *Astron. Astrophys.*, **126**, 440.
- Kodaira, K., Nakada, Y., & Backman, D.E., 1985. *Astrophys. J.*, **296**, 232.
- Kopylov, I.M., Kumaigorodskaya, R.N., & Somova, T.A., 1985. *Sov. Astron.*, **29**, 186.
- Kopylov, I.M., Kumaigorodskaya, R.N., Somova, N.N., Somova, T.A., & Fabrika, S.N., 1986. *Sov. Astron.*, **30**, 408.
- Koyama, K., Makishima, K., Tanaka, Y., & Tsunemi, H., 1986. *Publ. Astron. Soc. Japan*, **38**, 121.
- Kriss, G.A., Cioffi, D., & Canizares, C.R., 1983. *Astrophys. J.*, **272**, 439.
- Krolik, J.H., 1988. In: *Physics of Neutron Stars and Black Holes*, p.137, eds Tanaka, Y., Universal Academy Press, Tokyo.
- Kundt, W., 1987. eds *Astrophysical Jets and Their Engines*, (Reidel, Dordrecht)
- Kwan, J., & Krolik, J.H., 1981. *Astrophys. J.*, **250**, 478.
- Lamb, P., & Sanford, P.W., 1979. *Mon. Not. R. astr. Soc.*, **188**, 555.
- Lamb, R.C., Ling, J.C., Mahoney, W.A., Riegler, G.R., Wheaton, W.A., & Jacobson, A.S., 1983. *Nature*, **305**, 37.
- Lampton, M., Margon, B., & Bowyer, S., 1976. *Astrophys. J.*, **208**, 177.
- Lawrence, A., 1987. *Publ. Astron. Soc. Pacific*, **99**, 309.
- Leibowitz, E.M., 1984. *Mon. Not. R. astr. Soc.*, **210**, 279.

- Leibowitz, E.M., Mazeh, T., Mendelson, H., Kemp, J.C., Barbour, M.S., Takagishi, K., Jugaku, J., & Matsuoka, M., 1984. *Mon. Not. R. astr. Soc.*, **206**, 751.
- Lightman, A.P., & White, T.R., 1988. *Astrophys. J.*, **335**, 57.
- Lynden-Bell, D., 1978. *Phys. Scr.*, **17**, 185.
- Makino, F., 1987. *Astrophys. Lett. and Communications*, **25**, 223.
- Margon, B., Ford, H.C., Katz, J.I., Kwitter, K.B. Ulrich, R.K. Stone, R.P.S., & Kle-mola, A., 1979. *Astrophys. J. (Letters)*, **230**, L41.
- Margon, B., 1981. *Ann. NY Acad. Sci.* **374**, 403
- Margon, B., 1984. *Ann. Rev. Astron. Astrophys.*, **22**, 507.
- Marshall, F.E., Swank, J.H., Boldt, E.A., Holt, S.S. & Serlemitsos, P.J. 1979. *Astrophys. J. (Letters)*, **230**, L145.
- Marshall, N., Warwick, R.S., & Pounds, K.A., 1981. *Mon. Not. R. astr. Soc.*, **194**, 987.
- Matsuoka, M., Takano, S., & Makishima, K., 1986. *Mon. Not. R. astr. Soc.*, **222**, 605.
- McAlary, C.W., & McLaren, R.A., 1980. *Astrophys. J.*, **240**, 853.
- McAlary, C.W., McLaren, R.A., McGonegal, R.J., & Maza, J., 1983. *Astrophys. J. Suppl.*, **52**, 341.
- McHardy, I.M., Lawrence, A., Pye, J.P., & Pounds, K.A., 1981. *Mon. Not. R. astr. Soc.*, **197**, 893.
- Mihalas, D. & Winkler, K.-H.A., 1986. eds *Radiation Hydrodynamics in Stars and Compact Objects*, (Springer-Verlag).
- Milgrom, M., 1979. *Astron. Astrophys.*, **76**, L3.
- Milgrom, M., 1979. *Astron. Astrophys.*, **78**, L9.
- Milgrom, M., 1981. *Vista Astron.*, **25**, 141.
- Morrison, R., & McCammon, D., 1983. *Astrophys. J.*, **270**, 119.
- Murdin, P., Clark, D.H., & Martin, P.G., 1980. *Mon. Not. R. astr. Soc.*, **193**, 135.
- Mushotzky, R.F., 1982. *Astrophys. J.*, **256**, 92.
- Nandra, K., Pounds, K.A., Stewart, G.C., Fabian, A.C., & Rees, M.J., 1989. *Mon. Not. R. astr. Soc.*, **236**, 39.

- Netzer, H., 1987. In: *Astrophysical Jets and Their Engines*, p.103, eds Kundt, W., (Reidel, Dordrecht)
- Neugebauer, G., Soifer, B.T., Matthews, K., Margon, B., & Chanan, G.A., 1982. *Astrophys. J.*, **82**, 1639.
- Nobili, L., Calvani, M., & Turolla, R., 1985. *Mon. Not. R. astr. Soc.*, **214**, 161.
- Paczynski, B., 1971. *Ann. Rev. Astron. Astrophys.*, **9**, 183.
- Parmar, A.N., & Izzo, C., 1986. *EXOSAT Express*, **16**, 21.
- Peacock, A., Andresen, R.D., Manzo, G., Taylor, B.G., Villa, G., Re, S., Ives, J.C., & Kellock, S., 1981. *Space Sci. Rev.*, **30**, 525.
- Pekarevich, M., Piran, T., & Shaham, J., 1984., *Astrophys. J.*, **283**, 295.
- Peterson, L.E., 1975. *Ann. Rev. Astron. Astrophys.*, **13**, 423.
- Phillips, M.M., 1980. *Astrophys. J.*, **236**, L45.
- Piran, T., 1982. *Astrophys. J. (Letters)*, **257**, L23.
- Pounds, K.A., Stanger, V.J., Turner, T.J., King, A.R., & Czerny, B., 1986. *Mon. Not. R. astr. Soc.*, **224**, 443.
- Pozdnyakov, L.A., Sobol, I.M., & Sunyaev, R.A., 1979. *Astron. Astrophys.*, **75**, 214.
- Pringle, J.E., & Wade, R.A., 1985. *Interacting binary stars*, The University of Cambridge Press.
- Rees, M.J., Begelman, M.C., Blandford, R.D., & Phinney, E.S., 1982. *Nature*, **295**, 17.
- Reichert, G.A., Mushotzky, R.F., Petre, R., & Holt, S.S., 1985. *Astrophys. J.*, **296**, 69.
- Ricker, G.R., Clarke, G.W., Doxsey, R.E., Dower, R.G., Jernigan, J.G., Delvaille, J.P., MacAlpine, G.M., & Hjellming, R.M., 1978. *Nature*, **271**, 35.
- Ricker, G.R., Clarke, G.W., Doxsey, R.E., Dower, R.G., Jernigan, J.G., Canizares, C.R., Delvaille, J.P., MacAlpine, G.M., & Hjellming, R.M., 1979. *X-ray Astronomy*, P.281, eds Baity, W.A., & Peterson, L.E., Pergamon, Oxford
- Ricketts, M.J., Hall, R., Page, C.G., Pounds, K.A., & Sims, M.R., 1981. *Vista Astron.*, **25**, 71.
- Rothschild, R.E., Mushotzky, R.F., Baity, W.A., Gruber, D.E., Matteson, J.L., & Peterson, L.E., 1983. *Astrophys. J.*, **269**, 423.
- Ryle, M., Caswell, J.L., Hine, G. & Shakeshaft, J. 1978. *Nature*, **276**, 571.

- Sarazin, C.L., Begelman, M.C., & Hatchett, S.P., 1980.
Astrophys. J. (Letters), **238**, L129.
- Seaquist, E.R., 1981. *Vista Astron.*, **25**, 79.
- Seaquist, E.R., Gilmore, W.S., Johnston, K.J., & Grindlay, J.E., 1982.
Astrophys. J., **260**, 220.
- Seward, F., Grindlay, J., Seaquist, E., & Gilmore, W., 1980. *Nature*, **287**, 806.
- Seward, F.D., Page, C.G., Turner, M.J.L. & Pounds, K.A., 1976.
Mon. Not. R. astr. Soc., **175**, 39.
- Shaham, J., 1981. *Vista Astron.*, **25**, 217.
- Shapiro, P.R., Milgrom, M., & Rees, M.J., 1986. *Astrophys. J. Suppl.*, **60**, 393.
- Sikora, M., & Wilson, D.B., 1981. *Mon. Not. R. astr. Soc.*, **197**, 529.
- Smith M., Carswell, R., Whelan, J., Wilkes, B., Boksenberg, A., Clowes, R., Savage, A., Cannon, R., & Wall, J., 1981. *Mon. Not. R. astr. Soc.*, **195**, 437.
- Stewart, G.C., Watson, M.G., 1986. In: *The Physics of Accretion onto Compact Objects*, eds Mason, K.O, Watson, M.G., & White, N.E.
- Stewart, G.C., Watson, M.G., Matsuoka, M., Brinkmann, W., Jugaku, J., Takagishi, K., Omodaka, T., Kemp, J.C., Kenson, G.D., Kraus, D.J., Mazeh, T., Leibowitz, E.M., 1987. *Mon. Not. R. astr. Soc.*, **228**, 293.
- Strittmatter, P.A., & Williams R.E., 1976. *Ann. Rev. Astron. Astrophys.*, **14**, 307.
- Taylor, B.G., Andresen, R.D., Peacock, A., Zobl, R., 1981. *Space Sci. Rev.*, **30**, 479.
- Tucker, W.H., 1975. *Radiation Processes In Astrophysics*, The MIT Press.
- Turner, M.J.L., Smith, A., & Zimmermann, H.U., 1981. *Space Sci. Rev.*, **30**, 513.
- Turner, M.J.L., Thomas, H.D., Patchett, B.E., Reading, D.H., Makishima, K., Ohashi, T., Dotani, T., Hayashida, K., Inoue, H., Kondo, H., Koyama, K., Mitsuda, K., Ogawara, Y., Takano, S., Awaki, H., Tawara, Y., & Nakamura, N., 1989.
Publ. Astron. Soc. Japan, **41**, 345.
- Turner, T.J., & Pounds, K.A., 1989. *Mon. R. astr. Soc.*, in press.
- Ulrich, M.-H., 1988. *Mon. Not. R. astr. Soc.*, **230**, 121.
- van den Heuvel, E.P.J., Ostriker, J.P., & Petterson, J.A., 1980.
Astron. Astrophys., **81**, L7.
- Vermeulen, R., 1989. PhD Thesis, Leiden University.

- Wagner, R.M., 1983. *Bull. American Astron. Soc.*, **14**, 880.
- Warwick, R.S., Pounds, K.A., & Turner, T.J., 1988.
Mon. Not. R. astr. Soc., **231**, 1145.
- Warwick, R.S., Turner, M.J.L., Watson, M.G., & Willingale, R., 1985.
Nature, **317**, 218.
- Watson, M.G., Stewart, G.C., Brinkmann, W., & King, A.R., 1986.
Mon. Not. R. astr. Soc., **222**, 261.
- Watson, M.G., Willingale, R., Grindlay, J.E., & Seward, F.D., 1983.
Astrophys. J., **273**, 688.
- White, N.E., & Peacock, A., 1988. In: *X-Ray Astronomy With EXOSAT*, p.7, eds
Pallavicini, R., & White, N.E.
- Wynn-Williams, C.G., & Becklin, E.E., 1979. *Nature*, **282**, 810.
- Yaqoob, T., Warwick, R.S., & Pounds, K.A., 1989. *Mon. Not. R. astr. Soc.*, **236**, 153.
- Zealey, W.J., Dopita, M.A., & Malin, D., 1980. *Mon. Not. R. astr. Soc.*, **192**, 73.
- Zwitter, T., Calvani, M., Bodo, G., & Massaglia, S., 1989.
Fundamentals of Cosmic Physics.

Acknowledgements

The work reported in this thesis was carried out under the supervision of Gordon Stewart. It is my pleasure to express my deeply thanks to him, for his encouragement, constructive suggestions and his kindness. Without his help, this thesis would not have been possible.

I would like to extend my thanks to Ken Pounds for allowing me to do my PhD research in the X-ray astronomy group, to Mike Watson for his help and encouragement in the study of SS 433. I also owe a lot to Rees Williams for his patient and kind help in every aspect, to Alastair Edge for his help from the very beginning of this work. I would also like to express my hearty thanks to the many other people in the group for their friendship and assistance during the period I have been in Leicester.

I would like to take this chance to thank Prof. K. Makishima, Dr. T. Ohashi for their hospitality during a visit to Tokyo and their support, and Prof. W. Kundt for his stimulating discussions on SS 433.

Finally, I acknowledge receipt of a research studentship from the Chinese Academy of Sciences.

X-RAY OBSERVATIONS OF SS 433 AND THE QSO MR 2251 – 178

Hongchao Pan

ABSTRACT

This thesis reports the results of the X-ray observations of the galactic binary source SS 433 and the QSO MR 2251 – 178 made with the *EXOSAT* and *GINGA* X-ray satellites.

The *EXOSAT* and *GINGA* study of SS 433 shows that both the X-ray intensity and spectrum of the binary vary over the periods of the 163 day jet precession and the 13 day binary motion. The X-ray luminosity of SS 433 is high at the phase corresponding to the maximum separation of the Doppler-shifted optical lines, and low when the jets become edge-on. An intensity decrease of up to 50% can be seen in each energy channel while the source changes from high to low luminosity. Over the 13 day binary cycle, the X-ray sources are eclipsed by the companion star at the phase of the primary optical minimum. Five such events were observed by the *EXOSAT* and *GINGA* satellites at different phases of jet precession. The X-ray spectrum of SS 433 consists of a thermal continuum and a Doppler energy shifted broad emission line. It is proved, in this thesis, that the X-ray emission of SS 433 originates in the jets and is thermal in nature. The X-ray sources of SS 433 are stable and its properties are strongly modulated by the relativistic motion of the X-ray emitting material in the jets, the jet precession and the binary motion. With the constraints from the X-ray observations, a general picture of the X-ray jets of SS 433 is established in this thesis. The X-ray jets are a continuous super-sonic plasma flow and are generated inside the funnels of a thick accretion disc located around a black hole.

Variable X-ray absorption and soft X-ray excess are found in the X-ray spectrum of MR 2251 – 178 with the *EXOSAT* observations. While there is an overall correlation between the ME(2-10 keV) and LE(0.1-2 keV) fluxes the pattern of variability can not be described by simple intensity, absorption or slope variations. It is shown, in this thesis, that it is possible to explain all the observed features by adopting the 'warm' absorber model in which the absorbing material is partially ionized by the flux of extreme ultra-violet and X-ray photons from the central continuum source. The preferred location of the absorbing material is close to the central continuum source. The recent evidence for 'cool' material in the centre of Seyfert galaxies is thus extended to include an object of significantly higher luminosity.

